Title

Probing Active Sites and Their Evolution in Surface Catalysts: From Electrochemical to Thermal Environments

Permalink

https://escholarship.org/uc/item/1sq3s128

Author

Kumari, Simran

Publication Date

2023

UNIVERSITY OF CALIFORNIA

Los Angeles

Probing Active Sites and Their Evolution in Surface Catalysts: From Electrochemical to Thermal Environments

A dissertation submitted in partial satisfaction of the
requirements for the degree Doctor of Philosophy
in Chemical Engineering

by

Simran Kumari

2023

ABSTRACT OF THE DISSERTATION

Probing Active Sites and Their Evolution in Surface Catalysts: From Electrochemical to Thermal Environments

by

Simran Kumari
Doctor of Philosophy in Chemical Engineering
University of California, Los Angeles, 2023
Professor Philippe Sautet, Chair

The urgent global need for sustainable solutions has propelled the search for efficient catalytic systems. This thesis focuses on key reactions crucial for achieving a greener and more sustainable future. Employing computational techniques and theoretical models, the research investigates catalytic processes to unravel fundamental principles, guiding the design of advanced catalysts. The thesis leads to a comprehensive exploration of the hydrogen evolution reaction (HER), oxygen evolution reaction (OER), partial oxidation of methane to methanol, and CO_2 hydrogenation. By elucidating the structure, stability, and catalytic reactivity of diverse clusters and surfaces, the research aims to develop efficient and sustainable catalytic systems.

Emphasizing accurate characterization of active site composition and understanding catalyst behavior under reaction conditions, the thesis employs first-principles density functional theory (DFT) calculations to determine optimal doping sites and structures for Sn atoms on the

Sn-doped Indium Oxide (ITO) surface. The interaction between the ITO surface and Pt clusters is also explored, providing insights into the role of active sites in catalytic reactivity. Investigating small Pt clusters supported on ITO in HER, a size-dependent activity trend is uncovered, highlighting the catalytic potential of Pt hydride compounds. The inclusion of metastable isomers in microkinetic models emphasizes the significance of considering accessible isomer ensembles for accurate simulations of sub-nano supported cluster catalysts. Furthermore, the thesis unravels the intricate mechanism of OER, identifying the rate-determining step and changes in the oxidation state of Pt surface atoms (Pt-SA) during the catalytic cycle. Understanding electron transfer contributions from both Pt-SA and the ITO surface provides valuable insights for designing efficient OER catalysts. In the context of partial oxidation of methane to methanol, the research explores electrochemical methods for catalyst deposition, focusing on thin-film transition metal (oxy)hydroxides. The activity and selectivity of various catalysts are investigated, emphasizing control over kinetics and mass transfer for sustainable methanol production.

Finally, the thesis investigates CO_2 hydrogenation, a promising avenue for converting carbon dioxide into valuable chemicals. Analyzing the $Zr_3O_xOH_y\ (HCOO)_z/Cu111$ cluster under different reaction conditions, the research unveils the pivotal role of hydroxyls and HCOOs in shaping the reaction mechanism. Electronic insights guide the design of catalysts with optimal properties, potentially enhancing catalytic performance. By integrating computational modeling and experimental characterization techniques, this research enhances our understanding of critical catalytic reactions. The findings underscore the importance of active site composition, surface structures, and electronic properties in determining catalytic reactivity. The synergy between theory and experiment holds promising prospects for designing advanced catalysts with improved activity, selectivity, and stability.

The dissertation of Simran Kumari is approved.

Anastassia N. Alexandrova

Carlos G. Morales Guio

Dante A. Simonetti

Philippe Sautet, Committee Chair

University of California, Los Angeles

2023

Dedicated to my sister, mom, dad, and Buddh.

Table of Contents

List of Figures

List of Tables

Acknowledgements

Firstly, I would like to express my deepest gratitude to my advisor, Philippe Sautet, whose guidance, and unwavering support have been invaluable throughout the past five years. His vast knowledge and patient mentorship have been critical in making this dissertation a reality, and I am incredibly fortunate to have had such an exceptional advisor.

In addition, I extend my appreciation to Geng Sun and Vaidish Sumaria for their valuable assistance with grand canonical basin hopping simulations, and to Zisheng Zhang for their assistance with microkinetic simulations. I am also grateful to George Yan and Ziyang Wei for their assistance on numerous projects. Furthermore, I would like to acknowledge my experimental collaborators both in the US and around the world for their contributions to our collective research endeavors.

I wish to acknowledge the members of my dissertation committee, Anastassia Alexandrova, Dante Simonetti, and Carlos Morales-Guio, for their support, guidance, and courses that have enhanced my understanding of kinetics, reaction engineering, and electrochemistry, respectively. Anastassia Alexandrova deserves special recognition for her unwavering support not only in our collaborative projects but also in other personal aspects related to my PhD.

I would also like to extend my gratitude to all my colleagues for their help, stimulating discussions, and fruitful collaborations throughout my academic journey. I am particularly grateful to Celine Tesvara, Michael Ngan, and Dongfang Chang for their assistance and enlightening conversations.

Finally, I would like to acknowledge my family and friends for their unrelenting encouragement and unwavering support throughout this journey.

Several chapters in this dissertation contain material adapted from published, submitted, and unpublished manuscripts with multiple contributing authors, as noted in the following.

Chapter 2 contains figures and text adapted, with permission from Royal Society of Chemistry, from the article "Highly dispersed Pt atoms and clusters on hydroxylated indium tin oxide: a view from first-principles calculations", by Simran Kumari, and Philippe Sautet, *J. Mater. Chem. A*, 2021, 9, 15724-15733. https://doi.org/10.1039/D1TA03177E. PS conceptualized and supervised the work in the article. SK performed the computational studies. The draft was prepared and edited by SK and PS. This work was funded by DOE-BES grant DE-SC0020125. This work used computational and storage services associated with the Hoffman2 Shared Cluster provided by the UCLA Institute for Digital Research and Education Research Technology Group. This research used the resources of the National Energy Research Scientific Computing Center (NERSC), a U.S. Department of Energy Office of Science User Facility operated under Contract No. DE-AC02-05CH11231. The authors want to thank XSEDE SDSC's Comet, Expanse Supercomputer, and Bridges PSC for the computation time. This chapter also contains figures reproduced from the article "Surface structure of Sn-doped In_2O_3 (111) thin films by STM", by Erie H Morales, Yunbin He, Mykola Vinnichenko, Bernard Delley, and Ulrike Diebold, New Journal of Physics 10 (2008) 125030 (11pp), https://doi.org/ 10.1088/1367-2630/10/12/125030 and is reproduced with permission from IOP publishing.

Chapter 3 contains figures, tables, and text adapted, with permission from the American Chemical Society, from the article "Electrocatalytic Hydrogen Evolution at Full Atomic Utilization over ITO-Supported Sub-nano-Pt_n Clusters: High, Size-Dependent Activity Controlled by Fluxional Pt Hydride Species", authored by Simran Kumari, Tsugunosuke Masubuchi, Henry S. White, Anastassia Alexandrova, Scott L Anderson, Philippe Sautet, J. Am. Chem. Soc. 2023, 145, 10, 5834–5845, https://doi.org/10.1021/jacs.2c13063. PS and SLA conceptualized and supervised the work in the article. The manuscript was prepared and edited by SK, TM, HSW, AA, SLA and PS. TM and SLA prepared catalysts, evaluated electrocatalytic performance and performed other related experimental analysis. SK performed computational studies. AA, SLA, HSW and PS, AK and TM analyzed the data and findings. This work was grant DE-SC0020125 from the US Department of Energy, Office of Science, Basic Energy Science Program. SLA acknowledges support from the Henry Eyring Presidential Endowed Chair. This research used resources of the Argonne Leadership Computing Facility, which is a DOE Office of Science User Facility under grant name ‘DynCatalysis’. This work used computational and storage services associated with the Hoffman2 Shared Cluster provided by the UCLA Institute for Digital Research and Education Research Technology Group. This research used the resources of the National Energy Research Scientific Computing Center (NERSC), a U.S. Department of Energy Office of Science User Facility operated under Contract No. DE-AC02-05CH11231. The authors want to thank XSEDE SDSC's Comet, Expanse Supercomputer, and Bridges PSC for the computation time. We thank Ashley Cass for helpful discussions regarding the experiments. We thank Zisheng Zhang for helpful discussions regarding the Kinetic simulations.

Chapter 4 contains text and figures with permission from the American Chemical Society, from the article, “Elucidation of the Active Site for the Oxygen Evolution Reaction on a Single Pt Atom Supported on Indium Tin Oxide”, by Simran Kumari, and Philippe Sautet, *J. Phys. Chem. Lett.* 2023, 14, 10, 2635–2643. https://doi.org/10.1021/acs.jpclett.3c00160. PS conceptualized and supervised the work in the article. SK performed the computational studies. The draft was prepared and edited by SK and PS. This work was supported by the grant DE-SC0020125 from the US Department of Energy, Office of Science, Basic Energy Science Program.

This research used resources of the Innovative and Novel Computational Impact on Theory and Experiment (INCITE) program at the Argonne Leadership Computing Facility (theta machine, grant name 'DynCatalysis'), a U.S. Department of Energy Office of Science User Facility operated under Contract DE-AC02-06CH11357. This work used computational and storage services associated with the Hoffman2 Shared Cluster provided by the UCLA Institute for Digital Research and Education Research Technology Group. This research used the resources of the National Energy Research Scientific Computing Center (NERSC), a U.S. Department of Energy Office of Science User Facility operated under Contract No. DE-AC02-05CH11231. The authors want to thank XSEDE SDSC's Comet, Expanse Supercomputer, and Bridges PSC for the computation time. This chapter also contains figures from "Size-dependent electronic structure controls activity for ethanol electro-oxidation at Ptn/indium tin oxide (n = 1 to 14)" Alexander von Weber, Eric T. Baxter, Sebastian Proch, Matthew D. Kane, Michael Rosenfelder, Henry S. White and Scott L. Anderson, Phys. Chem. Chem. Phys., 2015,17, 17601-17610 and is reproduced with permission from Royal Society of Chemistry 2015.

Chapters 5 contains figures, tables, and text adapted, with permission from the American Chemical Society, from the article "Electrochemical Oxidation of Methane to Methanol on Electro-deposited Transition Metal Oxides", authored by Kangze Shen, Simran Kumari, Yu-Chao Huang, Joonbaek Jang, Philippe Sautet and Carlos G. Morales-Guio, J. Am. Chem. Soc. 2023, 145, 12, 6927–6943, https://doi.org/10.1021/jacs.3c00441. CGM-G conceptualized and supervised the work in the article. PS supervised the computational part of the work. The manuscript was prepared and edited by KS, SK, Y-CH, JJ, PS and CGM-G. KS, JJ and CGM-G prepared catalysts, evaluated electrocatalytic performance and performed other related experimental analysis. SK performed computational studies. KS, SK, Y-CH, JJ, PS and CGM-G analyzed the data and findings. CGM-G acknowledges financial support from a Scialog program sponsored jointly by Research Corporation for Science Advances and the Alfred P. Sloan Foundation and includes a grant No. G-2021-14160 by the Alfred P. Sloan Foundation. This work also used computational and storage services associated with the Hoffman2 Shared Cluster provided by the UCLA Institute for Digital Research and Education Research Technology Group. This research used the resources of the National Energy Research Scientific Computing Center (NERSC), a U.S. Department of Energy Office of Science User Facility operated under Contract No. DE-AC02-05CH11231. The authors want to thank XSEDE SDSC's Comet, Expanse Supercomputer, and Bridges PSC for the computation time.

Chapter 6 contains unpublished text and figures from a manuscript currently in preparation, by authors, Simran Kumari, Anastassia Alexandrova and Philippe Sautet. PS and AA conceptualized and supervised the work in the article. SK performed computational studies. The manuscript was prepared and edited by SK, AA and PS. This work used computational and storage services associated with the Hoffman2 Shared Cluster provided by the UCLA Institute for Digital Research and Education Research Technology Group. This research used the resources of the National Energy Research Scientific Computing Center (NERSC), a U.S. Department of Energy Office of Science User Facility operated under Contract No. DE-AC02-05CH11231. The authors want to thank XSEDE SDSC's Comet, Expanse Supercomputer, and Bridges PSC for the computation time.

Curriculum Vitae

2013 – 2015 B.S. (Chemical Sciences), Indian Institute of Science Education and Research, Kolkata

2015 – 2018 M.S. (Chemical Sciences), Indian Institute of Science Education and Research, Kolkata

Publications at UCLA

1. Kumari, Simran, and Philippe Sautet. "Highly dispersed Pt atoms and clusters on hydroxylated indium tin oxide: a view from first-principles calculations." *Journal of Materials Chemistry A* 9, no. 28 (2021): 15724-15733.
2. Kumari, Simran*, Tsugunosuke Masubuchi, Henry S. White, Anastassia Alexandrova, Scott L. Anderson, and Philippe Sautet. "Electrocatalytic Hydrogen Evolution at Full Atomic Utilization over ITO-Supported Sub-nano-Pt n Clusters: High, Size-Dependent Activity Controlled by Fluxional Pt Hydride Species." *Journal of the American Chemical Society* 145, no. 10 (2023): 5834-5845.
3. Fu, Xiaoyang, Dongfang Cheng, Chengzhang Wan, Simran Kumari, Hongtu Zhang, Ao Zhang, Huaixun Huyan et al. "Bifunctional ultrathin RhRu0. 5 alloy nanowire electrocatalysts for hydrazine assisted water splitting." *Advanced Materials* (2023): 2301533.
4. Shen, Kangze, Simran Kumari*, Yu-Chao Huang, Joonbaek Jang, Philippe Sautet, and Carlos G. Morales-Guio. "Electrochemical Oxidation of Methane to Methanol on

Electrodeposited Transition Metal Oxides." *Journal of the American Chemical Society* 145, no. 12 (2023): 6927–6943

5. Kumari, Simran, and Philippe Sautet. "Elucidation of the Active Site for the Oxygen Evolution Reaction on a Single Pt Atom Supported on Indium Tin Oxide." *The journal of physical chemistry letters* 14, no. 10 (2023): 2635-2643.

* : equal contribution

Chapter 1 Research Background

1.1 Heterogeneous catalysis

Heterogeneous catalysis[1–3] is an essential technology that underpins the chemicals and energy industries and plays a central role in driving the transition to carbon-neutral operation. The ultimate goal is to design active and robust catalytic processes that can improve the world. Ideally, materials with self-regenerating active sites under operating conditions could be created at the atomic level for critical catalytic processes. The pursuit of rational design in catalysis has been one of the "holy grails" of chemistry since the publication of articles by Breslow and by Bard and Fox in 1995, and this quest continues with greater urgency today.

The need for catalyst development has never been greater than it is now, particularly in key processes such as biomass upgrading, CO_2 reduction, water splitting, and light alkanes activation. The soaring demand for energy, chemical products, and food, along with the rise in anthropogenic CO_2 emissions worldwide, has made it essential to develop catalytic processes that can meet these needs sustainably. Catalytic processes are central to the production of chemicals, which accounts for approximately 25% of industrial energy use, and the most energy-intensive processes rely on heterogeneous catalysis. Therefore, there is a significant opportunity to decrease energy consumption and reduce environmental impact by increasing the efficiency of catalytic processes. Developing CO_2-neutral processes, efficient and sustainable production of H_2, selective oxidation of methane, and electrochemical production of ammonia are some of the most pressing challenges that require innovative catalytic technologies.

Overall, the importance of heterogeneous catalysis in enabling the sustainable development of the chemical and energy industries cannot be overstated. The design of efficient and sustainable catalytic processes will be essential for meeting the ever-increasing demand for energy, chemicals, and food while reducing the environmental impact of these industries. Therefore, investing in catalytic research and development is crucial for a sustainable future.

Heterogeneous catalysis (gas or liquid phase and solid catalyst) proceeds via adsorption of one or two reactant molecule(s) on the solid surface, enhancing the reactant(s) concentration on the surface and favoring its (their) activation. The first step of the reaction is thus the reactant(s) adsorption, whereas the reaction energy includes the activation barrier energies of adsorbed reactants, of adsorbed intermediates and of desorption of products. In other words, the degree of catalytic efficiency gained in following a given path is governed by the energetics of the various intermediates, which encompass adsorbed reactant, the activation energy required to convert the bound reactant into a surface intermediate and finally to a product and its desorption.

1.1.1 Metal Oxide Catalysts

Metal oxide catalysts hold a significant position in the realm of heterogeneous catalysis, encompassing a wide array of industrial processes and catalyst families. Examples include silica, alumina, clays, zeolites, TiO_2, ZnO, ZrO_2, porous and mesoporous metal oxides, polyoxometallates (POMs) like Keggin or Dawson types, as well as the phosphates family (e.g., VPO, $FePO_4$, silica phosphoric acid (SPA)). Multicomponent mixed oxides such as molybdates, antimonates, tungstates, MoVTe(Sb)Nb-O, perovskites, and hexaaluminates are also essential components.

Metal oxides emerged as significant catalysts in the mid-1950s due to their effectiveness in a wide range of reactions, particularly oxidation and acid-base reactions. They play vital roles in petrochemicals, intermediates, fine and pharmaceutical chemicals, and biomass conversion reactions. Additionally, they serve as the foundation for metallic catalysts, both mono- and pluri-metallic, hydrodesulphurization catalysts (e.g., $CoMoO^{4-}$, $NiMoO^{4-}$, $NiWO^{4-}$ based), deNOx and deSOx catalysts, as well as bulk single or mixed metal oxide catalysts. The catalytic domains encompass oxidation (selective or total), acid and base catalysis, photocatalysis, depollution, and biomass conversion.

Metal oxides[4,5] are categorized as inorganic materials with diverse properties and applications, including sensors, catalysts, and fuel cells. Oxide surfaces are terminated by oxide O^{2-} anions, which are much larger in size compared to Mn^{+} cations. Consequently, the surface symmetry and coordination of Mn^{+} cations are disrupted. Furthermore, oxide surfaces may exhibit various types of defects and environments, such as kinks, steps, and terraces, which significantly influence the catalytic phenomenon[6,7]. This surface unsaturation is often compensated by reacting with water vapor, resulting in the formation of surface hydroxyls through the reaction: $O^{2-} + H_2O \rightarrow 2OH^{-}$. OH, groups act as conjugated acids of lattice oxygen ions (O^{2-}), which function as strong bases and conjugated bases of water molecules.

1.1.2 Single Atom and Small Clusters supported on Surfaces.

Small nanoclusters and highly dispersed single atom catalysts, composed of a limited number of atoms, have emerged as highly promising catalysts in heterogeneous catalysis[8–12]. These nanoclusters possess unique properties attributed to their size, composition, and surface structure, making them effective in various catalytic reactions. By precisely controlling the cluster size and composition, their catalytic activity and selectivity can be finely tuned. Small nanoclusters offer advantages such as high atom utilization, increased surface-to-volume ratio, and enhanced accessibility of active sites, leading to improved catalytic efficiency. Moreover, their size-dependent electronic and geometric properties enable tailored reactivity, allowing for specific transformations and reaction pathways [13–16.] The confinement effect in small nanoclusters induces quantum size effects, resulting in discrete energy levels and altered electronic structures, which can significantly influence their catalytic behavior[17,18.] Additionally, the interaction between small nanoclusters and the support material plays a critical role in stabilizing the clusters, modifying their electronic structure, and influencing the catalytic performance[19,20] . Therefore, exploring small nanoclusters as catalysts opens exciting opportunities for developing efficient and selective heterogeneous catalytic systems. Their unique properties and tunability make them potential candidates for various applications, ranging from energy conversion and storage to environmental remediation and chemical synthesis.

1.2 Determining the "true" Active Site

Catalysts are crucial in many chemical reactions, as we have seen from the previous section. Modeling catalytic reactions requires an understanding of the structure and active site of the catalyst in realistic conditions. This task is especially difficult with surface-supported clusters and metal oxide surfaces because of various variables such as pressure, temperature, and adsorbate coverage.

One of the easiest ways to model surface supported clusters is to optimize a predetermined cluster in gas phase and then deposit it on the surface. Researchers then take this system as the active site for their reactions and study the full reaction mechanism on this active site. One clear problem with this method is that it does not take into consideration the effects of the interaction with the support, the effect of reaction conditions or the effect of restructuring induced by the adsorbates generated during the reactions. This led the researchers to shift their focus on determining the global minimum or most stable structure of the nanoclusters on metal or metal-oxide surfaces in the presence of ligands that are directly or indirectly involved in the reaction mechanism. However, the global minimum structure can be difficult to determine without any initial knowledge of the catalyst active site. Hence, to find the global minimum in the real reaction condition we need to utilize stochastic global optimizing and sampling methods. Different optimization techniques, such as Particle Swarm Optimization (PSO)[21,22], Genetic Algorithms[23–26], Basin Hopping[15,27–30] and Simulated Annealing[31] have been developed. These are combined with ab-initio electronic structure calculations to generate the free energy surface of the catalyst in the reaction condition. During the global sampling process not only the cluster shape is modified but compositional changes are also allowed that could affect the main backbone of the cluster itself. Such extensive studies have revealed that clusters can exhibit significant variations in appearance, charges, chemical bonds, and reactivity. For example, in an oxidizing environment, the metallic cluster may be able to uptake oxygen, but the amount depends on factors such as partial pressure, temperature, electrochemical potency (in the case of electrochemical systems), and cluster geometries. In the case of electrocatalysts, the interaction between the catalyst and water necessitates determining the coverage of hydroxyls and hydrogen on the catalyst.

However, the aforementioned approach assumes that the global minimum structure represents the "real" active site of the catalyst. Unlike extended surfaces, catalytic clusters are highly dynamic, with the ability to alter their composition, size, and shape in response to temperature, pressure, and other factors. Hence, it is crucial to determine which cluster compositions serve as the active sites in a reaction. Clusters can also experience partial poisoning or sintering, leading to a loss of their catalytic properties associated with specific sizes. This complex dynamic makes it challenging to predict the behavior of a catalytic system solely based on its initial structure.

Researchers have discovered that a single structure alone is insufficient to describe a catalyst[29,32,33]. The “real” active site comprises of numerous thermally accessible structural forms that collectively constitute the catalyst. This understanding has challenged the conventional belief that global minimum structures are catalytically active, suggesting instead that rare, transient structures with thermally populated surfaces drive the catalytic activity. This hypothesis gains support from the observation that nanoclusters with nearly flat potential energy surfaces can readily isomerize and explore multiple isomers within nanosecond timescales at catalytic temperatures. It emphasizes the dynamic nature of catalyst.

1.3 Reactions to be considered.

In this dissertation we have studied the following reactions on various heterogenous catalysts:

1.3.1 Hydrogen evolution Reaction

Hydrogen gas (H_2) is an attractive fuel known for its high energy density and environmentally friendly water byproduct when combusted[34–37]. However, the current method of H_2 production through steam reforming of fossil fuels is inefficient, resource-intensive, and contributes to CO_2 emissions. Electrochemical water splitting, or water electrolysis, offers a clean, efficient, and sustainable alternative for H_2 generation. By utilizing water as both the input and output, water electrolysis presents a promising solution to replace fossil fuels in the hydrogen economy. The process involves two half-cell reactions: the hydrogen evolution reaction (HER) and the oxygen evolution reaction (OER), both requiring suitable catalysts to minimize energy losses and enhance efficiency. While platinum group metal (PGM)-based catalysts have shown high performance, their limited availability and cost hinder widespread implementation[37,38]. Thus, the objective is to either reduce Pt usage while maintaining catalytic effectiveness or explore earth-abundant, non-noble metal alternatives with comparable catalytic activity.

1.3.2 Oxygen evolution reaction

The oxygen evolution reaction (OER) plays a crucial role in various processes that involve the production of molecular oxygen, such as water oxidation during oxygenic photosynthesis, electrolysis of water to generate oxygen and hydrogen, and electrocatalytic oxygen evolution from oxides and oxoacids [39–46]. Enhancing the performance of OER catalysts is essential for the advancement of renewable energy technologies, including solar fuels production and metal-air batteries. Currently, precious metal oxides like ruthenium and iridium oxides exhibit the highest OER activities[47–51]. However, their limited availability and high costs pose challenges for large-scale applications. Therefore, there is a need to develop alternative catalysts that are abundant, cost-effective, and exhibit comparable or even superior OER performance. Especially, efforts are being made to explore earth-abundant transition metal-based catalysts, such as manganese, cobalt, nickel, and iron oxides, as potential alternatives for precious metal catalysts [52–54]. These transition metal oxides have shown promising OER activities and offer the advantage of abundant reserves, reducing the reliance on scarce and expensive materials. Moreover, extensive research is being conducted to optimize the structure[45,48,55–60], composition[48–53], and morphology[61–64] of OER catalysts to enhance their catalytic efficiency. Nanoscale engineering, surface modification, and doping techniques are employed to tailor the active sites, improve charge transfer kinetics, and minimize energy losses during the OER process.

1.3.3 Partial Oxidation of Methane to Methanol

The conversion of methane to methanol is a topic of significant interest due to several reasons. First and foremost, methane is the main component of natural gas, which is a plentiful and widely available resource[65]. By converting methane to methanol, we can transform a gaseous fuel into a liquid form, which is more versatile and easier to handle for various applications [66,67].

Methanol itself is a valuable chemical compound with numerous uses. It serves as a crucial building block for the production of various chemicals and materials, including formaldehyde, acetic acid, and olefins. Methanol is also utilized as a transportation fuel, either directly or as an additive to gasoline or biodiesel. Its use in fuel cells and as an energy carrier for renewable energy systems is being explored as well. [68]Another important reason to consider methane to methanol conversion is the environmental aspect. Methane is a potent greenhouse gas, with a much higher global warming potential than carbon dioxide over a specific timeframe. Methane emissions from various sources, including natural gas production and livestock, contribute significantly to climate change. By converting methane to methanol, we can mitigate its environmental impact and utilize it as a cleaner-burning fuel or a precursor for sustainable chemical production. Furthermore, the methanol market is experiencing substantial growth, and demand is expected to continue rising in the coming years. While current methanol production relies heavily on natural gas and coal, there is an increasing interest in renewable and sustainable sources for methanol production. The development of efficient and economically viable methods for methane to methanol conversion can contribute to the diversification of feedstocks and reduce reliance on fossil fuels.

1.3.4 CO_2 hydrogenation

The study of CO_2 hydrogenation to methanol is of great significance due to its potential to address pressing environmental and energy challenges. This process involves converting carbon dioxide, a major contributor to climate change, into methanol, a valuable chemical compound and potential clean fuel. CO_2 hydrogenation to methanol offers a promising approach to mitigate CO_2 emissions by utilizing this greenhouse gas as a feedstock instead of releasing it into the atmosphere [69–80]. By transforming CO_2 into methanol, we can effectively recycle and reuse carbon dioxide emissions from various sources, closing the carbon cycle. Methanol derived from CO_2

hydrogenation has multiple applications. It can serve as a cleaner-burning fuel or fuel additive, offering an alternative to traditional hydrocarbon fuels. Additionally, methanol is a vital building block for the production of various chemicals and materials. By harnessing CO_2 as a raw material for methanol synthesis, we can reduce our reliance on fossil fuels and foster the development of a circular carbon economy. Furthermore, CO_2 hydrogenation to methanol holds promise for energy storage and the integration of renewable energy sources. It allows for the production of methanol using renewable electricity and green hydrogen, enabling the storage and utilization of excess energy generated from renewable sources. This process facilitates the conversion of intermittent renewable energy into a storable and transportable form, promoting its integration into existing energy infrastructure. In-depth studies of CO_2 hydrogenation to methanol are crucial for advancing the development of efficient and selective catalysts. Catalysts play a vital role in driving the reaction and optimizing its performance in terms of conversion efficiency, selectivity, and reaction rates. Understanding the underlying mechanisms and kinetics of this reaction is essential for designing and optimizing catalysts, enabling more sustainable and economically viable CO_2 utilization technologies. Overall, the study of CO_2 hydrogenation to methanol offers significant potential for carbon capture and utilization, renewable energy storage, and sustainable chemical production. By converting CO_2 into methanol, we can contribute to reducing greenhouse gas emissions, utilizing renewable energy, and transitioning to a more sustainable and circular economy[68].

1.4 Thesis Objectives

In this dissertation, we seek to investigate the true nature of the active site under reaction condition in both thermal- and electro- catalysts using state-of-the-art periodic DFT calculations, atomistic thermodynamics, enhanced sampling methods such as grand canonical basin hopping and microkinetic modeling.

Chapter 2 focuses on the using first-principles simulations to study small Pt_n (n: 1,2,3) clusters on indium oxide, tin doped indium oxide, and hydroxylated tin doped indium oxide. We report that the Pt_n cluster is stabilized in the presence of tin and that this is especially the case for Pt single atoms on the hydroxylated indium tin oxide support, which are anchored to the support *via* the hydroxyl group. On this support, the Pt single atoms become more stable than Pt_2 and Pt_3 clusters, hence decreasing sintering. These findings provide a promising way to design single-atom catalysts on electrically conducting supports for electrocatalytic applications and to better understand how functional groups on supports can increase the adhesion of cluster catalysts.

Chapters 3 focusses on using a combination of DFT and experiments with atomically size-selected Pt_n clusters deposited on indium-tin oxide (ITO) electrodes used to examine the effects of applied potential and Pt_n size on the electrocatalytic activity of Pt_n (n = 1, 4, 7, and 8) for the hydrogen evolution reaction (HER). Activity is found to be negligible for isolated Pt atoms on ITO, increasing rapidly with Pt_n size such that Pt_7/ITO and Pt_8/ITO have roughly double the activity per Pt atom compared to atoms in the surface layer of polycrystalline Pt. The exception is Pt_1/ITO, where H adsorption at the HER threshold potential is energetically unfavorable. The theory combines global optimization with grand canonical approaches for the influence of potential, uncovering the fact that several metastable structures contribute to the HER, changing with the applied potential. It is hence critical to include reactions of the ensemble of energetically accessible Pt_nH_x/ITO structures to correctly predict the activity vs Pt_n size and applied potential. For the small clusters, spillover of Hads from the clusters to the ITO support is significant, resulting in a competing channel for loss of Hads, particularly at slow potential scan rates.

Chapter 4 focusses on using density functional theory calculations and grand canonical basin hopping to theoretically investigate the active site for the oxygen evolution reaction (OER) on a single Pt atom supported on indium tin oxide, including the influence of the electrochemical potential. We show that the ligands on the Pt atom change from Pt–OH in the absence of electrochemical potential to $PtO(OH)_4$ in electrochemical conditions. This change of the chemical state of Pt is associated with a decrease of 0.3 V for the OER overpotential. This highlights the importance of accurately identifying the nature of the active site under reaction conditions and the impact of adsorbates on the electrocatalytic activity. This theoretical investigation enhances our understanding of SACs for the OER.

In Chapter 5, we utilize a combination of control experiments and DFT calculations to shed light on the intrinsic activity of high valence transition metal oxides for the activation and oxidation of methane to methanol at ambient temperatures. Our calculations reveal that electrocatalytic oxidation allows for the attainment of an optimum potential window, in which both methane activation to form methanol and methanol desorption are thermodynamically favored. Additionally, we find that methanol desorption is favored due to competitive adsorption with hydroxide anions. Notably, our results demonstrate that the oxidized form of as-deposited (oxy)hydroxide catalyst films exhibit activity for the thermal oxidation of methane to methanol even without the application of bias potential.

Chapter 6 focusses on addressing the growing concern over the escalating levels of anthropogenic CO_2 emissions necessitates effective strategies for its conversion into valuable chemicals and fuels. In this work, we embark on a comprehensive investigation of the zirconia-copper inverse catalyst's true nature under CO_2 hydrogenation conditions. To achieve this, we employ density functional theory calculations in combination with Grand Canonical Basin

Hopping search, enabling an exploration of the complete free energy surface within the relevant reaction conditions. Our focus centers on the $Zr_3O_xOH_y(HCOO)_z$/Cu111 cluster, revealing noteworthy changes in the active site induced by various reaction parameters such as pressure, temperature, conversion levels, and CO_2:H_2 feed ratios._Through our analysis, we have unveiled intriguing insights into the dynamic behavior of the catalyst. Specifically, under reaction conditions, we observe a relatively flat free energy surface, suggesting that the active site should be regarded as an ensemble of diverse structures, especially involving changes of the type, number, and binding sites of adsorbates, rather than being solely dictated by the global minimum. This finding challenges the traditional notion of a single dominant structure and emphasizes the importance of considering the ensemble nature of the active site for an accurate understanding of the CO_2 hydrogenation process.

Chapter 2 Highly dispersed Pt atoms and clusters on hydroxylated indium tin oxide: a view from first-principles calculations

2.1 Introduction

Assembling metal clusters on high-surface-area supports has been extensively explored to achieve high activity and stability in heterogeneous catalysis[81–84]. Other applications of supported metal clusters include nanoscience, information storage, and magnetism[85–89]. Sub-nanometer scale metal clusters present the advantage of an optimal dispersion, where nearly all the atoms present on the surface contribute towards improving the catalytic activity, which is vital since the active phase is often formed by rare and expensive transition metals such as Pt or Rh[90–92]. Pt-based catalysts have long attracted scientists' attention because of their importance in catalyzing a large range of chemical reactions, including emission control of toxic gases, production of chemicals, and energy conversion in fuel cells[93–96]. Theoretical modeling and experimental research on Pt-based catalysts' properties have been extensive[97–100]. Under the regime of supported metal catalysts, the control of the metallic particle size is a fundamental question[101]. The general behavior is that an increase of metallic coordination number, and hence size, improves the stability. Therefore, the small, bare metallic particles tend to sinter into larger ones, leading to a loss of activity and selectivity. As a result, one of the primary barriers to the industrial application of supported metal catalysts is their stability. Scientists have focused on studying the sintering of supported metal catalysts, and a sizeable metal-support interaction has proven to be vital for the stability of heterogeneous catalysts. Sub-nanometer-sized metal particles present specific electronic and chemical properties.[102,103] Hence, understanding the mechanisms that allow small particles' stabilization is crucial for many application fields including catalysis.

High-surface area supports such as metal oxides have been thoroughly investigated to study their interaction with small metal clusters and have been found to favor small particles kinetically. This approach is used in heterogeneous catalysis, in which the optimal stabilization of small particles by the support is of significant importance to slow down the often-unavoidable sintering into larger particles and the loss of catalytic activity. One way to increase the stability of small metal particles on supports is to increase the adhesion energy between the particle and the support. This can be accomplished by modifying the oxide interfacial properties, such as defect concentration[104–106] , surface termination, functionalization[107] or reaction conditions[108,109]. Hydroxyls represent one of the most common functional groups, often omnipresent in realistic conditions and essential for metal support interaction[110,111]. Scientists have already noted evidence of enhanced interactions between the supported metals and the hydroxylated metal oxide for Pd/ɣ-Al_2O_3[111], Pt/Al_2O_3[112], Co/Al_2O_3(0001)[113], Pt/ TiO2(011)- 2 x 1[114], Rh/ZrO_2 [115,116], Ru/ZrO2[117], Pt/TiO_2 [118], Ir/In_2O_3 [119], Pd/MgO[120] and Pd/Fe_3O_4 [121] etc. These interactions cause thermal stabilization and hence more durable catalytic activity of the single-atom or, more generally, highly dispersed catalysts. Understanding how the support and its chemical nature control particle stability as a function of size is key to the conscious design of well-controlled, monodispersed, supported catalysts.

In_2O_3 is a wide band-gap semiconductor used in semiconductor gas sensors[122] and more recently has also been explored as a potential catalyst for CO_2 hydrogenation[123,124]. On doping with Sn, it becomes Indium Tin Oxide (ITO), a transparent conducting oxide that has optical transparency in the visible range with metal-like conductivity. This material has applications in transparent electrodes for electro-optical displays, e.g., liquid crystal displays and solar cells[125].

Each has been a subject of intensive research and development activities. Sn doped Indium oxide demonstrates high conductivity, crucial for application in electrocatalysis. These properties have incited scientists to investigate these conductive oxides as supports for Pt-metal clusters for electrocatalytic applications in water [126–128], where the surface might be hydroxylated.

In this first chapter, we report first-principles DFT calculations of Pt single atom and small clusters supported on the defect-free $In_2O_3(111)$, Sn-doped $In_2O_3(111)$, and hydroxylated Sn-doped $In_2O_3(111)$ surfaces. By analyzing the structural and electronic properties of the metal clusters on the supports, including the detailed sampling of geometric configurations, we provide insights on the metal-support interactions and the effects of hydroxyl groups. We show that H atoms from hydroxyl groups migrate on the cluster and that this is a crucial mechanism to stabilize and anchor the cluster on the support. This effect is proportionally more substantial on Pt single atom, and therefore hydroxylated support better stabilize Pt_1 compared to Pt_2 or Pt_3 clusters, hence hindering sintering. The manuscript is organized as follows: In Sec. 2.2, we present calculation details and the grand canonical methods used in this work. In Sec. 2.3, we discuss in detail the doping of $In_2O_3(111)$ by Sn to produce the ITO (111) surface, the water adsorption on ITO (111) , and finally, we discuss the structures of $Pt_n(n=1,2,3)$ clusters on the three different supports, their stability, and their electronic and structural properties.

2.2 Methods

2.2.1 Total Energy Calculations

All calculations were carried out within the density functional theory framework using the Vienna ab-initio simulation package (VASP). [129,130] The electron-ion interactions are treated using the projector augmented wave (PAW) method.[131] We use the Perdew–Burke–Ernzerhof (PBE) functional to treat the exchange-correlation interactions.[132] The Gaussian smearing method with a smearing of 0.01 eV is used to improve K point convergence. The valence electronic states are expanded in plane-wave basis sets with an energy cutoff of 500 eV. The structures are optimized until the force on each atom is less than 0.01 eV/A$^{\circ-1}$.

2.2.2 Models

The calculated lattice parameters of the bulk Indium Oxide (a= b = c = 10.352Å), which agree well with experiments [133], were used to construct the periodic slabs (111) surface calculations., were used to construct the periodic slabs (111) surface calculations. The In_2O_3(111) unit dimension in the surface plane is 14.63 x 14.63 x 28 Å, including a vacuum region of ~20 Å. The In_2O_3(111) unit cell model contains four tri-layers of O-In-O in that order; each unit cell has 64 Indium atoms and 96 Oxygen atoms, out of which 16 In atoms are 6 coordinated(6c), 48 In atoms are 5c, 48 O atoms are 3c, and other 48 O atoms are 4c. There are 6 non-equivalent In atoms present in the unit cell, and a top view of the slab surface is shown in Figure 2-1.The different colors represent the non-equivalent metal atoms; light blue : In(6c) bonded with 3O(3c) and 3 O(4c), dark blue : In(6c) bonded with 3O(3c), 2O(4c), red : In(5c) bonded with 3O(3c) and 1O(4c), dark green : In(5c) bonded with 2O(3c) and 3O(4c), lime : In(5c) bonded with 2O(3c) and 2O(4c) and yellow: In(5c) bonded with 1O(3c) and 3O(4c). All the metal atoms, except the light blue atom, also have 1-O interaction from the second layer and are located at the same z-value on the surface layer. Only the atoms exposed on the surface were shown in the figure. The atoms in the lower layers were removed for clarity. The structures were first studied on 2-Layer slabs, after which the structures with reasonable stability were recalculated on a thicker slab containing four tri-layers. This was done to save computational time and resources. The atoms in the two lower In layers of the 4-layer system and the associated O layers, i.e., the lower half of the slab, were fixed at their bulk positions for all the calculations. The Brillouin-zone (BZ) integration is sampled by adopting the Monkhorst–Pack[134] k-point grids of 5x5x1 for all the surfaces.

2.2.3 Pt-cluster structure exploration.

We used the Basin Hopping global optimization method to explore possible adsorption sites for the Pt-SA on the hydroxylated ITO (111) surface and Pt_2 and Pt_3 adsorption structure and site on $In_2O_3(111)$, ITO(111), and Hydroxylated ITO(111). The premise behind the Basin hopping method is very similar to that of canonical Monte Carlo (MC) simulation, [135], where the algorithm perturbs the coordinates of the current structure by a random displacement (called perturbation) and then optimizes the new geometry to a local minimum. The optimized structure can be either discarded or accepted, and the algorithm decides this by evaluating the probability that depends on the energy difference between the previously accepted structure and the temperature (full description of the method is provided in Basin Hopping Algorithm). The motivation to use basin hopping for our studies was from Sun et al., where they used this method to study Pt_8 cluster on alumina under a pressure of hydrogen.[15]

2.2.3 Energetic Analysis

The doping energy for the Sn doping onto the $In_2O_3(111)$ surface is defined by the following equation:

$$n\ SnO_{2bulk} + In_{32}O_{48}\ (111\ slab) \rightarrow Sn_nIn_{(32\text{-}n)}O_{48}\ (111\ slab) + \frac{n}{2}In_2O_{3bulk} + \frac{n}{4}O_{2gas} \quad (1)$$

Hence, the doping energy can be calculated as:

$$E(\text{doping}) = E(\text{Sn}_n\text{In}_{(32-n)}\text{O}_{48}\ 111\ \text{slab}) + \frac{n}{2}E(\text{In}_2\text{O}_{3\text{Bulk}}) + \frac{n}{4}E(\text{O}_{2_\text{gas}}) - nE(\text{SnO}_{2\text{Bulk}}) - E(\text{In}_{32}\text{O}_{48}\ (111\ \text{slab}))$$

Where $E(Sn_nIn_{(32-n)}O_{48}$ 111 slab) is the energy of the slab with n-Sn dopants, $E(In_{32}O_{48}$(111 slab)) is the energy of the In_2O_3(111) slab, $E(In_2O_{3bulk})$ and $E(SnO_{2bulk})$ are the energies for the bulk structures of In_2O_3 and SnO_2 respectively, $E(O_{2gas})$ is the energy of the gas phase O_2 molecule.

The adsorption energy of H_2O on the ITO (111) surface is defined by:

$$G(\text{Adsorption}) = E(\text{Sn}_n\text{In}_{(32-n)}\text{O}_{48} + pH_2\text{O}\ 111\ \text{slab}) - E(\text{Sn}_n\text{In}_{(32-n)}\text{O}_{48}\ 111\ \text{slab}) - pG(H_2\text{O (gas)})$$

Where $G(H_2O\ gas)$ is the Gibbs free energy for gas-phase H_2O and p is the number of H_2O molecules chemisorbed on the surface, $E(Sn_nIn_{(32-n)}O_{48} + pH_2O$ 111 slab) is the energy of the slab with p-H_2O molecules, and $E(Sn_nIn_{(32-n)}O_{48}$ 111 slab) is the energy of ITO(111) surface slab.

To analyze the evolution of the stability of the clusters on each of the four surfaces, the normalized cluster binding energy, $E_{binding}$, in the presence of the surface was calculated, with the Pt bulk and the bare oxide surface as a reference, following eq:

$$E_{\text{binding}} = \frac{E_{\text{nPt + surface}} - E_{\text{surface}} - E_{\text{Pt-bulk}}}{n}$$

Here, $E_{\text{nPt + surface}}$ is the energy of the Pt cluster with n Pt atoms on the surface, E_{surface} is the energy of the oxide support and, $E_{\text{Pt-bulk}}$ is the energy of Pt-bulk. $E_{binding}$ is positive (meaning less stable) and corresponds to the energy loss, normalized to 1 Pt atom, for the supported cluster compared to Pt bulk.

2.3 Results and Discussion

Before presenting the results of Pt_n (n = 1,2,3) interaction with the surface of $In_2O_3(111)$, ITO (111), and hydroxylated ITO (111), we first determine the most energetically desirable structure for our ITO (111) surface. To do this, we begin with doping Sn onto each of the non-equivalent sites (Figure 2-1a). After a detailed analysis, the Sn prefers to reside in the light blue(6c) and the red(5c) sites and at a vertical z coordinate 0.14 Å higher than that of the In they substitute. We increased the Sn doping concentration from 1.25% (1Sn atom for 80 atom bilayer slab) to 5% (4Sn atoms for a 80 atom bilayer slab). We observe that as we increase the doping level, the surface energy decreases; hence the substitution of In by Sn stabilizes the surface (Appendix A.2). We have considered 5% ITO (111) for our studies in this work as it has been previously reported to provide an optimum Tin doping level for the highest carrier density [136]. In the case of 5% doping, we find that all Sn atoms prefer to locate in the surface layer. For a four-layer slab, 8 Sn atoms are present, 4 in the top and 4 in the bottom layer. 3 Sn atoms replace the In atoms in the red 5 coordinated sites, and 1 Sn atom replaces the In in the light blue 6 coordinated site. The Appendix A shows detailed results of the different doping energies of all the possible sites (Figure A.2). We also did not observe any dependence of doping energies on the Sn-Sn distance in the slab (**Error! Reference source not found.**). In Figure 2-1b and c, we show the simulated empty state STM image (Vsample = 1.7V) using the p4vasp code alongside the experimental image (Figure 2-1d) for the Sn doped $In_2O_3(111)$ surface. We observe that the calculated and experimental STM images are very similar with very prominent dark triangular features (marked in yellow on the simulated images of Figure 2-1b and c). These black zones correspond to the triangle defined by the In (6c) atoms (blue in Figure 2-1a), one Sn atoms being at its center (light blue position). The repeat vector for these black features from our simulations (14.65 Å) also compares well with the experimental value (14.44 Å)[137]. The 6 coordinated Indium atoms are saturated, and hence the local density of empty states is decreased. The slightly brighter points between the dark triangles on the simulated STM image are the Sn atoms in the red positions. The contrast in the STM image is explained by the electronic density of states (DOS) projected on each surface atom of ITO(111) , between the Fermi level and the Fermi level + 1.7 eV (Appendix A Figure A.7(a), (b)): 6-coordinated Sn (light blue) and In (blue) show a very low DOS and hence appear dark in the image, while 5-coordinated Sn (red) provide the largest DOS and appear brightest.

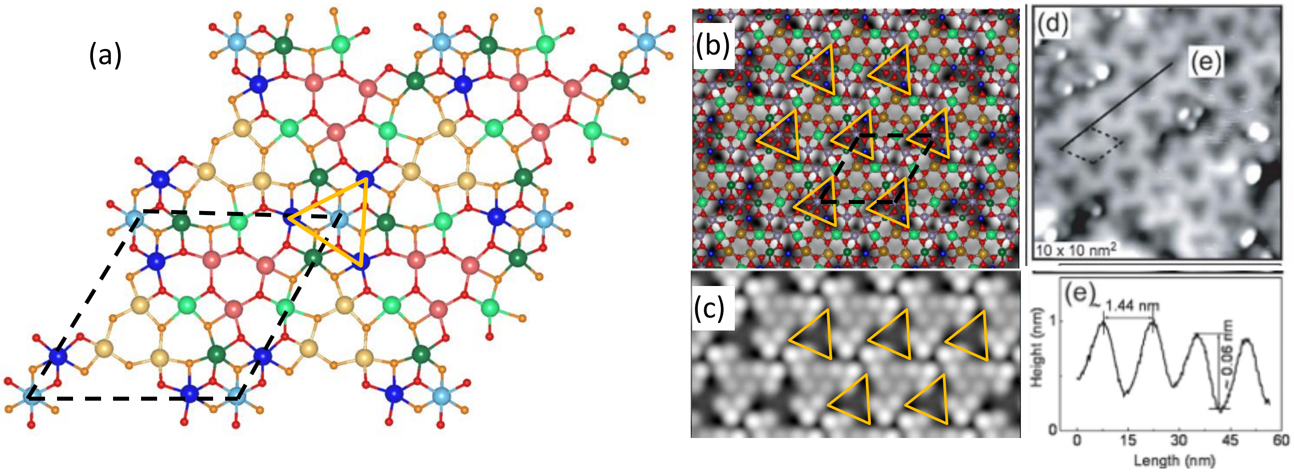

Figure 2-1 Structure of the first layer of the $In_2O_3(111)$ 2x2 surface. The different color In atoms represent the non-equivalent In atoms (see text). The orange balls are the O atoms that are 3-coordinated and the red balls are the O that are 4-coordinated. (b) and (c): Calculated STM image of the 5% Sn doped $In_2O_3(111)$ surface. In (a) and (b), the black dotted line represents one unit cell and in (a), (b) and (c) the yellow triangles highlight the lower current (dark) regions. d) experimental STM image of the 5% Sn doped $In_2O_3(111)$ surface (I_{tunnel} = 0.4nA and Vsample = +1.7V) from [137] (e) topographic profile along the line marked in (d) gives an experimental lattice constant of 14.44Å for the dark areas which is very close to the lattice constant of 14.65Å from our calculations.

2.3.1 H_2O interaction with the ITO (111) surfaces

To study the interaction of Pt-clusters with the hydroxylated surface of ITO (111), we first need to resolve the structure of the hydroxylated ITO (111) surface. We performed a series of DFT calculations to determine the adsorbed water structure on the ITO (111) surface to achieve this goal. The first step was to start with the 1-H_2O molecule and study the configurations of both dissociative and molecular adsorptions onto the surface. The supplementary information gives a detailed analysis of the adsorption energies of the different configurations. The calculations show that molecular adsorption of water molecule takes place via their oxygen atom, O_W, to the unsaturated In (5c) sites, and in the case of dissociative adsorption, the proton converts an O(3c) surface oxygen, O_S, to a hydroxyl (O_SH). The remaining O_WH group from the water molecule takes either an on-top or a bridging position at the In(5c) sites. Dissociative adsorption is preferred over molecular adsorption by 0.23eV. In the most favorable configuration (Figure 2-2 (a)), the proton adsorbs on one of the three O(3c) binding to two In(6c) and one In(5c). The remaining O_WH group adsorbs in a bridging position between the two In(5c) closest to the O_SH group. Subsequently, a second, third and fourth water molecule was added to the surface unit cell; in this case, only a handful of adsorption sites were considered depending on the adsorption energies they had with respect to 1-H_2O molecule adsorption. In the most favorable configurations, the water molecule was dissociatively adsorbed until 2-H_2O adsorption. After this, any additional water molecule would be molecularly adsorbed. The two hydroxyls adsorb to two of the three symmetrically equivalent sites (Figure 2-2 (b)). However, the third site favors the molecular adsorption of H_2O over dissociative adsorption (Figure 2-2 (c)). The fourth H_2O took the second most favorable site for molecular adsorption (Figure 2-2 (d)). We can notice a direct H-bonding between the dissociated H_2O and nearby molecularly adsorbed H_2O. The direct adsorbate-

adsorbate interaction contributes to the stabilization of partially dissociated H_2O over completely dissociated and intact H_2O molecules. This behavior is also observed in methanol adsorption on rutile TiO_2(110). [138]

The binding energy per molecule decreases slightly from -1.02 to -0.97 to -0.90 and -0.88 eV when going from one to two to three and four water molecules, respectively. The decrease in the binding energy can be attributed to the slight, surface-mediated repulsion between the molecules due to the surface re-relaxation. This re-relaxation contributes to the binding energy and affects the first adsorbate to the fullest, after which it starts reducing. This phenomenon is of general importance for oxides[138,139]. On the surface stability diagram Figure 2-2 (e), the pink shaded region corresponds to the chemical potential range for water where the surface would only contain hydroxyls but no water molecules. As we move beyond the pink region, we observe that any additional water molecule would undergo molecular adsorption. Hence, the maximum hydroxyl coverage on the ITO (111) surface is 1.1 hydroxyl per unit area of the cell. The vertical black dotted line marks the water chemical potential at room temperature and standard pressure.[140] We also studied solvation effects on water adsorption by including an explicit solvent and found that the conclusions are not qualitatively modified.

Our primary motivation to resolving the structure of hydroxyl/water adsorption on the ITO (111) surface is that when we move forward to study the Pt-cluster adsorption on the hydroxylated surface, the hydroxyls will become very important as they might provide extra anchoring to the Pt-clusters. On the other hand, the intact water molecules are less critical because they do not have any strong chemical interactions with the Pt-cluster and can also move around on the surface upon Pt-cluster adsorption. Hence, keeping this in mind, we move forward with the $4H_2O$ on ITO (111) surface as it provides the maximum number of hydroxyl groups, and even if additional water molecules could be molecularly adsorbed on the surface.

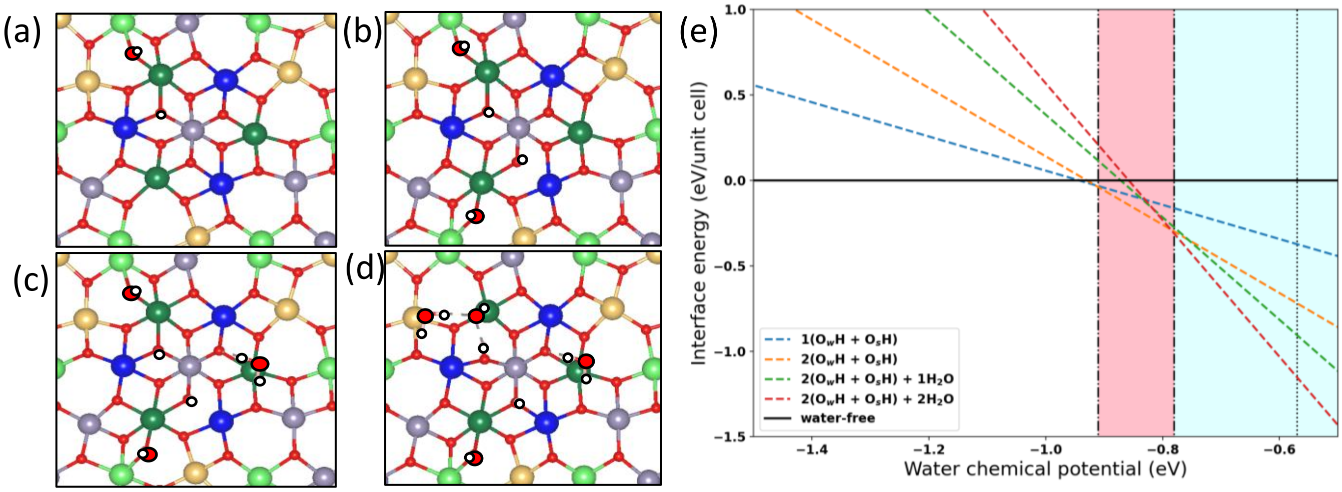

Figure 2-2 (a), (b), (c), (d) gives the best structures for H_2O adsorption on the ITO(111) surface.(a) $1H_2O$ dissociative adsorption (b) $2H_2O$ dissociative adsorption (c) $3H_2O$: $2H_2O$ dissociative adsorption + $1H_2O$ molecular adsorption (d) $4H_2O$: $2H_2O$ dissociative adsorption +2 H_2O molecular adsorption. The atoms with black border represent the atoms from water (e) The phase diagram at constant room temperature. The dotted line is the liquid water chemical potential at room temperature and 1atm pressure. The red shaded region is the region where the hydroxylated surface is stable, and the blue shaded region is where the molecular + dissociative adsorption is more stable.

2.3.2 Pt_n (n=1,2,3) on the In_2O_3(111) and ITO (111) surfaces

Pt-SA: We systematically probed all non-equivalent adsorption sites on the In_2O_3(111) and ITO (111) surfaces for Pt-Single atoms (SA). In total, we found six stable sites for the Pt-SA adsorption. These different sites for In_2O_3(111) and ITO (111) are shown in Chapter 7A.7. Figure 2-3 shows the adsorption energy for every site, while the structure of the best site is shown in Figure 2-4 (a) and (d), for $In_2O_{3(111)}$ and ITO (111) , respectively. In the case of $In_2O_{3(111)}$, site 3 is the most stable adsorption site for the Pt-SA, where Pt is located 1.20 Å above the top layer of the surface and is interacting with one In(6), two In(5), and two O atoms (Pt-O bond distances of 2.01 and 2.05 Å which is very close to the bond distances observed in PtO_2, 1.97Å). A significant restructuring of the oxide support occurs with the displacement of each of these two O atoms by 1.06 Å, including a vertical move by 0.62Å, breaking two In(6)-O bonds and forming two Pt-O bonds. The adsorption of Pt on In_2O_3 is hence markedly reactive, Pt inserting into two In(6)-O bonds. On the ITO(111) surface, Pt is similarly located 1.16 Å above the plane of the surface, but the adsorption site differs: the most favorable site is site 1, Pt interacting with two nearby Sn atoms and one In, displacing the O atom between these 3 atoms by 2 Å. The Pt-O bond distance is 1.99 Å, the Pt-Sn distances are 2.6 and 2.52 Å, and the Pt-In distance is 2.63 Å. The oxide surface is again markedly modified, with one In(5)-O and one Sn-O bond broken.

One key aspect to explain the change in the adsorption site preference is the very different work functions for the two supports: In_2O_3(6.12eV) and ITO(111) (4.46eV). This difference arises from the filling in ITO(111) of bands initially vacant in In_2O_3 since the Sn atom substituting In has one more electron. On In_2O_3, the Pt atom is, depending on the binding site, neutral (as evaluated from the Bader charge) or slightly electronically depleted by transfer to the support (by 0.3e at most on-site 4). On ITO(111), and its much lower work function, the electronic transfer is very different, and Pt is generally electronically enriched. Site 3 (Pt atom attached to 1 In(6), 1 In(5) and 1 Sn(5c)) and site 4 (Pt atom attached to 1 In(6), 1 In(5), and 1 Sn(6c)) however, do not follow this trend and keep a small depletion on Pt. As a consequence, their adsorption energy on ITO(111) is significantly weakened. The best binding site for Pt shifts to site 1, which is well adapted for a transfer (0.30e) from ITO(111) to Pt due to the strong interactions with the nearby Sn atoms. The DOS of the most energetically favored structures are given in Appendix A.6. We observe that for

Pt-SA on In$_2$O$_3$(111), the Fermi energy moves towards the conduction band, whereas, for Pt-SA on ITO (111) , the Fermi energy moves towards the valence band. This movement of Fermi level confirms that the transfer of electrons occurs from Pt(4d) to In$_2$O$_3$(111) surface and from ITO (111) surface to Pt(4d), as discussed above. When we dope 4 Sn in the In$_2$O$_3$(111) surface, the four extra electrons from the Sn do not distribute uniformly but accumulates in the area surrounding the doping site. The heterogeneity of electron distribution in the ITO (111) surface causes the charge to play a role in the Pt adsorption, inducing the Pt SA to choose a site that will help Pt gain electrons from the ITO (111) surface. Hence, both the adsorption environment and the charge distribution play a significant role in the Pt-SA adsorption. The adsorption energies of all the systems are positive with respect to bulk, which means that the Pt atoms in the bulk phase are more stable than the Pt atom adsorbed on the supports.

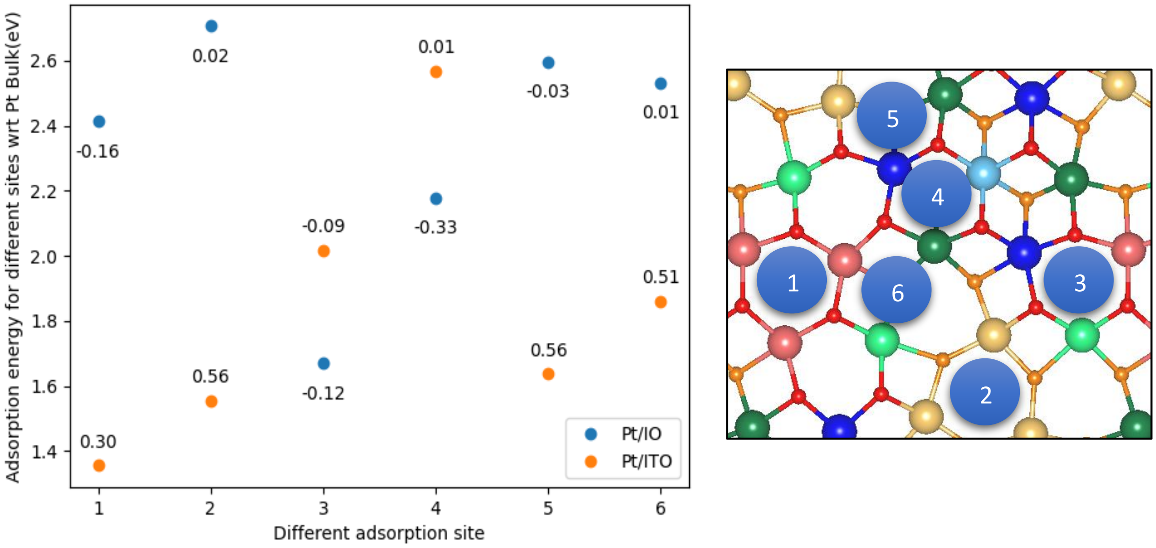

Figure 2-3 Adsorption energy of Pt-SA adsorption on the different sites on In$_2$O$_3$(111) and ITO(111) alongside the different sites shown on the surface. The different sites ae marked on the surface in the Appendix A Figure A.8, A.9. The bader charges are given on the respective points for the different Pt adsorption sites. It is calculated as (electrons on Pt – 10). Hence, positive means

higher electron density-gain in charge from the support whereas negative means lower charge density- loss in charge to the support. (In case of ITO(111) red and light blue sites are Tin)

Another aspect to consider is if the Pt-SA would displace the Sn atoms leading to formations of Sn defect sites. This can be simulated when we consider reactions between the ITO(111) slab, In_2O_3 bulk, and Pt-bulk in an oxygen rich environment, leading to $PtSn_7In_{56}O_{96}$ (with one Pt substituting an Sn) and ITO(111) bulk. We observe that the Pt-SA will stay as a single atom on the surface until an oxygen chemical potential of -1.48eV, and as we increase the oxygen chemical potential, the Pt-SA would displace Sn and interact directly with the surface through the defect site (SI-Section:5)

Pt_2/Pt_3: To explore the possible configurations of the Pt-dimer and trimer on the In_2O_3(111) and ITO(111) surfaces, we employed the basin hopping method. The procedure generated a total of around 300 optimized structures in both cases. We concluded our basin hopping algorithm once all the sites on the slab were covered, and no new structure was found for ~100 steps. We have presented a few of the best structures for both the dimer and trimer cases, along with their relative energies in the Appendix A-7.On In_2O_3(111), the dimer prefers the triangular region containing the In(6c) atoms (marked with a yellow line in Figure 2.1 (a), In(6c) being blue). The preferred sites for Pt-SA (site-3 and site-4) are also close to this triangular region. Three oxygen atoms are displaced, five In-O bonds are broken (four In(6)-O and one In(5)-O), and four Pt-O bonds are created, one O bridging two Pt atoms. Hence the dimer adsorption involves a rearrangement of the support. In the case of the trimer, even though the most energetically favored structure does not sit in the triangular region, 4 out of the 5 best structures (Appendix A- Figure A.14) have the Pt_3 cluster interacting with the specific triangular region. On the most stable structure of Figure.

2-4 (c), the Pt_3 structure is gaining stability by its interaction with the neighboring 3 In(5c) (2.67 Å) and 3 O (1.93 Å) and sits on the site in a perfect triangular shape (Pt-Pt = 2.61 Å), displacing three O atoms. Again, a substantial reconstruction of the O atoms occurs, breaking two In(5c)-O bond for each involved O. In contrast, on ITO(111) , the dimers/trimers do not prefer the triangular region but interact more favorably with the Sn atoms in between these triangular regions for the same reason the Pt-SA did. The Bader

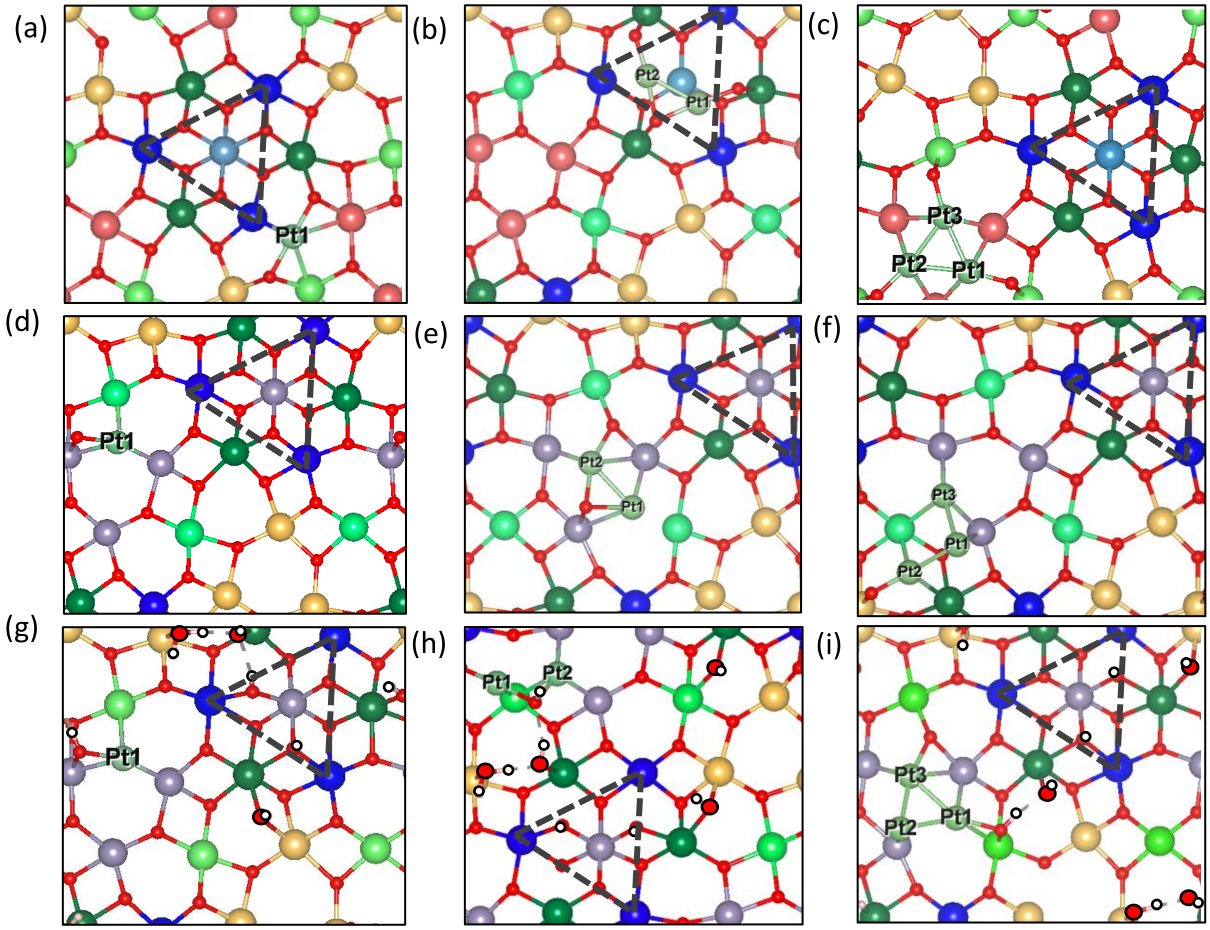

Figure 2-4 Pt-SA, dimer, trimer respectively on (a), (b), (c) In_2O_3 111 (d), (e), (f) ITO(111) and (g), (h), (i) on hydroxylated ITO(111) .

charge analysis shows that the dimer and trimer on In_2O_3(111) lose a total electronic population of 0.62 and 0.06 e, respectively. Whereas in the case of ITO(111) , the dimer and trimer gain a total electronic population of 0.27 and 0.70 e, respectively. This loss or gain in the electronic population is again in line with the work functions of these materials, as discussed above. The adsorption energy per Pt-atom on In_2O_3(111), referenced to Pt bulk, stabilizes from +1.67eV to +1.45eV to +1.21eV as we move from Pt-SA to dimer and trimer, hence slowly trending towards the bulk value of zero. Similarly, for the case of ITO(111) , the adsorption energy of Pt-atom, reference to Pt-bulk, stabilizes from +1.36eV to +1.29eV to +1.19eV when we move from Pt-SA to dimer to trimer. This implies that the Pt-SA would sinter to a larger cluster or particles on In_2O_3(111) and ITO(111). We also studied the stabilization of the dimer and trimer on the surface relative to 2 and 3 separated adsorbed Pt-atoms. The energy of the dimer and trimer were 0.83eV and 0.57eV lower than that of their fragmented counterparts for In_2O_3(111), verifying the better stability of these clusters on the In_2O_3(111), with respect to the SA.

2.3.3 Pt_n (n: 1,2,3) on hydroxylated ITO(111) surface

Finally, we studied the effects of surface hydroxyls and water molecules on the adsorption of the Pt clusters. We used the $4H_2O$-ITO(111) surface, including two dissociated water molecules (hence 4 surface OH groups) and two molecularly adsorbed waters, as our starting point, and we introduced the Pt-clusters. We employed the basin hopping approach for finding the best possible adsorption site and structure for our Pt – structures. The most important point to remember in this case is that the -OH/H_2O groups can move around the support to find a new binding site depending on where the Pt-cluster prefers to bind. We considered the possibility of -OH/-H/-H_2O migrations throughout the surface and reverse spillover of these groups onto the Pt-clusters. Ultimately, after

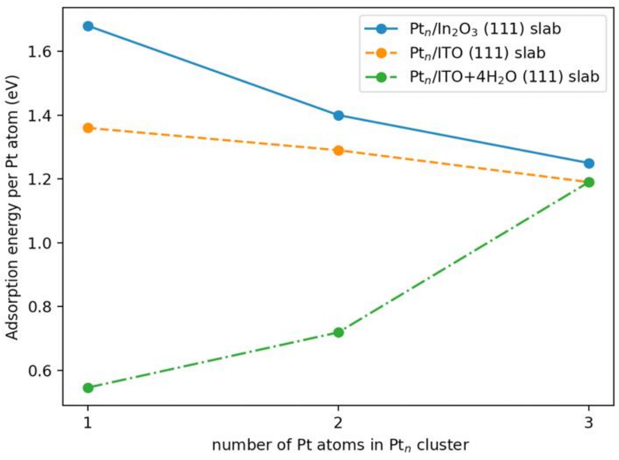

Figure 2-5 Pt-SA, dimer, trimer respectively on (a), (b), (c) In_2O_3 111 (d), (e), (f) ITO(111) and (g), (h), (i) on hydroxylated ITO(111) .

around 350 local optimizations, we were able to find the putative global minimum structures for our Pt-SA, dimer, and trimer structures, shown in Figure. 2-4 (g), (h), (i). The few of the best structures for Pt-SA, dimer, and trimer are given in the supplementary information along with their relative energies (Appendix A-8). Pt-SA is best located in the Sn rich area of the surface, similarly to the non-hydrated case, and it displaces an O atom to interact with that O atom, two Sn and one In. In addition, that O atoms become protonated, forming an OH group bridging Pt and Sn. The low coordinated bridging O is markedly stabilized by the interaction with the proton, explaining the more stable energy of the Pt-SA on the hydroxylated ITO(111) surface. The Pt-SA atom moves farther from the surface compared to that of the non-hydroxylated ITO(111) surface by 0.08 Å. The dimer maintains one Pt in the position of the SA and adds a second Pt bridged by the OH group, with a Pt-Pt bond distance of 2.74 Å (2.5% shorter than in Pt bulk). The trimer also sits close to the tin atoms, interacting with 3 Sn sharing 1 O and one OH with neighboring In. The Pt trimer has an average Pt-Pt bond distance of 2.62Å (6.8% shorter than in Pt bulk). A comparison of adsorption energies of all the structures of Pt-SA, dimer, trimer for the In_2O_3(111), ITO(111), and hydroxylated-ITO(111) supports of is given in Figure 2-5. We observe that the presence of water/hydroxyls stabilizes all three Pt-structures compared to In_2O_3(111), and ITO(111), but the stabilization per Pt atom is much larger for Pt_1, followed by Pt_2, and is very small on Pt_3. Consequently, the Pt-SA becomes more stable than the dimer and trimer.

The adsorption energy per Pt-atom on the hydroxylated surface is destabilized from 0.52eV to 0.71eV to 1.20eV when going from Pt_1 to Pt_2 and Pt_3. Although the adsorption energy of the Pt-SA is still slightly positive, indicative of a global small thermodynamic trend to sintering, the nucleation of a larger cluster is kinetically not favorable. This sintering resistant adsorption of Pt-SA on the $4H_2O$-ITO(111) can be attributed to the strong anchoring provided by the nearby hydroxyl. This observation is also corroborated by Weber et al[128] in their study of size selected Pt_n clusters (n=1-14) deposited on ITO(111) , where they suggested from their electrochemical study that even at a high Pt_1 coverage (0.1 monolayer) a substantial fraction of the deposited Pt_1 remain isolated and do not sinter into larger Pt-clusters. In the case of the non-hydroxylated ITO(111)

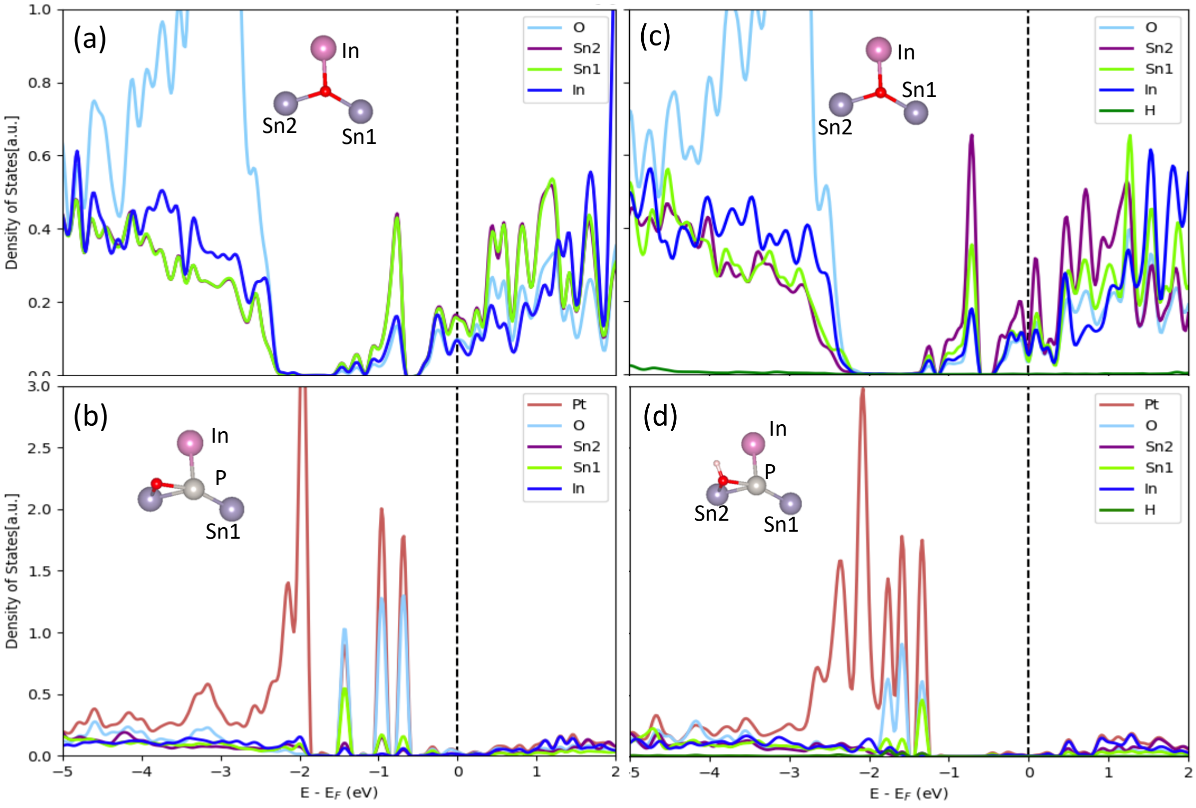

Figure 2-6 Atom-resolved density of states corresponding to the atoms interacting with Pt before deposition of (a) ITO(111) (b) ITO(111)+$4H_2O$ and after deposition (c) Pt-SA/ITO(111) (d) Pt-SA/ITO(111)+$4H_2O$

surface, the surface restructuring upon Pt interaction displaces a O atom, putting it in a bridge position between Sn and Pt. This low coordination O atom is reactive (electronic depletion of 0.23e) and water molecules are introduced on the surface this O gets protonated, which helps stabilizing the Pt atom. This is also visible through the density of states presented in Figure 2-6(c) and 6(d), where we observe well defined Pt states that primarily mix with orbitals of the bridging O and of Sn1, and where these states are lying lower in energy into the valence band of the hydroxylated system than in the case of the non-hydroxylated system. In the case of the dimer, we observe the complete migration of an OH from the oxide support to the metal, also called reverse-spillover, which is a feature that is also observed on Pt/Al_2O_3. Whereas for the trimer, we see the interaction with a nearby -OH group, but the energy stabilization compared to the non-hydrated ITO(111) is very modest. Spillover of OH is hence of utmost importance for the stabilization of highly dispersed Pt clusters on hydroxylated ITO(111). The Bader charge analysis shows that all the three Pt clusters gained charge from the 4H_2O-ITO(111) surface. The Pt-SA, dimer, and trimer gained an electronic population of 0.33, 0.15, and 0.51 e, respectively.

An influence of surface hydroxyl groups on the binding of single atoms on oxide surfaces was also observed and the authors provided three possible reasons for the stability:

1) An enhanced binding of adatoms to surface sites adjacent to hydroxyl groups as observed in the case of Pd/ɣ-Al_2O_3[111], Pt/Al_2O_3 [112], Co/Al_2O_3(0001)[113], Rh/ZrO_2 [115,116], Ru/ZrO2[117], Pt/TiO_2[53], Pd/MgO[120], Pd/Fe_3O_4[121]. This metal - hydroxyl interaction will be different for different adatoms and might in some cases lead to decreased stability and hence increased mobility and sintering as observed in Au/TiO_2(110)[141].
2) The hydroxyls can provide excess oxygen to oxidize the metal adatom leading to formations of MO_x type moieties as observed in Ru/ZrO2[117] and Pt/TiO_2[118].

3) The increased stability of the smaller clusters can also be caused due to the higher surface diffusion barriers of the metal atoms which reduces the mobility and the sintering effects. This diffusion barrier is the direct consequence of the high hydroxyl coverage on the support. As the metal coverage is increased the hydroxyl coverage decreases because of the reverse spillover of -H/-OH atoms from the support to the cluster. This causes increase in the mobility of the clusters followed by sintering which is observed in Pt/ TiO_2(011)- 2 x 1[114]. In this case oxide supports, which inherently have a higher hydroxyl coverage and binds them strongly (not allowing reverse spillovers to the cluster) might be a strategy to stabilize the small metal clusters.

2.4 Conclusion

We used first-principles DFT calculations to determine the best doping sites and structure for the Sn doped Indium Oxide(111) surface. Sn atoms substitute In atoms and prefer to reside in the surface layer. Two locations for Sn are seen. The Sn atom can be 6 coordinated with O, in the middle of a triangle of 6 coordinated In atoms. In this case, Sn is saturated, does not show in the STM image, and is not reactive. Alternatively, Sn can be 5 coordinated with O, bright in the STM image and reactive with Pt clusters. We also study the ITO(111) surface after exposure to water at room temperature. ITO(111) is one of the most frequently used materials in flat panel displays; despite its popularity, very little is known about its reactivity with water. From our calculations, the maximum hydroxyl coverage is relatively low, with only 1.1 hydroxyl per nm^2. After which, the H_2O molecules tend to stay in the molecular form on the surface. The four hydroxyls bridge 5-coordinated In atoms at pairs of symmetrically equivalent sites. Even though a third pair of symmetrically equivalent site was present, the third H_2O chooses to adsorb molecularly and not dissociatively. This, therefore, means the hydroxyl coverage is not site-dependent but surface dependent. The stability of intact water molecules over hydroxyls with increasing water coverage can be attributed to the attractive adsorbate - adsorbate interaction (in this case, the H-bonding) and the repulsive substrate mediate adsorbate-adsorbate interaction.

The adsorption of Pt clusters on the In_2O_3, ITO(111), and 4-H_2O-ITO(111) surface is markedly reactive, displacing O atoms to form Pt-In or Pt-Sn bonds. The adsorption site on In_2O_3(111) involves the electronically deficient area which encompasses the In(6c) and In(5c) whereas on ITO(111) the Pt adsorbs on the electronically enriched site encompassing the Sn(5c). This change in adsorption site is attributed to the different work functions and the heterogeneity in the two surface's charge density. This heterogeneity is the direct consequence of the Sn-doping in the In_2O_3(111) surface that injects 4 electrons in the surface unit cell. On ITO(111) , Pt clusters adsorb preferentially on the reactive 5-coordinated Sn atoms, also bridging with neighboring unsaturated In atoms and displacing a O atom. The adsorption energy per Pt atom is decreased as the number of Pt atoms is increased in the adsorbed clusters due to the formation of the strong Pt-Pt bonds in the case of In_2O_3(111) and ITO(111) , which thus tells us that the Pt-SA is not globally stable and can sinter to a dimer, trimer and eventually to bigger Pt-clusters. This sintering behavior is modified by introducing hydroxyls/water on the surface of ITO(111) . The Pt-clusters interaction with hydroxyls and water stabilizes the Pt-SA and the dimer by ~0.5 eV while the trimer is not significantly stabilized. This results in a considerable energy cost to form the trimer on the hydrated ITO(111) surfaces (0.6 eV) such that sintering becomes more difficult to sinter and that Pt-SA can remain metastable at moderate temperature.

Chapter 3 Electrocatalytic hydrogen evolution at full atomic utilization over ITO-supported sub-nano Pt_n clusters: High, size-dependent activity controlled by fluxional Pt hydride species.

3.1 Introduction

The hydrogen evolution reaction (HER) is a major process for energy conversion and storage, motivating considerable interest in improving the cost-effectiveness of electrolyzers.[34–37,45] To lower the high cost of the electrocatalysts, which are currently made of expensive metals like platinum[37,38] and iridium[142], the precious metal concentration must be decreased. Dispersing the metals on supports as single atoms or sub-nanometer clusters can help lower the metal content by ensuring that every metal atom is accessible throughout the catalytic process. Due to their unique topologies and electronic properties, which are crucial to understanding their chemisorption properties, small nanoclusters are also interesting from a fundamental perspective. There may be substantial adsorbate-induced reconstructions for such a small cluster, altering the geometry and electronic structure of the active sites during the reaction [143–145], maybe for the better. There is also the possibility for adsorbate- or potential-induced sintering or cluster disintegration, modifying the catalyst properties and possibly reducing the catalyst lifetime[146]. These small clusters can also exhibit fluxionality, which denotes their capacity to not only reorganize under reaction conditions but also to access not just a single but a collection of low-free energy structures[147].

To maximize insights regarding the activity of sub-nano clusters it is important that the electrocatalysts be atomically monodisperse, and theory must follow the ensemble of dynamically coupled isomers, rather than focusing on just a static global minimum structure. For example, Sun *et al.* reported that the most stable isomer of Cu_4O_3 was inactive for alkane oxidative dehydrogenation, however, barrierless isomerization to metastable isomers with low barrier facilitated its catalytic activity[30]. Pt_{13} can populate low-energy metastable structures under hydrogen pressure, which play a major role in its catalytic reactivity[29]. Pure and alloyed Pt clusters supported on Al_2O_3 were also extensively studied theoretically and experimentally[148–150], showing that at temperatures typical for catalysis, the cluster geometry changes frequently. For the catalysis of CO oxidation, Ghosh et al.[151] investigated Au clusters deposited on CeO_2 (111) with O vacancies. They discovered that, in this case, cluster fluxionality promotes the reaction. In the presence of CO, Au_2 on ceria dissociates, whereas Au_3 survives. Reorganization of supported clusters under electrochemical potential and adsorbates of oxygen reduction reaction was also recently reported[143,145].

While small, electrode-supported Pt clusters allow reactant access to all the Pt atoms, it is unclear how cluster size affects reactivity of the atoms. The hydrogen adsorption energy is a key reactivity descriptor for HER, and extended Pt surfaces, such as Pt(111), have H binding energies slightly more negative, but close to the theoretical optimum(ΔG_{ads}~0eV)[152]. The Pt atoms in small Pt clusters have lower Pt-Pt coordination, and have H adsorption energies at low coverage which are more negative (i.e. more stable) than those for extended surfaces[153], and on this basis would appear to be poor candidates for HER catalysts. This low H coverage picture is, however, insufficient because high H coverages can adsorb on such small Pt clusters under HER conditions[154,155]. Sun *et al.* have used DFT calculations to study the Pt_{13} cluster under high coverage of hydrogen ($Pt_{13}H_{26}$)[29]. They showed that the most stable structure presents a compact cuboctahedra structure and a H adsorption energy at least 0.2 eV stronger (more negative) than Pt (111): it would, therefore, not be a good catalyst for HER. Metastable isomers of $Pt_{13}H_{26}$ can provide optimal H adsorption energies that would give high HER activity, but they are too energetically unstable and do not have significant populations at room temperature. As a result,

$Pt_{13}H_{26}$ was predicted to be a poor HER catalyst. In contrast, here we show by a combination of experiments and simulations, that smaller supported cluster sizes (n=4, 7, 8) have high HER activity.

The development of single atom and cluster-based catalysts, where cluster size-dependent activity was observed, has received a lot of attention over the past few decades. Indeed, recent advances in experimental techniques made it possible to prepare and observe catalysts consisting of atomically dispersed species[156]. It has been reported that highly dispersed Pt atoms and clusters on transition metal oxide layers have a higher catalytic activity toward the HER compared to bulk Pt and commercial Pt nanoparticles[157–159]. In addition, size effects of sub-nano cluster catalysts are also of fundamental interest, as adding or removing a single atom can cause large, non-monotonic variations of the clusters' electronic and chemical properties, with contrasted impact for different reactions. An excellent perspective paper by Vajda and coworkers[160,161] reviewed size- and composition-dependent cluster catalysis and electrocatalysis, and the Vajda group has reported several cluster electrochemistry studies with strong size effects[161,162]. Heiz, Arenz, and coworkers[163,164] provided an experimental framework addressing electrocatalytic processes that are mediated by size-selected Pt clusters and nanoparticles, with a particular focus on the oxygen reduction reaction (ORR) and potential-induced sintering. In this regard, von Weber *et al.* showed non-monotonic order-of-magnitude variations in the activity of Pt_n ($n = 1 - 14$) deposited on indium tin oxide (ITO) electrodes for ethanol electro-oxidation[165] and showed that the activity correlated with Pt electronic properties probed by X-ray photoelectron spectroscopy (XPS), but the same Pt_n/ITO electrodes showed a monotonic size effect on the branching between water and H_2O_2 products in the oxygen reduction reaction (ORR)[127]. Sun and coworkers[166] produced ensembles of single Pt atoms using atomic layer deposition (ALD) and investigated how size affected the HER. Other research teams have examined the catalysis of single Pt atom ensembles in a variety of settings, including the HER on Pt-doped MoS_2 substrates[167] and CO oxidation on FeO_x substrates[168].

Here, we present a comprehensive study of the effects of Pt cluster size on the HER activity for atomically size-selected Pt atoms and clusters deposited on ITO electrodes. ITO is a transparent conducting oxide prepared by doping In_2O_3 with Sn (~5%)[123,124,144], and is common in both electrochemical and photoelectrochemical investigations. To understand how size affects the HER mechanism, the experiments used mass-selected cluster ion deposition in ultra-high vacuum to prepare atomically monodisperse electrodes, and density functional theory (DFT) was used along with the grand canonical basin hopping method (GCBH) to explore the structural diversity of small Pt-clusters deposited on ITO under electrochemical conditions. We explored the effects of cluster restructuring and multiple accessible adsorption isomers on the catalytic surface and HER activity.

3.2 Methods

3.2.1 Total-Energy Calculations

All calculations were carried out within the density functional theory framework using the Vienna ab-initio simulation package (VASP). [169,170] The electron-ion interactions are treated using the projector augmented wave (PAW) method.[171] We use the Perdew–Burke–Ernzerhof (PBE) functional to treat the exchange-correlation interactions.[172] The Gaussian smearing method with a smearing of 0.01 eV is used to improve K point convergence. The valence electronic states are expanded in plane-wave basis sets with an energy cutoff of 500 eV. The structures are optimized until the force on each atom is less than 0.01 $eV/A^{\circ-1}$. ITO is not considered to be strongly correlated material as both Sn and In have low electron density. As a result, we have chosen not to apply any Hubbard corrections in our calculations as PBE would be sufficient for accurately describing the electronic properties of ITO. The Brillouin-zone (BZ) integration is sampled by adopting the Monkhorst–Pack (MP) k-point grids of 5x5x1 for all the surfaces. During the geometry relaxations of the surface, only the outer atoms were allowed to relax. The cell parameters and inner atoms (in a 2 Å thick middle layer) were fixed to those determined for bulk ITO. Inversion symmetry was kept in all calculations to nullify the dipole moment. Structures were relaxed until the force on each atom was less than 0.01 eV/ Å $^{-1}$. Accounting for solvation effects was achieved by exploiting the implicit solvation model implemented by Hennig and co-workers under the name VASPsol[173–175]. The electrochemical potential was modified using a surface-charging method based on the linearized Poisson–Boltzmann (PB) equation implemented in the VASPsol[174,176]. This equation allows us to include an idealized electrolyte distribution in the electronic structure computations. This electrolyte distribution also balances the surface charge without correction terms, in contrast to a surface-charging model relying on a homogeneous background charge.[177] The cavity surface tension was set at 0.00, and the electrolyte concentration within the linearized PB equation was set as 1.0 M. The vaccum for surface charging calculations have been set to 60Å. The surface charging method is a generalized approach for modeling electrochemical systems that involves approximations in order to simplify the calculations and make them more computationally efficient. However, this method should be used with caution and with a full understanding of its limitations. Despite this, it is still a valuable tool for studying large systems and performing multiple calculations. This is because it is more computationally viable compared to other explicit models. Additionally, the surface charging method has been previously used to study electrochemical reactions and has been benchmarked against experimental results[178].

This gives confidence in using this method for our work as it has been found to be reliable in previous studies[179–182].

3.2.2 Models

We have modelled 5% doped ITO (111) as our ITO substrate model, in link with our experiments, as it has been previously reported to provide an optimum tin doping level for the highest carrier density[136], we found that all Sn atoms prefer to locate in the surface layer. For a four-layer slab, with unit cell dimension in the surface plane of 14.65 x 14.65 Å, 8 Sn (5% atom) atoms are present, 4 in the top and 4 in the bottom layer. 3 Sn atoms replace the In atoms in 5 coordinated sites, and 1 Sn atom replaces the In in the 6 coordinated site. The unit dimension in the surface plane for ITO is 14.65 x 14.65 x 60 Å. From our previous study, the surface has 4 H_2O molecules *per* cell; two are dissociatively adsorbed, and the other two are adsorbed intact. For full details of the surface structure and water interaction with the surface, we refer the reader to our previous work[144]. To explore possible adsorption sites and shapes of the Pt_n (n = 1, 4, 7, 8) clusters, we used the Grand Canonical Basin Hopping (GCBH) global optimization method. The motivation to use basin hopping for our studies was from Sun *et al*[15] *and* our previous work[144]. The full details of the GCBH method are provided in the Appendix A.9.

3.3 Results and Discussion

3.3.1 Potential Energy Surface exploration under the electrochemical reaction condition

In this section, we explore the structures of Pt_1H_x, Pt_4H_x, Pt_7H_x, and Pt_8H_x clusters supported on ITO at a potential of E = 0V vs. SHE and pH = 1 using the GCBH method (Appendix A.9). For this free energy surface (FES) exploration, we use the following mutations in our GCBH method:

A. The cluster can move randomly over the ITO surface to find its most stable adsorption site.

B. The cluster shape can change randomly by a move of one Pt atom to find the most stable cluster shape.

C. The H coverage is mutated grand canonically to find the most stable H coverage across the different clusters. The changing H coverage under the electrochemical reaction condition can also modify the cluster shape and the adsorption site.

D. The hydroxyl groups on the ITO surface can move around and transfer to the cluster.

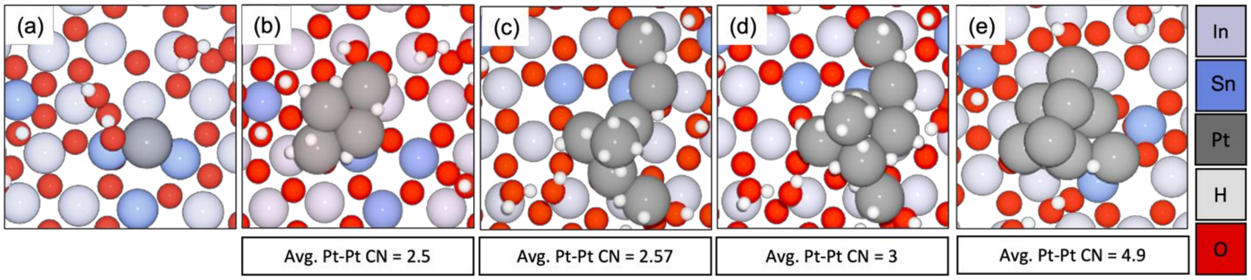

Figure 3-1 Most stable structure for Pt_1, Pt_4, Pt_7 and Pt_8 on ITO (111) at a potential E = 0 vs SHE, pH = 1. (a) Pt_1H_0/ITO (b) Pt_4H_7/ITO (c) Pt_7H_{12}/ITO (d) Pt_8H_{16}/ITO. The optimal structure for Pt_8/ITO with no added H atom is given for comparison in (e). The average Pt-Pt coordination number (CN) is indicated for b, c, d and e.

Using the above four mutations together, we generated 2343, 2894, and 3222 unique structures for Pt_4H_x, Pt_7H_x, and Pt_8H_x, respectively. The FES for the clusters with varying hydrogen coverages is given in the Appendix B.1. The global minimum for the Pt_1 structure was taken from our previous work[144].The optimum global minimum H coverage and structures for the different cluster sizes at U = 0V vs. SHE and pH=1 are given in Figure 3-1 (a,b,c,d). For comparison, Figure 3-1e provides the Pt_8/ITO structure found via GCBH with no H coverage (E = 0 V vs SHE) , showing how the Pt cluster core structure changes due to the high H coverage under electrochemical conditions. We find that, independent of the cluster size, the Pt atoms tend to stay in close interaction with the surface Sn atoms on the ITO surface. This result is consistent with our previous work, in which Pt_1, Pt_2, and Pt_3 all preferred interacting with the Sn. The nearby hydroxyls and O atoms also help anchor the clusters, stabilizing them and restricting them from diffusing across the support[144].

Except for Pt_1, all other cluster sizes were observed to have high optimum hydrogen coverage at E = 0 (vs SHE) and pH = 1, averaging at ~2 H/Pt atom. As the potential goes negative, the optimum hydrogen coverage increases, as shown in Figure 3-2(e). focusing on the window from +0.025 to -0.1V to -0.1V vs. SHE, i.e., at potentials above and below the HER onset potential (Appendix B). In the case of Pt_1, we observe that in the potential range from 0 to -0.1 V vs. SHE, the most stable structure was Pt_1H_0/ITO, i.e., there is zero H adsorption in the UPD and HER region. Only after the potential reaches an overpotential of -0.3 V does the Pt_1H_2/ITO structure become the most stable one (Appendix B.2). On the other hand, all the other cluster sizes (4, 7, and 8) show a very high hydrogen coverage in the potential range from 0.025 to -0.1eV. The high overall H content (~2H/Pt) shows that the initially metallic Pt cluster transforms in electroreduction conditions to Pt hydride species. Pt di-hydride species are known for ligated Pt

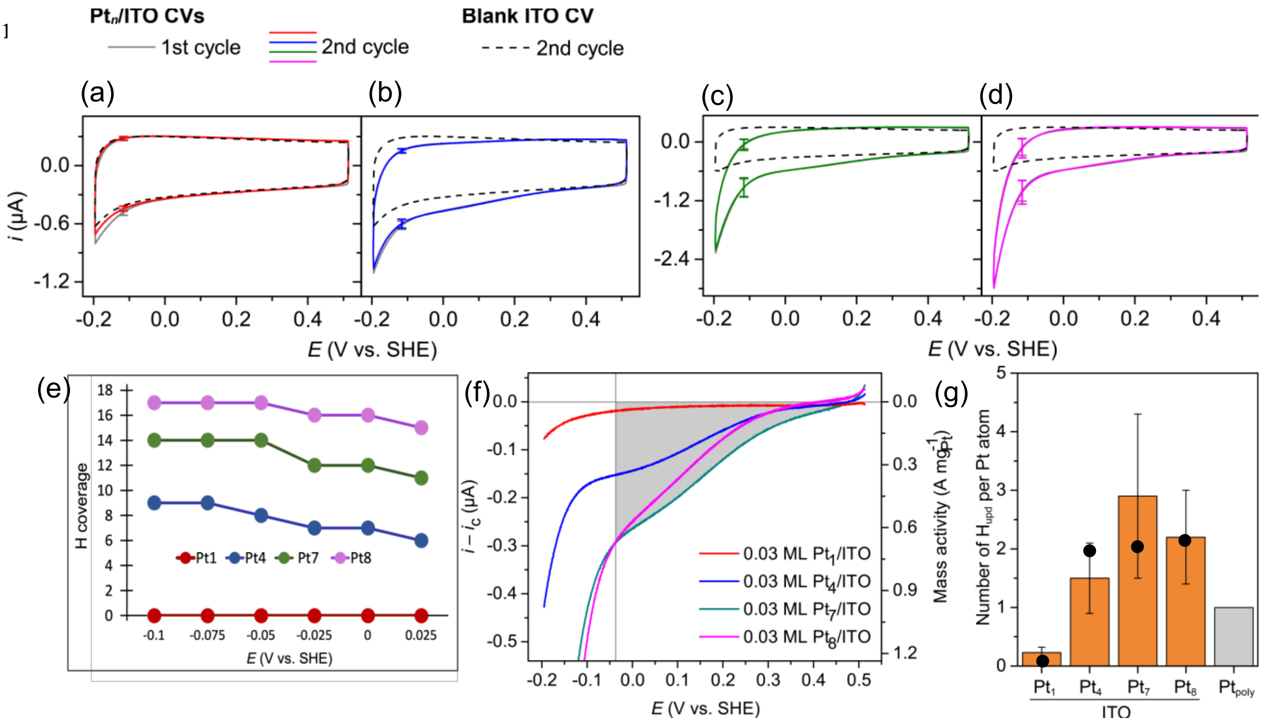

Figure 3-2 CVs obtained for (a) 0.03 ML Pt_1/ITO, (b) 0.03 ML Pt_4/ITO, (c) 0.03 ML Pt_7/ITO, (d) 0.03 ML Pt_8/ITO, from left to right. in Ar-saturated 0.1 M $HClO_4$ at a scan rate of 0.1 V s^{-1}. For each cluster electrode, the first and second CV cycles are shown as gray and colored solid curves, overlapping closely except for Pt_1. The dashed curves show the second CV for Pt-free ITO recorded under the identical conditions. The error bars represent the standard deviations of repeated measurements. (e) H atom coverages on the global minima for Pt_1, Pt_4, Pt_7, and Pt_8 on ITO(111) at varying potentials. (f) Negative sweep of the voltammograms for 0.03 ML Pt_n/ITO (n = 1, 4, 7, 8) after subtracting the capacitive background current from ITO, i_c. The subtracted currents were integrated to calculate the total charge transferred in the H_{upd} potential region, assumed to extend to -0.036 V. For example, the integration area for Pt_7/ITO is shaded gray. (g) Bars give the size-dependent numbers of H atoms per Pt atom adsorbed in the UPD region, estimated from the integrated H_{upd} currents from (g). Error bars represent standard deviations of repeated measurements. The black dots represent the H atom coverage per Pt atom determined from GCBH and DFT at the potential E = -0.05V vs SHE.

spectroscopy supplemented with theory[184].

Pt hydride species have also been computationally proposed in the case of small Pt_n clusters (n=8,13) on alumina exposed to a gas phase of hydrogen[15,107], and hence are not specific to electroreduction conditions. Bulk Pt, in the form of nanoparticles for example, does not form a hydride under normal catalytic or electrocatalytic conditions becoming covered by just a monolayer of H, i.e. a 1:1 H:Pt ratio for Pt surface atoms, hence giving a smaller H/Pt ratio. The bulk hydride species PtH is only formed at high pressure (>20 GPa)[185].

System	Avg. Pt-H (Å)	Avg Pt-Pt (Å)
Pt_4H_7/ITO	1.65	2.71
Pt_7H_{12}/ITO	1.66	2.75
Pt_8H_{16}/ITO	1.68	2.76
Pt_3/ITO[34]	-	2.62
Pt_8/ITO	-	2.66
Pt bulk	-	2.81

Table 3-1 Avg. Pt-H and Avg. Pt-Pt bond lengths for different systems

To accommodate such high hydrogen coverage, our calculations show that the clusters tend to form open structures with an average Pt-Pt coordination number (CN) of 2.5, 2.57, and 3 for Pt_4H_7, Pt_7H_{12}, and Pt_8H_{16}, respectively (r_{cutoff} for Pt-Pt distance is taken as 2.87 Å). These CNs are low compared to the CNs for bulk Pt surfaces (e.g. CN = 9 for Pt(111)) and for Pt_8H_{16} compared to that of the bare supported Pt_8 cluster (4.9). The avg. bond lengths of first-neighbor Pt-Pt pairs and Pt-H pairs are given in Table 3-1. All Pt-Pt distances are compressed compared with bulk Pt. Both the avg. Pt-H and Pt-Pt bond length increases as we increase the Pt cluster size. We also compare the avg. Pt-Pt distance of the Pt_nH_x/ITO systems with Pt_3/ITO from our previous work and Pt_8/ITO (global minimum structure from GCBH of Pt_8 cluster on ITO, (Figure 3-1(e)), showing that with H coverage, the avg. Pt-Pt bond distance increases. This result agrees well with previous work by Itoi *et al.*[186] and Sun *et al.*[29] , where they observed the contraction of the Pt-Pt bond for nanoparticles below 1 nm and Pt-Pt bond expansion upon H_2 adsorption. It is important to note that the Pt_n clusters are not static but adapt their shape and support interaction in response to the hydrogen coverage, itself determined by the electrochemical potential value, as can be seen in Fig 1 for the example of Pt_8.

Figure 3-2 (a-d) shows the first and second cyclic voltammetry (CV) data for each Pt_n/ITO electrode in the potential range between –0.196 and 0.514 V vs. SHE, showing the absolute currents. As noted, each electrode contained precisely 0.03 ML-equivalent of Pt in the form of different size Pt_n. Except for Pt_1, the first and second CVs are essentially superimposable, i.e., the voltammetric responses are already essentially in steady state during first CV cycle. The dashed curves show the currents observed in the second CV for Pt-free ITO, primarily due to non-faradaic (capacitive) contributions. Note that because all Pt_n/ITO samples had the same 0.434 ng of Pt present, the relative activities are directly proportional to the measured currents.

Figure 3-2(f) shows the faradaic current responses of the 0.03 ML Pt_n/ITO electrodes in the potential range near the thermodynamic HER threshold (gray vertical line), obtained by subtracting the ITO background current from the voltammograms in Fig. 3-2. At potentials negative of the threshold, the Pt_n/ITO electrodes catalyze HER, with activities increasing rapidly with cluster size, and negligible activity for Pt_1/ITO. These background-subtracted currents are reported as mass activities, i.e., currents normalized to the Pt mass, as discussed in the Appendix B.16.

In addition to HER, for n = 4, 7, 8, the experiments also find large reduction currents at potentials positive of the HER threshold, in the H underpotential deposition (H_{upd}) region, where protons adsorb, building up H_{ads} coverage. The currents are proportional to the scan rate, which is characteristic of an electrode-adsorbed species involved in the reaction[8] (see Figs. B.10 and B.11). For reference Fig. B.10 shows CVs for polycrystalline Pt (Pt_{poly}) taken using the same cell and electrolyte, showing the expected H_{upd} structure in the potential range between ~0.3 and 0 V vs. SHE. We rule out the possibility of other reduction reactions contributing to the currents in the H_{upd} region, as no further reduction signals appeared even when the potential was cycled over the potential range up to 1.2 V (see Figure B.9 top). We also measured ORR in electrolyte that was not Ar-purged (Figure B9 bottom), showing that the potential dependence of the ORR current is quite different from the currents observed for Ar-purged electrolyte, extending well positive of the H_{upd} region. Thus, we conclude that the currents in the H_{upd} region for Ar-purged electrolyte are not significantly contaminated by ORR currents.

Since the H_{upd} feature in acidic media represents the one-electron Volmer reaction ($H^+ + e^- \rightarrow H_{ads}$), integration of the H_{upd} current allows quantification of the number of H atoms adsorbed on each Pt_n cluster in the H_{upd} potential range, as summarized in Figure 3-2(g) with details in Table B.1. Except for Pt_1, the Pt_n clusters were found to adsorb well over 1 H atom/Pt atom in the H_{upd} potential range, i.e., substantially more H/Pt than is observed for bulk Pt and most Pt-based electrocatalysts.[9] The measured high H_{upd} coverage is consistent, however, with the large number of adsorbed H atoms predicted by theory at the same potential (~2H per Pt) discussed above. Furthermore, the onset potential for H_{upd} on Pt_n/ITO electrodes (~0.45 V vs. SHE) was found to be substantially higher than that for Pt_{poly} (~0.3 V vs. SHE, Fig. S3), consistent with the theoretical finding that the H adsorption energy on small Pt clusters is higher than on bulk Pt at low coverages[153]. Finally, we note that the fact that such high H_{upd} signals were observed, in agreement with the DFT predictions, is evidence that air exposure during transfer to the electrochemical cell did not irreversibly poison or block H adsorption sites on the clusters.

3.3.2 Ensemble of structures for HER via thermodynamic analysis.

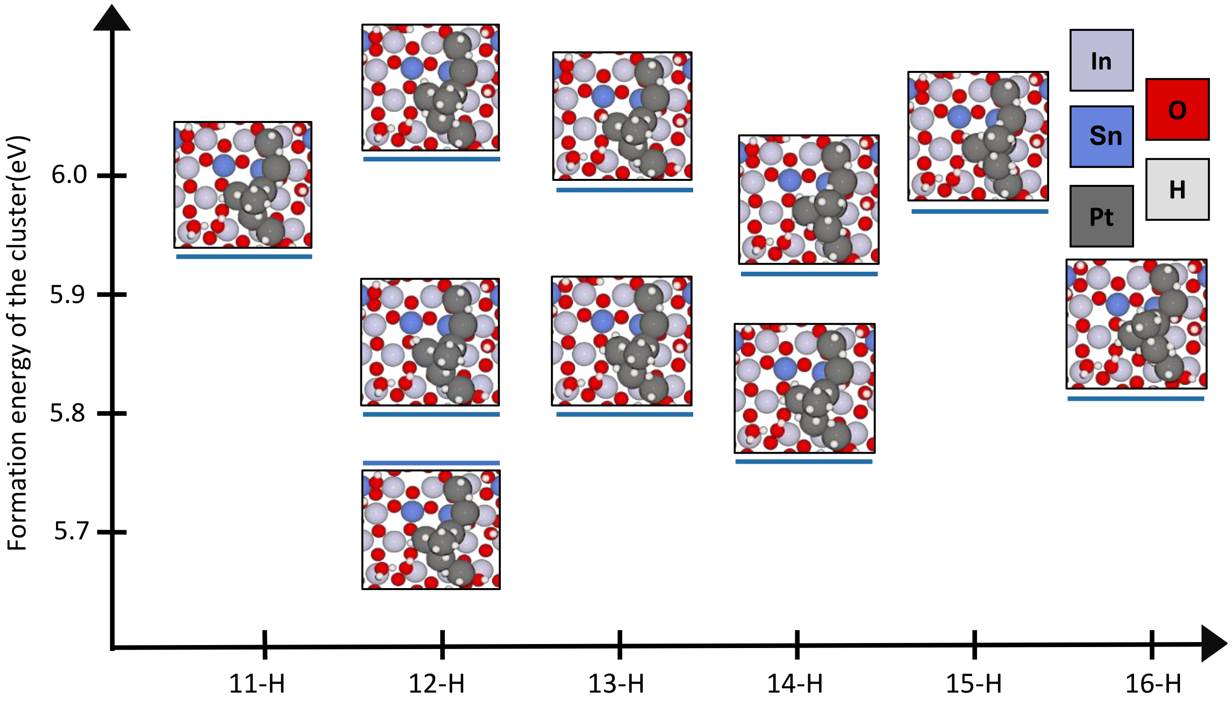

Figure 3-3 Formation energies of the ensemble of low energy structures for Pt_7H_x/ITO from each hydrogen coverage value evaluated using the surface charging method. Electrochemical condition: E = 0 V vs SHE, pH = 1.

To model the HER activity of the clusters under electrochemical conditions, we first need to determine the ensemble of cluster structures that would be energetically accessible to perform HER in the relevant potential range and not only the global minimum, as previously shown on Figure 3-1. To determine this ensemble of structures, we have exploited first-principles thermodynamics to calculate the formation energy of the various Pt_nH_x isomers, using Pt bulk as a reference and the surface charging method to express the potential dependence.

We consider the ensemble of structures within 0.3 eV in free energy of formation from the global minima (GM) for the various cluster sizes. These not only include the metastable structures (MS) with the same hydrogen coverage as the GM but also include structures from other hydrogen coverages neighboring the minima. Figure 3-3 presents the ensemble of structures for Pt_7H_x/ITO

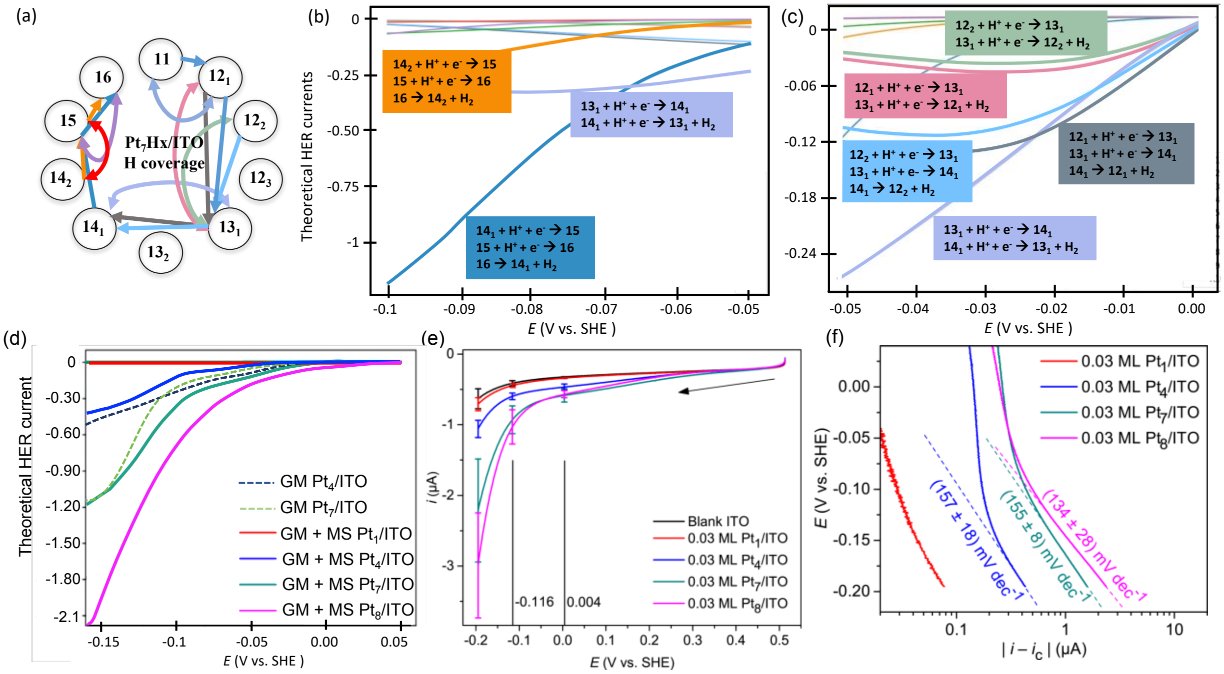

Figure 3-4 HER current plot from the Butler Volmer type kinetic modeling for Pt_7H_x/ITO; (a) network of various elementary reactions on Pt_7H_x/ITO where energetically accessible structures of the Pt_7Hx cluster are connected by curved arrows representing 2-step Volmer-Heyrovsky reactions, and pairs of straight arrows representing 3-step Volmer-Tafel reactions. The HER currents for the reactions in (a) are given in the potential range (b) -0.10 – -0.05 V vs SHE and (c) -0.05 – 0 V vs SHE (d) Total simulated HER currents obtained by combining all the currents from various reaction channels for Pt_n/ITO (n = 1, 4, 7, 8), considering all accessible (i.e., GM+MS) structures are shown by solid lines. Currents calculated considering only GM structures are shown as dashed lines. (e) Raw experimental voltammograms for 0.03 ML Pt_n/ITO (n = 1, 4, 7, 8) in an Ar-saturated 0.1 M $HClO_4$ solution at a scan rate of 0.1 V s^{-1}. The capacitive current from ITO has not been subtracted, and only the negative-going sweeps are shown. The error bars represent the standard deviations of repeated measurements. (f) Tafel plots of 0.03 ML Pt_n/ITO (n = 1, 4, 7, 8) obtained from (a). Tafel slopes are indicated for n = 4, 7, 8.

at E = 0 V vs SHE, pH = 1. As previously mentioned, Pt_7H_{12} is the GM, but there is still a significant Boltzmann probability (at T = 294K) that other structures are populated under reaction conditions and participate in the HER reaction network. The ensembles of low energy structures for the other cluster sizes Pt_1H_x, Pt_4H_x, and Pt_8H_x are provided in the Appendix B.4. Note that in the low energy ensemble, the Pt_n core structures and their adsorption geometries on the ITO support are unaffected by the (slightly) varying H coverages, i.e., the clusters are fluxional only in the sense that hydrogen numbers and adsorption sites are quite variable. This comment is valid only for the limited ranges of hydrogen coverages predicted to be present near the HER threshold potential. As shown in Figure 3-1 for Pt_8, the cluster structure is quite different for that at zero H coverage.

3.3.3 Hydrogen evolution reaction: Microkinetic Analysis and Role of Metastable states.

A factor that is important to consider is the fluxionality of the Pt_nH_x/ITO structures and the ensembles of reaction channels that contribute to the HER activity. These effects are illustrated in Figure 3-4a-c for the case of Pt_7H_x/ITO, which is the most fluxional of the cluster sizes studied, judging by the number of accessible isomers. We first construct a network of reaction paths that contribute to HER (Figure 3-4a) involving all the accessible isomers with different H coverages. The hydrogen coverages and isomers are indicated by numbers within in the circles. For example 12_n indicates the nth isomer of Pt_7H_{12} with higher n indicating higher energy isomers. Figure 3-4b and 3-4c shows contributions from each path to the HER currents, simulated using a Butler-Volmer-type formulation as explained in the Appendix B.1. The analogous networks and simulations for the other cluster sizes are given in the Appendix B.6 and B.7.

To build reaction networks, we need to consider the ensemble of structures, such as those for Pt_7H_x/ITO from Figure 3-3. In acidic electrochemical conditions, HER can proceed via two different catalytic cycles: the Volmer-Tafel reaction, where two protons adsorb on the catalyst, neutralize, and combine to form H_2:

$$\text{Volmer step}\ \ \mathrm{H^{+}_{(aq)} + e^{-} \rightarrow H_{ad}}$$

$$\text{Tafel step}\ \ \mathrm{H_{ad} + H_{ad} \rightarrow H_{2,gas}}$$

and the Volmer-Heyrovsky reaction, where just one proton adsorbs, reacting with a second proton impinging from solution to form H_2.

$$\text{Volmer step}\ \ \mathrm{H^{+}_{(aq)} + e^{-} \rightarrow H_{ad}}$$

$$\text{Heyrovsky step}\ \ \mathrm{H^{+}_{(aq)} + H_{ad} + e^{-} \rightarrow H_{2,\,gas}}$$

The reaction network for Pt_7H_x/ITO is illustrated in Figure 3-4(a). The hydrogen coverages and isomers are shown in the circles. For example, 12_n indicates the n^th isomer (higher n = higher energy) of Pt_7H_{12}. 2-step Volmer-Heyrovsky catalytic cycles (e.g., 11H → $12H_1$ → 11H) are represented in Fig. 4a by single curved arrows, which pairs of straight arrows represent 3-step Volmer-Tafel reactions (e.g., 11H → $12H_1$ → $13H_1$ →11H). The arrow colors differentiate between various possible reactions in the reaction network.

To evaluate the HER activity contribution, we calculated HER currents for all the reactions from the reaction network and plotted them as a function of potential in Figure 3-4(b,c) for two different potential ranges. The kinetic formulation used here for simulating HER activities is directly adapted from the work of Zhang *et al*[187] and is explained thoroughly in the Appendix B.1. At low negative potential (range [-0.05, 0] V vs. SHE) the HER current mainly involves structures with 12, 13, and 14 H coverage, and both the Volmer-Tafel and Volmer-Heyrovsky reaction mechanisms come into play (Figure 3-4(c)).

As we move toward more negative potentials in Figure 3-4(b), the dominant contributions to the HER current shift to 14, 15, and 16 H coverage. This is directly related to the fact that as we move toward negative potential, the optimum hydrogen coverage on the cluster increases (Figure 3-2e).

To compare the HER activity for the different cluster sizes, we combine the individual currents from the different reaction pathways (e.g., Figure 3-4(b,c) and Appendix B.16, B.17) for each cluster size to give the total theoretical currents for that cluster size, which are shown in Figure 3-4(d). The experimental voltammograms are shown in Figure 3-4(e), where only the cathodic current responses are shown, and the ITO capacitive current has not been subtracted. For reference, the currents for blank, Pt-free ITO is also shown.

Both simulations and experiments show that the HER activity is strongly dependent on the cluster size, with negligible activity for $\mathrm{Pt_1}$/ITO and increasing activity with size in the order $0 \approx \mathrm{Pt_1} \ll \mathrm{Pt_4} < \mathrm{Pt_7} < \mathrm{Pt_8}$. Because the $\mathrm{Pt_n}$/ITO samples contained identical amounts of Pt (0.434 ng),

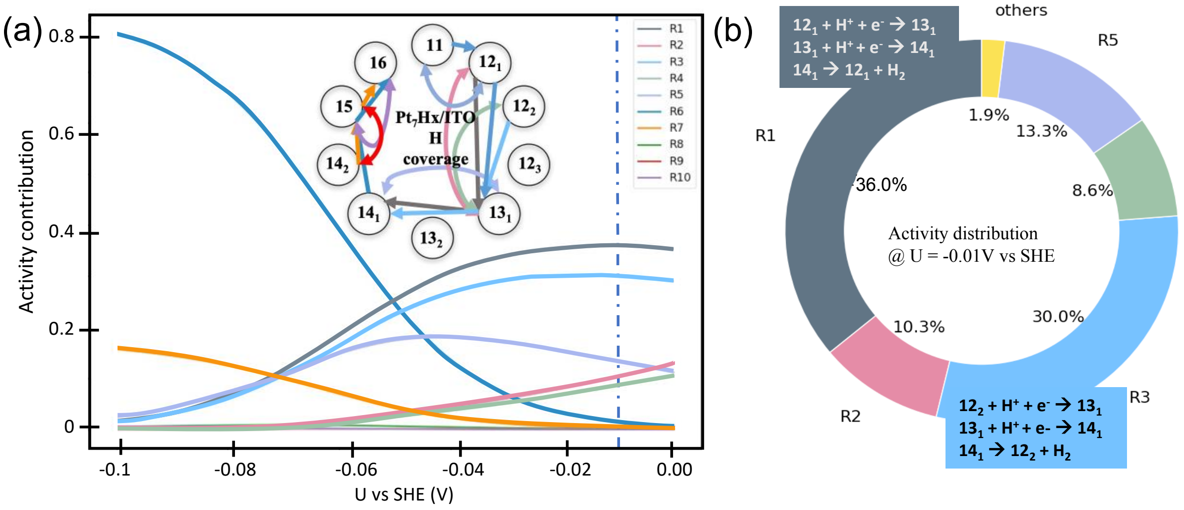

Figure 3-5 (a) Normalized activity contribution from various elementary reactions vs the potential. (b) The contribution from various reactions at -0.01V vs SHE (marked as the blue dashed line on (a)).

ng), the differences in currents show that the activity *per* Pt atom increases with cluster size. The low activity for Pt_1/ITO is theoretically found to result from the H adsorption step from Pt_1H_0/ITO → Pt_1H_1/ITO being energetically unfavorable, with an overpotential of -0.3V vs. SHE. This also explains why Pt_1/ITO shows no H_{upd} current (Figure 3-1). The observed low activity of single Pt atoms on ITO contrasts with other results in the literature for Pt_1 on nitrogen-doped graphene nanosheets[158] or WOx[159] support. One explanation of the difference could be a distinct influence of the support, or that the single Pt atom sinter into larger catalytically active clusters.

The sharp increase in HER activity with increasing cluster size raises the question of what particle size would be optimum. One point is certain, that as the clusters become larger, eventually they will adopt more compact structures with higher Pt-Pt coordination, and with an increasing fraction of the Pt no longer in the surface layer. The Pt atoms in the core would no longer be catalytically accessible, which would result in activity/Pt loss. Therefore, the HER activity will be high till these clusters remain very open where every Pt atoms is catalytically utilized.

The theoretical HER currents shown as solid lines in Fig. 3-3d include the contributions from all the structures present in the energetically accessible ensembles of structures for each cluster size. Figure 3-3d also shows theoretical voltammograms evaluated considering only the GM structures (dashed lines), to emphasize the importance of including contributions from the metastable structures. Note that if only GM structures are included, the predicted HER activity has an incorrect dependence on cluster size ($Pt_1 < Pt_7 < Pt_4 < Pt_8$) versus experiment because the metastable structures make a strong contribution to the Pt_7H_x/ITO HER current, increasing it by upto ~60 %. To probe this issue further, we evaluated the normalized activity contributions at varying potentials, as shown in Figure 3-5(a). Consider the potential E = -0.01V vs. SHE; at this potential, the dominant reactions are shown in Figure 3-5(b). The dominant contribution (36%) is the Volmer-Tafel reaction between structures $12H_1$,$13H_1$ and $14H_1$, which all are global minima for the respective hydrogen coverages. There is a 30% contribution from another Volmer-Tafel reaction involving the metastable structure 12_2 and the GM structures for 13 and 14 H coverages. There are also significant contributions from Volmer-Heyrovsky reactions involving metastable structures, including $13_2 \rightarrow 14 \rightarrow 13_2$ (R5), $12_1 \rightarrow 13 \rightarrow 12_1$ (R2), and $12_3 \rightarrow 13_2 \rightarrow 12_3$ (R4), representing a total of 31.2% to the HER current. Clearly, it is essential to include the ensemble of accessible structures in calculating activity for sub-nano cluster catalysts.

Another intriguing finding is that for Pt_4H_x/ITO, adding the metastable structures reduces the overall HER current, in contrast to the Pt_7H_x/ITO system. This can happen when some of the thermally populated metastable structures are catalytically inactive but reduce the populations of the catalytically active structures. In this case, the GM isomers are considerably more catalytically active than some of the energetically accessible metastable isomers, so that populating metastable isomers reduces the total activity. Again, this demonstrates the importance of considering the full ensemble of accessible isomers.

Our results also show that Volmer-Tafel reactions are dominant over Volmer-Heyrovsky reactions in the case of Pt_7H_x/ITO. For Pt_8H_x/ITO, the HER current comes solely from the Volmer-Tafel reaction between 16, 17, and 18 H-coverages in the potential range above -0.05V vs. SHE (Figure B.4). For Pt_4H_x/ITO, however, there are significant contributions from both Volmer-Tafel and Volmer-Heyrovsky reactions, with Volmer-Tafel dominating (Figure B.3). Therefore, the Volmer-Tafel mechanism appear to be dominant (or exclusive) for Pt_4, Pt_7 and Pt_8. In addition, in each case a Volmer step was found to be the rate determining step at a potential -0.15 V vs SHE. From the experimental viewpoint, the Tafel plots shown in Figure 3-4(f), show that the Pt_n/ITO (*n* = 4, 7, and 8) catalysts all show similar Tafel slopes of 130-160 mV dec^{-1}. From the experimental viewpoint, the Tafel plots shown in Figure 3-4(f), show that the Pt_n/ITO (n = 4, 7, and 8) catalysts all show similar Tafel slopes of 130-160 mV dec^{-1}. These values are fully compatible with a Volmer rate-determining step involving one electron transfer.[188] The theoretical Tafel slopes are also given in Figure B.6, which predicts a similar trend of the slope as $Pt_4 \approxeq Pt_7 > Pt_8$. However, because small, supported clusters have very different properties than bulk Pt or Pt nanoparticles, specifically in the amount of adsorbed H and adsorption energies, it is not obvious that the Tafel plots can be interpreted in a manner analogous to macroscopic Pt surfaces.

3.3.4 Size-dependent stability analysis of the clusters in electrochemical conditions.

We have evaluated the relative thermodynamic stability of the 4 different cluster sizes at 3 different potentials (0, -0.05, -0.1 V vs. SHE) given in Figure 3-6(a), to qualitatively explore whether the larger clusters might disintegrate or sinter under electrochemical conditions. The hydrogen coverages at different potentials from Figure 3-2(f) were mapped to evaluate the formation energy per Pt atom. The positive formation energy (details on how the formation energy

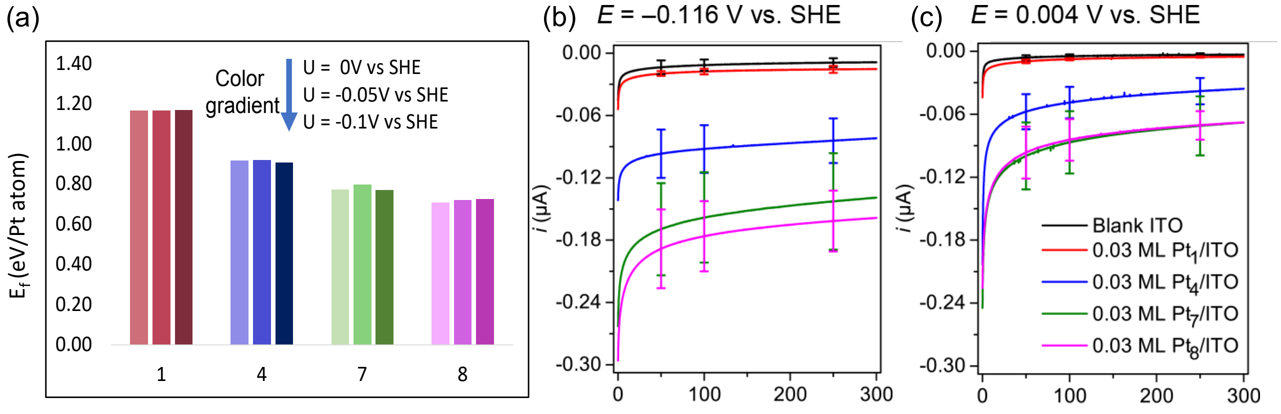

Figure 3-6 (a) Formation energies per Pt atom (E_f/Pt atom) for the supported Pt_nH_x clusters as a function of the particle size w.r.t Pt bulk. Chronoamperometry of 0.03 ML Pt_n/ITO (n = 1, 4, 7, 8) and blank ITO electrodes in an Ar-saturated 0.1 M $HClO_4$ solution at applied potentials of (b) –0.116 and (c) 0.004 V vs. SHE. The error bars represent the standard deviations of repeated measurements.

is evaluated is given in Appendix B.1) here that clusters are slightly less stable than bulk platinum, as expected, and a less positive value indicates a more stable structure. For each cluster size, the formation energy *per* Pt atom is almost independent of the applied potential, but the stability increases with cluster size (smaller the formation energy the more stable the cluster), suggesting that larger clusters should not disintegrate into smaller clusters under the HER conditions of our study. To study the effect of hydrogen coverage on stability, we also compare the formation energy/Pt atom of Pt_8H_x/ITO (~0.7eV) and Pt_8/ITO (0.89eV). The decrease in formation energy is directly related to the increased number of adsorbed H, which stabilize the cluster by ~0.2 eV. Therefore, the hydride clusters formed in electroreduction conditions are more stable than bare clusters, and thus should have reduced tendency to sinter.

Experimentally, we probed the stability of the Pt_n/ITO catalysts by chronoamperometry. As shown in Figure 3-6(b), the Pt_n/ITO catalysts gave that initially declined, but appeared to be leveling off, remaining active after 300s at –0.116 V, and the size-dependent magnitude of the HER current ($Pt_8 > Pt_7 > Pt_4 > Pt_1$) was consistent with the HER activity order observed in the voltammograms in Figure 3-4 (e). The decrease may relate to cluster degradation of some sort; however, we note that small clusters at low loadings are extremely sensitive to poisoning by contaminants in the electrolyte[165].

The amperograms in Figure 3-6(c) were obtained at a potential of 0.004 V, which is slightly positive of the thermodynamic HER threshold, but because the H_2 pressure is essentially zero, some HER may occur, in addition to hydrogen underpotential deposition. Note that for ITO and Pt_1/ITO, there were no significant currents apart from the initial double-layer-charging peak. For the cluster/ITO electrodes, small but significant currents were observed, persisting long after the initial capacitive charging current decayed. This could be due to HER driven by the negligible H_2

product pressure, but as discussed below there is also evidence for some non-electrochemical process that removes adsorbed H atoms from the Pt clusters, which would free sites for additional proton adsorption.

If there is, indeed, such a non-electrochemical H removal process, we might expect that little or no H desorption signal (i.e., $H_{ads} \rightarrow H^+ + e^-$) would be observed during scans to positive potentials, and that is the case for slow potential scan speeds, as shown in Figure 3-2(a-d). As shown in Figure B.10 and B.11, however, significant H desorption signals were observed for high scan rates, implying that this non-electrochemical H removal process is slow, allowing significant H coverage to remain adsorbed on the few-second time scale.

Our experiment provides no direct insight into the nature of this non-electrochemical H_{ads} removal process; however, we might expect that H spillover to the ITO support would be more significant for sub-nano Pt_n clusters compared to larger Pt nanoparticles. Indeed, on some sub-nano Pt-based catalytic systems, spillover of adsorbed species has been found to be quite efficient, due to the short pathways from Pt to oxide supports.[159,189–192] The fate of H spilled over to the oxide support is unclear, but possibilities include incorporation into the oxide lattice or recombinative desorption as H_2.

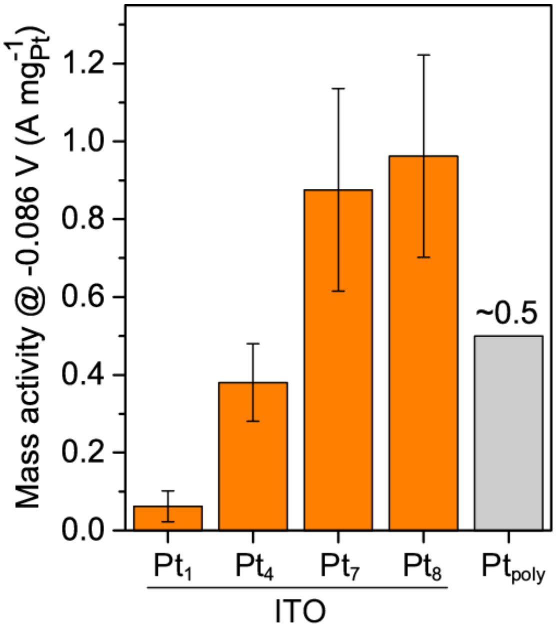

Figure 3-7 Comparison of mass activities measured under identical conditions for 0.03 ML Ptn/ITO (n = 1, 4, 7, 8) and polycrystalline Pt (Ptpoly), all at -0.086 V vs. SHE, corresponding to an overpotential η =0.05V. The calculation method for the mass activities can be found in the main text.

3.3.5 Mass activity comparison with other Pt-based HER catalysts

The sharp increase in HER activity with increasing cluster size raises the question of what particle size would be optimum, and how the activity of the Pt_n/ITO compares to other HER catalysts. Because our samples have a precisely known amount of Pt deposited (0.434 ng), it is straightforward to convert the background-subtracted HER currents (Figure 3-1g) to mass activities, i.e., currents per milligram of Pt deposited. Figure 3-7 compares the mass activities at a potential of -0.086 V vs. SHE, corresponding to an overpotential $\eta = 0.05$ V, for our 0.03 ML Pt_n/ITO electrodes and polycrystalline Pt (Pt_{poly}). For Pt_{poly} a true mass activity cannot be calculated, and the "mass activity" reported in the figure is a "top layer mass activity", i.e., the measured current normalized to the mass of just the top monolayer of the wetted Pt_{poly}

electrode area, which was estimated using the electrochemically active surface area measured in the same cell and under the same conditions as the Pt_n/ITO measurements (see Figure B.10a for the Pt_{poly} CVs). This top layer mass activity represents an upper limit on the actual Pt_{poly} mass activity, but it allows the mass activity of the clusters to be compared to the activity of the exposed surface atoms of a standard Pt electrode.

As noted, Pt_1/ITO is the least active Pt_n/ITO electrode, with a mass activity of just 0.06 ± 0.04 A mg_{Pt}^{-1}. For Pt_4, Pt_7, and Pt_8 on ITO, the mass activities are 0.38 ± 0.10 A mg_{Pt}^{-1}, 0.88 ± 0.26 A mg_{Pt}^{-1}, and 0.96 ± 0.26 A mg_{Pt}^{-1}, respectively. The Pt_{poly} top layer mass activity was ~0.5 A mg_{Pt}^{-1}. Thus, activity *per* Pt atom of Pt_4/ITO was already nearly as high as the activity *per* surface atom for Pt_{poly}, and the activities *per* atom of the Pt_7 and Pt_8/ITO electrodes were substantially greater.

3.4 Conclusion

We demonstrated that the HER activity of small ITO-supported Pt clusters is strongly cluster-size dependent, with Pt_1/ITO being inactive, and the activity per Pt mass significantly rising from Pt_4/ITO to Pt_8/ITO, with Pt_7/ITO and Pt_8/ITO having activity *per* Pt atom roughly double the activity *per* surface atom for Pt_{poly} under the same conditions. Additionally, the clusters present H_{upd} currents *per* Pt atom roughly twice as large as those reported for bulk Pt or large Pt nanoparticles, equating to adsorption of ~2 H atoms per Pt atom. The large H_{upd} currents are consistent with the DFT results, which found open, low Pt-Pt coordination Pt_nH_x/ITO structures under electrochemical conditions, with $x \sim 2n$. The cluster catalysts under electrocatalytic conditions are hence best described as a Pt hydride compound, significantly departing from a metallic Pt cluster.

The use of global optimization techniques and first-principles thermodynamics to predict structural ensembles, factoring in the changing numbers of adsorbates at various electrochemical potentials was also proven to be effective in predicting the observed currents using microkinetic models based on Butler-Volmer-type equations. Low-energy metastable isomers were shown to contribute significantly to the experimentally observed HER activities, sometimes increasing but sometimes decreasing the activity, pointing out the importance of considering the accessible isomer ensembles when simulating properties of sub-nano supported cluster catalysts. On the formed open Pt hydride clusters under potential, HER can occur on a very flat free energy surface. We analyzed the mechanisms that account for the HER currents for varying cluster sizes and showed that Volmer-Tafel mechanisms combining two proton reductive adsorptions and a non-electrochemical H_2 desorption step dominate. We are also able to better understand the stability of the clusters under reaction conditions with the use of computational thermodynamic analysis and chronoamperometry measurements. This study demonstrates that clusters are stabilized by the H overlayer and only show a small increase of stability with cluster size, in the range n=4-8. The clusters are further anchored to the support by the hydroxyls and oxygen on the ITO surface, which should tend to limit the clusters' ability to diffuse across the surface, thereby decreasing the likelihood that they may sinter.

Small Pt clusters on ITO bind hydrogen strongly, which at first sight can be considered as very unfavorable for HER. However, as shown in this paper, they transform under potential to a hydride compound $(PtH_2)_n$, which, in the case of large enough clusters (n=7,8), provide multiple sites with optimal binding energy for H and hence high HER activity. These clusters, exposing all Pt atoms, have high mass activity for HER.

The finding that it is crucial to include the ensembles of accessible metastable structures under reaction conditions to predict catalytic activity correctly is expected to apply to many other types of electrocatalysts where a local rearrangement would produce a slightly less stable but much more reactive site. Such metastability-induced surface reactivity may be important to not only catalysis but also film growth and surface reactions.

Chapter 4 Elucidation of Active Site for the Oxygen Evolution Reaction on Single Pt Atom Supported on Indium Tin Oxide

4.1 Introduction

Single-atom catalysts (SACs), with their potential maximized atom utilization efficiency, have attracted significant attention due to their high catalytic activity and selectivity[193,194]. These catalysts have been applied to a large range of reactions, including CO oxidation,[195–200] hydrogenation[201], dehydrogenation[201,202] and other electrocatalytic reactions[203–205]. For the expensive and in-demand noble metal catalysts like Ir, Pd, and Pt, SACs represent an ultimate dispersion of the metal with all the atoms exposed[206–208] and, if activity remains high compared to nanoparticle catalysts, an optimal utilization and cost. Additionally, SACs might open up particular reaction pathways, different from that of larger particles, and are well suited for a molecular-level understanding of the active-site structure and reaction mechanism by utilizing a variety of element-specific analytical tools supplemented by in situ/operando characterization and coupled with computational modeling[197,209–211]. There is now strong evidence that SACs are not static catalysts, but that they respond to reaction conditions by adapting their set of ligands and their mode of interaction with the support, making the determination of the active site challenging[108] Significant effort has been devoted to obtaining a thorough understanding of SACs through unique characterization techniques and theoretical calculations[212–214].

The oxygen evolution reaction (OER) is a key bottleneck in the electrocatalytic water splitting process, which is a promising method for producing hydrogen in an environmentally friendly manner[39–46] . The two half-processes that makeup water splitting, hydrogen, and oxygen evolution reactions (HER and OER) are carried out in acidic or alkaline environments, but the high overpotential required for OER in acidic conditions has limited the efficiency of acidic water electrolysis, despite its other advantages such as higher current density and pressure[215]. While numerous materials have been studied for OER, a lack of efficiency, durability, and high cost have hindered their widespread industrial use. Single-atom catalysts (SACs) have received significant attention for their potential to improve the efficiency and durability of OER catalysts, as they have a large fraction of exposed active sites, high durability, and good stability in aggressive environments[216].

4.2 Methods

4.2.1 Total energy calculations

All calculations were carried out within the density functional theory framework using the Vienna ab-initio simulation package (VASP). [169,170] The electron-ion interactions are treated using the projector augmented wave (PAW) method.[171] We use the Perdew–Burke–Ernzerhof (PBE) functional to treat the exchange-correlation interactions.[172] The Gaussian smearing method with a smearing of 0.01 eV is used to improve K point convergence. The valence electronic states are expanded in plane-wave basis sets with an energy cutoff of 500 eV. The structures are optimized until the force on each atom is less than 0.01 eV/A$^{\circ -1}$. The Gaussian smearing method with a smearing of 0.01eV is used to improve K-point convergence. The valence electronic states are expanded in plane-wave basis sets with an energy cutoff of 500 eV. The Brillouin-zone (BZ) integration is sampled by adopting the Monkhorst–Pack (MP) k-point grids of 5x5x1 for all the surfaces. During the geometry relaxations of the surface, only the outer atoms were allowed to relax. The cell parameters and inner atoms (in a 2 Å thick middle layer) were fixed to those determined for bulk ITO. Inversion symmetry was kept in all calculations to nullify the dipole moment. Structures were relaxed until the force on each atom was less than 0.01 eV/ Å $^{-1}$. Accounting for solvation effects was achieved by exploiting the implicit solvation model implemented by Hennig and co-workers under the name VASPsol[173–175]. The electrochemical potential was modified using the surface-charging method, the counter charge in the model electrolyte being based on the linearized Poisson–Boltzmann (PB) equation implemented in VASPsol[174,176]. This equation allows us to include an idealized electrolyte distribution in the electronic structure computations. This electrolyte distribution also balances the surface charge without correction terms, in contrast to a surface-charging model relying on a homogeneous background charge.[177] The cavity surface tension was set at 0.00, and the electrolyte concentration within the linearized PB equation was set as 1.0 M. The vacuum for surface charging calculations have been set to 60Å. Because we are dealing with a grand canonical description of the electrons from the surface charging methods, the energies reported in this work are free energies. The influence of the change in zero-point energy (ZPE) was found to be small in other works.[217,218] Therefore, considering the number of intermediates, the influence of ZPE was not computed here.

4.2.2 Oxygen Evolution Reaction Mechanism

In the oxygen evolution reaction (OER), oxygen gas is produced from water through a 4-electron transfer process. This means that four electrons are transferred from the anode to the cathode during the reaction, which drives the production of oxygen gas. The OER elementary mechanisms can be written as:

$$\mathrm{H_2O(l)} + {}^{*} \rightarrow {}^{*}\mathrm{OH} + \mathrm{H^+} + \mathrm{e^-} \tag{1}$$

$${}^{*}\mathrm{OH} \rightarrow {}^{*}\mathrm{O} + \mathrm{H^+} + \mathrm{e^-} \tag{2}$$

$$\mathrm{H_2O(l)} + {}^{*}\mathrm{O} \rightarrow {}^{*}\mathrm{OOH} + \mathrm{H^+} + \mathrm{e^-} \tag{3}$$

$${}^{*}\mathrm{OOH} \rightarrow {}^{*} + \mathrm{O_2(g)} + \mathrm{H^+} + \mathrm{e^-} \tag{4}$$

Where * represents the active site of the catalyst, (g) and (l) refer to the gas and liquid phase respectively, and *OH, *O, and *OOH represent the reaction intermediates adsorbed on the active site. The catalytic activity for OER is typically characterized by calculating the Gibbs free energies of the individual reaction steps as a function of the electrochemical potential defined using the standard hydrogen electrode (SHE) as a reference. The acidic mechanism involves the production of $\mathrm{H}^+ + \mathrm{e}^-$ pairs, and their Gibbs free energy is calculated from the equilibrium:

$$\mathrm{H}^+ + \mathrm{e}^- \leftrightarrow \tfrac{1}{2}\mathrm{H}_2$$

in the SHE at standard conditions (pH = 0, pressure p_{H_2}= 1 bar, and T = 298.15 K) and using the Gibbs free energy of hydrogen gas. The reaction Gibbs free energies, which stem from the binding strength between the catalyst and OER intermediates, are affected by the electronic properties of the active site. The typical procedure widely used in the literature to calculate the reaction Gibbs free energies, $\Delta\mathrm{G}_\mathrm{n}$ corresponding to equations (1)–(4) at standard conditions is shown in equations in the SI-S2; more details about the derivation can be found in reference[219]

4.2.3 Model

In_2O_3 is a wide bandgap semiconductor that has been used in gas sensors[122] and has also been explored as a potential catalyst for CO_2 hydrogenation[123,220] . When doped with Sn, it becomes indium tin oxide (ITO), a transparent conducting oxide with metal-like conductivity and optical transparency in the visible range. This material is used in transparent electrodes for electro-optical displays, such as liquid crystal displays and solar cells[221]. Sn-doped indium oxide has high conductivity, making it useful for electrocatalysis applications in water. Researchers have therefore been interested in using these conductive oxides as supports for Pt-metal clusters in electrocatalytic applications[126–128,222] .The electrochemical behavior of ITO in acidic solutions with pH 1 can be affected by dissolution at high anodic and cathodic potential. However, in our study we have taken precautions to prevent this be carefully selecting the potential window for our calculations and limiting the potential to below 2V vs SHE. This potential range has been reported in literature to result in stable ITO behaviors in acidic solutions with pH 1[223]. Following the experimental studies, we modeled the (111) surface of 5% doped ITO as our substrate model and determined that all Sn atoms prefer to reside in the surface layer, which has been previously reported to give the maximum carrier density.[136] We chose the 111 termination for the ITO surface because it has the lowest surface energy and hence higher stability when compared to other surface terminations[224] . For a four-layer slab, with unit cell dimension in the surface plane of 14.65 x 14.65 Å, 8 Sn (5% atom) atoms are present, 4 in the top and 4 in the bottom layer. 3 Sn atoms replace the In atoms in 5 coordinated sites, and 1 Sn atom replaces the In in the 6 coordinated site. The unit cell dimension for ITO(111) is 14.65 x 14.65 x 60 Å. From our previous study (Chapter 2), the surface has 4 H_2O molecules chemisorbed *per* cell; two are dissociatively adsorbed, and the other two are adsorbed intact. For full details of the surface structure and water interaction with the surface, we refer the reader to our previous work[144]. To explore possible adsorption sites of Pt on ITO and to determine the optimum O and OH ligand number for the surface PtO_xOH_y complex, we used the Grand Canonical Basin Hopping (GCBH) global optimization method. The full details of the GCBH method are provided in the Appendix A.9. According to our earlier research, the presence of hydroxyls and water on the ITO surface plays a significant role in anchoring Pt single atoms (Pt-SA). The hydroxyls that are formed on the surface of ITO in the presence of water would interact with the Pt-SA and assist stabilize it by preventing it from sintering into larger clusters. We refer the reader to our earlier study for complete details on the surface and Pt-SA structure and water interaction with the surface[224] .

4.3 Results and Discussion

As a first step in investigating the OER activity on a Pt-SA/ITO system, we utilized a Pt-SA/ITO structure previously determined in our previous work[16,224]. The structure, shown in Fig. 1(a) as 1, consists of Pt atoms bound to two Sn atoms and one hydroxyl group in a Pt-Sn bridging position, acting as an anchor for the SA. Further details of the structure can be found in the previous works that is explained thoroughly in the previous chapters[224]. To determine the most stable adsorption site for the Pt surface complex, we employed a basin hopping method to optimize the position of the Pt atom and the movement of hydroxyls and water already present on the surface, under vacuum conditions and without considering electrochemical conditions such as pH and potential. OER was experimentally investigated on dispersed Pt atoms on ITO by Weber et al.[128] From the experimental findings reprinted in Figure 4-1(c), three distinct peaks in the positive sweep of the cyclic-voltammogram are seen at pH 1. On the positive-going sweep, the first and second oxidation peaks are present at 0.82 V, and 1.28 V vs SHE. Additionally, the onset for OER is seen at ~ 1.5 V. Our study focused specifically on the anodic sweep and the characterization of the oxygen evolution reaction (OER) on ITO. As a result, we did not include any computational calculations or analysis in the cathodic region. While the reactions occurring during the cathodic sweep are not the primary focus of our work, they have been thoroughly addressed in the experimental paper. With this information, we investigated the overpotential of OER on Pt-SA/ITO.

4.3.1 OER activity on a Pt-SA/ITO system: The usual way.

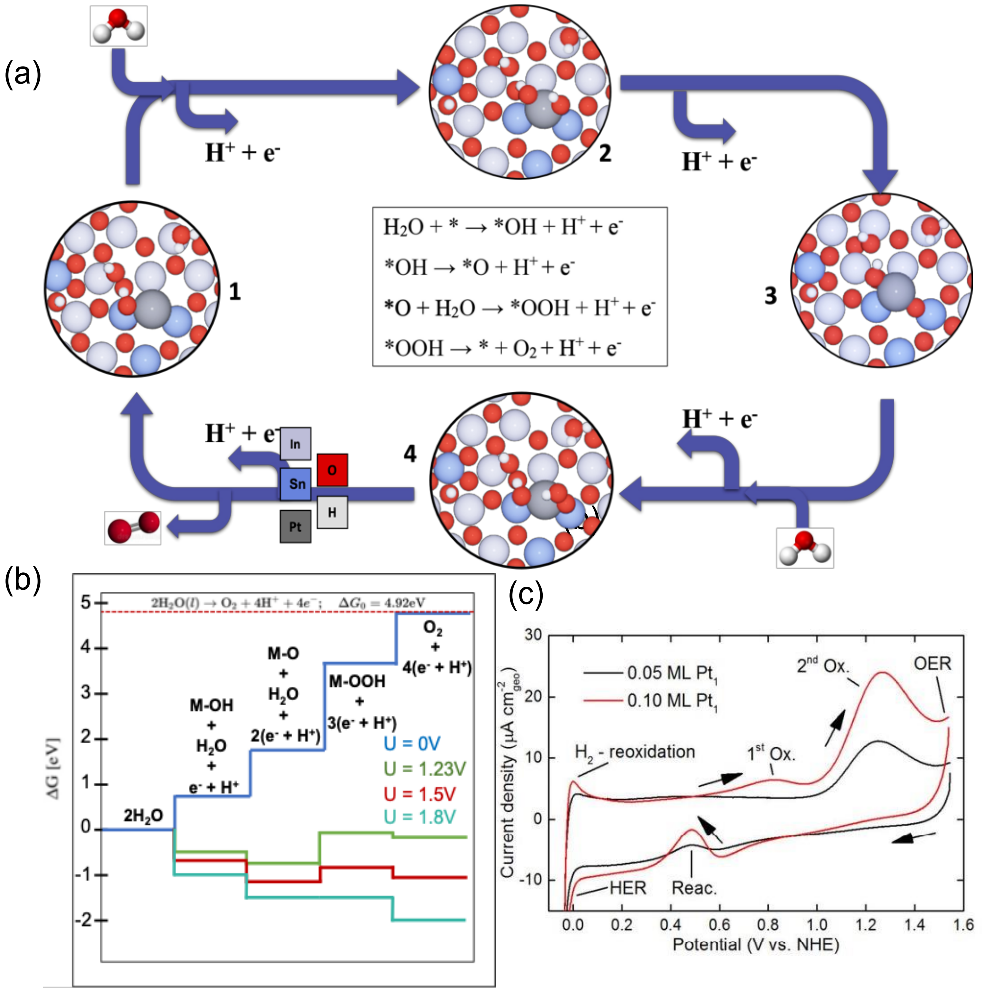

Figure 4-1 OER reaction mechanism on our initial structure for a Pt single atom on ITO determined in vacuum and in the absence of electrochemical potential (a) 4 electron step reaction mechanism (b) reaction energy profile for the 4 OER reaction steps at potential U = 0 V vs SHE (Blue), U= 1.23V vs SHE (Green), U = 1.5 V vs SHE(Red) and U = 1.8 V vs SHE (Cyan). (c) experimental cyclic-voltammograms for Pt_1/ITO at 0.05 ML and 0.01 ML

The four-step OER reaction mechanism is given in Figure 4-1 (a), and the corresponding reaction free-energy diagram is given in Figure 4-1(b) for four potential values (U = 0, 1.23,1.5

and 1.9 V vs SHE) at a pH=1. For the catalytic cycle starting with our initial Pt-SA/ITO structure, we determine the third step as the rate-determining step with an overpotential of 0.57 V. This is 0.3 V higher than what is found experimentally (overpotential = 0.27 V). We interpret this high discrepancy in the overpotential values as an indication that the active center of the catalyst we are using to simulate the OER reaction mechanism, determined in the absence of electrode polarization, is not correct. The functional groups generated in reaction conditions (positive potential vs SHE) can largely affect/modify the active site and hence should be properly investigated.

Due to the presence of water molecules, hydroxyl, and oxygen adsorbates in the OER reaction condition, it is of utmost importance to determine the true nature of the active site of the catalyst. This is very important in the case of SACs, as the metal atom is not surrounded by any other metal atoms, and the active site is more exposed to the reactants. To better understand the active site of the catalyst and the nature of the interaction with the reactants, the interaction of the Pt-SA with the hydroxyl and oxygen species needs to be explicitly studied. The characterization of SAC catalysts under realistic reaction conditions is a relatively unexplored field. However, in-situ techniques such as operando X-ray absorption spectroscopy (XAS) have demonstrated potential in understanding the dynamic electronic and local environments of these structures and identifying the nature of their active sites[225–230]. Li et al observed the formation of a stable Pt oxide during ORR on Pt single atoms (2.0 wt%) on graphitic carbon nitride (g-C_3N_4) derived N-doped carbon nanosheets (NCNS), which may suppress the adsorption and activation of O_2 and therefore be detrimental to ORR [231]. Cao et al. were able to achieve atomically dispersed $Fe_1(OH)_x$ on Pt nanoparticles (NPs), resulting in a 30-fold increase in mass activity compared to conventional catalysts and 100% CO selectivity over a wide temperature range for the preferential oxidation of

CO in hydrogen. The in-situ XAS results revealed selective deposition of iron hydroxide on the surface of Pt NPs and illustrated that the $Fe_1(OH)_x/Pt$ interface can easily react with CO and facilitate oxygen activation[232]. Furthermore, Cao and co-workers used operando XAS to study the formation of a high-valence $HO-Co_1-N_2$ (Single atomic Co supported on phosphorized carbon nitride) moiety and were able to successfully demonstrate the formation of the reaction intermediate $H_2O-(HO-Co_1-N_2)$. Theoretical calculation results further confirmed that the highly oxidized and reconstructed Co1 single atoms decreased the energy barrier for water dissociation, thus resulting in high catalytic performance for HER in alkaline media[233].

4.3.2 Optimum coverage of ligands

To find the optimum coverage of -OH/-O/-OOH around the Pt-SA supported on ITO at varying electrochemical potential and for different Pt adsorption sites on the oxide, we used the Grand Canonical Basin Hopping [15,29,30] (GCBH) method (Appendix A.9). For this free energy surface (FES) exploration, we use the following mutations in our GCBH method:

A. The Pt-SA can move randomly over the ITO surface to find its most stable adsorption site.

B. The -OH/-O/-OOH coverage is mutated grand canonically to find the most stable coverage of the adsorbates on the Pt-SA. The changing adsorbate coverage under the electrochemical reaction condition can also modify the adsorption site. Hence, it’s also important to simultaneously move the Pt-SA. The adsorbates can also attach to the ITO surface. Hence the adsorbates are not restricted to the Pt-SA but can access the whole catalyst surface.

C. The $-OH/-H_2O$ groups already present on the ITO surface can move around and transfer onto the Pt-SA.

The three above-mentioned mutations are carried out simultaneously and one can affect the other so that the effect of all three needs to be studied simultaneously. The free energy surface explored by GCBH relies on the formation free energy of PtO_xOH_y/ITO at pH = 1 and temperature(T) = 298K. This formation free energy is calculated as follows:

$$\text{Formation free Energy} = \mathrm{G}\big(\mathrm{PtO_xOH_y(U)}\big) - \mathrm{G}(\mathrm{Pt\,SA_{ITO}(U)}) - \mathrm{x}\mu_\mathrm{O} - \mathrm{y}\mu_\mathrm{OH}$$

Where, $\mathrm{G}\big(\mathrm{PtO_xOH_y(U)}\big)$ is the potential dependent energy of $\mathrm{PtO_xOH_y}$ and $\mathrm{G}(\mathrm{Pt\,SA_{ITO}(U)})$ is the potential depended energy fo the initial state of Pt-SA ITO calculated via the surface charging method (Appendix C.2), μ_O is the chemical potential of oxygen and is obtained from the experimental formation energy of O with respect to water, since the O_2 molecule is not very well described within DFT. μ_OH is the chemical potential of hydroxyl. The chemical potential is evaluated via the following equations:

$$\mu_\mathrm{OH} = \mu_\mathrm{H_2O(l)} - (\mu_\mathrm{H^+}(\mathrm{U,pH}) + \mu_\mathrm{e^-}(\mathrm{U,pH})); \mu_\mathrm{O} = \mu_\mathrm{H_2O(l)} - 2(\mu_\mathrm{H^+}(\mathrm{U,pH}) + \mu_\mathrm{e^-}(\mathrm{U,pH}));$$

Here, $\mu_\mathrm{H_2O(l)}$ is the chemical potential of liquid water, at room temperature and 1 atm pressure take from the work of Munnik et al.58 and $\mu_\mathrm{H^+}(\mathrm{U,pH}) + \mu_\mathrm{e^-}(\mathrm{U,pH})$ can be calculated using the reference hydrogen electrode59.

$$\mu_\mathrm{H^+}(\mathrm{U,pH}) + \mu_\mathrm{e^-}(\mathrm{U,pH}) = \frac{1}{2}\mu(\mathrm{H_2}) - \mathrm{eU} + \mathrm{k_BTpHln10}$$

One more important factor to keep in mind while exploring the free energy surface in these cases is the electrochemical potential at which we perform the GCBH. The catalytic active site would be different at varying electrochemical potential; hence in this work, we have chosen four different potentials to perform the GCBH, U = 0 V vs. SHE, U = 0.75 V vs. SHE, U = 1.4 V vs. SHE, and

U = 1.5 V vs. SHE. We choose these potential values based on the experimental findings (Fig 1c) as already discussed. Our simulation model uses surface charging to maintain a constant potential, with surface charge adjusted to reach the desired potential (in this case the onset potential of 1.5V vs SHE). Figure 4-2 provides the free energy surface found via GCBH at U = 1.5 V vs. SHE and

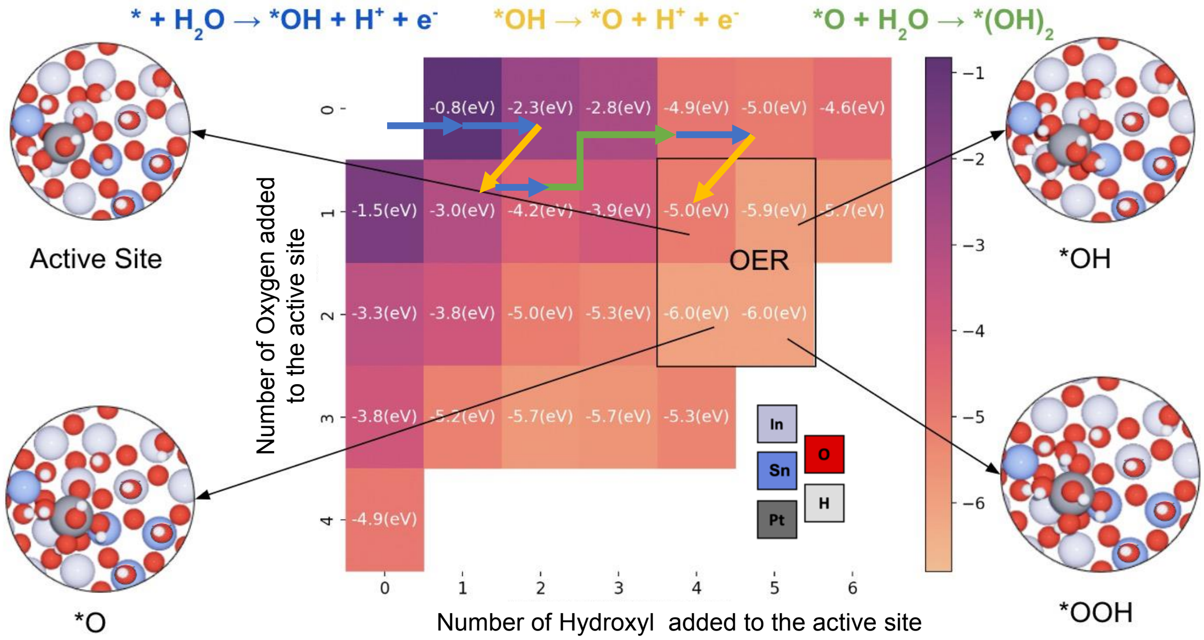

Figure 4-2 Free energy surface exploration via GCBH. The heat plot shows the formation energy of the active site configurations, as a function of the number of hydroxyl groups and O atoms added. The blue arrows represent the electrochemical reaction $* + H_2O \rightarrow OH + H^+ + e^-$, the yellow arrow the electrochemical reaction $*OH \rightarrow *O + H^+ + e^-$ and the green arrow the chemical dissociative adsorption of H_2O. The black box shows the active site and intermediates of the OER mechanism. The structures of the active site along with the OER intermediates are also shown, Blue: Sn , Light Blue: In, Grey : Pt, Red : O and White : H. The X and Y axis indicate the number of Hydroxyls and Oxygen added to the initial Pt-SA/ITO. The electrochemical conditions correspond to a potential U = 1.5 V vs SHE and pH = 1.

pH = 1, which corresponds to the experimental electrochemical potential for OER found for Pt-SA deposited on ITO.

We start with the most stable Pt-SA/ITO found in our previous work[224]. At any given catalytic active structure, there are three possibilities for evolution: (1) electrochemical addition of OH on the active site: $* + H_2O \rightarrow *OH + H^+ + e^-$, (2) After the addition of OH on the active site, this can electrochemically convert to *O : $*OH \rightarrow *O + H^+ + e^-$ and (3) is the dissociative chemical adsorption of H_2O ($H_2O \rightarrow H^+ + OH^-$) on the active site where the H^+ will adsorb on *O and OH^- will adsorb directly on the SA. We need to consider all the three possibilities above at each step to get to the active site of OER at the considered conditions. The reaction pathway to reach the active site at U = 1.5 V vs SHE is represented by differently colored arrows on the free energy surface. The blue arrow represents electrochemical reaction (1), yellow represents electrochemical reaction (2) and green represents chemical reaction (3). The numbers given inside the boxes in Figure 4-2 are the formation energy of PtO_xOH_y/ITO. To jump to the next configuration via reactions 1, 2 or 3 the thermodynamics should be favorable at a particular potential. The thermodynamically favored transformations are indicated by colored arrows in Figure 4-2. This will then decide at any electrochemical potential what the configuration of the active site is.

Figure 4-3 provides the full pathway of forming the active site at U = 1.5 V vs SHE from Pt-SA/ITO (*) which were previously represented as arrows on Figure 4-2. We start with our initial structure for Pt-SA/ITO, where the Pt atom is already interacting with a hydroxyl present on the surface, which is represented in green throughout the reaction pathway. At the electrochemical potential of 1.5 V vs SHE, the first step is the adsorption of a hydroxyl via the reaction (1) (blue): $* + H_2O \rightarrow *OH + H^+ + e^-$. The hydroxyl adsorbs on the Pt atom, causes a change in the adsorption

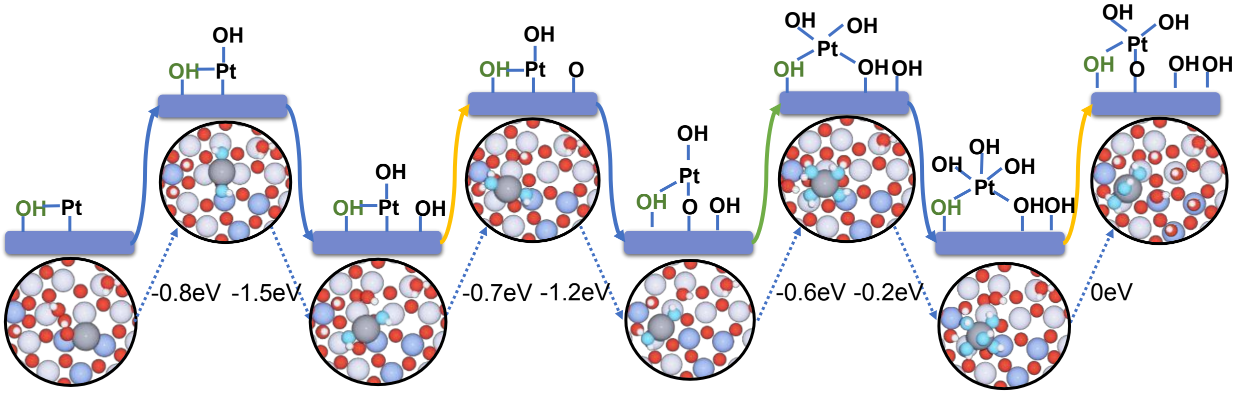

Figure 4-3 Full mechanism of formation of the active site for Pt-SA/ITO in electrochemical conditions found via GCBH. The blue arrow corresponds to the hydroxylation step, which is the first step of OER ($* + H_2O \rightarrow {*OH} + H^+ + e^-$). The hydroxyl in green represents the hydroxyl already present on the surface in our initial Pt-SA structure. The yellow arrows correspond to the second OER step ($*OH \rightarrow {*O} + H^+ + e^-$). The green arrow corresponds to water dissociation ($H_2O \rightarrow {*OH} + {*H}$). The Final structure is the proposed active site for OER. The reaction free energies are given for each step and are calculated at a potential U = 1.5 V vs SHE and pH=1 for electrochemical steps. The hydroxyl and oxygens attached to Pt and directly participating in the active site are represented in light blue.

site of the Pt atom and leads to the formation of a $Pt(OH)_2$ species. The Pt atom, which was previously interacting with 2 Sn atoms, now interacts with 2 In atoms. In the next reaction step, Pt is once again hydroxylated, but one of the -OH from the previously formed $Pt(OH)_2$ group spills over on the ITO support so that a $Pt(OH)_2$ ITO-OH species is formed, with still 2 OH on the Pt (here ITO-OH represents the hydroxyl attached to ITO which spilled over on the surface). Concomitantly Pt moves to a Sn-In bridge site. The next more favorable step is to extract a proton via the reaction $*OH \rightarrow {*O} + H^+ + e^-$ from a neighboring hydroxyl present on the surface instead from the hydroxyl attached to $Pt(OH)_2$, leading to the formation of $Pt(OH)_2$ ITO-O. The surface oxygen species from ITO-O transfers onto the $Pt(OH)_2$ group in the following step, moving from the surface to a position immediately below the Pt, and another OH species occupies the vacant O site in the same concerted step to create $PtO(OH)_2$ITO-OH species. In the next step, we observe the dissociative adsorption of a H_2O molecule onto $PtO(OH)_2$ITO-OH, where H^+ attaches to the O and OH attaches to Pt, to form $Pt(OH)_4$ITO-OH. This is followed by an electrochemical addition of OH to the Pt site, making $Pt(OH)_5$ITO-OH, and finally in the next step of deprotonation of a *-OH from the Pt site, we form $PtO(OH)_4$ITO-OH which is the active site for OER.

4.3.2 Evaluating the Oxidation States

Calculations also provide insights on the dependence of the Pt hydroxylation level on the electrochemical potential. We now depict the same free energy surface shown in Figure 4-2 but with an electrochemical potential of 0.75 V and 1.4 V vs. SHE to show the potential-dependent formation process and the oxidation states (OS) of the active site. These electrochemical potentials are chosen to closely represent the oxidation peaks identified experimentally in the cyclic voltammogram. The free energy surface is shown in Figure 4-4(a) at U = 0.75 V vs. SHE, and in (b), it is shown at U = 1.4 V vs. SHE. We find that the most stable active site composition is $PtO_0(OH)_4$ITO-OH at U = 0.75V versus SHE. The chemical route depicted by the arrows creates this active site. (PtO_0OH_1 → $PtO_0(OH)_2$ → $PtO_0(OH)_2$ITO-OH → $PtO_0(OH)_2$ITO-O → $PtO_1(OH)_2$ITO-OH → $PtO_0(OH)_4$ITO-OH). Along the reaction pathway, we also illustrate the Pt OS at various PtO_xOH_y compositions (Figure 4-4c). By comparing the Bader charge of Pt in the active site with the Bader charges of known Pt compounds with well-defined oxidation states, for example, OS 0 for Pt(111), OS 2 for PtO, OS 2.66 for Pt_2O_3, and OS 4 for PtO_2, the OS for each composition was estimated. PtO_0OH_1 has an OS of 0 in its initial state, which is similar to metallic Pt. Despite requiring four electrochemical steps to reach the state $Pt(OH)_2$ITO-O, the OS of Pt

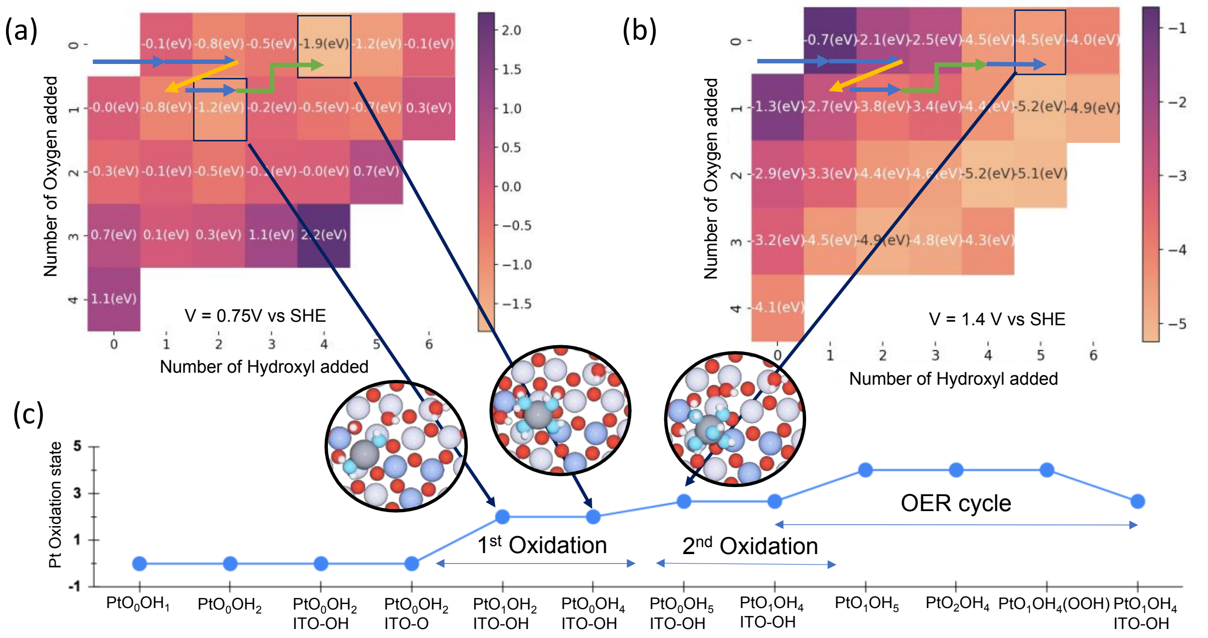

Figure 4-4 Free energy surface for Pt-SA/ITO in OER conditions at (a) U = 0.75V vs SHE (b) U = 1.4V vs SHE and pH=1. The black box on the free energy surface represents the energetically favorable composition for Pt-SA/ITO at the corresponding potential. The arrows represent the combination of reaction pathways needed to reach the favorable composition. (c) Oxidation state (OS) of the Pt atom as a function of the composition of the active site. The 1st oxidation of Pt from 0 →2 takes place at U = 0.75 V vs SHE, the second oxidation from 2→2.66 takes place at U = 1.4 V vs SHE and finally within the OER catalytic cycle, Pt cycles between the OS of 2.66 and 4.

remains 0. This could be the result of ITO surface oxidation rather than Pt active site oxidation. When the composition changes to $PtO_1(OH)_2$ITO-OH in the following step, we see an increase in the OS to +2 because of the above-described migration of O to Pt accompanying the electrochemical addition of OH on ITO, which takes place at a potential of 0.75V versus SHE. The next composition of PtO_0OH_4 is formed by chemical dissociative adsorption of H_2O on PtO_1OH_2 which doesn't cause any change in the OS as this is a non-electrochemical step. At the electrochemical potential of 1.4 V vs SHE, the $PtO_0(OH)_4$ITO-OH can further oxidize to

$PtO_0(OH)_5$ITO-OH, where the Pt OS is around 2.66. At a slightly higher potential of 1.5 V vs SHE, we observe the formation of the active site for the OER which is $PtO_1(OH)_4$ITO-OH. This step doesn't cause any change in the OS of the Pt, which means that this electrochemical step has caused further oxidation of ITO. At this potential, we also observe the extensive hydroxylation of the support surface where the surface In and Sn sites gets completely covered with hydroxyls. This surface hydroxylation of ITO at positive potentials was also observed by Lebedev et al[46].

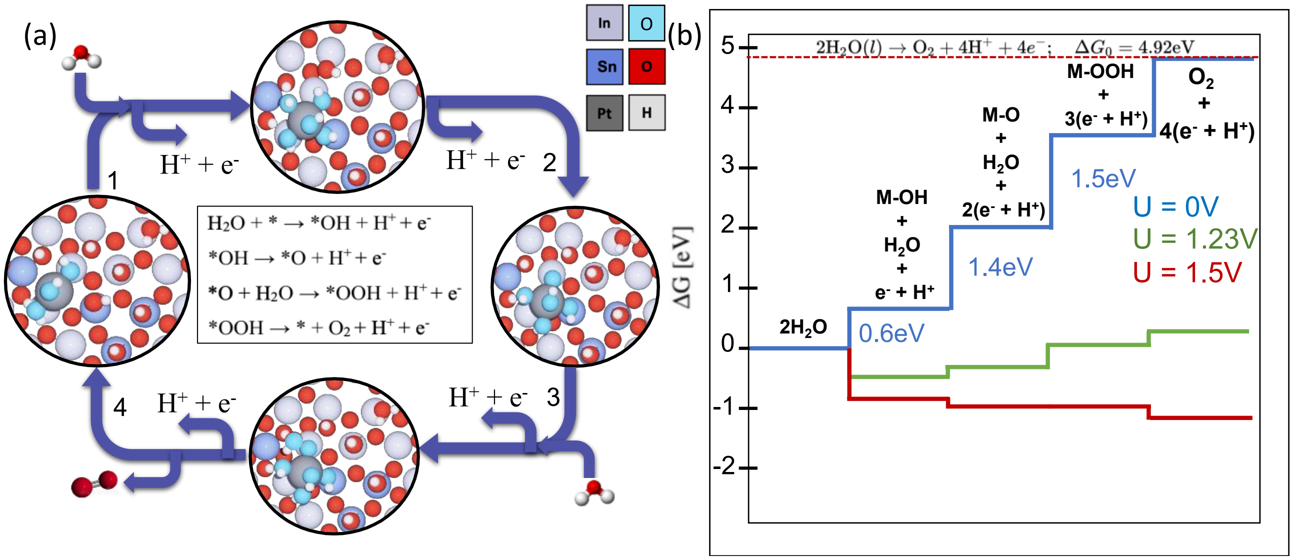

Figure 4-5 OER reaction mechanism on the active site of Pt-SA/ITO (PtO_1OH_4) found via GCBH as discussed in Fig 3, at the electrochemical reaction conditions (potential U = 1.5 V vs SHE). (a) 4 step OER reaction mechanism (b) Reaction energy profile at U = 0 V vs SHE(Blue), U = 1.23V vs SHE (Green) and U = 1.5 V vs SHE (Red).

4.3.2 OER activity on a Pt-SA/ITO system: from the "optimal" active site.

In Figure 4-5, we finally investigate the reaction mechanism of OER starting from the "optimal" active site found via GCBH as discussed earlier, for a potential of 1.5V vs SHE. In the first reaction of the 4-step OER mechanism, the OH adsorbs on the active site at a bridge position between the Pt-SA and Sn. In the next step, a proton is evolved from another hydroxyl located on the bridging position of Pt and In. Deprotonation of other hydroxyl groups are not as favorable; this means that the acidity of the various hydroxyls is very different. After the deprotonation another hydroxyl adorbs on the *O forming *OOH. This then produces O_2 and regenerates the active site. The reaction diagram of this OER pathway is given in Figure 4-5(b), where we find the third step to be the rate determining step with an overpotential of 0.27 V vs SHE. This overpotential value is in excellent agreement with the experimental data (0.27 V). It should be noted however that exact coincidence is fortuitous, since calculations present several approximations in model and method aspects. During this catalytic cycle the oxidation state of Pt cycles between 2.66 and 4. Not all the 4 electrons required for the oxygen evolution reaction come from Pt-SA, other electrons come from the reduction of the ITO surface itself. It becomes abundantly evident that there is a significant discrepancy of 0.3V vs. SHE between the overpotential computed using the active site formed in electrooxidation conditions and the overpotential calculated using the initial non-optimal active site. Only the approach using the active site determined at U=1.5 V vs SHE is self-consistent and physically meaningful, since the onset potential is 1.5 V, potential for which the determined active site is stable.

4.4 Conclusion

In this chapter, the reaction mechanism of oxygen evolution reaction (OER) was investigated using the "optimal" active site obtained via GCBH. The OER mechanism involved a four-step process starting with the adsorption of OH on the active site, followed by proton evolution, deprotonation, and finally O_2 production. It was found that the third step was the rate-determining step with an overpotential of 0.27 V vs SHE, which was found to be in excellent agreement with experimental data.

It was noted that during the catalytic cycle, the oxidation state of Pt cycled between 2.66 and 4, and that not all the 4 electrons required for the oxygen evolution reaction came from Pt-SA, as other electrons came from the reduction of the ITO surface itself. It was also emphasized that identifying the composition and geometry of the active site under the reaction conditions was crucial, as the numerous adsorbates from the original initial structure could greatly change it. This change could be in both the adsorption site of the Pt atom on the support and in the composition of the active site in terms of ligands.

The computational approach used in this study helped in identifying the active site composition at oxidation peaks to understand the electrocatalytic process and species involved, as well as determining the oxidation state of Pt-SA at these peaks. This work also emphasizes how crucial it is to identify, using operando computational approaches, the composition and geometry active site under the reaction conditions which may change greatly due to the numerous adsorbates from the original initial structure. This change could be in both the adsorption site of the Pt atom on the support and in the composition of the active site in terms of ligands. This computational approach also helped us identify the active site composition at oxidation peaks to understand the electrocatalytic process and species involved, as well as determining the oxidation state of Pt-SA at these peaks. Such a first-principle determination of the nature of the active site in electrocatalytic conditions, coupled with experimental operando characterization, opens major perspectives for our fundamental understanding of electrocatalysis and for the design of efficient catalysts.

Chapter 5 Electrochemical Oxidation of Methane to Methanol on Electrodeposited Transition Metal Oxides

5.1 Introduction

The direct partial oxidation of methane to methanol is one of the grand challenges in the area of catalysis and energy[67]. Methane is the major constituent of associated petroleum gas which is routinely flared at remote oil fields where its collection and use are unprofitable[236,237]. The energy losses associated with flaring are roughly equivalent to the natural gas demand of Central and South America resulting in significant economic losses, while the associated greenhouse gas (GHG) emissions result in adverse effects on the climate and environment. In 2021 alone, gas flaring was responsible for the emission of 361 million metric tons (MMT) of CO_2, 39 MMT of CO_2 equivalent in non-combusted methane, and other GHGs and pollutants. There are large environmental and economic incentives to develop technologies for the decentralized transformation of methane into easy-to-transport liquid methanol as these would reduce GHG emissions,[66,67] increase global carbon utilization, and expand the global methanol production capacity. Methanol current annual global demand is close to 100 MMT and is further projected to rise at a compound annual growth rate of over 5% to double by 2030.[238] This increase in methanol demand is primarily due to expansion of consumption by the automotive and olefin industries. Therefore, new and efficient technologies for the production of methanol from methane at medium and small scales could offer a paradigm shift by connecting directly stranded carbon and energy resources to the base chemicals and energy markets.

The direct transformation of methane to methanol in remote locations requires selective catalysts capable of operating at near-ambient temperatures inside a modular device.[239–243] Although various catalytic systems have been studied for more than 100 years,[244–247] these have never reached commercialization due to low yields and poor selectivity. The main challenge in developing a selective and efficient catalyst for the direct partial oxidation of methane to methanol originates from the difficulty to simultaneously control the kinetics for i) the regeneration of the catalytic active site, ii) the transport, activation and hydroxylation of methane, and iii) the desorption and removal of the produced methanol (Figure 5-1). Traditional catalytic systems require high temperatures or use strong oxidizing agents to regenerate the catalytic site and overcome the barrier for methane C-H bond activation. Under these reaction conditions, it is difficult to prevent over-oxidation of methanol to CO and CO_2. Particularly, the oxygen atom in the produced methanol binds strongly to the metal site and re quires the use of a solvent (i.e. H_2O in Figure 5-1) to desorb methanol and stabilize the reduced catalyst center.[248] Slow methanol desorption makes the product complex prone to over-oxidation and introduces additional layers of complexity.[249,250] Because of the multiple steps that need to be simultaneously controlled during the direct transformation of methane to methanol, developing selective and efficient catalysts[251] for this transformation has become one of the most remarkable challenges in synthetic catalysis.

Enzymatic systems, on the other hand, offer clues on how to selectively catalyze this transformation. Methane monooxygenase, for example, catalyzes the transformation of methane directly to methanol with exceptional selectivity under ambient conditions. This is achieved through the exquisite control on the transport of oxygen, methane, protons and electrons to the transition iron(IV)-oxo complex in the active center.[249,252] Conformational changes prevent consecutive oxidation and back diffusion and are responsible for the isolation of the active site and the exceptionally high selectivity for methanol.[253]

Electrocatalysis offers a precise control over the surface oxidative power via the applied potential and is a promising approach to control kinetics and impart product selectivity in the oxidation of methane to methanol just as in the enzymatic system.[67] Electrocatalysts can also replicate many of the mechanistic features in methane monooxygenases through the rational design and control of the electrostatic interactions between catalytic sites on the electrode surface, and the reactants and products penetrating the relatively immobile solvated ions that make up the coordination environment at the electric double layer. Advanced methane to methanol electrocatalyst should i) bring methane into the active site in the appropriate orientation to lower activation energy barriers and accelerate the rates of transformation, ii) regenerate metal-oxo species on electrode surfaces directly from water and remove electrons at slow rates relative to methanol desorption and over-oxidation, and iii) have an electrode architecture with a high density of active sites connected to fast methanol transport and collection networks.

Over the last decade, the use of transition metal oxides as catalyst for the electrochemical partial oxidation of methane to methanol has drawn significant interest. Mustain and co-workers, for example, have shown that binary transition metal oxides of NiO/ZrO_2 catalyze the electrochemical oxidation of methane in carbonate electrolytes.[254–256] Park and co-workers also utilized a chemical precipitation method to prepare Co_3O_4/ZrO_2 nanocomposites and Co_3O_4 powder/ZrO_2 nanotubes that show activity for the production of higher alcohols such as 1-propanol and 2-propanol.[257,258] In these works, the introduction of zirconia to unary transition metal oxides has been suggested to be indispensable in order to promote methane partial oxidation in the presence of the carbonate ions. The challenge in these works utilizing particle catalysts is, however, that zirconia has multiple additional effects on transport which are poorly understood and must be deconvoluted. For example, the introduction of the catalytically inert, non-conductive zirconium oxide leads to different catalyst morphologies and spatial distributions of the active phase of the catalyst. These differences should be expected to affect selectivity as these modify the residence time of the methanol intermediate near the oxide surface and thus modify the probability for methanol over-oxidation.[259] The requirement to use carbonate as mild oxidant is also not fully understood. Porous hollow fiber NiO/Ni anodes and iron nickel hydroxide nanosheets have also been reported to produce methanol and ethanol as methane electrochemical oxidation products in aqueous hydroxide solutions where carbonate is not present in significant amounts.[260–262] CO_2 generated by the overoxidation of methane is likely to react with the highly alkaline environment to form carbonate in solution, but whether this carbonate can in turn become the major oxidant is not clear. It must also be noted that the faradaic efficiencies (FEs) in some of these systems exceed 100% (Table S1) implying that chemical reactions between methane and stoichiometric oxidants in the oxide catalyst or the electrolyte contribute to methane oxidation and could be responsible in part for the production of oxygenates. The production of methanol and other carbon products could also be the result of the degradation of carbon conductive materials and binders added in the preparation of the catalyst inks in some of these systems. To date, the intrinsic mechanisms for the activation of methane and the formation of methanol are largely unknown and are likely obscured by the lack of consistency across the existing literature with regards to the electrochemical setups used, the morphology of the catalysts, the composition of the electrolytes, the analytical tools used for product quantification, as well as the standards used for the reporting of activity, selectivity, and faradaic efficiency.

Recently, Prajapati *et al*. demonstrated a comprehensive work that avoids the use of carbon conductive materials or binders and utilizes the surface oxides formed on metals upon electrochemical oxidation to show that four types of different transition metal oxides (TiO_2, IrO_2, PbO_2, and PtO_2) are active for the electrochemical methane oxidation reaction to CO_2 at oxidative potentials positive of 1.1 V vs SHE. A bimetallic Cu_2O_3 on TiO_2 catalyst was reported, where Cu was proposed to modify the reaction barrier for the key intermediates and facilitate the desorption of CH_3OH showing faradaic efficiencies for methanol of up to 6%.[263] Although these electrocatalysts have been shown to activate methane, none of the unary metal oxides was reported to produce methanol. Potential-dependent theoretical studies have suggested that methane oxidation on oxidized transition metal surfaces proceeds favorably at oxidative potentials where oxygen evolution also occurs.[263–265] The mechanism for the formation of methanol and the factors controlling its selectivity, however, are not well understood.

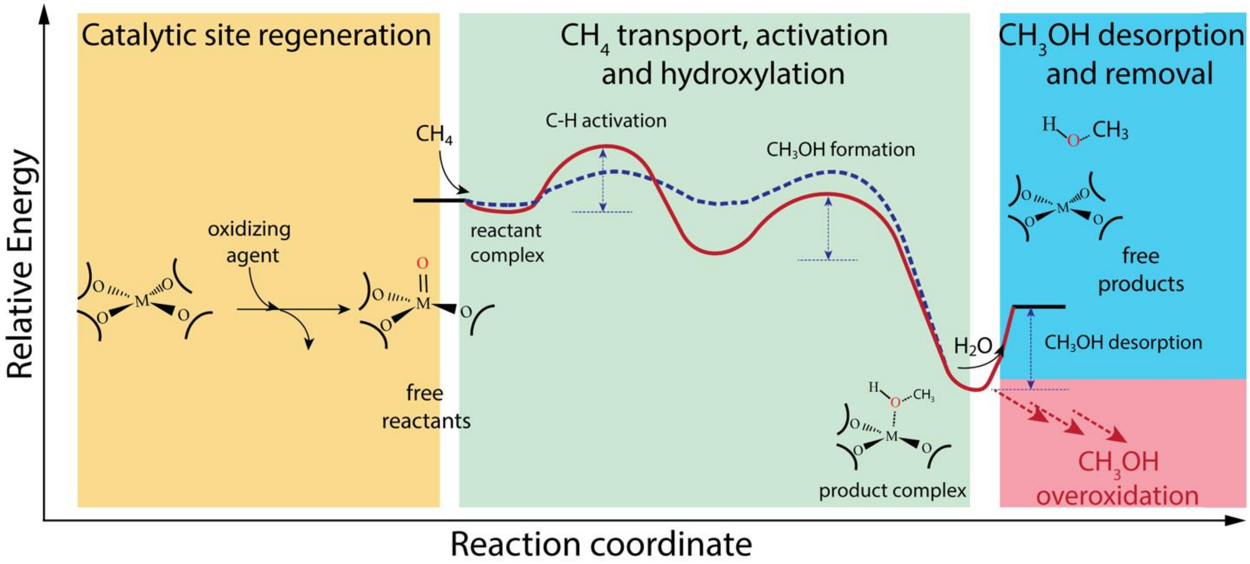

Figure 5-1 Schematic representation of the most important steps in direct methane to methanol oxidation. The simplified reaction energy diagram includes: the regeneration of the active site by an oxidizing agent or electron collector, the activation and hydroxylation of methane through two hypothetic reaction pathways (ionic in red trace and radical in blue trace), and the endothermic solvent-assisted desorption of methanol along the competing methanol overoxidation. Parasitic decomposition of the regenerated catalytic site and non-catalytic oxidation of methanol are not shown for simplicity.

In order to gain a better understanding of the underlying mechanisms for methane partial oxidation, we have systematically approached this reaction through the breakdown of the three competing rates in the oxidation of methane to methanol (Figure 5-1), namely, we have attempted to determine to the best of our abilities i) the rate of catalytic site regeneration and oxygen evolution; ii) the rate of methane transport, activation and hydroxylation; and iii) the rate of desorption and removal of the produced methanol. We have done this through the combination of high sensitivity product quantification tools, the use of advanced electrochemical reactors with well-characterized transport properties, and the design of experiments tailored to systematically decouple the multiple convoluted steps summarized in Figure 5-1. These experiments are combined to first-principle atomistic simulations to provide mechanistic understanding.

As a first step, we have decided to circumvent the use of catalyst inks. Here, we have used a one-step electrodeposition method for the preparation of transition metal (oxy)hydroxides as electrocatalysts. The oxidative electrodeposition method utilized here is self-limiting in growth and allows the deposition of largely amorphous, thin-film conductive metal (oxy)hydroxide films of known activity for water oxidation, well-defined charge transport mechanisms and measurable charge transport resistance.[266] Upon testing of these materials, we discover that CoO_x, NiO_x, CuO_x and MnO_x prepared via electrodeposition are active for the methane partial oxidation to methanol. In this work, we show that the detection and quantification of methanol and other oxidation products depends on the electrochemical cells used and the conditions for the collection of liquid and gas samples as reaction-transport kinetics control methanol product selectivity. Through the utilization of an advanced gas-tight cell with a rotating cylinder electrode, unique conditions of hydrodynamics for the partial oxidation of methane are realized, elucidating the importance of the control on both kinetics and mass transfer for each of the steps involved in the reaction. Calculations show an optimum potential window for selective methane oxidation into methanol.

5.2 Methods

5.2.1 DFT Calculations

All calculations were carried out within the density functional theory framework using the Vienna ab-initio simulation package (VASP). [129,130] The electron-ion interactions are treated using the projector augmented wave (PAW) method.[131] We use the Perdew–Burke–Ernzerhof (PBE) functional to treat the exchange-correlation interactions.[132] Oxide catalyst surface were modelled with periodic slabs, with supercell vectors of size 5.75 Å and a 4x4x1 Monkhorst-Pack grid was used for the k-point sampling of the first Brillouin zone. The cut-off energy for the plane wave was set at 600 eV, and the energy convergence threshold for the self-consistent-field (SCF) cycles was set at 10^{-6} eV per cell. Dispersion interactions were included according to the dDsC correction.[172,267,268]

Accounting for solvation effects was achieved by exploiting the implicit solvation model implemented by Hennig and co-workers under the name VASPsol[173–175]. The electrochemical potential was modified using the surface-charging method, the counter charge in the model electrolyte being based on the linearized Poisson–Boltzmann (PB) equation implemented in VASPsol[174,176]. This equation allows us to include an idealized electrolyte distribution in the electronic structure computations. This electrolyte distribution also balances the surface charge without correction terms, in contrast to a surface-charging model relying on a homogeneous background charge.[177] The cavity surface tension was set at 0.00, and the electrolyte concentration within the linearized PB equation was set as 1.0 M. The vacuum for surface charging calculations have been set to 60Å. Because we are dealing with a grand canonical description of the electrons from the surface charging methods, the energies reported in this work are free energies. The influence of the change in zero-point energy (ZPE) was found to be small in other works.[217,218] Therefore, considering the number of intermediates, the influence of ZPE was not computed here.

5.2.2 Catalyst Model

Since β-CoOOH (*R3m* space group) was found to be the cobalt oxide phase that was most active under alkaline pH and oxidative circumstances, preliminary bulk full relaxation was conducted on this compound.[267,269,270] According to Bajdich *et al.*,[268] the reference surface slab was taken as a 2x2 supercell of the primitive surface cell cut from bulk β -CoOOH in the most active (10-14) direction. Convergence in the adsorption energies and recovery of the bulk magnetic ordering of the center layers was obtained with a minimum thickness of four Co oxide layers and 30 Å of vacuum. To complete their octahedral coordination shell, each surface Co atom was liganded with one hydroxyl group, which would be expected in electrochemical conditions under liquid water.[217,224,267,270] All model slabs show two identical surface and present an inversion symmetry to cancel any dipole moment in the perpendicular direction. Only the outer atoms were allowed to relax during the surface geometry relaxations; the inside atoms (in a 2 Å large intermediate layer) and cell parameters remained fixed at the values established for the bulk β-CoOOH. These relaxations were continued until the residual forces were less than 0.02 eV $Å^{-1}$. A Fermi smearing of 0.026 eV, or 298 K in temperature, was used to calculate the electronic occupancies. To better describe the electronic structure of this high electronic correlation material, a model Hubbard Hamiltonian (designated + U) was included in the calculations On the basis of previous works, the formalism proposed by Dudarev *et al*.[271] was used, along with the *U–J* value of 3.52 eV for the cobalt 3d electrons. [267,268]

5.3 Results

The results section of this chapter is organized in the chronological order in which we approached the research of methane oxidation catalysts. First, we describe the deposition and physical characterization of the thin-film transition metal (oxy)hydroxides. Second, we describe the catalytic activity of transition metal (oxy)hydroxides for the partial electrochemical oxidation of methane and the results obtained during the systematic interrogation of these materials to separate the transport, electrochemical and thermochemical contributions to the experimental performance. Finally, we present our DFT study of the reaction mechanism and potential dependence and show that there is an optimal window of potential for selective methanol oxidation.

5.3.1 Catalyst Preparation

Unary transition metal (oxy)hydroxides of CoO_x, CuO_x, NiO_x, FeO_x, and MnO_x were prepared by electrodeposition as described in the experimental section.[272] Scanning electron microscopy (SEM) was used to characterize the morphology and microstructure of different transition metal (oxy)hydroxides on the surface of the titanium substrate (Figure Appendix D.2) before and after electrochemical oxidation of methane for 2 hours. The titanium substrate showed a relatively flat surface after mechanical polishing and immersion in the HCl solution to remove the surface oxide. Electrodeposited cobalt (oxy)hydroxide shows the typical dense film morphology observed for electrodeposited cobalt oxides.[273] Cracking of the films is observed upon drying and the pulling of vacuum for electron microscopy. After electrochemical testing over 2 hours, some of the cobalt oxide film was lost (Figure Appendix D.2b). The electrodeposited copper oxide (Figure Appendix D.2c) showed angular particles before oxidation with edges and corners closely packed on the surface of the titanium substrate. The copper oxide film after 2 hours of testing appeared less densely packed while the particle edges were still well defined. Nickel (oxy)hydroxide (Figure

D.2d) exhibited a porous film morphology formed by small nanoplates. This nanoplate morphology was maintained after methane partial oxidation and is similar to those obtained during electrodeposition of other nickel (oxy)hydroxides[272]. Manganese (oxy)hydroxide (Figure Appendix D.1e) showed larger nanoplates compared to the nickel oxide catalyst. The MnO_x film also showed cracks upon drying. Iron (oxy)hydroxide (Figure Appendix D.2f) showed a porous structure in a dense film similar to NiO_x before oxidation, while its porous microstructure could not be clearly resolved after oxidation. In general, the oxidatively electrodeposited transition metal (oxy)hydroxide films can be characterized as porous thin films while CuO_x is dense and nonporous. The thickness of the catalyst films varies between a few nanometers for the films deposited with only 5 LSVs to a few hundred nanometers for the films deposited with 100 LSVs. The maximum catalyst loading achieved by oxidative electrodeposition is of less than 100 μg per cm^2 as determined by electrochemical quartz crystal microbalance measurements.[272]

5.3.2 Product analysis of electrochemical methane oxidation reaction.

Product analysis using NMR shows methanol and acetate are the major products during the electrochemical partial oxidation of methane on the various transition metal (oxy)hydroxides at a potential of 1.06 V vs SHE (Figure 5-2). By collecting and analyzing samples at 20-min intervals, we have observed fluctuations in the concentration of the liquid products over time. These fluctuations reveal the dynamic nature of partial oxidation studies in the RCE cell as the produced methanol accumulates in the bulk of the electrolyte and can be further oxidized over time.

Two different thickness of the various transition metals were tested. Catalysts deposited using more linear sweep cycles result in lower methanol and acetate concentrations at the same applied

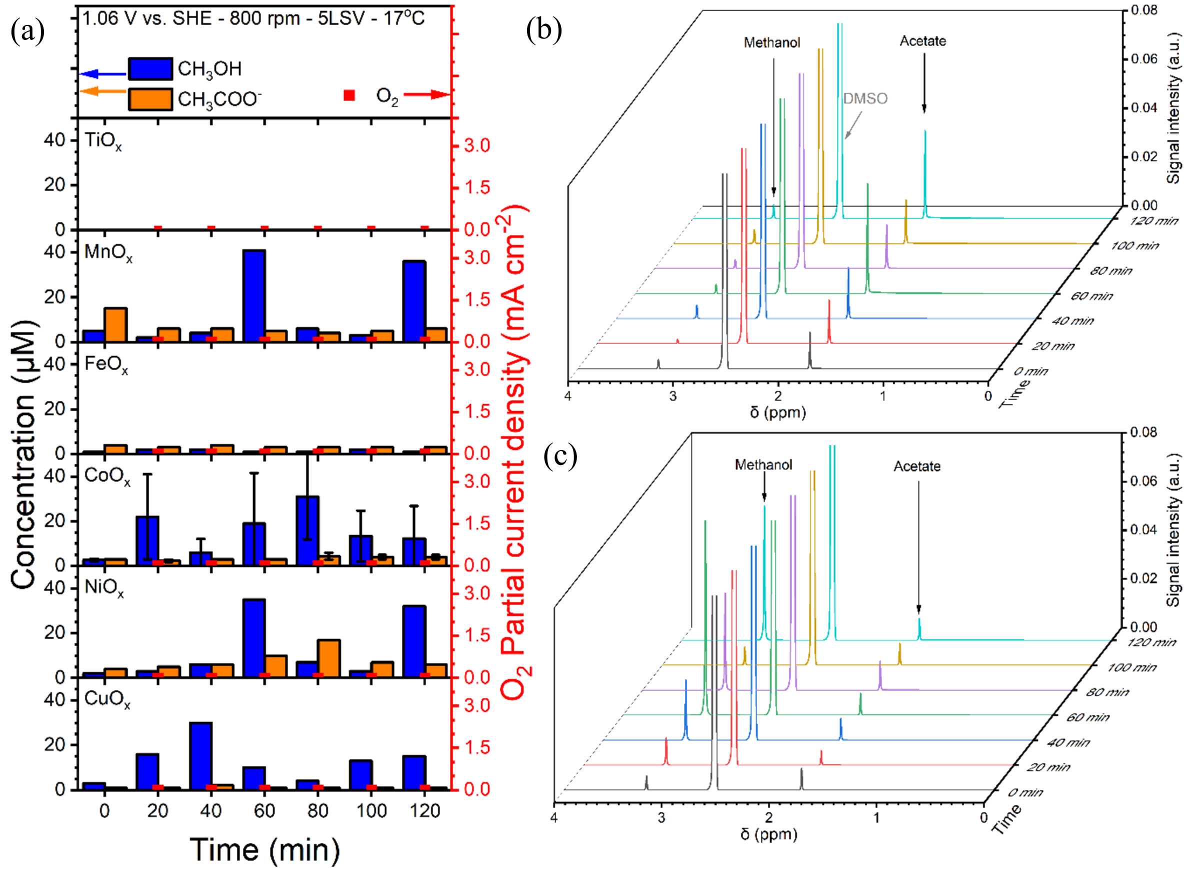

Figure 5-2 (a) Production distributions of methanol and acetate on different transition metal oxides, TiO_x, MnO_x, FeO_x, CoO_x, NiO_x, and CuO_x, for electrochemical methane oxidation reaction at multiple reaction times (20 minutes intervals) within two-hours experiments using chronoamperometry performed at 1.06 V vs SHE under rotational speed: 800 rpm, catalyst loading: 5 cycles of linear sweep voltammetry, and temperature: 17°C. NMR spectra for liquid products of electrochemical partial oxidation of methane on electrodeposited CoO_x taken at 20-minute interval (b) under an applied potential: 0.8 V vs. SHE, rotational speed: 800 rpm, catalyst loading: 100 LSV, and temperature: 17°C and (c) under an applied potential: 1.06 V vs. SHE, rotational speed: 800rpm, catalyst loading: 5 LSV, and temperature: 17°C.

potential. Methanol production for films prepared by 100 LSV cycles are shown in Figure S8. Among all the electrocatalysts tested, CoO_x, NiO_x, MnO_x, and CuO_x are found to be active to produce methanol and acetate while FeO_x produces O_2 and the titanium substrate (TiO_x) is largely inactive. Although the FeO_x catalyst can generate reactive oxygen species and evolve oxygen, the catalyst either does not activate methane or oxidizes it completely to CO_2 which cannot be measured accurately in our system due to the dissolution of CO_2 in the alkaline carbonate electrolyte and the ubiquitous CO_2 background signal from the CO_2 and carbonate buffer equilibrium observed in the GC. Measurement of the electrolyte pH before and after testing shows a decrease in pH of between 0.08 and 0.1 pH units when methane is the reactive gas for all the transition metals including FeO_x. This pH drop is not observed when Ar is flowed through the cell in control electrolysis experiments even when the current densities are similar. The decrease in pH in the Argon control electrolysis experiments is below 0.01 pH units and within the pH meter experimental error. This suggest that methane is indeed oxidized on all the transition metal oxides under the applied potential of 1.06 V vs SHE although no significant amounts of methanol are observed for the FeO_x film. We have not made any attempts to quantify CO_2 from the decrease in pH in the electrolyte.

Interestingly, at the beginning of the methane partial oxidation experiments (t=0 min), methanol and acetate are already detected although at low concentrations indicating that the production of methanol and acetate is thermodynamically favorable even before the application of oxidative potentials due to the likely participation of thermal reactions between the methane and the electrodeposited metal (oxy)hydroxide. Figure 5-2 (b) and (c) shows the ^1H NMR spectra as a function of time for two experiments carried out at two different potentials for a CoO_x catalyst. Before the start of the chronoamperometry experiments, a similar amount of acetate and methanol can be observed in both experiments. These products come from the chemical reaction of methane with the electrodeposited film. At a less negative applied potential of 0.8 V vs SHE (Figure 5-3 a), the methanol concentration remains low and fluctuates over time although the changes in concentration are not significant while the acetate concentration increases over the first 60 minutes of the experiment and then decreases to reach again a second maximum at the end of the experiment.

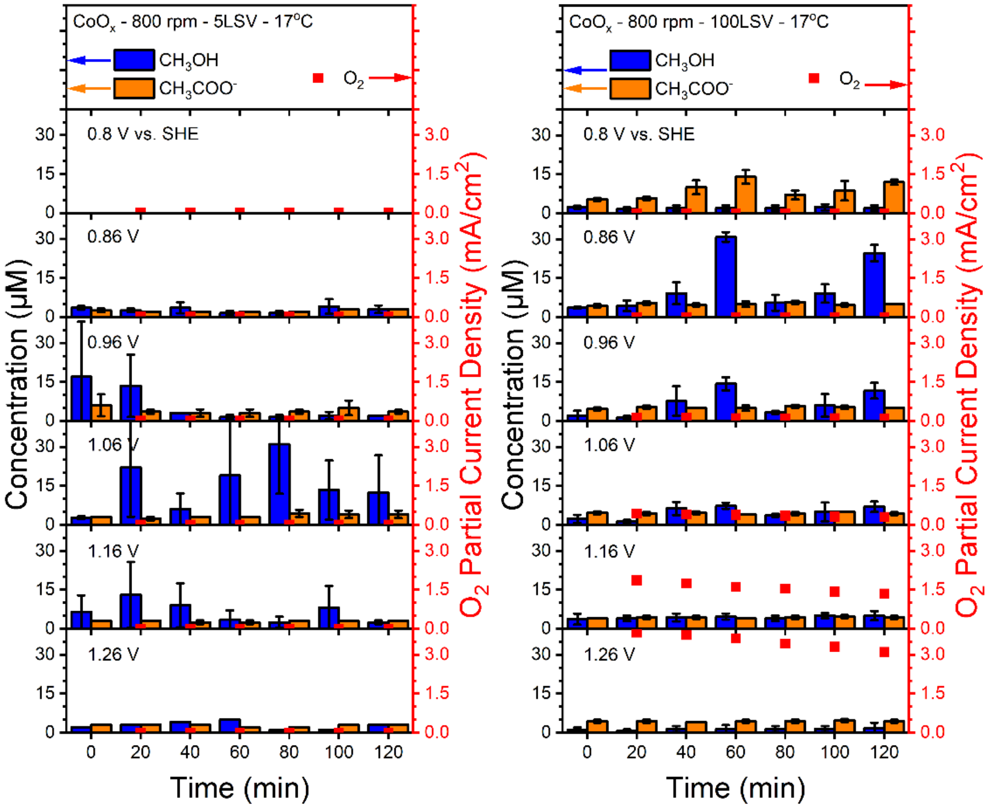

Figure 5-3 Production distributions of methanol and acetate on cobalt oxides, CoOx, for the electrochemical partial oxidation of methane at multiple reaction times (20 minutes intervals) within two-hours experiments using chronoamperometry performed at different applied potentials: 0.8, 0.86, 0.96, 1.06, 1.16, and 1.26 V vs SHE under rotational speed: 800rpms, temperature: 17°C with (a) catalyst loading: 5 cycles of linear sweep voltammetry and (b) catalyst loading: 100 cycles of linear sweep voltammetry.

At higher applied potentials of 1.06V vs SHE (Figure 5-3 b), the acetate concentration remained low over the duration of the experiment while the methanol concentration increased and also reached a maximum at 60 min. The methanol concentration then decreased almost to the initial values and then increased again for the last sample at 120 min. The generation of methanol and further oxidation makes the determination of faradaic efficiencies difficult as the net rates of methanol formation cannot be measured.

5.3.3 Effect of Applied Potential

The driving force for the partial oxidation of methane and the overoxidation of methanol changes as the applied potential is increased. At low applied potentials of around 0.8 V vs SHE, acetate is preferentially accumulated in the electrochemical cell for the thicker CoO_x films (Figure 5-3 a). This indicates that although the activation of methane occurs readily, the activated methane intermediate likely reacts with the carbonate or the CO_2 generated from the complete oxidation of methane to produce acetate. At potentials higher than 0.86 V vs SHE, the selectivity changes to methanol reaching a maximum accumulation of methanol at intermediate overpotentials. Higher overpotentials lead to the complete oxidation of methanol as corroborated by the decrease in the pH at the end of the experiments while the pH does not change in experiments under Ar flow. Higher applied potentials indeed modify the density of high valence oxidation states available for catalysis which are also needed to conduct charges in the porous transition metal (oxy)hydroxide films. Therefore, electrochemical partial oxidation of methane to methanol should be more favorable at relatively intermediate overpotentials where enough of the higher oxidation states of the catalysts are present on the surface of the catalyst but before the oxygen evolution reaction becomes dominant at high overpotentials.

5.3.2 Insights into the Reaction Mechanism

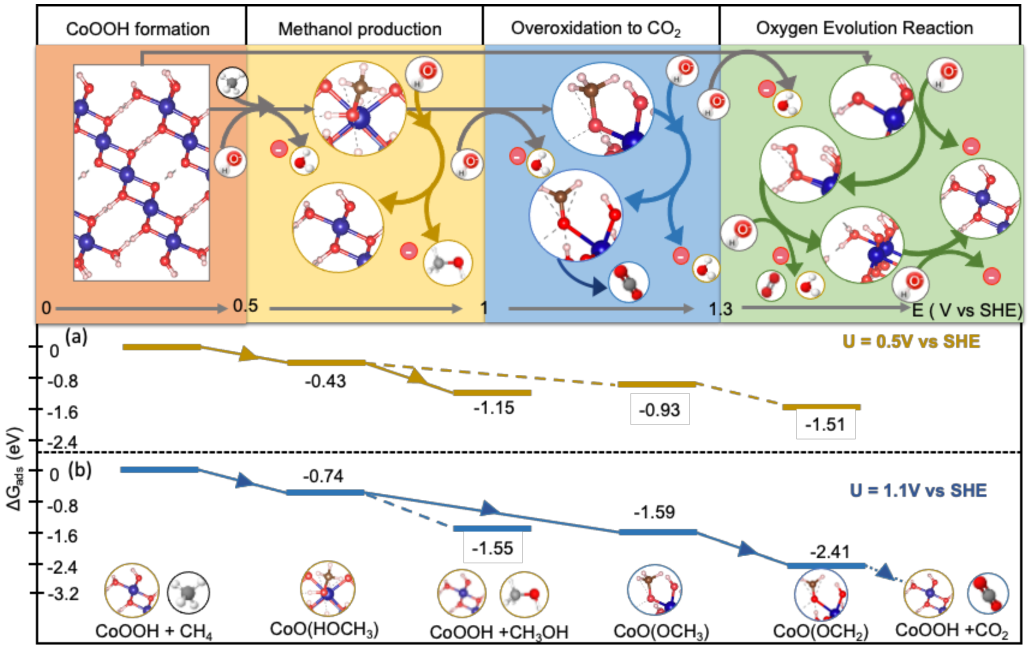

Figure 5-4 Reaction mechanism and reaction energy diagram at (a) U = 0.5 V vs SHE (b) U = 1.1 V vs SHE. The top panel shows the most favorable reactions at certain electrochemical potential windows. In the red box the CoOOH formation takes place starting from 0.5 V vs SHE.[41] The yellow box shows methanol production in the potential range of 0.5 – 1 V vs SHE after which the most favorable reaction would be the overoxidation of methane to CO$_2$ competing with the oxygen evolution reaction starting from U = 1.3 V vs SHE. The reaction diagrams are evaluated at pH = 12.

To understand the mechanism during the electrocatalytic methane oxidation process, DFT simulations were performed. The reaction mechanism and thermodynamic analysis are shown in Figure 5-4. The focus is on the main reaction pathway for methane to methanol and CO$_2$, while the side reaction dealing with acetate formation was not explored as it is the major product only in a very narrow potential window for the thicker CoO$_x$ film. Understanding the Cobalt oxide stability in reaction conditions is the first step in this process. CoOOH is the most stable phase for Cobalt oxide that is observed in the potential range of U = 0.5 to 1.5 V versus SHE at highly alkaline pH.[267,268] Therefore, we consider that the catalyst is CoOOH as soon as the potential reaches 0.5 V vs SHE. Experimentally, the formation of CoOOH was achieved by activating the surface by performing CV measurement and reaching potentials more positive than 0.5V vs SHE. The open circuit potential for CoO_x films after deposition and electrochemical activation were indeed between 0.55 and 0.75 V vs SHE depending on the final potential applied during the activation cycle. The open circuit potentials also change upon the switch of the atmosphere from argon to methane. The activated surface then can perform partial oxidation of methane via the electrochemical reaction between methane and high oxidation states of the catalyst, even without an applied potential. Understanding the thermodynamic branching between various reaction mechanisms when the electrochemical potential is modified then becomes the primary objective of this section of the work. As CoOOH is only stable in the potential range of 0.5 – 1.5 V vs SHE at alkaline pH we have studied the various reactions in the same potential range. From our calculations, three main reaction mechanism are at play, the predominant one depending on the potential, as shown in Figure 5-4

(a) Selective methane oxidation to methanol.

$$^{*}OH + CH_4 + OH^- \rightarrow CH_3OH + H_2O + e^- \qquad (1)$$

$$^{*}CH_3OH + OH^- \rightarrow CH_3OH + {}^{*}OH + e^- \qquad (2)$$

$$^{*}CH_3OH + OH^- \rightarrow {}^{*}OCH_3 + H_2O + e^- \qquad (3)$$

In the initial potential window of 0.5 – 1 V vs SHE, where methanol formation is favored, the first reaction step is to activate the C—H bond of methane, and this happens electrochemically on the hydroxyl group of the CoOOH surface (Equation 1). Figure 5-4 (yellow zone) shows the reaction diagram of methane oxidation to methanol. At 0.5 V vs SHE (Figure 5-4a), we observe the electrochemical methane activation to be thermodynamically favorable (-0.43 eV). This step (Equation 1) combines electrochemical activation of the C-H bond of methane with OH^- and concerted rebinding of the CH_3 fragment with a surface adsorbed OH (*OH). The formed adsorbed *CH_3OH on the surface has two options (1) the CH_3OH group on the surface can desorb and the hydroxyl group on the surface can be replenished electrochemically by hydroxyl ion to give back the initial catalyst (CoOOH), represented in Equation 2. (2) the *CH_3OH can further oxidize to *OCH_3 (Equation 4). We have studied both possibilities and observe that the selectivity between the two reaction is potential dependent. At lower overpotential (< 1V vs SHE), electrochemical desorption of methanol is thermodynamically favorable (Figure 5-4a). As we move toward more positive potential (> 1V vs SHE), the methanol oxidation to *OCH_3 becomes more favorable. This can be seen on Figure 5-4b, where the potential (1.1 V) is just above 1V, and the *OCH_3 species (ΔG_{ads}= -1.59 eV) is becoming more stable than desorbed methanol and hydroxylated CoOOH surface site (-1.55 eV). Increase in potential causes the H on the methanol attached to the surface to become more acidic, which then reacts with a OH^- in the solution to produce *OCH_3 and water, which actively encourages the oxidation of *CH_3OH. At 1 V vs. SHE, the thermodynamic favorability of the two reactions switches. Thus, thermodynamics informs us that CoOOH behaves as an excellent catalyst for the selective oxidation of methane into methanol at an intermediate window of potential (0.5 – 1 V versus SHE), which is in good agreement with our experimental observations.

(b) Methane overoxidation to CO_2.

$$^{*}OCH_3 + OH^- \rightarrow\ ^{*}OCH_2 + H_2O + e^- \qquad (4)$$

$$^{*}OCH_2 \rightarrow \cdots \rightarrow CO_2\ evolution$$

As already mentioned above, if we go towards a sufficiently large overpotential, the surface methanol is overoxidized to *OCH_3 (above 1 V vs SHE, Figure 5-4 blue zone), *OCH_3 then oxidizes to *OCH_2, a step again thermodynamically favorable (Equation 4). These are the first steps toward the overoxidation of methane to CO_2 which is captured as carbonate in the alkaline electrolyte. The other favorable oxidation steps after $*OCH_2$ were not explicitly calculated here.

(c) Oxygen evolution reaction

$$^{*}OH + OH^{-} \rightarrow\ ^{*}O + H_2O + e^{-} \quad (5)$$

$$^{*}O + OH^{-} \rightarrow\ ^{*}OOH + e^{-} \quad (6)$$

$$^{*}OOH + OH^{-} \rightarrow\ ^{*} + O_2 + H_2O + e^{-} \quad (7)$$

$$OH^{-} +\ ^{*} \rightarrow\ ^{*}OH + e^{-} \quad (8)$$

Finally, at sufficiently large overpotentials, we will observe the oxygen revolution reaction which would be directly competing with methane overoxidation to CO_2. The reaction mechanism for OER in alkaline conditions is given in the Equations 5-8. OER reaction on CoOOH has been extensively studied in the literature.[267–269] We find that the OER occurs at a potential on 1.28 V vs SHE in pH = 12 with the rate determining step (RDS) as the desorption of O_2 (Equation 7). This matches very well with what has already been reported by Curutchet *et al.*[217]

The competition between the OER process and the methane oxidation reaction for the active site is an essential element to consider in the reaction condition. Methane activation can interfere with OER intermediates at two different reaction stages. First, as seen above, surface *OH can be used to form $*OHCH_3$ (Equation 1), preventing their conversion into *O (Equation 5). Second, *O intermediates might interact with methane and OH^- to form $*OCH_3$ (Equation 10), preventing the formation of *OOH (through Equation 6).

$$^{*}O + CH_4 + OH^{-} \rightarrow\ ^{*}OCH_3 + H_2O + e^{-} \quad (9)$$

Both reactions occur at high overpotentials and are thermodynamically favorable. For example, Equation 1 will have a ΔG of -0.8 eV at a potential of 1.3 V vs SHE, but Equation 5 will have a ΔG of -0.15 eV. Similarly, equation 10 will have a ΔG of -1.4eV at the same potential but equation

6 will only have a ΔG of -0.1 eV. In any scenario, the two competing reactions mentioned above will have a significant impact on OER but have no impact on the formation of methanol at moderate overpotentials.

5.4 Discussion

From a thermodynamic perspective, the electrochemical partial oxidation of methane to methanol in alkaline electrolytes (Equation 10) requires a relatively low oxidative potential of only 0.18 V vs SHE at pH 14 compared to the oxygen evolution reaction (OER, Equation 11) which requires an additional 0.22V. Despite methane partial oxidation to methanol being thermodynamically accessible in an electrochemical cell, this reaction is kinetically difficult and requires an adequate catalyst to reduce activation energy and a large overpotential to drive measurable partial current densities. Driving large enough currents often requires biasing the electrode to oxidative potentials at which oxygen evolution also takes place despite this reaction also being kinetically slow.

$$CH_4 + 2OH^- \rightleftharpoons CH_3OH + H_2O + 2e^- \quad E^0 = 0.18V \qquad (10)$$

$$2OH^- \rightleftharpoons 0.5O_2 + H_2O + 2e^- \quad E^0 = 0.40V \qquad (11)$$

At very high oxidative potentials, the oxygen evolution reaction outcompetes the methane oxidation reaction and oxygen or CO_2 are predominantly formed.[264] An often ignored fact is that high overpotentials are also needed to transport charges on porous oxide electrodes as these materials are electrically insulating and become conductive only when the population of high oxidation states in the catalyst film is high.[272,274] This means that we cannot expect to see methane activation until transition metal (oxy)hydroxides become oxidized and conductive.

The first point is to form on the catalyst surface the right oxidation number at the considered transition metal for electronic conductivity and methane oxidation. Figure 5-5 shows the ranges of applied potentials vs SHE at which electrodeposited transition metal (oxy)hydroxides[272,275] become conductive by changing the valence state from +2 to +3 for the Co, Ni, Fe, and Mn (oxy)hydroxides in 1 M KOH. At potentials positive of the water oxidation potential (0.4 V vs SHE in pH 14), many of these metal (oxy)hydroxides enter higher oxidation states and become active for both the methane partial oxidation reaction and the oxygen evolution reaction requiring somewhere between 250 and 500 mV overpotential to sustain meaningful oxidative currents.[275]

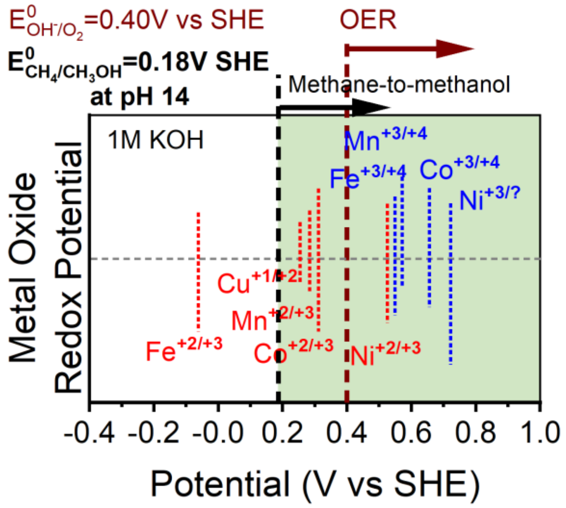

Figure 5-5 Redox potentials experimentally measured for oxidatively electrodeposited transition metal (oxy)hydroxide in 1 M KOH.

From a purely experimental perspective, the potential window between 0.5 and 1.0 V vs SHE is thus optimal to enable any of the transition metal (oxy)hydroxides to be conductive while accessing a large population of metal-oxo sites on the surface of the catalysts to activate and oxidize methane. It must be noted, however, that the redox potentials in Figure 10 and the rates of water oxidation are a function of pH and will change in a different manner for each metal (oxy)hydroxide relative to the 0 V vs SHE.[276] That is, the onset of conductivity and the population of high oxidation states on the surface of the catalyst during operation is a complex function of the potential and the local pH. Based on previous theoretical works for the activation of methane,[277,278] and on the DFT results on CoOOH presented here, we hypothesize that indeed various transition metal oxides are active for the transformation of methane to methanol at ambient temperatures provided four conditions are met: 1) enough methane is supplied to the catalyst surface, 2) the transition metal oxide is conductive without the need of large overpotentials where OER could become dominant, 3) the potential is low enough so that methanol can be preferentially desorbed versus the formation of methoxy and further oxidation, and 4) the catalyst architecture and the transport properties of the cell allow methanol to be transported away from the electrode before it can be further oxidized. Indeed, our DFT calculations on CoOOH show for a potential below ~1 V, desorption of methanol coupled with adsorption of OH^- on the Co site is thermodynamically favored versus further oxidation to methoxy, so that electrocatalytic oxidation with the control of the potential could open a possibility of selective formation of methanol.

We have shown here that partial oxidation of methane proceeds via the chemical reaction between methane and high oxidation states of the catalyst, even without an applied potential beyond the one needed to maintain the oxidation state of the site. Faradaic efficiency may then no longer be a good descriptor for selectivity in the partial oxidation of methane to methanol. We consider the following steps for the partial oxidation of methane on metal-oxo sites. At intermediate overpotentials (0.5 - 1 V vs SHE), the methane is activated electrochemically by dissociation of a C-H bond via reaction with a hydroxyl anion and concerted rebinding with a hydroxyl located on the surface of the electrode to form adsorbed methanol (Equation 1). Methanol can desorb from the site, and this reaction is made exothermic by a concerted electrochemical adsorption of OH^-. At larger overpotentials (1 - 1.3 V), the hydroxyl group attached to the methanol on the surface becomes acidic leading to the formation of methoxy which subsequently over-oxidizes to CO_2 which is captured as carbonate in the alkaline electrolyte. At even higher overpotentials (>1.3 V), the oxygen evolution process becomes a competitive reaction as well.

According to thermodynamics of the reactions, methane overoxidation to CO_2 by methoxy formation would be preferable over OER. A significantly greater methane concentration might result in a drop in OER and an increase in over-oxidation since both processes utilize the same active site. However, at moderate methane concentration not all active sites would be occupied/deactivated by methoxy, hence we would observe significant OER on the CoOOH surface at large overpotentials.

5.5 Conclusion

In summary, we have demonstrated the use of electrochemical methods for the deposition of a family of thin-film transition metal (oxy)hydroxides, which is a simple, clean, and efficient strategy for the fabrication of electrodes for the partial oxidation of methane to methanol in a carbonate electrolyte. CoO_x, NiO_x, MnO_x and CuO_x are active for the partial oxidation of methane to methanol while FeO_x oxidized methane entirely to CO_2 in the potentials tested. We have extensively studied CoOx as the prototypical catalyst for understanding the reaction mechanism of the partial oxidation of methane to methanol. We also found Acetate to be a side-product at low overpotentials (0.8V vs SHE) while methanol is the favored product at medium overpotentials (0.86~1.06V vs SHE). This very interesting potential regime where selective oxidation of methane to methanol is seen is confirmed and explained by our DFT simulations. We find an optimum potential window in which methane activation forming methanol and methanol desorption are both thermodynamically favorable on fully hydroxylated CoOOH. Methanol desorption from the site is favored due to the stabilizing concerted electrochemical adsorption of a OH^- from the solution.

The selectivity is hence explained by competitive adsorption with hydroxide anion, which expels the methanol from the site, and by the transport of methanol away from the electrode. High overpotentials (above 1.16 V vs SHE) result in the over-oxidation of the produced methanol to CO2, since electrooxidation of methanol to methoxy becomes more favorable than its desorption, and the production of oxygen through OER.

Through the use of the gas-tight rotating cylinder electrode cell, unique conditions of hydrodynamics for the partial oxidation of methane show the importance of the control on both kinetics and mass transfer of each step during the reaction. Consequently, this work demonstrates electrodeposition as a viable strategy for catalyst fabrication and may pave the way for efficient strategies of catalyst preparation for further studies of the electrochemical partial oxidation of methane under ambient conditions as well as well-defined conditions of mass, heat, and charge transport.

The transition metal (oxy)hydroxide catalysts reported here should enable the decentralized production of methane to methanol utilizing electrochemical units engineered for optimal methane delivery to the electrode surface as well as rapid methanol product removal and collection. Modular electrochemical devices with advanced electrode architectures for methane and methanol transport can one day enable the efficient and decentralized partial oxidation of methane to methanol at ambient temperatures. In this chapter we have provided a first understanding of how to tackle the design of these devices.

Chapter 6 Elucidating the True Nature of Zirconia–Copper Inverse Catalyst under CO_2 Hydrogenation Conditions

6.1 Introduction

By the end of the century, it is anticipated that the amount of anthropogenic CO_2 produced by human activity would have greatly increased. The burning of fossil fuels, which emits CO_2 into the atmosphere, is primarily to blame for this increase. Being one of the main greenhouse gases causing climate change and global warming, the growing concentration of CO_2 is a serious worry. However, CO_2 may also be seen as an alternative feedstock, and recycling it into value-added chemicals can produce a fuel cycle that is carbon neutral. The process of CO_2 hydrogenation, which turns CO_2 into methanol using hydrogen, is one possible method of CO_2 recycling [69–80]. Methanol is a great liquid fuel that may be used as a substitute for gasoline in the transportation sector. Furthermore, using the MTO (methanol-to-olefins) method, methanol may be directly transformed into useful compounds like ethylene and utilized as a raw material for synthesizing higher hydrocarbons and oxygenates.

Copper-based catalysts have become the standard choice for methanol synthesis [279–281]. In particular, the commercial $Cu/ZnO/Al_2O_3$ catalyst has been widely used to convert synthesis gas, which is a mixture of CO, hydrogen, and some CO_2, into methanol at temperatures ranging from 220-300 °C and pressures of 50-100 bar [74,282,283] ._Significant efforts have been devoted to improving the catalytic performance of the Cu-based catalysts. An enhancement in CO_2 conversion and CH_3OH selectivity was achieved by forming Cu alloys[284,285], and using metal oxides as support for Cu. Among the Cu/oxides studied, Zirconia-modified copper catalysts have been shown to be effective in CO_2/H_2 conversion to methanol due to their high stability under reducing or oxidizing conditions [280,286–300]. Kattel et al. (2016) reported that ZrO_2 can optimize the CO_2

conversion to methanol on Cu[299] . Larmier et al. (2017) found that ZrO_2 enhances both the methanol production rate and the selectivity[301]. Samson et al. (2014) studied Cu/ ZrO_2 catalysts obtained by impregnation of ZrO_2 and complexation with citric acid for CO_2 hydrogenation to methanol[298]. In recent works, inverse ZrO_2/Cu catalysts have also gained a lot of traction as they display high activity, selectivity, and stability during the conversion of CO_2 to Methanol. Rodriguez et al. (2021) investigated the CO_2 hydrogenation on ZrO_2/Cu (111) surfaces and found that the ZrO_2/Cu (111) is an inverse oxide/metal catalyst that displays high activity and stability for the hydrogenation of CO_2 into methanol at 500-600 K[286] . The study also found that at elevated temperatures, ZrO_2 grows on a CuOx/Cu (111) substrate forming islands of 10-12 nm in size and an average height of ~3 Å. Wu et al. (2020) reported that inverse ZrO_2/Cu catalysts with a tunable Zr/Cu ratio have been prepared via an oxalate co-precipitation method, showing excellent performance for CO_2 hydrogenation to methanol[291]. White et al. also studied CO_2 hydrogenation for the model inverse Zr/Cu_2O/Cu (111) catalyst and found the promotional effects of small amorphous zirconia particles for increasing CO_2 adsorption and the formation of hydrogenated intermediates on the CuO_2/Cu(111) surface[302].

Numerous scientific studies have been conducted to explore the adsorbates that accumulate on catalyst surfaces under reaction conditions. This line of research is crucial as these adsorbates can significantly alter the size and shape of the catalytic clusters. Hydroxyls and formates are commonly identified as the primary ligands that accumulate on the catalyst surface, with certain formates undergoing further hydrogenation to produce methoxy and methanol. However, the quantity and diversity of adsorbates on the surface can vary considerably depending on the specific reaction conditions. For instance, White et al. observed that formates, methoxy, and hydroxyls were the main species present on the catalyst. However, the amount of formate was relatively lower compared to other ligands such as methoxy, and the number of hydroxyls decreased with increasing temperature[302]. In contrast, Rodriguez et al. reported the presence of higher number of formate and methoxy species. Interestingly, the formates on the ZrO_2 cluster exhibited low reactivity and remained inactive throughout the reaction, while the formate at the interface displayed high activity[291]. These studies underscore the significance of considering the structure of the catalytic cluster when exposed to different ligands (-O, -OH, -HCOO) during reaction conditions. Such an understanding is essential for fully comprehending the real active site and the mechanism of CO_2 hydrogenation on these catalysts. In the current work, our focus is on determining the ensemble of structures that potentially harbor the collective active site for CO_2 hydrogenation, which is highly dependent on reaction conditions and the type and quantity of adsorbates on the cluster. Furthermore, we aim to investigate the electronic states of the structure to explore the synergy between Zr and Cu at the interface and their potential role in activating or facilitating CO_2 adsorption. The manuscript is structured into five sections. Initially, we examine how different reaction conditions impact the free energy surface of the catalyst in the presence of ligands from a detailed sampling of multi-adsorbates configurations using first principle grand canonical basin hoping. Subsequently, we delve into specific cases of reaction conditions to thoroughly investigate the observed phenomena. Finally, we discuss the electronic structure of our structures, providing insights into the electronic properties and potential mechanisms underlying CO_2 hydrogenation. We show that under reaction conditions, the catalytic surface has a relatively flat free energy surface, suggesting that the active site should be regarded as an ensemble of diverse structures, especially involving changes of the type, number and binding sites of adsorbates rather than being solely dictated by the global minimum.

6.2 Methods

6.2.1 Model

The Cu 111 surface was selected, along with a small Zr cluster consisting of three Zr atoms, as the model for studying the catalytic properties of the Zirconia-Copper inverse catalyst under CO_2 hydrogenation conditions. The Cu 111 surface is a commonly used model for studying the catalytic properties of copper-based catalysts due to its high stability and well-defined surface structure. The small Zr cluster consisting of three Zr atoms was chosen to reduce the computational cost of our calculations while still accurately representing the active sites of the Zirconia-Copper inverse catalyst. This also represents a 12% coverage of Zr on Cu surface which was found to be the optimum coverage for the highest CH_3OH conversion and selectivity[291]. Using this model, the optimum coverage of oxygen, hydroxyl, and HCOO species on the Zirconia-Copper inverse catalyst under CO_2 hydrogenation conditions was investigated. The goal was to identify the most stable configurations of these adsorbates on the surface of the Zr cluster, which could provide valuable insights into the catalytic activity of the material.

6.2.2. Total Energy Calculations

All calculations were carried out within the density functional theory framework using the Vienna ab-initio simulation package (VASP)[169,170]. The electron-ion interactions are treated using the projector augmented wave (PAW) method[171]. We use the Perdew–Burke–Ernzerhof (PBE) functional to treat the exchange-correlation interactions[172]. The Gaussian smearing method with a smearing of 0.1eV is used to improve K-point convergence. The valence electronic states are expanded in plane-wave basis sets with an energy cutoff of 400 eV. The Brillouin-zone (BZ) integration is sampled by adopting the Monkhorst–Pack (MP) k-point grids of 3x3x1 (lattice constant: 12.76 x 12.76 Å) for all the surfaces. During the geometry relaxations of the surface, only the outer atoms were allowed to relax. The cell parameters and the bottom two of total five layers of Cu were fixed to those determined for bulk Cu. Dipole corrections were included to nullify the dipole moment. Structures were relaxed until the force on each atom was less than 0.01 eV/ Å $^{-1}$.

6.2.3. Grand Canonical Basin Hopping

To investigate the possible adsorption sites of the cluster on the Cu surface (fcc, hcp,top etc), cluster shapes, and optimum number of adsorbates and its positions for the Zirconia-Copper inverse catalyst under CO_2 hydrogenation conditions, we employed the Grand Canonical Basin Hopping (GCBH) method. The GCBH method has been used in the field of catalysis to explore the free energy surface of clusters and identify the most stable structures[15,16,29,30,187,224,303–305]. By using this method, we aimed to gain insights into the active sites of the catalyst under the reaction conditions.

1. The Zr atoms were allowed to move freely on the surface, enabling them to find various modes of adsorption.
2. Oxygen and hydroxyls were added grand canonically in the GCBH process, enabling us to investigate their effect on the cluster.
3. The adsorption site and geometry of the overall cluster could also be altered by the oxygens and hydroxyls.
4. The formates were added one at a time, up to a maximum of four formates, and we explored the free energy surface for a fixed number of adsorbates. The addition of formates could also change the adsorption site for O and OH adspecies, the geometry, and its binding mode with the Cu(111) support.

5. The formates were moved such that the formates can either adsorb on the Zr/Cu interface, the Cu surface, at the bridging position of two Zr atoms or directly interact with just one Zr atom.

6.2.4. Chemical potential of adsorbates

To accurately replicate the reaction conditions for the CO_2 hydrogenation reaction, it is essential to calculate the chemical potentials of all species involved. To define the accurate reaction condition, four main parameters are considered: (a) total pressure, (b) the CO_2: H_2 in the initial feed, (c) the temperature at which the reaction is conducted, and (d) the conversion of the reaction shown in the following equation, which provides the partial pressure of reactants and products:

$$CO_2 + 3H_2 \rightarrow HCOO + 2.5H_2 \rightarrow CH_3OH + H_2O$$

The chemical potential of O is calculated using the formula $\mu(O) = \mu(H_2O) - \mu(H_2)$, where $\mu(H_2O)$ represents the chemical potential of water. The chemical potential of OH is calculated using the formula $\mu(OH) = \mu(H_2O) - 0.5\mu(H_2)$, The chemical potential of HCOO is calculated using the formula $\mu(HCOO) = \mu(CO_2) + 0.5\mu(H_2)$, where $\mu(CO_2)$ is the chemical potential of CO_2. The chemical potential of H_2 and H_2O is calculated in the vapor phase using the ideal gas approximation.

6.2.5. Adsorbate interaction energy

The adsorption energy reported throughout the work is evaluated via the following equation:

$$\Delta G = E\,(Zr_3O_xOH_y(HCOO)_z/Cu111) - E\,(Zr_3O_6/Cu111) - (x-6)\,\mu_O - y\mu_{OH} - z\mu_{HCOO}$$

Here the $Zr_3O_xOH_y(HCOO)_z$ /Cu111 represents the energy of the $Zr_3O_xOH_y(HCOO)_z$ cluster supported on Cu 111 surface. Here, x, y, and z signify the number of O, OH, and HCOO on the cluster, respectively. Additionally, we use Zr_3O_6 /Cu111 as the frame of reference, which is the global minimum energy state of the Zr_3O_6 cluster supported on Cu 111 surface. We selected Zr_3O_6

/Cu111 as our reference point since it is one of the most used representative systems for studying CO_2 hydrogenation on inverse ZrO_2/Cu catalysts[299,306,307]. Moreover, we denote the free energy of O, OH, and HCOO as μ_{O}, μ_{OH}, and μ_{HCOO}, respectively.

6.3 Results

6.3.1 Free energy surface of $Zr_3O_xOH_y(HCOO)_z$ /Cu111 at different reaction condition

In the first part of this work, our objective was to determine the free energy surface of the $Zr_3O_xOH_y(HCOO)_z$ /Cu111 system. To achieve this goal, we employed the GCBH method, which is well-suited for exploring the complex energy landscapes of heterogeneous catalysts. Three different reaction conditions were chosen to represent a variety of literature works. These conditions were (a) pressure = 0.013atm, temp = 500K, CO_2/H_2 ratio = 9, and, conversion = 2% corresponding to the work of White et al. [302], (b) pressure = 4.93 atm, temp = 493.15K, , CO_2/H_2 ratio = 1:3, and, conversion = 0.8% corresponding to the work of Chen and Liu et al [299] and (c) pressure = 30 atm, temp = 493.15 K ,CO_2/H_2 ratio = 3, and conversion = 19.7% (equilibrium conversion for CO_2 hydrogenation) corresponding to the work of Wen, Rodriguez and Ma et al [291]. The free energy search is depicted in Figure 6-1(a), with the purple lines representing condition (a), the blue lines representing condition (b), and the green lines representing condition (c). The structures within the energy range of 0.75 eV from the global minima (GM) for each number of formates, ranging from 0 formate to 4 formates, are shown in the plot. The energy landscape of the $Zr_3O_xOH_y(HCOO)_z$ /Cu111 system exhibits significant changes under different reaction conditions. This shows that the reaction conditions play a crucial role in determining the most stable ensemble of configurations for the system. As the initial feed pressure increases, the HCOO/Zr ratio of the system also changes. We can clearly observe this change as we increase the pressure. The formate/Zr ratio for the most stable configurations increases as we go from low initial pressure to higher initial pressures. However, this ratio also depends on the conversion. As we approach the equilibrium conversion of CO_2 hydrogenation, the formate/Zr ratio becomes 1:1. It is noteworthy to mention that the stability of the various adsorbates (-O, -OH, -HCOO) on the $Zr_3O_xOH_y(HCOO)_z$ /Cu111 cluster is not only influenced by the composition of the cluster, but

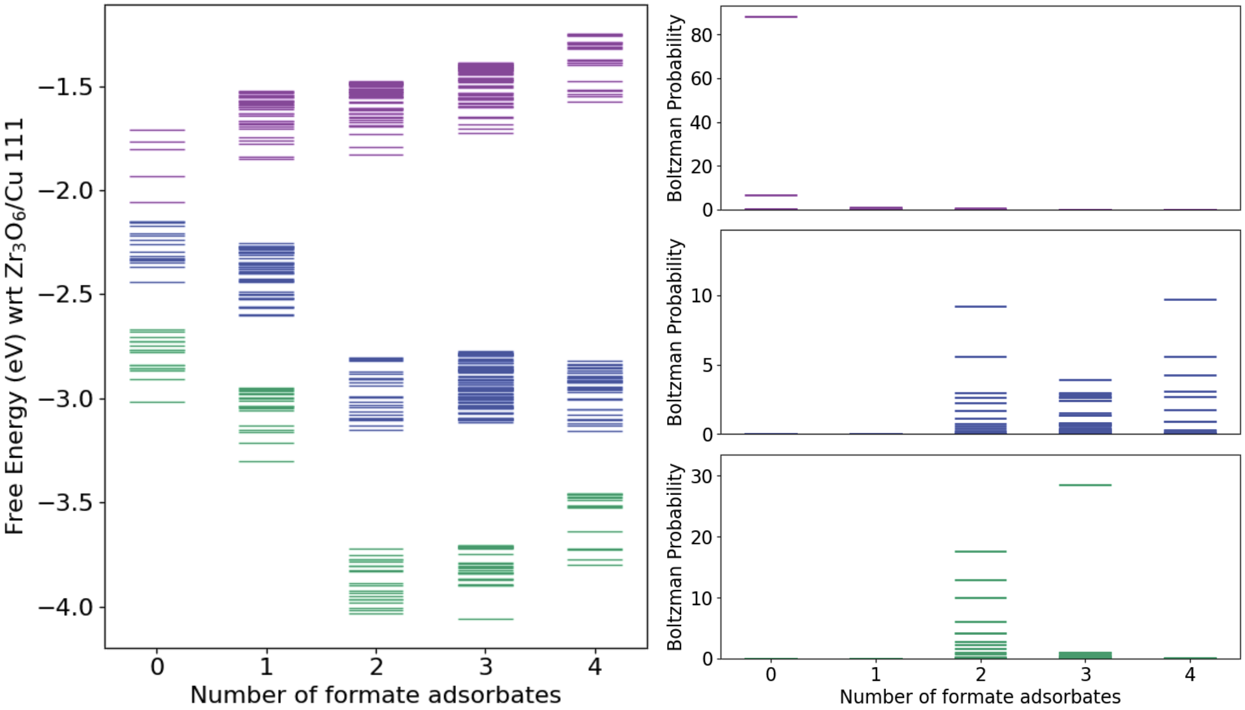

Figure 6-1 (a) The FES of $Zr_3O_xOH_y(HCOO)_z$ /Cu111 surface. The y-axis represents the adsorption energies of ligands such as -O, -OH and -HCOO on the cluster relative to Zr_3O_6/Cu 111 system. The x axis represents the number of formates on the cluster. The three different colors on the plot represents the three different reaction condition. Purple: pressure = 0.013atm, conversion = 2%, CO_2/H_2 ratio = 9, and temp = 500K, Blue: pressure = 4.93 atm, conversion = 0.8%, CO_2/H_2 ratio = 1:3, and temp = 493.15K and Green: pressure = 30 atm, conversion = 19.7%, CO_2/H_2 ratio = 3, and temp = 493.15 K . (b) The Boltzmann probability of the corresponding structures shown in (a) for the three different reaction condition.

also by the reaction conditions. Upon increasing the pressure of the initial feed, the overall stability of the adsorbates on the cluster in relation to the Zr_3O_6/Cu111 system also shows an upward trend.

To further investigate the probability distribution of different configurations at respective reaction condition temperatures, we calculated the Boltzmann probability $P_m = \frac{1}{z}\exp\left[\frac{-\Delta E}{K_B T}\right]$ for each structure in the FES. This probability provided insights into the relative stability of the structures and their likelihood of occurrence under specific reaction conditions. For the case (a), we observe the Boltzmann probability to be accumulated one structure (88% probability), with one minor configuration (5%). However, for case (b), we observe a very flat free energy surface around the 2, 3 and 4 formate structures, which leads to highly distributed Boltzmann probability across a large ensemble of structures. In the last case (c), we observe the Boltzmann probability to be only distributed around the 2 and 3 formate structures.

The structures identified through the GCBH simulations for the various reaction conditions are further analyzed in the subsequent sections of this study. The goal is to gain a deeper understanding of the true nature of these clusters and their behavior during the actual reaction.

6.3.2. Reaction condition: Pressure = 0.013atm, Conversion = 2%, Temperature = 500K, CO_2/H_2 ratio: 1:9

In the study, the free energy surface of the $Zr_3O_x(OH)_y(HCOO)_z$/Cu111 system was thoroughly explored at given reaction conditions. In figure 6-2 we present the side and top views of the 5 energetically most favorable structures found via GCBH in the reaction condition: pressure = 0.013atm, conversion = 2%, CO_2/H_2 ratio = 9, and temp = 500K. The bottom-colored panel show the Boltzmann distribution of all the unique structures explored in the reaction condition. The $Zr_3O_3(OH)_3$ configuration was found to be the most dominant one, with a massive 88% of the population occupying it. It was also observed that a smaller population of $Zr_3O_4(OH)_3$ was present, indicating that this configuration may also have some importance in the reaction mechanism. In the energetically most favorable structures, the hydroxyl groups in the cluster were found to prefer interacting with Zr and not Cu atoms, forming Zr-OH bonds. On the other hand, the oxygen atoms in the cluster tend to form Zr-O-Zr bonds, linking the Zr atoms together. As the number of oxygen atoms increases, as in the case of $Zr_3O_4(OH)_3$, the oxygen atoms also start interacting with the Cu surface, acting as an anchor for the cluster on the Cu111 surface.

Additionally, the study also observed a relatively small population of formate-containing clusters, such as $Zr_3O_3(OH)_2HCOO$, $Zr_3O_3(OH)_3HCOO$, and $Zr_3O_3(OH)_2(HCOO)_2$ with a total Boltzmann population of 4.55% (includes all formate containing structures). The relative energies of each structure relative to the GM are also provided right below the structure. The presence of formate-containing clusters is relevant as it has been suggested that formate is an intermediate in the conversion of CO_2 to methanol and can accumulate on the cluster. Therefore, understanding the formation and stability of formate-containing clusters could provide further insight into the reaction mechanism. The formate group in the $Zr_3O_3(OH)_2HCOO$ cluster replaces one of the hydroxyl groups in the $Zr_3O_3(OH)_3$ cluster and attaches to the same Zr atom in a bidentate fashion. As the number of hydroxyl groups increases, as in the case of $Zr_3O_3(OH)_3HCOO$, the hydroxyl groups occupy the same sites as they do in $Zr_3O_3(OH)_3$, but the formate group attaches itself on the bridging position between the two Zr atoms in a bidentate fashion.

Interestingly, White et al [302] found that vibrational bands associated with formate were generally weak in the IRAS spectra, and the peaks assigned to formate in the C 1s XPS spectra were also weak compared to other intermediates in regions of the surface with zirconia. These observations suggests that formate is not accumulating on the surface during the reaction conditions. These findings support the results obtained in our current study, where the global minimum of the cluster composition was observed as $Zr_3O_3(OH)_3$, whereas the structures with formates were found to be metastable.

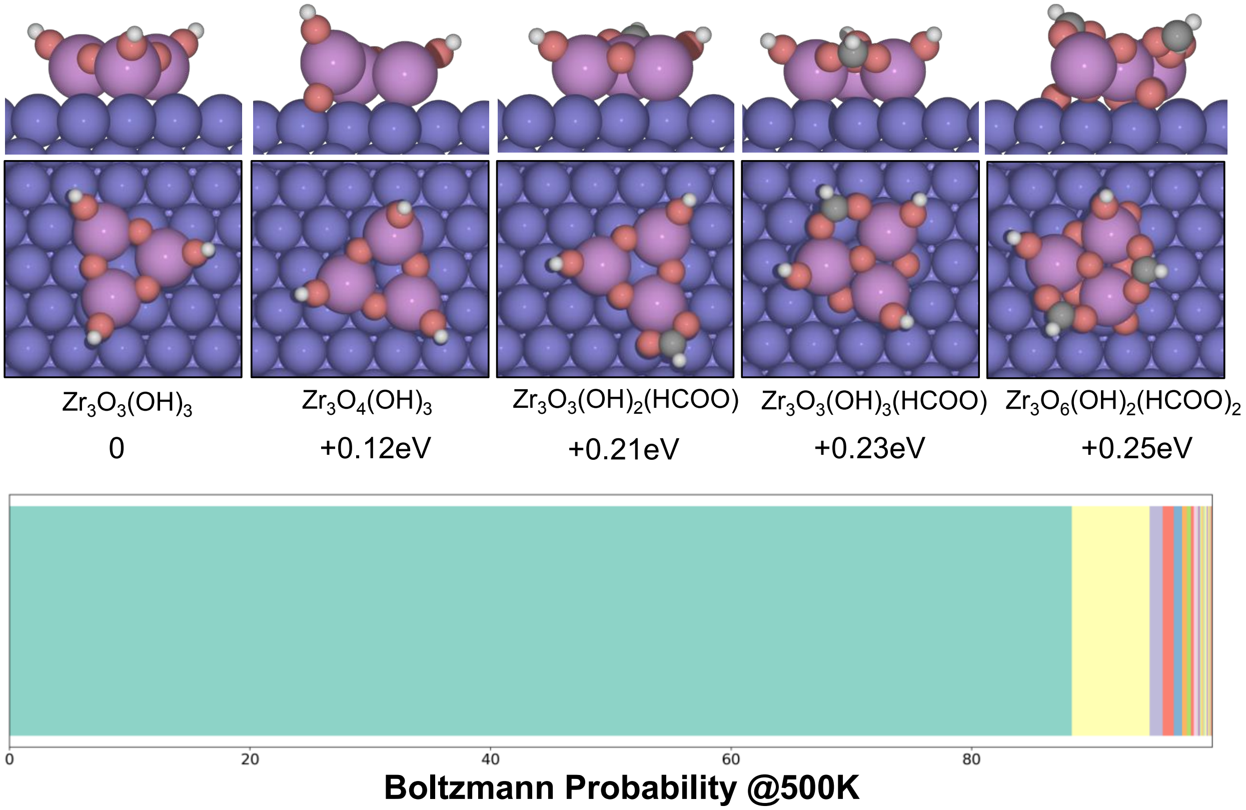

Figure 6-2 The side and top views for the 5 energetically most favorable structures found via GCBH in the reaction condition: pressure = 0.013atm, conversion = 2%, CO_2/H_2 ratio = 9, and temp = 500K (condition a in the text). The bottom colored panel show the Boltzmann distribution of all the unique structures explored in the reaction condition.

In the CO_2 hydrogenation process, the hydrogenation of formate is the rate-determining step, which means that the rate of the overall reaction is limited by the speed at which this step occurs. To make this step happen faster, we need to lower the barriers to the hydrogenation of formate. One way to do this is to either weaken the strength of the adsorption of formate on the catalyst surface or enhance the adsorption of the hydrogenated product H_2COO. In our current reaction conditions, we have observed that the adsorption of formate on the catalyst surface is not very strong, but it is also not very weak. The importance of accurately determining the real-time catalyst composition under the reaction conditions cannot be overstated, as it enables the identification of the ensemble of structures that could represent or contain the active site.

As part of our comprehensive investigation into the $Zr_3O_x(OH)_y(HCOO)_z$/Cu111 system, we also studied the impact of temperature on the hydroxyl content of the cluster. It is known that hydroxyls are often bound on zirconia surfaces and their presence can arise from various sources, including H atom spillover from Cu surfaces and water formation via surface reactions like RWGS. Our findings revealed that hydroxyls are indeed bound to the zirconia surfaces of the cluster, and their concentration exhibits a significant decrease as the temperature is increased from 300K to 1000K. This is an important finding as the coverage of hydroxyls on the surface is anticipated to have a substantial influence on the reaction mechanism. At lower temperatures, when higher hydroxyl coverages are observed, all the sites would be occupied by hydroxyl, which would make it exceedingly difficult to bind CO_2 and initiate the CO_2 hydrogenation process. It is important to mention that White et al [302] also reported on the XPS O 1s spectra from their experiments, which

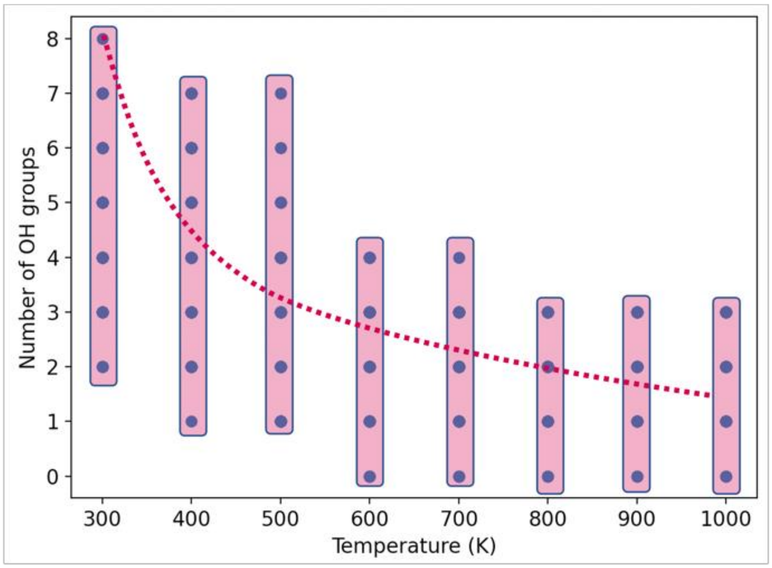

Figure 6-3 The number of hydroxyls on the most favorable structures at a specific temperature. The structures within the range of 0.35 eV from the global minima were considered at each temperature value.

illustrate that the surface concentration of OH* drops rapidly above ~ 450 K. This decrease in surface hydroxyl content could have significant implications for the hydrogenation of intermediates bound to zirconia and might contribute to the accumulation of H_xCO^* and CH_3O^* at higher temperatures. As a result, the coverage of hydroxyls on the surface is critically dependent on temperature, and the rapid decrease above ~ 450 K could play a pivotal role in the reaction pathway.

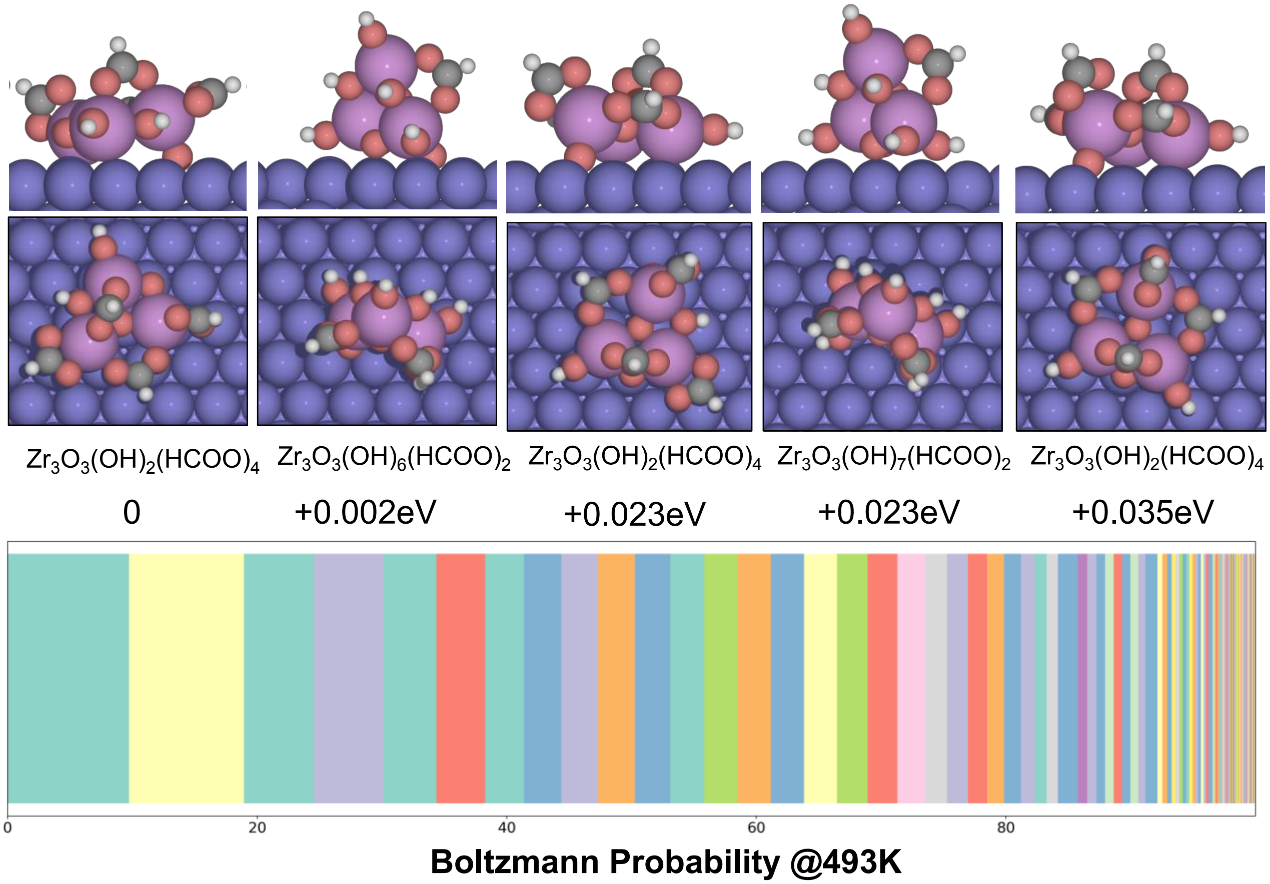

Figure 6-4 The side and top profile of the 5 energetically most favorable structures found via GCBH in the reaction condition: pressure = 4.93 atm, conversion = 0.8%, CO_2/H_2 ratio = 1:3, and temp = 493.15K The bottom colored-panel show the Boltzmann distribution of all the unique structures explored in the reaction condition. The colors correspond to a specific configuration of $Zr_3O_x(OH)_y(HCOO)_z$/ Cu .

6.3.3. Reaction condition: Pressure = 4.93 atm, Conversion = 0.8%, CO_2/H_2 ratio = 1:3, and Temperature = 493.15K

In this section, we will delve into a thorough analysis of another reaction condition, which represents a more realistic catalytic condition but at a lower conversion, to gain a more comprehensive understanding of the catalytic mechanism at play and identify the true nature of the catalyst in the reaction condition. In Figure 6-4, we show the 5 most stable structures in the top panel and on the lower panel, we show the distribution of Boltzmann probability among the ensemble of structures. We can clearly observe that the Boltzmann probability is distributed over a broad range of different clusters compositions and geometries. Compared to the low-pressure case a key difference, in this case, is that the population of formate-containing systems is very high (100% of probability), so the catalyst is covered by two to four formate molecules. When considering the five best structures which only represent 35% of the total probability, we find that three out of the five structures have four formates on the cluster, while the other two have two formates on the cluster. Moreover, the number of hydroxyls present in the cluster varies significantly across the structures, but the energy doesn't change considerably. This observation suggests that the potential energy surface is very flat relative to the number of hydroxyls and formates present in the cluster. Therefore, the cluster serves as a reservoir for hydroxyls and formates that can be utilized in subsequent steps of the reaction mechanism.

The overall probability of finding 1,2,3,4 formate on the cluster is 0, 27.9,41.8 and 30.8 % respectively. To understand the relative thermodynamics in between the ensemble of structures containing 0,1,2,3 and 4 formates it was very important to calculate the entropic energy of the system at different number of formates. A statistical definition of entropy utilizing the Boltzmann probabilities of these discrete states (different number of formates) was applied to obtain the entropy $S_G = k_B \sum_I P_I \ln(P_I)$, where $P_I = \frac{e^{-E_I/k_BT}}{\sum e^{-E_I/k_BT}}$ and E_I is calculated the as described in Section II.4, k_B is the Boltzmann constant and T is the temperature. We can then include the entropy to calculate the Helmholtz Free energy of the system as: $F = U - TS_G$. This method has been utilized in other works, Alexandrova et al used it to describe the free energy of clusters with different ratios of Pt:Pd[308], Manoharan et al used this method to determine the free energy landscape of Clusters[309]. Using this method, we provide the thermodynamics between the different number of formates in Figure 6-5. We can observe that the energies start to stabilize as we reach the 2HCOO, 3HCOO and 4HCOO structure with minima reaching at 3HCOO structure. This is also evidenced by the highest level of probability observed for 3HCOO at 41.8%.

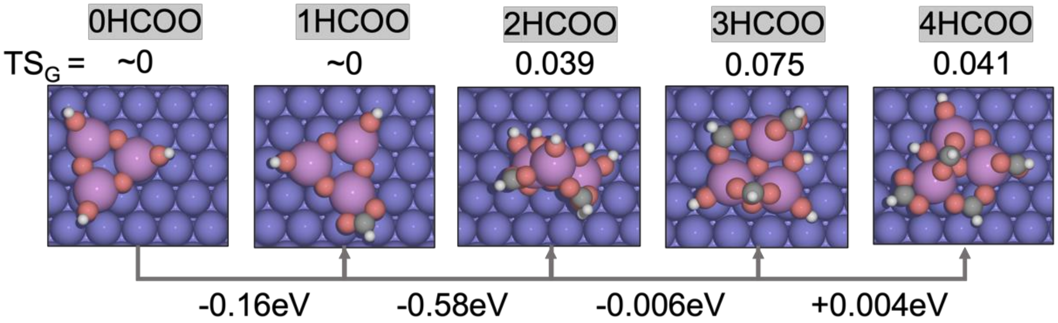

Figure 6-5 Energy for formate adsorption on the cluster at each step starting from $Zr_3O_3(OH)_3$. The energy for each formate adsorption step in given under the arrow in eV.

In order to gain a more comprehensive understanding of the distribution of formate, OH, and O species on the cluster, we have plotted the probability distribution in Figure 6-6. The size of the circles in the plot corresponds to the prevalence of a specific configuration in the FES (i.e., a large circle corresponds to a high Boltzmann probability for the given configuration). The darker shades indicate a higher number of structures associated with that configuration. The probability distribution of the number of formats, hydroxyl, and oxygens are also given in the green box on the respective axis. The analysis reveals that the probability distribution is spread across various configurations, particularly between 2-4 formates, 2-7 hydroxyls, and 2-4 oxygens on the cluster. The probability range spans from 0% to 9.5%. This indicates that in the present reaction condition, no single state exhibits clear dominance, in contrast to our observations in the previous section (Case a). Instead, we observe a statistical ensemble of multiple states, which more accurately represents the catalytic behavior under catalytic conditions. It is important to note that the global minimum structure, which indicates the most stable configuration, may not hold significant meaning in this specific reaction condition. Therefore, when studying the CO_2 reaction mechanism, it is crucial for readers and researchers to exercise caution when considering a single active site as a starting point. The ensemble of states observed here emphasizes the need for a

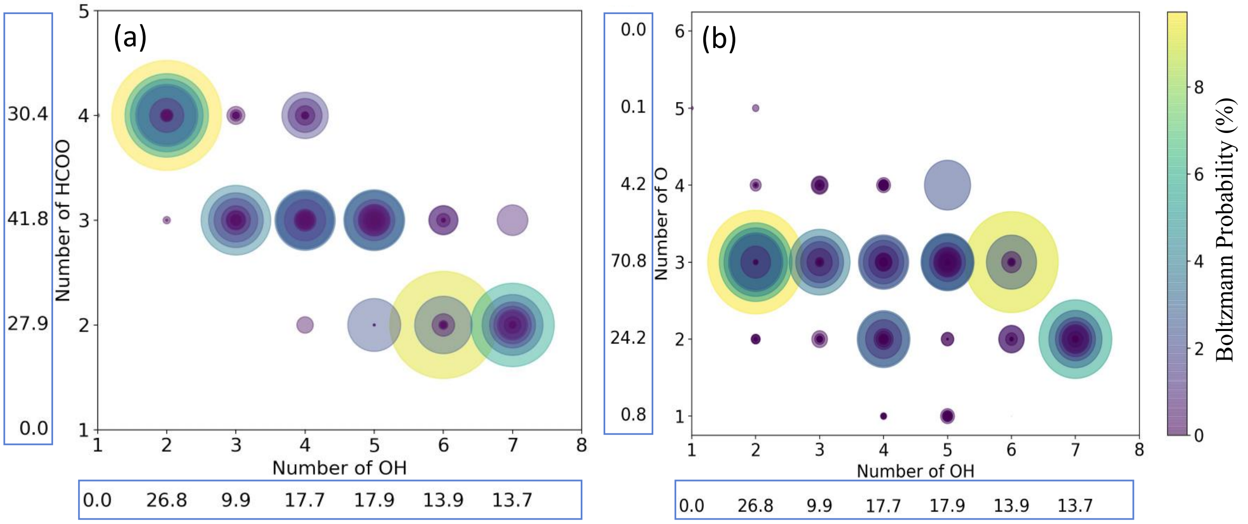

Figure 6-6 Heat bubble plot with the (a) y axis as the number of formates and the x axis as the number of hydroxyls on the cluster, (b)) y axis as the number of oxygens and the x axis as the number of hydroxyls on the cluster. The heat map represents the Boltzmann probability for the structure with bigger bubble meaning higher probability of occurrence. The total probability of finding a specific number of ligands is also provided in the green box on the ligand specific axis alongside the number of ligands.

comprehensive and dynamic understanding of the catalytic behavior, accounting for the statistical distribution of species on the cluster.

The presence of a diverse ensemble of easily accessible structures within the system provides significant advantages in facilitating the reaction mechanism and the formation of hydrogenated intermediate products. This diversity enables flexible adjustment of the hydrogen and formate content without incurring significant energy costs. The accumulation of formate species on the cluster is a commonly observed phenomenon in studies related to CO_2 hydrogenation. Prior research by Liu et al [299] , has highlighted the high adsorption energy of formate on the cluster, as determined through DFT simulations. Experimental evidence obtained through in situ DRIFTS measurements further supports this observation. Consistent with these previous findings, our work confirms the high coverage of formate on the cluster. We also observe that the adsorption of formate on the cluster reaches an optimal coverage, where the adsorption energy of formate stabilizes. This behavior is clearly illustrated in Figure 1(a) by the blue lines. This finding suggests that formate is adsorbed on the surface in a manner that is neither too strongly nor too weakly bound, which is conducive to further hydrogenation to form H_2COO. Furthermore, the hydroxyls present on the cluster serve as a hydrogen reservoir, providing an additional source of hydrogen not only for the hydrogenation of formates but also for other intermediate species. This role of hydroxyls contributes significantly to the overall reaction mechanism, ultimately leading to the production of methanol.

6.3.4. HCOOs at the interface

Numerous studies have found that the zirconia/copper interface plays a crucial role in the CO_2 hydrogenation reaction by facilitating the conversion of formate intermediates to methanol. One such study was conducted by Coperet et al[301], who utilized a combined experimental and computational approach with realistic models, including kinetics, in situ IR and NMR spectroscopies, and isotopic labeling strategies. This study demonstrated that the reaction takes place specifically at the interface between zirconia and copper particles and that the formate species are stabilized at the interface between the Zr and Cu.

Another study conducted by Rodriguez et al[291] utilized IR measurements and observed a peak at 1350 cm^{-1} (HCOO-Cu) which is attributed to the O-C-O vibration of the formate species bonded on Cu or the interface. This peak was found to be about 18 cm^{-1} lower than that for formate adsorbed on the ZrO_2 (bidentate formate). The authors also observed that the generation and consumption of formate-Cu were extremely fast under transient conditions compared with the formate species on zirconia. This indicates that highly reactive pathways exist on the inverse catalyst. The Cu sites at the zirconia/copper interface were proposed to serve as the adsorption site for the formate intermediate, facilitating its hydrogenation conversion to methanol. This enhances the turnover frequencies (TOF) of the oxygenates on the inverse catalysts. Therefore, the zirconia/copper interface plays a crucial molecular role in the CO_2 hydrogenation reaction, as it promotes the conversion of formate intermediates to methanol.

Hence, our primary objective now is to investigate the structures that contain formates adsorbed on the interface of the Cu-Zr interface. We still are under the more realistic catalytic condition as represented in case b. To this end, we present a bar graph in Figure 6-7, which illustrates the number of structures versus the energy of the structure from the global minimum. The lighter shade bar indicates the total number of structures in the specific energy range, while the darker shade represents the number of structures (a subset of the total structures) that have formates adsorbed on the interface of Zr-Cu. It is important to note that the formate adsorbs at the interface in a bidentate manner, with one oxygen atom interacting with Zr and the other interacting

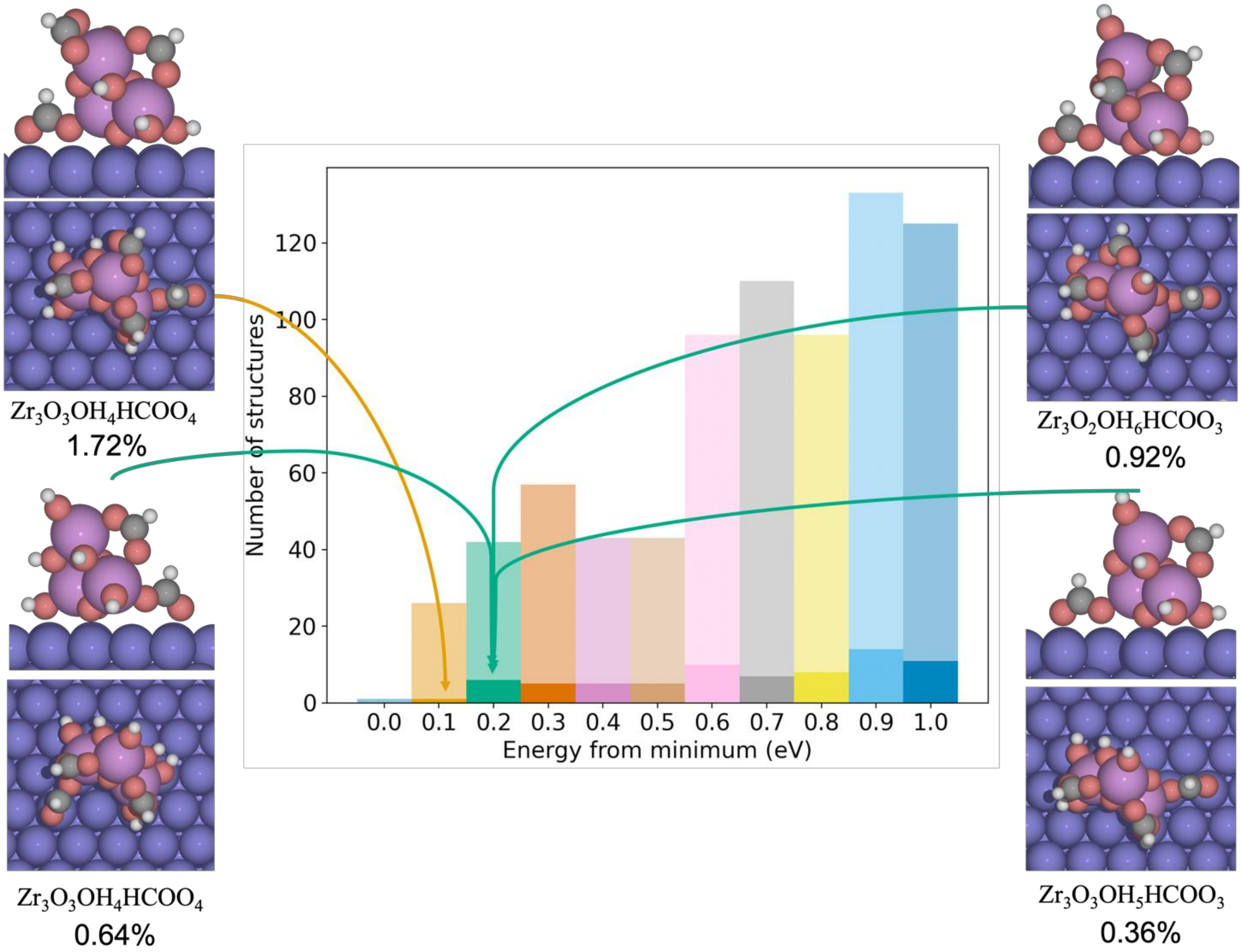

Figure 6-7 The bar-graph represents the number of structures vs the energy of the structure from the global minimum for the reaction condition (b). The lighter shade bar represents the total number of structures in the specific energy range, whereas the darker shade represents the number of structures that have HCOOs adsorbed at the interface between Zr and Cu. The arrows from the bar point toward the side and top profile of the corresponding structures. The Boltzmann probability of the structures shown are given under the respective structures.

with the Cu surface. Upon analyzing the results, we observe that the number of structures with formate adsorbed at the interface is considerably lower than the total number of unique structures found via the GCBH. Additionally, we provide the side and top profiles of the four most favorable structures that include interface formate, along with their Boltzmann probability in Figure 6. The four most favorable structures are (in increasing energy order) $Zr_3O_3(OH)_4(HCOO)_4$, $Zr_3O_3(OH)_4(HCOO)_4$, $Zr_3O_2(OH)_6(HCOO)_3$, $Zr_3O_3(OH)_5(HCOO)_3$ with the Boltzmann probability as 1.72%, 0.92%, 0.64% and 0.34% respectively. All the structures identified in our study contain a high level of hydroxylation. This is an encouraging observation as the hydrogen on the hydroxyl groups could potentially aid in the hydrogenation of formate to H_2COO at the interface between Zr and Cu. However, we notice a lower probability of occurrence of these structures in the FES, which could be due to the possibility that these might be transient formates that turn over to methanol via further hydrogenation. There are instances from our previous work where species with a probability of ~1% were shown to be completely responsible for the catalytic reactivity[16,29,187].

6.3.5. Electronic structure analysis

It is widely acknowledged in scientific literature that metallic copper and oxidized copper play crucial roles in the formation of methanol. Metallic copper facilitates the dissociative adsorption of hydrogen, which leads to the generation of atomic hydrogen by breaking apart H_2 molecules.

It is widely acknowledged in the scientific literature that metallic copper and oxidized copper play crucial roles in the formation of methanol. Metallic copper facilitates the dissociative adsorption of hydrogen, which leads to the generation of atomic hydrogen. This atomic hydrogen directly participates in the hydrogenation process of CO_2, contributing to the production of methanol. Conversely, oxidized copper is considered the active site for methanol formation, and its presence is essential for achieving high selectivity for methanol and low selectivity for CO under operating conditions.

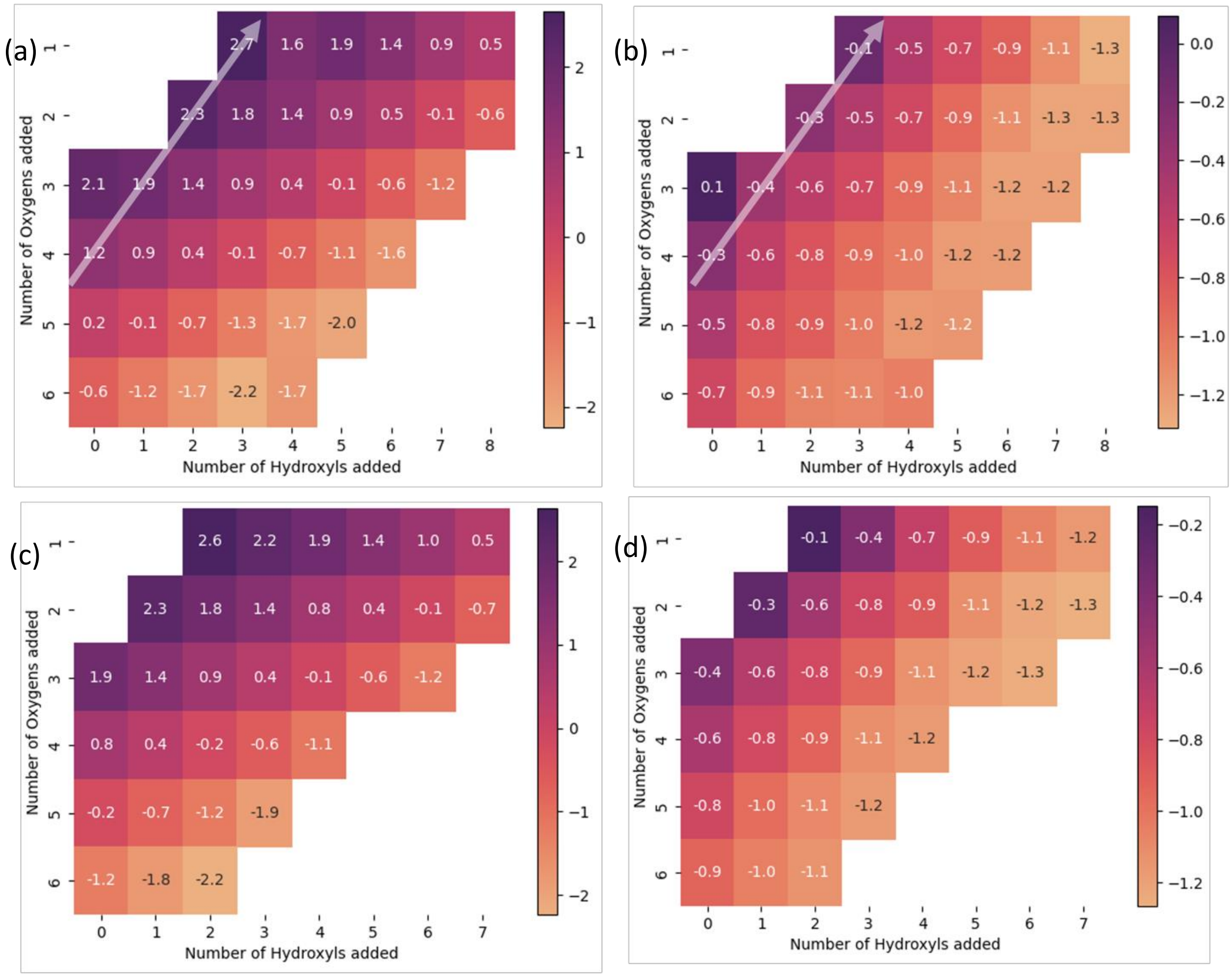

Figure 6-8 Bader charge on the (a) first layer of the Cu surface which supports the $Zr_3O_x(OH)_y(HCOO)_2$ cluster (b) three Zr atoms in the $Zr_3O_x(OH)_y(HCOO)_2$ cluster (c) first layer of the Cu surface which supports the $Zr_3O_x(OH)_y(HCOO)_3$ cluster and (d) three Zr atoms in the $Zr_3O_x(OH)_y(HCOO)_3$ cluster. The Bader charges are calculated with respect to the global minima of Zr_3O_6/Cu 111 surface. The x axis is the number of hydroxyls on the cluster whereas the y axis is the number of oxygens on the cluster. The yellow arrow represents the change in the number of hydrogens on the cluster, with the number of hydrogens increasing in the direction of the arrow. Similarly, the white arrow represents the increase in the number of oxygens. The annotated value on the heat plot is the difference in the Bader charges with more negative value meaning the atoms are oxidized w.r.t Zr_3O_6/Cu 111.

Interestingly, it has been observed that metallic copper is more conducive to the Reverse Water Gas Shift (RWGS) reaction than partially oxidized copper, as previously documented in the literature[310]. The participation of Cu^+ species in the CO_2 hydrogenation to methanol has already been proposed, and researchers have explored this concept extensively. For instance, Klier et al proposed that Cu^+ ions dissolved in ZnO lattice serve as active sites for methanol synthesis from syngas and CO_2/H_2 mixtures on Cu/ZnO-based catalysts [311] .

Furthermore, Chinchen and Waugh et al conducted a study using a series of $CO/CO_2/H_2$ mixtures over a commercial $Cu/ZnO/Al_2O_3$ catalyst. They discovered that the surface of the catalyst contained both metallic and oxidized copper under real methanol synthesis conditions, and the copper on the surface was more oxidized with a higher CO_2/CO ratio[312] . Similarly, Saito et al. reported comparable findings regarding methanol synthesis from CO_2/H_2, attributing the high performance of $Cu/ZnO/ZrO_2/Al_2O_3/Ga_2O_3$ to an optimal Cu^+/Cu ratio of approximately 0.7[313]. Homs et al also observed the presence of Cu+ states in the gallium-promoted ZnO-supported catalyst [314] .

The Cu cations act as Lewis acid centers by accepting electrons, while OH groups serve for further hydrogenation steps. These groups help to strengthen CO_2 adsorption and effectively activate the inert molecules. In summary, the interplay between metallic and oxidized copper plays a crucial role in the formation of methanol and involves complex chemical mechanisms that rely on the properties of copper species, including their oxidation state and associated acid-base characteristics.

In Figure 6-8, we aim to investigate the impact of adsorbates on the Bader charges of the structure and try to see if we observe any oxidation of the Cu atoms due to the adsorbates. All Bader charges reported are referenced to the global minimum of the Zr_3O_6/Cu 111 system. Our analysis focuses on the Bader charges in the first layer of the Cu surface, where it interacts with the cluster, as well as the changes in Bader charges on the Zr atoms. Panels (a) and (b) depict the system with 2HCOO, while panels (c) and (d) represent the system with 3HCOO. The yellow arrow indicates the change in the number of hydrogen atoms in the structure, with its direction representing an increase in the number of hydrogen atoms. Conversely, the gray arrow represents the change in the number of oxygen atoms in the system.

In panels (a) and (c), we observe the Bader charge difference on the first layer of Cu, whereas panels (b) and (d) illustrate the Bader charge difference of the Zr atoms, both relative to the Zr_3O_6/Cu 111 system. Notably, the addition or removal of hydrogen atoms does not cause any change in the charges on Zr (as observed in panels (b) and (d)), but it does affect the charges on the Cu surface (as seen in panels (a) and (c)). In this case, Cu acts as an "electron reservoir" adjusting to any changes in the electronic state caused by the addition or removal of the Hydrogen atoms. On the other hand, alterations in the number of oxygen atoms impact both Zr and Cu charges. The changes in Zr charges are attributed to variations in the coordination caused by the addition or subtraction of O in the cluster which directly influences the electronic states of Zr. Conversely, the addition of hydrogen does not significantly alter the Zr cluster's coordination, as hydrogen interacts directly with oxygen to form hydroxyl groups, keeping the overall coordination of Zr constant before and after the addition of H. Like the case of O, formates do have an effect on the charges of both Zr and Cu as it again changes the coordinate states of Zr and also interact with Cu. In the most energetically favorable structures, which are the hydroxyls range of (2-6) and oxygen range of (2-4) we can clearly observe on Figure 8 the high oxidation of the Cu surface making it Cu^{+}.

Furthermore, we explored the interaction between the cluster and the Cu surface, particularly the changes that occur across the global minimum structures as the formate content increases. This involved subtracting the charges of the individual cluster and individual copper surface from the total charge density of the system to determine any changes in charges upon cluster adsorption on the surface. Figure 6-9 illustrates the resulting charge density difference, with the top panel displaying the isosurfaces and the bottom panel showing the corresponding structures. The red isosurface represents charge accumulation, while the green isosurface represents charge depletion. The global minimum structure was $Zr_3O_3OH_3$/Cu when no formates were present. Upon calculating the oxidation state of the individual Zr in $Zr_3O_3OH_3$, it was determined to be Zr^{3+}, while the Zr atom is typically in the Zr^{4+} state. The extra electron remaining on Zr accumulates between the cluster and the Cu support, hence creating a bond between the two partners. Copper

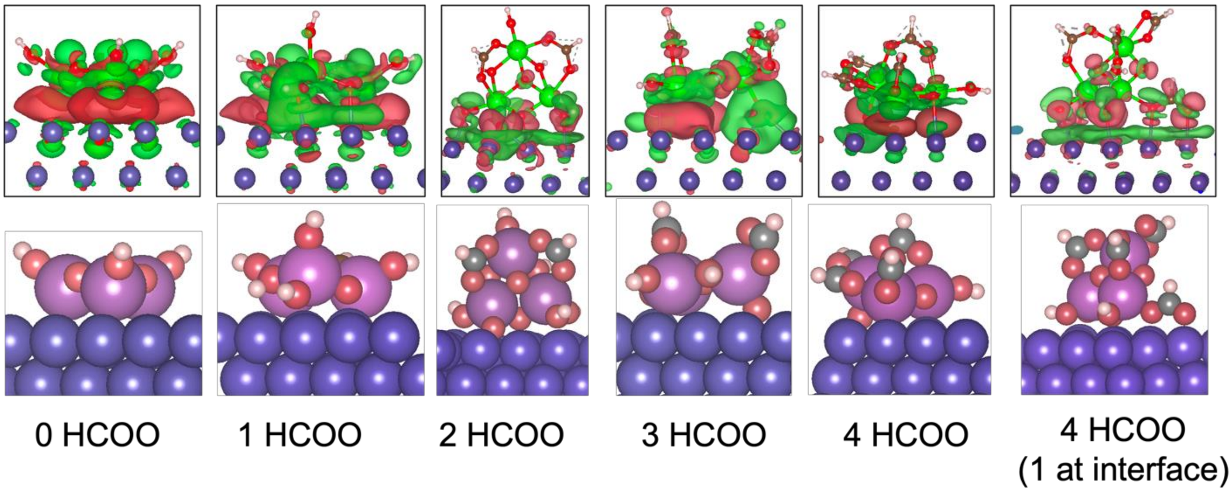

Figure 6-9 : Charge density difference iso-surface along with the side view of different structures. The green represents the negative iso-surface (Charge depletion) whereas the red represents the positive iso-surface (Charge accumulation).

also contributes to this charge accumulation and leads to the oxidation of copper atoms. The electrons from the copper and Zr clusters are located precisely at the interface between the Cu-Zr bonds (as seen in red for the 0HCOO case in Figure 9). As the formate concentration increases, the electron count modifies, with Zr being as Zr^{4+}, fewer electrons are available for the binding of the Zr atoms with Cu. The presence of formate also dramatically changes the concentration of other ligands on the cluster, such as -O and -OH. This increase in concentration with the increase in lack of electrons causes the Zr atoms to move further away from Cu, with the hydroxyls and oxygens anchoring the Zr atoms to the Cu surface. This results in a depletion of charges at the interface and the electronic concentration is centered around the oxygen and hydroxyl centers.

6.4 Conclusion

In conclusion, our investigation into the $Zr_3O_xOH_y(HCOO)_z$ /Cu111 system has highlighted the significant changes in the active site due to reaction conditions, such as pressure, temperature, conversion, and CO_2:H_2 feed ratio. The evolution of the active site under particular reaction conditions is crucial for understanding the mechanism of CO_2 hydrogenation.

We found that the free energy surface is relatively flat at the reaction condition with respect to the number of hydroxyls and formates, suggesting that these groups play a vital role in facilitating the CO_2 hydrogenation reaction. The cluster can act as a reservoir for hydrogen, as the free energy surface does not change significantly with the gain or loss of hydrogens.

Furthermore, we identified an ensemble of metastable structures with formates at the interface and including them in our future work to determine the reaction pathway would be essential. The results of this study have significant implications for the design of effective catalysts for CO_2 hydrogenation. By understanding the changes in the active site and the role of hydroxyls and formates, we can better engineer catalysts to promote this reaction. Our results show that care should be given when studying the catalyst in model conditions, such as low pressure, since different surface configurations occur under these circumstances.

Our investigation also revealed significant changes in the electronic state with the variation in oxygens, hydroxyls, and formates in the system. We observed partial oxidation of Cu as well as oxidation of Zr. Literature has shown that Cu^+ may be crucial in the CO_2 hydrogenation reaction. Our findings on the electronic state changes highlight the need to consider the impact of reaction conditions on the catalyst's electronic structure. This could guide the design of catalysts with optimal electronic properties, potentially leading to improved catalytic performance.

Chapter 7 Conclusion

Throughout this dissertation, we have undertaken a comprehensive exploration of catalytic reactions, employing a range of computational techniques and theoretical models to shed light on the structure, stability, and catalytic reactivity of diverse clusters and surfaces. By delving into the intricacies of hydrogen evolution reaction (HER), oxygen evolution reaction (OER), partial oxidation of methane to methanol, and CO2 hydrogenation, we have unraveled key insights into these catalytic systems. In this concluding chapter, we aim to synthesize the findings from each chapter, weaving them together to present a cohesive narrative that aligns with the themes and objectives outlined in the introduction.

We began our journey in Chapter 2, where our focus was on the Sn-doped Indium Oxide (ITO) surface. Through the application of first-principles DFT calculations, we investigated the optimal doping sites and structures. Our findings revealed that Sn atoms preferentially substitute In atoms within the surface layer. We identified two distinct locations for Sn: a 6-coordinated configuration, where Sn is saturated and non-reactive, and a 5-coordinated configuration, which appears bright in STM images and exhibits reactivity with Pt clusters. Additionally, we explored the reactivity of the ITO (111) surface with water at room temperature, shedding light on its limited hydroxyl coverage and molecular adsorption behavior. Furthermore, our investigations into the adsorption of Pt clusters on the In2O3, ITO (111), and 4-H2O-ITO(111) surfaces uncovered the marked reactivity and bond formation with Pt-In or Pt-Sn species.

Moving forward to Chapter 3, we ventured into the realm of HER and examined the behavior of small Pt clusters supported on ITO. Our investigations revealed a strong dependence of HER activity on the cluster size, with Pt1/ITO being inactive and a remarkable rise in activity per Pt mass observed from Pt4/ITO to Pt8/ITO. Furthermore, we discerned that these cluster catalysts deviate significantly from metallic Pt clusters and should be best described as Pt hydride compounds. The inclusion of metastable isomers in our microkinetic models underscored the importance of accounting for accessible isomer ensembles to simulate the properties of sub-nano supported cluster catalysts accurately.

Shifting our focus to the OER in Chapter 4, we embarked on a quest to unravel its intricate mechanism. By utilizing "optimal" active sites obtained via Grand Canonical Basin Hopping (GCBH) simulations, we unveiled a four-step process governing the OER, with the third step identified as the rate-determining step. Our computational approach not only allowed us to understand the reaction pathway but also shed light on the changes in the oxidation state of Pt-SA during the catalytic cycle. Furthermore, we emphasized the importance of discerning the active site composition and geometry under reaction conditions, as numerous adsorbates from the initial structure can profoundly impact the catalytic landscape.

In Chapter 5, our attention shifted towards the partial oxidation of methane to methanol, a process of significant interest in sustainable chemistry. Here, we demonstrated the efficacy of electrochemical methods for the deposition of thin-film transition metal (oxy)hydroxides as catalysts. Our investigations revealed the activity of CoOx, NiOx, MnOx, and CuOx in the partial oxidation of methane to methanol. CoOx surfaces showed the best catalytic capabilities and the selectivity for methanol production was found to be influenced by overpotentials, with medium overpotentials favoring methanol as the primary product. Unique hydrodynamic conditions provided by the gas-tight rotating cylinder electrode cell highlighted the significance of controlling both kinetics and mass transfer during the reaction, thus offering promising prospects for the efficient and decentralized production of methanol from methane under ambient conditions.

Lastly, in Chapter 6, we delved into the intriguing realm of CO_2 hydrogenation, a promising avenue for the conversion of carbon dioxide into valuable chemicals. By scrutinizing the $Zr_3O_xOH_y$ $(HCOO)_z$/Cu111 cluster under different reaction conditions, we discerned substantial changes occurring within the active site. Hydroxyls and HCOOs emerged as crucial players in facilitating the CO_2 hydrogenation reaction, with the cluster acting as a reservoir for hydrogen. Furthermore, we uncovered the pivotal role played by HCOOs at the interface in shaping the reaction mechanism. Identifying an ensemble of metastable structures containing HCOOs at the interface proved instrumental in determining the true active site for CO_2 hydrogenation.

In conclusion, our collective investigations into HER, OER, partial oxidation of methane to methanol, and CO_2 hydrogenation have provided invaluable insights into the structure, reactivity, and performance of catalysts in these systems. Our utilization of DFT calculations, Grand Canonical Basin Hopping simulations, microkinetic modeling, and electrochemical modeling has synergistically unraveled the intricate details governing these catalytic processes. The findings from each chapter intertwine to form a cohesive narrative, highlighting the significance of active site composition, reaction mechanisms, and the influence of reaction conditions on catalytic performance.

The overarching story that emerges from this thesis underscores the importance of understanding the fundamental principles governing catalysis and how this understanding can drive the design of more efficient catalysts. By utilizing computational approaches, we have elucidated the behavior of catalysts at the atomic and molecular levels, unveiling reaction pathways, and identifying key factors influencing catalytic performance. Our investigations have emphasized the pivotal role played by active site composition, surface structures, and electronic properties in determining catalytic reactivity.

Moreover, our research highlights the synergy between computational modeling and experimental characterization techniques. The insights gained from our theoretical investigations can be used to guide and interpret experimental studies, providing a deeper understanding of catalytic processes. This integrated approach, encompassing both theory and experiment, holds the key to the design of advanced catalysts with improved activity, selectivity, and stability.

In summary, this thesis contributes to the broader field of catalysis by advancing our understanding of critical catalytic reactions. The findings presented herein pave the way for the design of more efficient and sustainable catalytic systems, holding tremendous potential for addressing global challenges, such as energy conversion, carbon capture, and utilization. Through the collaboration of computational and experimental approaches, we are poised to unlock new frontiers in catalysis and drive the development of transformative technologies for a greener and more sustainable future.

Appendix A Supplementary Information for Chapter 2

A.1 Bulk Indium Oxide

Indium Oxide (In_2O_3) exists in three different phases characterized by space group symmetries $I2_13$, Ia3, and R3 referred to as In_2O_3-type I, In_2O_3-type II, and In_2O_3-type III, respectively. The bulk structural differences of these phases are as follows:

In_2O_3-type I: It crystallizes in a cubic bixbyite-type structure (space group No. 199) with 8 f.u.per unit cell, with those containing three types of In and two kinds of O atoms occupying 8a, 12b, 12b, 24c, and 24c Wyckoff positions, respectively.

In_2O_3-type II: It also crystallizes in cubic bixbyite-type structure with space group No. 206 and 8 f.u. per unit cell. This phase consists of two types of In and one kind of O atom.

In_2O_3-type III: It crystallizes in corundum structure with 2 f.u. per unit cell and space group No. 167. It consists of one type of In and one type of O.

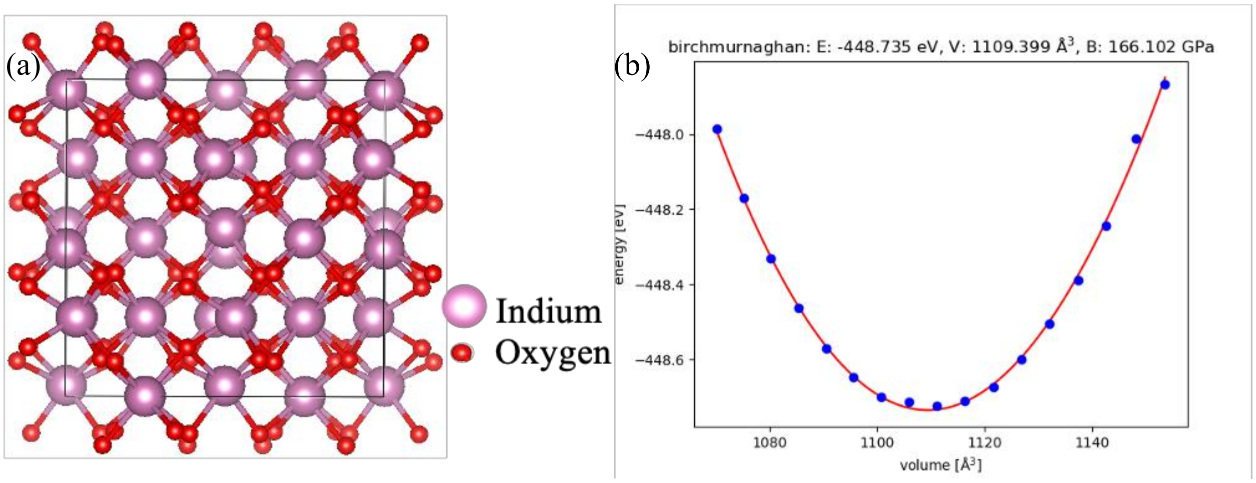

Figure A.1 (a) Bulk structure of In_2O_3-II where Pink and Red represent Indium and Oxygen atoms respectively. (b) Solving the Equation of State to find the optimum Lattice Constant for In_2O_3-II Bulk structure

Indium Oxide crystalizes in In_2O_3-type II structure under standard conditions, shown in **Error! Reference source not found.**(a). We optimized the bulk structure of Indium Oxide to find the optimum Lattice constants. We see in in **Error! Reference source not found.**((b) that by solving the equation of state, the lowest energy corresponds to the volume of 1109.399($Å^3$). This corresponds to a lattice constant of 10.35Å, which is very close to the experimental value of 10.12Å[1]. While considering different directions for slicing the bulk to make a slab, we need to keep in mind that polar surfaces cannot have bulk-like surface terminations. Utilizing the notation of Tasker for ionic surfaces[2], the (100) termination can be classified as a type III polar surface. In contrast, both the (110) and (111) surfaces have non-polar terminations. Walsh et al. [3] said that the 111 surface is the most thermodynamically favored termination of the In_2O_3 slab. Hence, we used our optimized and relaxed bulk structure to create the In_2O_3 111 structure.

● : In(6c) bonded with 3O(3c) and 3 O(4c)
● : In(6c) bonded with 3O(3c), 2O(4c)
● : In(5c) bonded with 3O(3c) and 1O(4c)
● : In(5c) bonded with 2O(3c) and 3O(4c)
● : In(5c) bonded with 2O(3c) and 2O(4c)
● : In(5c) bonded with 1O(3c) and 3O(4c)

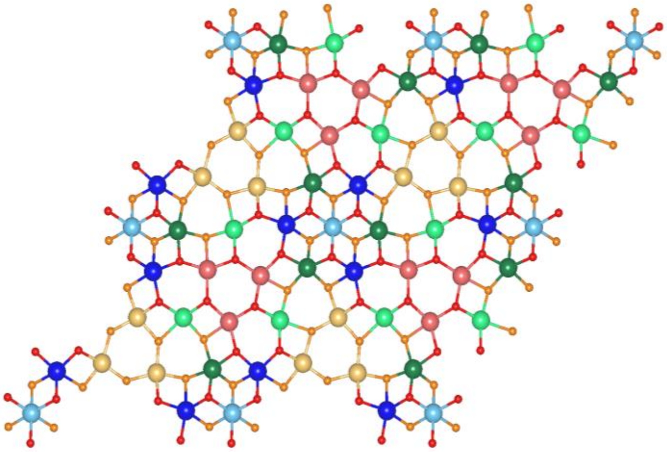

Figure A.2 The different site representation of In2O3 111 surface

A.2 Sn doping in In_2O_3 (111)

We conducted an extensive study to prepare the Tin doped In_2O_3 111 slab by finding the best Sn doping positions. We first started with doping 1 Sn atom at various In locations, and then we moved onto higher doping concentrations up to 5% (8 atoms of Sn in 160 atoms of the unit cell).

1.25% doping: For studying the doping of 1 Sn onto the In_2O_3 111 slab, we considered the different In sites on the 2-Layer slab. In total, there are six non-equivalent In atoms, and the doping energies for all the sites are given in **Error! Reference source not found.**. The colors on the bar chart represent the color-coding of the In atom where the Sn is doped. We can see that the best site is the light blue site which is the In(6c) site, followed by the red, blue, and green sites. The light blue site has an adsorption energy of -1.11eV wrt to SnO_2 bulk, followed by -1.02eV for the red site. The dark blue and dark green sites are very close contenders of doping after the red site with doping energies of-0.94eV and -0.93eV, respectively.

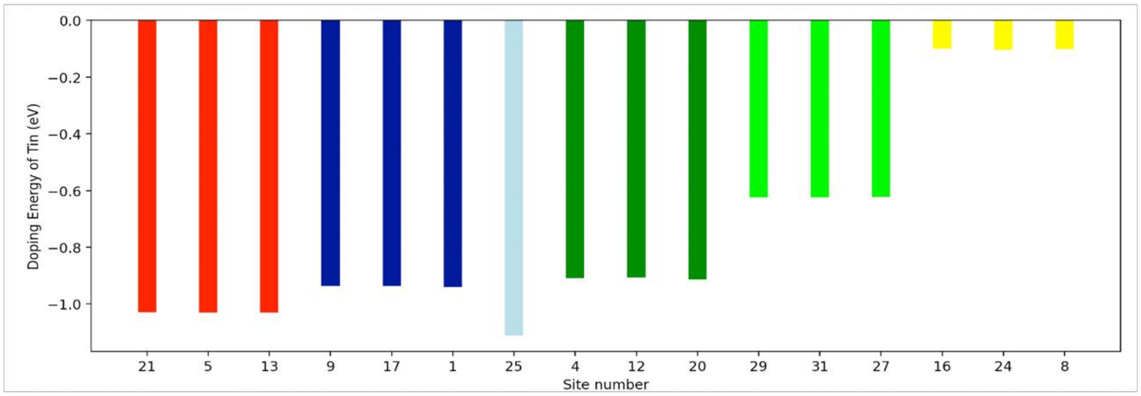

Figure A.3 Doping energy of 1 Sn doping on to the different In sites (represented by the color).

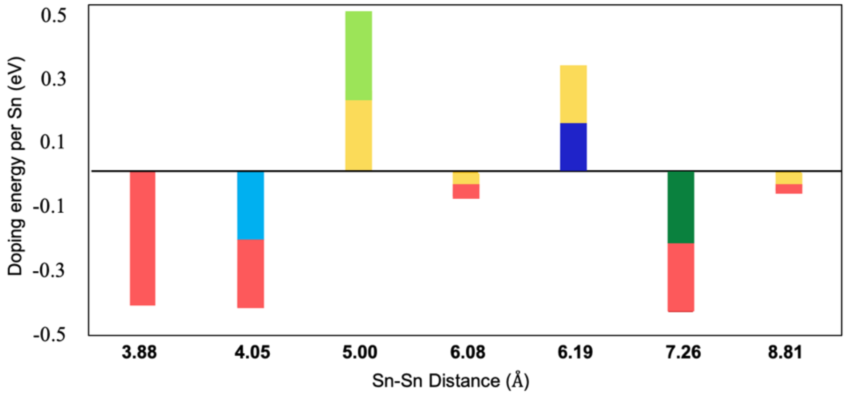

Figure A.4 Doping energy wrt to different doping sites and the Sn-Sn distance in 2.5% Sn dopant.

2.5% doping: After doing an extensive study on the dependence of doping energy on the different sites, we studied the doping energies when 2 Sn atoms are doped into In_2O_3 111 slab. One factor that can contribute to the doping energy, in this case, is the distance between the two Sn atoms. Hence, we varied both the doping sites and the distance between the Sn atoms. **Error! Reference source not found.** gives a complete analysis of doping energy dependence on the sites and the Sn-Sn distance. The range of Sn-Sn distance goes from 3.88Å to 8.8Å, and the different color mixtures on the bar chart represent the different color-coded In sites that are doped with Sn. We can observe no dependence on the doping energy on the Sn-Sn distance but only on the doping sites. The two Sn atoms prefer to stay in any combination of the blue, green, or red sites, which also correspond to the preferred site for 1 Sn doping.

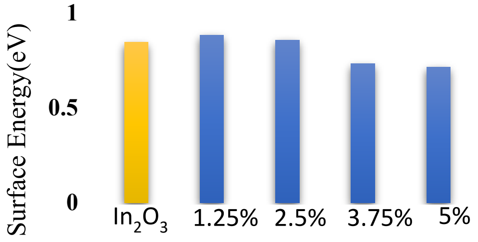

Figure A.5 Surface energies of In_2O_3 111 slab and different doping levels of ITO wrt their bulk energies.

5% doping: As we move to the higher doping levels, we observed that the surface energy decreases; hence the

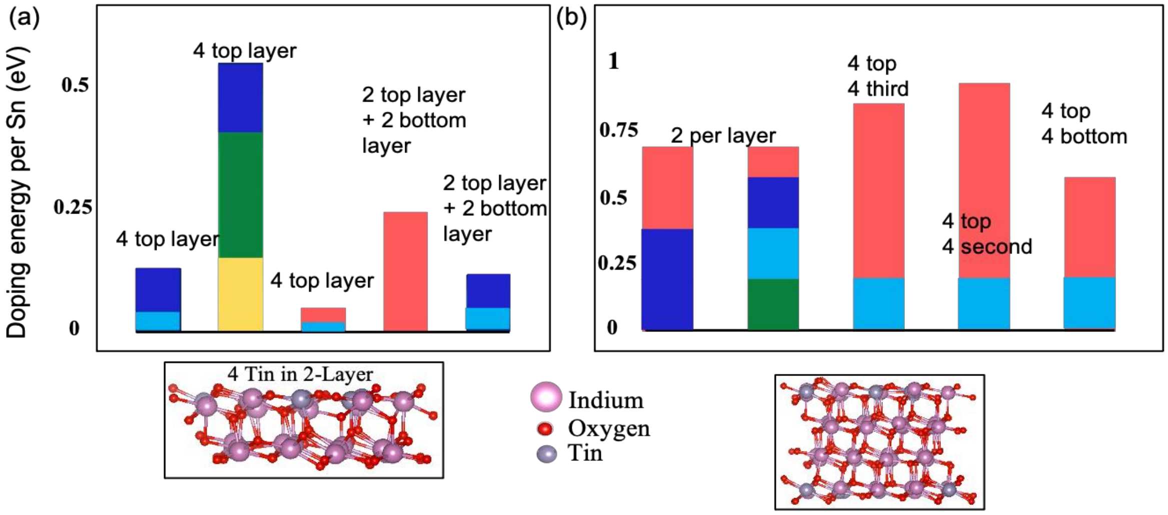

Figure A.6 Doping Energies at different sites represented by the different colors for 5% doping in (a) 2-Layer ITO (b) 4 Layer substitution of In by Sn stabilizes the surface wrt their bulk configuration (**Error! Reference source not found.**). In the case of 5% doping, we found that all Sn atoms prefer to locate in the surface layer.

In Fig - 6, we observe that in a 2-layer slab, the 4 Sn atoms tend to stay on the first layer on the red and blue sites (**Error! Reference source not found.** (a)). We extrapolated our findings to the 4-Layer structure (**Error! Reference source not found.** (b)). We replaced 8 In atoms with 8 Sn atoms, and we studied where Sn atoms would prefer to stay with respect to the layers. We found that the 8 Sn atoms would distribute equally in the first and the last layer. There would be no Sn in the middle layers. The doping site in the 4-Layer structure stays the same as the 2-Layer, which is the 1-light blue and 3 red sites in the first layer and the last layer.

Density of states: **Error! Reference source not found.** shows the density of states projected on surface metal atoms for $In_2O_3(111)$ (a) and ITO (111) (b). For ITO(111), the most significant contribution to the DOS is seen on the surface 5 coordinated Sn (red sites), in a large energy interval around the Fermi Level, therefore explain the bright nature of these Sn atoms in the STM

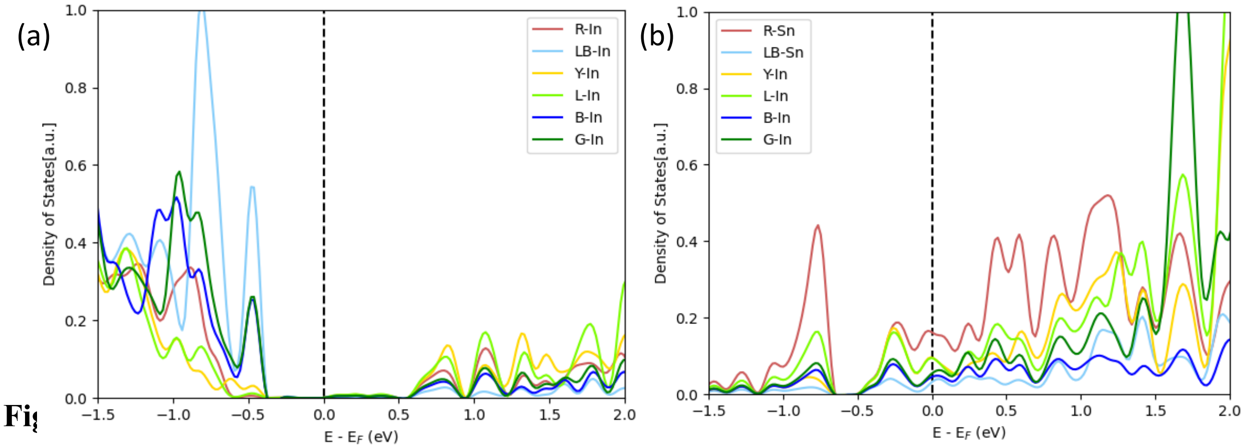

Fi

in the figures are - R: Red; LB: Light Blue; Y : Yellow; L: Lime; B: Blue; G: Green ; In : Indium ; Sn : Tin image, while 6 coordinated Sn (light blue) and In (dark blue) show a low projected DOS around the Fermi level, and form a dark triangle in the STM image.

A.3 H_2O adsorption on ITO (111)

To define the different configurations of water molecules in the (1x1) unit cell on the ITO(111 slab), we have used different notations for the oxygen atoms and different colors for the metal atoms. These are represented in **Error! Reference source not found.** (a).

Molecular adsorption: Generally, water molecules coordinate via their O-atoms to the metal atom on the oxide surfaces. After a complete analysis, we found that the H_2O would adsorb by their O_w to the low coordinated metal atoms (In or Sn). After relaxation, the water molecule adsorbs relatively flat on the surface and both H's point towards the O(3c) atoms neighboring the In(5c).

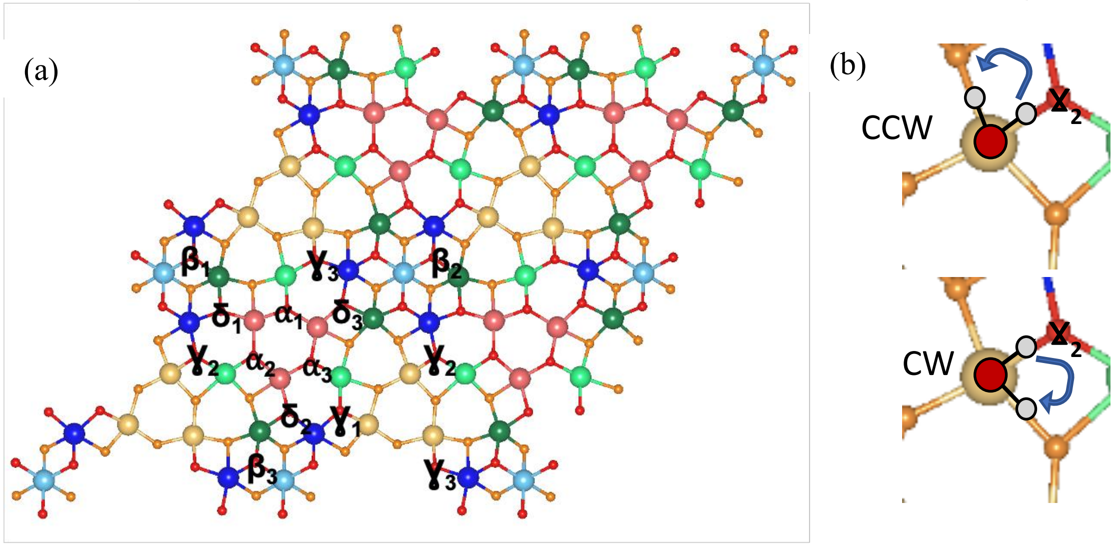

Figure A.8 (a) The different Oxygen sites marked as different Greek letters on the ITO surface. The metal atoms are marked with different colors, red and light blue balls are Tin atoms whereas lime, yellow, blue, and green are Indium atoms. (b) The clockwise and counterclockwise notation for H2O adsorption.

All the adsorption energies at different sites and different orientations are given in **Error! Reference source not found.**. Each site is defined by the type (color) of the surface Sn or In on which the O atom of water is bound and by the O atoms' labels (alpha, delta, etc.) towards which the H atoms are pointing. When there is no O(3c) neighboring the water adsorption, the H's direction can be defined using clockwise (CW) or counterclockwise (CCW) from the ɣ - O(3c) atom (**Error! Reference source not found.** (b)).

Sites	Binding energy (eV)
Red towards α, δ	-0.50
Red towards α, α	-0.46
Yellow CW	-0.53
Yellow CCW	-0.58
Light Green towards ɣ, α	-0.55
Dark Green towards β, δ	-0.63

Table A.1 Adsorption energy of water molecules on the different top sites defined by the color of the surface metal site on which water O is bound and type of O atom (defined by greek symbols) toward which the H atoms are pointing.

Dissociative adsorption: Dissociation of water and formation of O_wH and O_sH groups (O_w : oxygen atom from water, O_s : oxygen atom from the surface) has been considered on all possible sites on the ITO surface (top sites on the In and Sn, bridge sites between the two metals, and hollow sites). The proton from the water, H_w, can adsorb to any of the O(3c) present on the slab, but we observe that the proton prefers to occupy the O(3c) that is shared with the metal that adsorbs O_wH. The adsorption energies of all the sites are given in **Error! Reference source not found.**.

Site-OH	Sites (OH+H)	Binding energy (eV)
TOP	Red + α	-0.27
	Red + δ	-0.54
	Yellow + ɣ	-0.41
	Light Green + α	-0.32
	Light Green + ɣ	-0.29
	Dark Green + δ	-0.36
	Dark Green + β	-0.68
Bridge	Dark Green - Light Green + δ	-0.49
	Dark Green - Light Green + γ_1	-0.19
	Dark Green - Light Green + β_3	-0.89
	Yellow - Dark Green + β	-0.80
	Dark Green - Light Green + α_2	-0.71
	Dark Green - Light Green + α_3	-0.28
	Dark Green - Light Green + δ_2	-0.58
	Dark Green - Light Green + β_1	-0.82
	Dark Green - Light Green + γ_2	-0.63
	Dark Green - Light Green + γ_3	-0.32
Hollow	Yellow + ɣ	-0.16
	Yellow + δ	-0.29
	Yellow + α	0.10
	Yellow + β	-0.56

Table A.2 Adsorption energy of Hydroxyls on different sites given by the color of the surface metal and adsorption of H on different Oxygens specified by the greek letters. For $1H_2O$ dissociation, we have done our studies on 2-Layer ITO to save computational time.

As we move further towards increasing the water adsorption, we increase the water molecules one by one until $4H_2O$. The adsorption energies of the different adsorption modes are given in the **Error! Reference source not found.**.

$2H_2O$	BE/H_2O
2 molecular	-0.63
1 dissociative + 1 molecular	-0.71
2 dissociative	-0.73
$3H_2O$	BE/H_2O
3 molecular	-0.76
1 dissociative + 2 molecular	-0.84
2 dissociative + 1 molecular	-0.90
3 dissociative	-0.80
$4H_2O$	BE/H_2O
1 dissociative + 3 molecular	-0.71
2 dissociative + 2 molecular	-0.88
3 dissociative + 1 molecular	-0.63
4 dissociative	-0.83

Table A.3 Adsorption energy of water in different configurations on the ITO surface

A.4 Pt-SA adsorption on In_2O_3(111) and ITO (111)

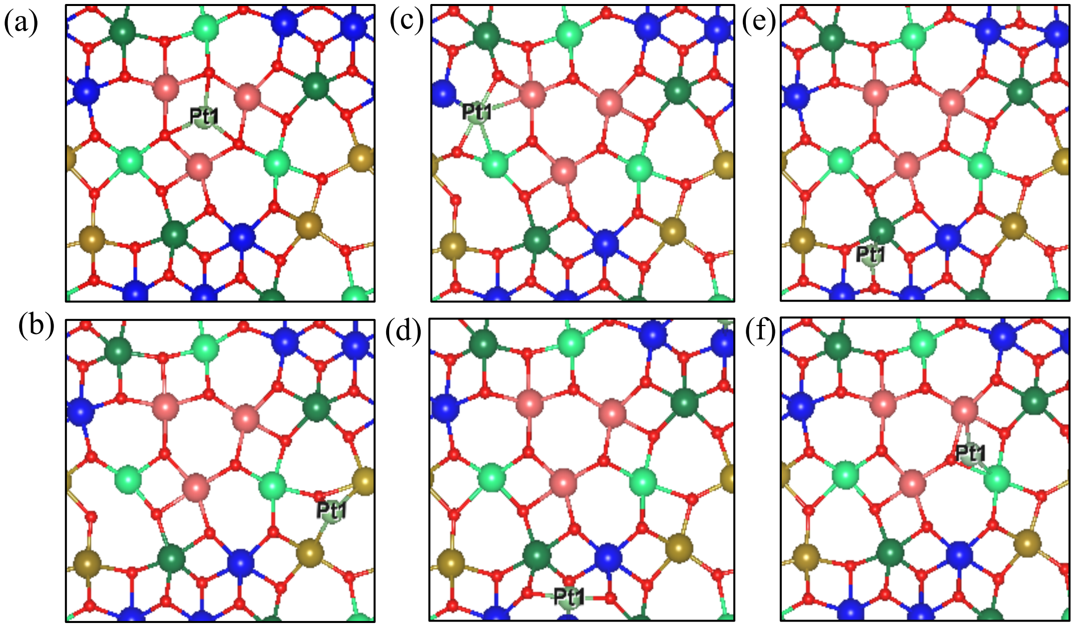

Figure A.9 Different sites of Pt-Single Atom adsorption on the In_2O_3 111 surface. The different colored atoms represent the non-equivalent In atoms. The Platinum atom is marked.

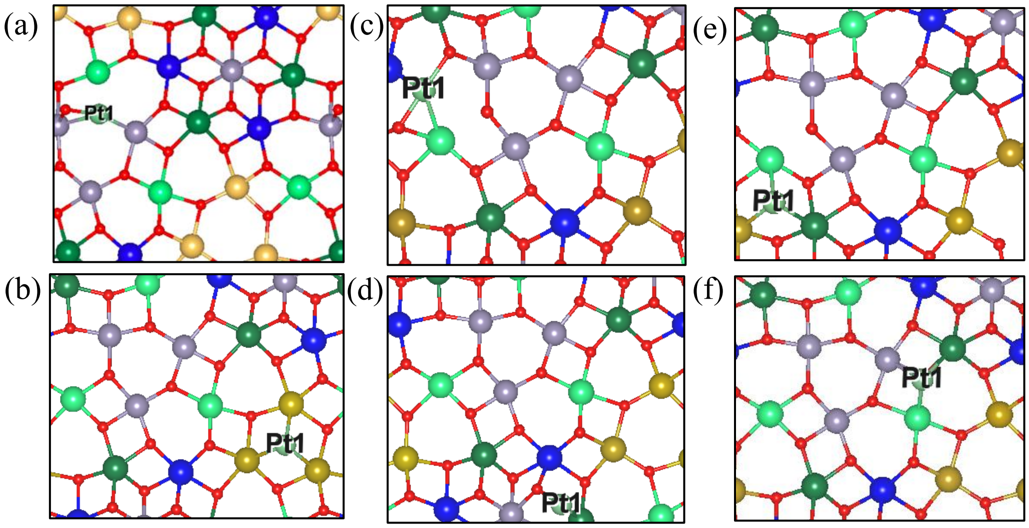

Figure A.10 Different sites of Pt-Single Atom adsorption on the ITO 111 surface. The different colored atoms represent the non-equivalent In atoms and the grey atom represent the Tin. The Platinum atom is marked.

A.5 Pt substituting the Sn atom in the ITO (111) slab

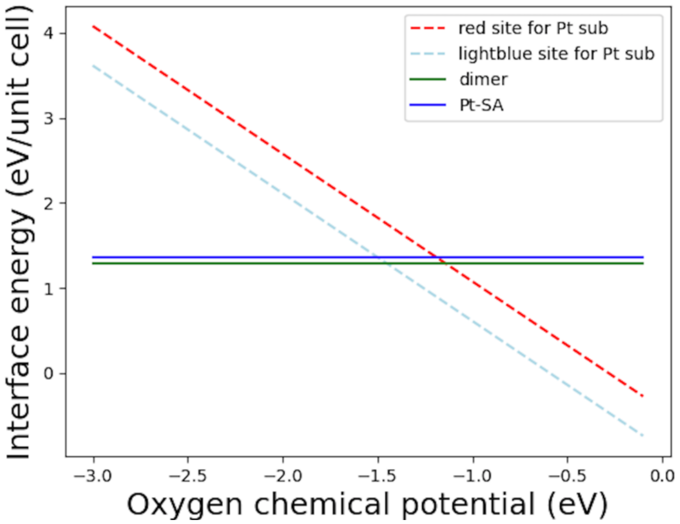

Figure A.11 Interface energy dependence on the O_2 chemical potential when the Sn is substituted with a Pt atom in the ITO 111 support.

We have also studied if the Pt-SA would substitute any Sn atoms in an oxygen environment. For this, we have considered the reaction between the ITO 111 slab, In_2O_3 bulk, and Pt-bulk in an oxygen environment which leads to the formation of $PtSn_7In_{56}O_{96}$ and ITO bulk. We can observe from Fig. A.11 that the Pt-SA adsorption on the ITO surface is preferred until an oxygen chemical potential of -1.48eV, after which Pt would substitute the Sn atom present on the light blue site to bind directly with the surface.

$$\mu(\text{ system }) = E(PtSn_7In_{56}O_{96}) + \frac{1}{4}E(\mathrm{In}_{28}Sn_4O_{48}bulk) - \frac{1}{4}E(Pt_4Bulk) - E(Sn_8In_{56}O_{96}) - \frac{7}{32}E(\mathrm{In}_{32}O_{48}bulk) - \frac{3}{4}\mu(O_2)$$

$$\text{and } \mu(O_2) = E(O_2) + 2\Delta\mu(O)$$

A.6 Density of States

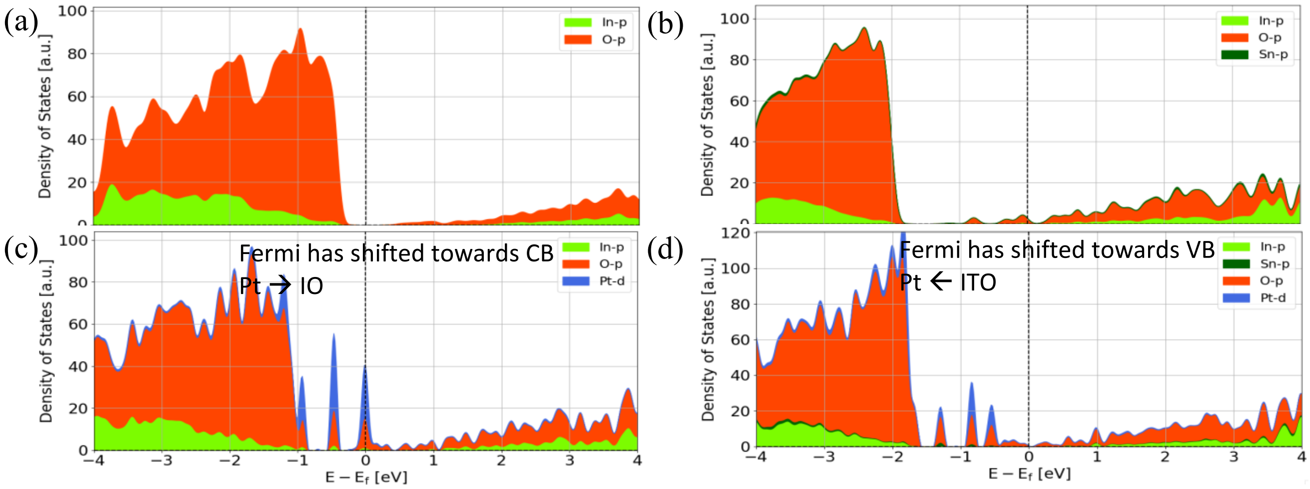

Figure A.12 A comparison of the DOS projected on O p orbitals, In or Sn p orbitals and Pt d orbitals between (a) In2O3 (111) (b) ITO (111) (c) Pt-SA on In2O3 (111) and (d) Pt-SA on ITO (111).

A.7 Pt-dimer/trimer adsorption on In_2O_3(111) and ITO(111)

We found a total of ~350 structures for each of the Pt clusters on different supports. The five or four lowest energy structures for each cluster size and support are given below, along with their relative energies.

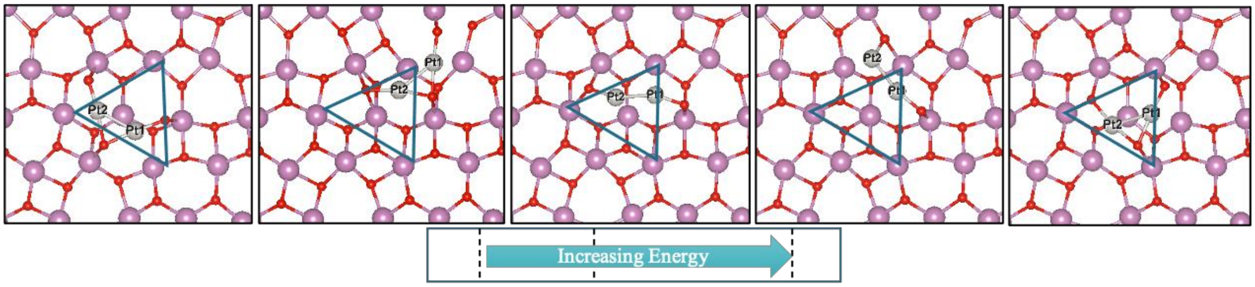

Figure A.13 The 5 best Pt dimer structures on In_2O_3(111) surface obtained using Basin Hopping. The relative energies of the structures are given below. The first structure on the left is the energetically most favorable.

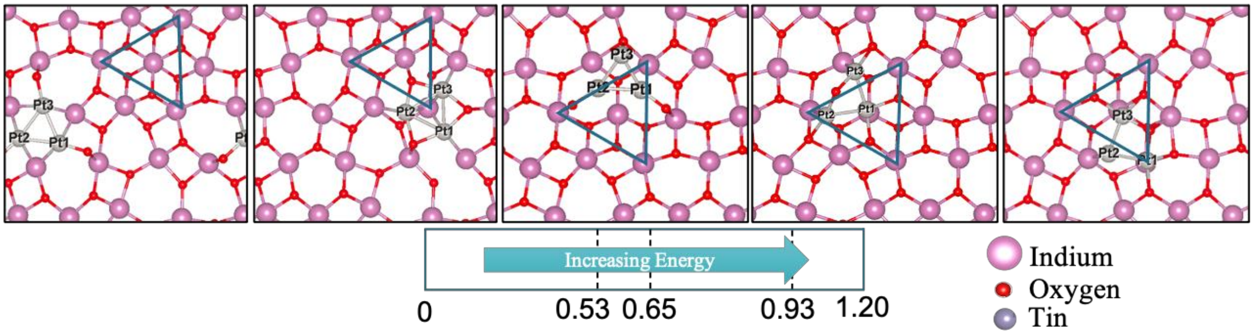

Figure A.14 The 5 best Pt trimer structures on In_2O_3 (111) surface obtained using Basin Hopping. The relative energies of the structures are given below. The first structure on the left is the energetically most favorable.

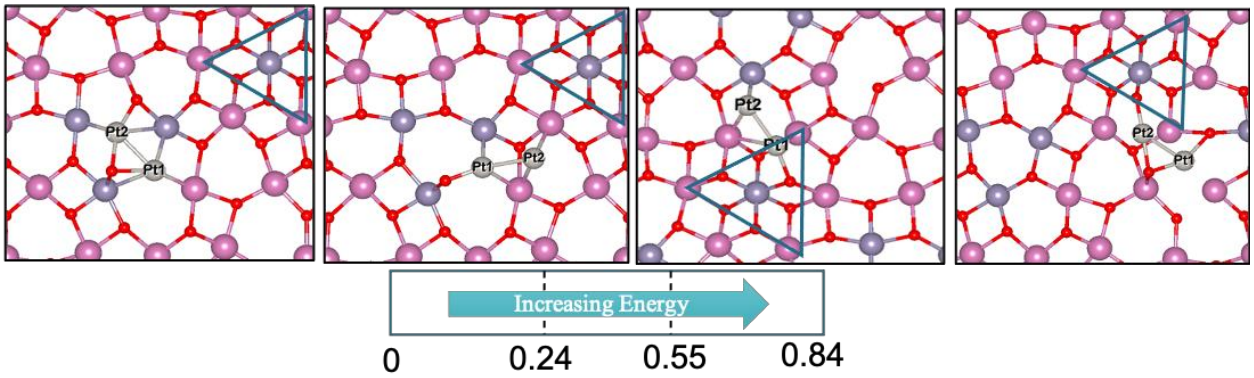

Figure A.15 The 4 best Pt dimer structures on ITO (111) surface obtained using Basin Hopping. The relative energies of the structures are given below. The first structure on the left is the energetically most favorable.

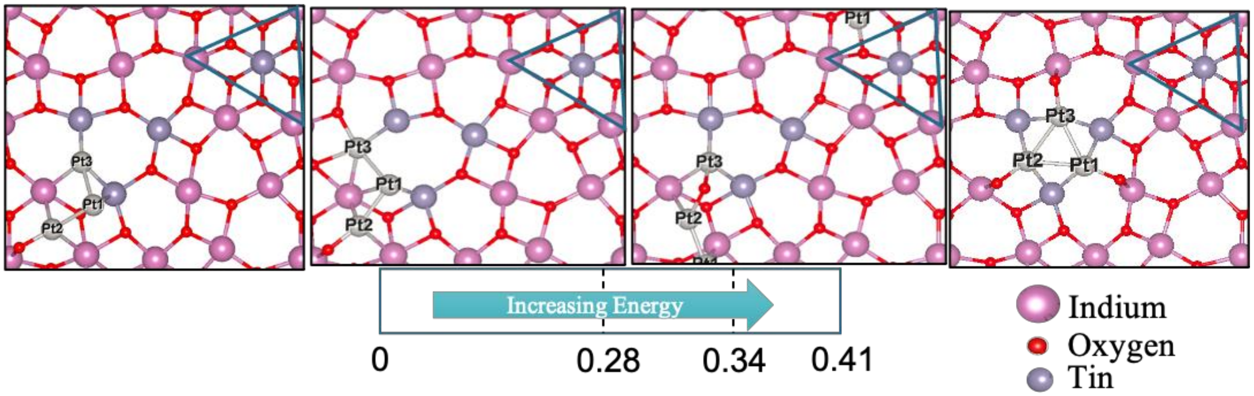

Figure A.16 The 4 best Pt trimer structures on ITO (111) surface obtained using Basin Hopping. The relative energies of the structures are given below. The first structure on the left is the energetically most favorable.

A.8 Pt$_n$(n:1,2,3) adsorption on hydroxylated ITO (111)

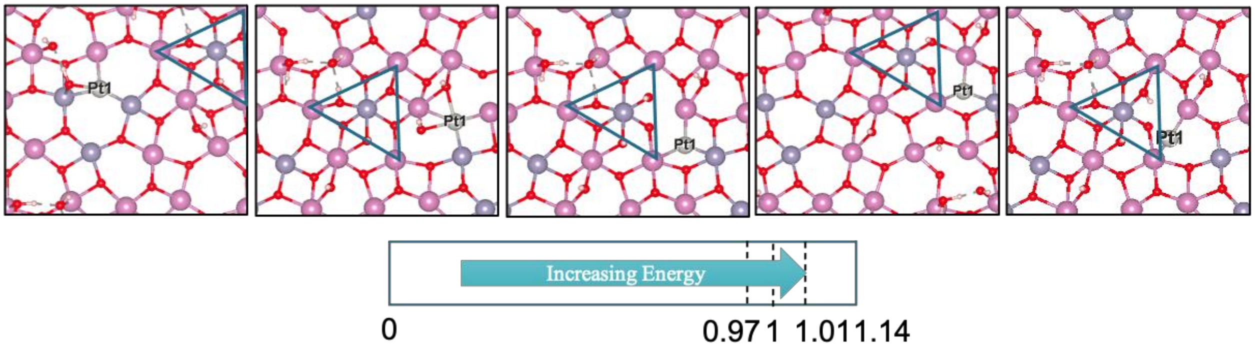

Figure A.17 The 5 best Pt-SA structures on Hydroxylated ITO (111) surface obtained using Basin Hopping. The relative energies of the structures are given below. The first structure on the left is the energetically most favorable.

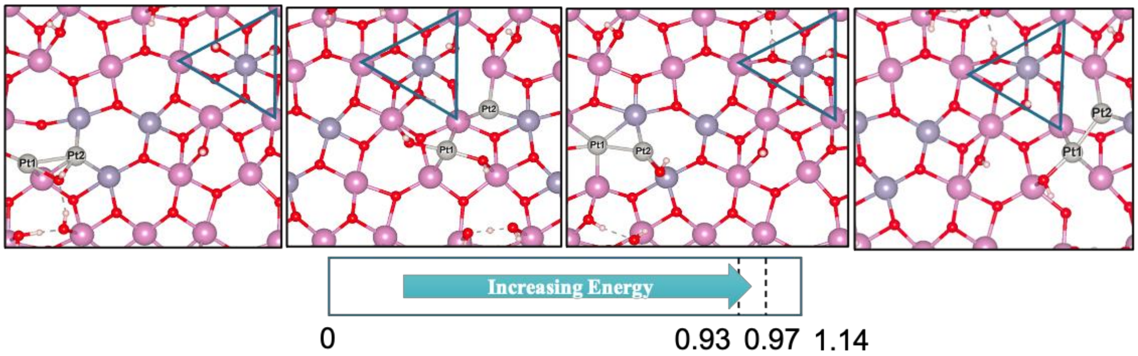

Figure A.18 The 4 best Pt dimer structures on Hydroxylated ITO (111) surface obtained using Basin Hopping. The relative energies of the structures are given below. The first structure on the left is the energetically most favorable.

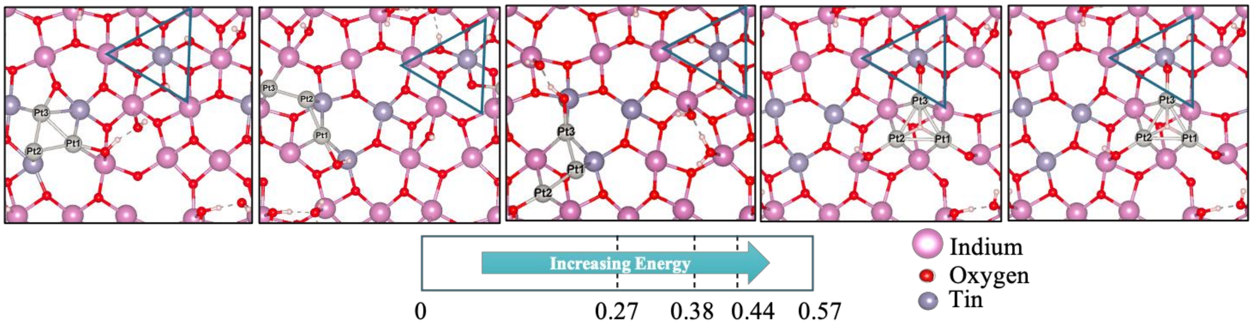

Figure A.19 The 5 best Pt trimer structures on Hydroxylated ITO (111) surface obtained using Basin Hopping. The relative energies of the structures are given below. The first structure on the left is the energetically most favorable.

A.9 Basin Hopping Algorithm

Basin Hopping (BH) Global Optimization is a sampling method used for finding meta-stable and stable chemical structures. This BH algorithm, when used alongside the Monte Carlo method of displacement, can efficiently sample a large potential energy surface to find local and global minimums. The basic algorithm is represented in the flowchart displayed in Fig. A.20. We start with a random initial configuration of the system (cluster + support) and minimize its energy and forces. After this, we displace the cluster on the support in a random direction to generate a new site for the cluster adsorption on the support and randomly move the atoms in the cluster, essentially changing the cluster's shape on the support. This new structure is relaxed and compared against the old structure using the Metropolis algorithm to accept or reject the structure. The Metropolis algorithm is explained in the flowchart represented in Fig. A.21(a).

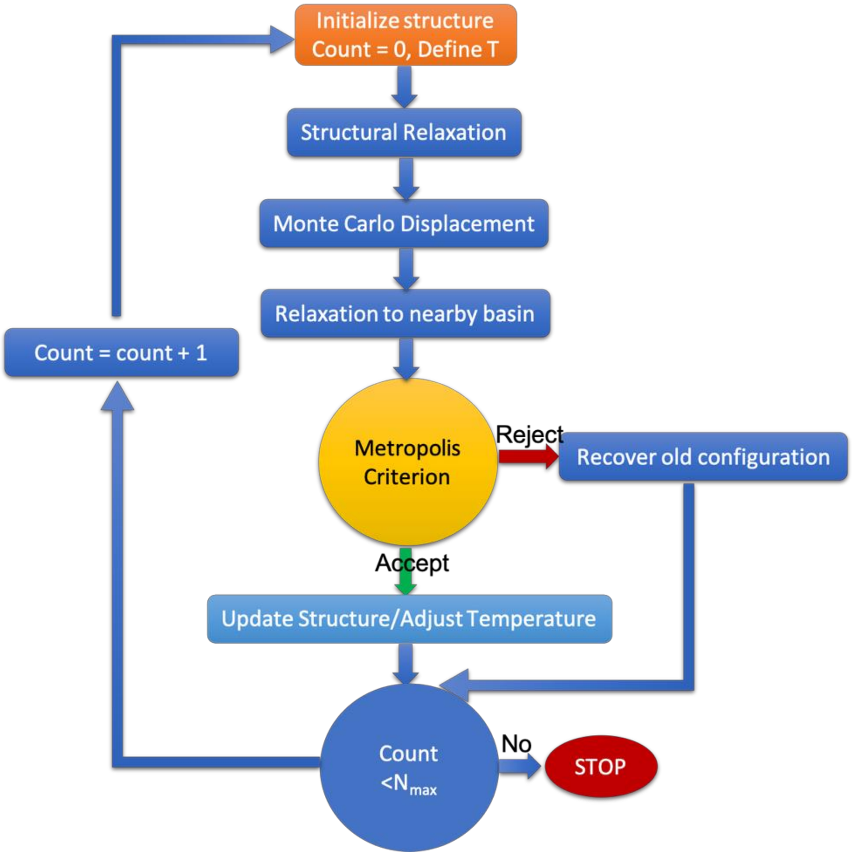

Figure A.20 Basin Hopping Algorithm

In the metropolis algorithm, the new structure is always accepted if its free energy is lower than the free energy of the old structure. But in case the energy is higher, then the structure is only accepted if the probability exp $[(G_{old} - G_{new}/k_BT]$ is higher than the number drawn randomly from [0,1]. The free energy is calculated by subtracting the reference chemical potential (which is a function of temperature and pressure) of individual species from the energy derived by density functional theory. Once the structure is accepted, the temperature of the BH run is adjusted accordingly (this is the same temperature used to calculate the probability). The algorithm to adjust temperature is given in Fig. A.21(b). Based on the acceptance and rejection of the structures while running the BH simulation, the temperature increases if the acceptance ratio is too low and decreases if the acceptance ratio is too high.

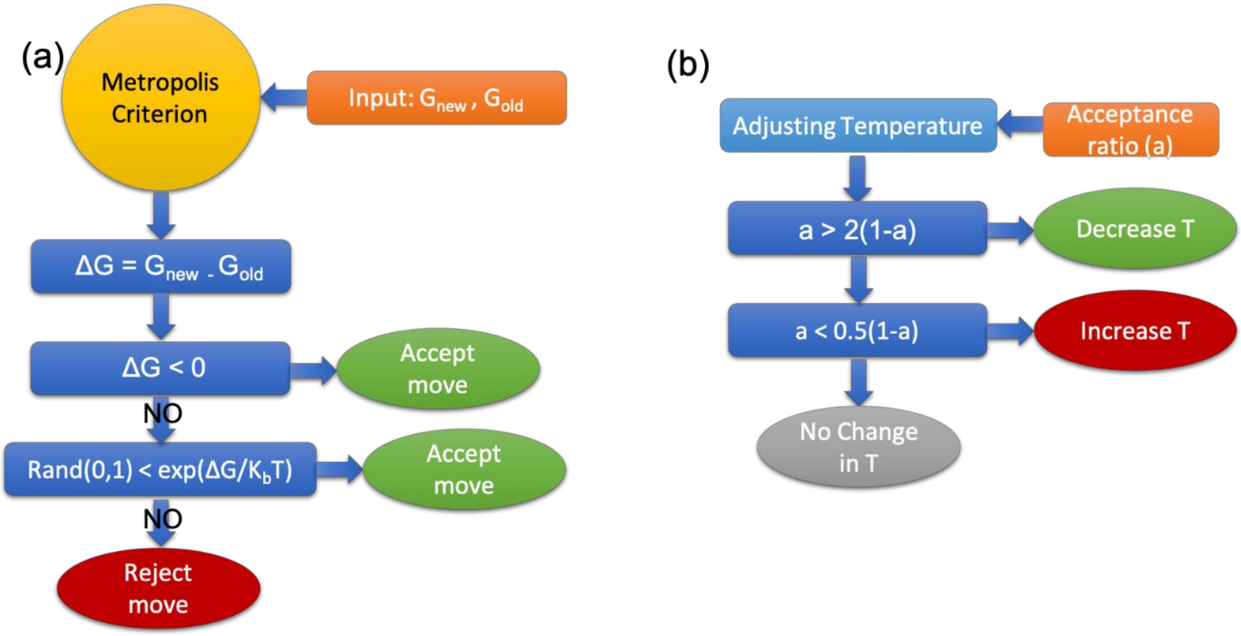

Figure A.21 (a) Metropolis Algorithm (b) Adjusting Temperature in Basin Hopping.

If none of the above criteria comes true, then the algorithm moves on with the old structure. The algorithm continues until the step count is smaller than a prespecified value N_{max}. Once N_{max} has reached, the algorithm stops.

A.10 Pt Cluster structure exploration

We used the Basin Hopping global optimization method to explore possible adsorption sites for the Pt-SA on the hydroxylated ITO surface and bigger Pt-cluster adsorption adsorption on

In_2O_3(111), ITO, and Hydroxylated ITO. Detailed theoretical background on the algorithm is provided in chapter-2, sec-2.8. The GCBH explorations are carried out by an in-house code written by Dr. Geng Sun, which is developed based on Atomic Simulation Environment (ASE) package. GCBH explores the configuration and composition space simultaneously to minimize targeted function, which is the free energy or the formation energy of the system. The moves followed in GCBH to generate new structures change depending on the system.

Moves on the non-hydroxylated surfaces:

Minimizing Function:

(3.1) $\mathrm{G(Pt}_n\mathrm{(n{:}\,2{,}3)@In_2O_3111,ITO))} = \mathrm{E(Pt}_n\mathrm{(n{:}\,2{,}3)@In_2O_3111,ITO)}\Big) + \sum_{j=1}^{M_{\text{species}}} \mu_j N_j$

Moves:

1 Randomly find a (X, Y) on the surface.

2 Put the Pt cluster on the (X, Y) point.

3 Randomize the Pt cluster.

Moves on hydroxylated surfaces: Minimizing Function:

$$\mathrm{G(Pt}_n\mathrm{(n{:}\,1{,}2{,}3)@4H_2O + ITO))} = \mathrm{E(Pt}_n\mathrm{(n{:}\,1{,}2{,}3)@4H_2O + ITO)}\Big) + \sum_{j=1}^{M_{\text{species}}} \mu_j N_j$$

Moves:

1 Randomly find a (X, Y) on the surface.

2 Put the Pt cluster on the (X, Y) point.

3 Randomize the Pt cluster.

4 Choose one of the following ways to put the hydroxyls/water/H. They can randomly choose any position on the surface/cluster.

a) $-\mathrm{OH}/\mathrm{H_2O}/-\mathrm{H}$ on surface and nothing on cluster.

b) $-\mathrm{OH}/-\mathrm{H_2O}$ on surface and $-\mathrm{H}$ on cluster .

c) $-\mathrm{H_2O}/-\mathrm{H}$ on surface and $-\mathrm{OH}$ on cluster.

Moves on hydroxylated surface under $\mathrm{H_2}$ pressure:

In this particular case when the system is under a Hydrogen pressure the number of $\mathrm{H_2}$ in the system can change which is also chosen randomly on the fly. Minimizing Function:

$$\begin{aligned}
&\mathrm{G}(\mathrm{Pt}_n(\mathrm{n{:}\,7{,}8})@4\mathrm{H_2O} + \mathrm{ITO} + \mathrm{pH_2}) \\
&\qquad = \mathrm{E}(\mathrm{Pt}_n(\mathrm{n{:}\,7{,}8})@4\mathrm{H_2O} + \mathrm{ITO} + \mathrm{pH_2}) - \mathrm{G}(4\mathrm{H_2O} + \mathrm{ITO}) - \frac{p}{2}\mathrm{G}(\mathrm{H_2}) \\
&\qquad - \sum_{j=1}^{M_{\mathrm{species}}} \mu_j N_j
\end{aligned}$$

where $\mathrm{G}(\mathrm{H_2}) = \mathrm{E}(\mathrm{H_2}) + \mathrm{ZPE}(\mathrm{H_2}) + \mathrm{TS}(\mathrm{H_2})$ and $\mu_H = -\mathrm{eU}_{SHE} - 2.3\mathrm{kTpH}$ and $\mathrm{U}_{SHE} = -0.016\mathrm{eV}$; $\mathrm{pH} = 1$

Moves:

1 Randomly find a (X, Y) on the surface.

2 Put the Pt cluster on the (X, Y) point.

3 Randomize the Pt cluster.

4 Choose one of the following ways to put the hydroxyls/water/H. They can randomly choose any position on the surface/cluster.

a) $-\mathrm{OH}/-\mathrm{H_2O}/-\mathrm{H}$ on surface and nothing on cluster.

b) $-\mathrm{OH}/\mathrm{H_2O}$ on surface and $-\mathrm{H}$ on cluster .

c) $-\mathrm{H_2O}/-\mathrm{H}$ on surface and $-\mathrm{OH}$ on cluster.

5 Randomly distribute the $\mathrm{pH_2}$ on the cluster.

Appendix B Supplementary Information for Chapter 3

B.1 Modeling Hydrogen Evolution Reaction in electrochemical acidic condition:

The HER occurs in stepwise reactions:

1. Volmer or discharge step: aqueous protons are electrochemically reduced to atomic hydrogen and adsorbed on the metal surface

2. Tafel or combination step: molecular hydrogen is formed combination of two adsorbed H atoms.

3. Heyrovsky (ion + atom) step: reaction of an aqueous proton with an adsorbed H atoms to produce H_2.

Steps	Under acidic conditions	Under alkaline conditions
Volmer step	$H^+_{(aq)} + e^- \rightarrow H_{ad}$	$H_2O + e^- \rightarrow H_{ad} + OH^-$
Tafel step	$H_{ad} + H_{ad} \rightarrow H_{2,\,ad}$	$H_{ad} + H_{ad} \rightarrow H_{2,\,ad}$
Heyrovsky step	$H^+_{(aq)} + H_{ad} + e^- \rightarrow H_{2,\,ad}$	$H_2O + H_{ad} + e^- \rightarrow H_{2,ad} + OH^-$

The Volmer-Tafel catalytic cycle thus consists of H_{ads} formation by the Volmer step (twice), followed by H_2 formation via the Tafel step. The Volmer-Heyrovsky cycle consists of a Volmer step, followed by H_2 formation via the Heyrovsky mechanism. We focus on acidic condition reactions and will be considering the Tafel and Heyrovsky reactions as possible rate-determining step. To model the kinetics of hydrogen evolution reaction, we have used the Butler-Volmer type formalism[315].

(a) The first step is to calculate each surface state's grand canonical free energy with varying Hydrogen coverage. This could be described as follows:

$$\Omega = A(*\,n\mathrm{H}, \mathrm{U}) - n\mu_{\mathrm{H}^+}(\mathrm{U}, p\mathrm{H}) - n\mu_{\mathrm{e}^-}(\mathrm{U}, p\mathrm{H})$$

Here, $A(*\,n\mathrm{H}, \mathrm{U})$ is the potential dependent free energy of the surface state 'A, 'with a hydrogen coverage of n. $\mu_{\mathrm{H}^+}(\mathrm{U}, p\mathrm{H})$ and $\mu_{\mathrm{e}^-}(\mathrm{U}, p\mathrm{H})$ are the electrochemical potentials of protons and electrons, respectively. This formulation of the chemical potential of the proton and the electrons comes directly from the Computational Hydrogen electrode model described in the below:

Computational Hydrogen electrode (CHE):

Under the CHE scheme, the chemical potential of an electron−proton pair can be approximated in reference to the free energy of half a dihydrogen molecule, and it also allows the effect of the applied potential and pH to be easily included in the model.

$$\mu_{\mathrm{H}^+}(\mathrm{U}, p\mathrm{H}) + \mu_{\mathrm{e}^-}(\mathrm{U}, p\mathrm{H}) = \frac{1}{2}\mu(\mathrm{H}_2) - eU + k_{\mathrm{B}}T\mathrm{pH}$$

Surface Charging (SC) method:

Under the CHE approach, the electrochemical potential is assumed to affect only the chemical potential of the exchanged electrons. Thus, electronic energy is independent with respect to the potential and is taken from neutral systems. However, the free energy for the sites and the intermediates in the "neutral" situation is not the same as the U = 0.0 V situation. To evaluate the potential dependent free energy ($A(*\,n\mathrm{H}, \mathrm{U})$) of each state in the potential range of -0.3 – 0V vs SHE we have used the surface charging approach.

(b) One crucial assumption in this kinetic formulation is that at finite temperature, the aqueous solution can act as a proton reservoir; hence, protons can diffuse through the water−hydronium network without any kinetic barrier. With this assumption, the surface states with varying hydrogen coverage can interconvert without any kinetic barrier and reach equilibrium. In this case, the population of each surface state can be calculated by the Boltzmann distribution as follows:

$$p_i = \frac{\exp\left(-\frac{\Omega_i}{kT}\right)}{\sum_{j=1}^{N} \exp\left(-\frac{\Omega_j}{kT}\right)}$$

The probability of each surface state (p_i) is calculated at T = 298K and is dependent on the potential (U).

(c) In this model, we choose both the $|\Delta G| = |\Omega_i - \Omega_j|$, and the population (*p*) as descriptors for the HER activity. The rates of forward and reverse reactions can be described as follows:

$$\text{step 1}\left(*_i + \mathrm{H}^+ + \mathrm{e}^- \rightarrow * H_j\right):\ r_{\mathrm{f},ij} = k_{\mathrm{f},ij}[*] \propto \exp\left(-\frac{\Delta G_{\mathrm{f}}(U)}{kT}\right) \cdot p_i$$

$$\text{step 2}\left(* H_j + \mathrm{H}^+ + \mathrm{e}^- \rightarrow *_i + \mathrm{H}_2\right):\ r_{\mathrm{r},ij} = k_{\mathrm{r},ij}[\cdot *] \propto \exp\left(-\frac{\Delta G_{\mathrm{r}}(U)}{kT}\right) \cdot p_j$$

Where $\Delta G_f(U)$ and $\Delta G_r(U)$ are the potential-dependent free energy change of the forward (1) and reverse (2) reaction steps, and p_i and p_j are the populations of the *and *H sites calculated from the Boltzmann distribution in the grand canonical ensemble, respectively.

(d) Finally, we can derive the overall rate (r_{ij}) for the steps i,j via the Butler-Volmer type equation as following:

$$r_{ij} \propto \exp\left(-\alpha\frac{\Delta G_{\mathrm{f}}(U)}{kT}\right) \cdot p_i - \exp\left(-(1-\alpha)\frac{\Delta G_{\mathrm{r}}(U)}{kT}\right) \cdot p_j$$

where $\alpha \in [0,1]$ is the mechanistic symmetry factor. Here, we adopt the value of $\alpha = 0.5$ assuming no asymmetry about the equilibrium potential.

B.2 Formation Energy Evaluation:

The formation energy is calculated by

$$\Delta E_{\mathrm{H}} = E(* n\mathrm{H}, \mathrm{U}) - E(ITO, U) - E(Pt\ Bulk) - n\mu_{\mathrm{H}^+}(\mathrm{U}, p\mathrm{H}) - n\mu_{\mathrm{e}^-}(\mathrm{U}, p\mathrm{H})$$

Where the * stands for the adsorption site, $E(Pt\ Bulk)$ is the energy of bulk Pt and $E(ITO, U)$ is the potential dependent energy of the 5% ITO + $4H_2O$ surface. The adsorption free energy of H is calculated by

$$\Delta G_{\mathrm{H}} = \Delta E_{\mathrm{H}^*} + \Delta E_{ZPE} - T\Delta S_{\mathrm{H}}$$

ΔE_{ZPE} and ΔS_H are the change in the zero-point energy and entropy upon H adsorption calculated with respect to the free H_2 molecule in the gas phase and n is defined as the H coverage on the cluster.

B.3 Equation of Thermodynamics

The stability of any cluster on a support is defined by the adsorption energy of the cluster on the support at a given temperature and pressure. Moreover, whenever there is an influence of a reactive gas phase, such as water, hydrogen, etc. we need to use the first-principle atomistic thermodynamics approach to study the stability of the clusters on the support. For any given structure the Gibbs Free Energy is defined as:

$$G = H - TS$$

where H is the enthalpy, S is the entropy and T is the temperature. The enthalpy of any gas phase reactant can be defined as:

$$H(T) = E_{\mathrm{elec}} + E_{\mathrm{ZPE}} + \int_0^T C_P \, \mathrm{d}T$$

Where, E_{elec} = Electronic energy, E_{ZPE} = zero point energy and last term is the integral over the constant-pressure heat capacity (C_p).

$$E_{\mathrm{ZPE}} = \frac{1}{2}\sum_i^{\mathrm{vib}} \epsilon_i$$

Where $\epsilon_i = \mathrm{h}\omega_i$ are the energies associated with vibrational frequencies ω_i. The constant volume heat capacity can be measured separately for translational $(C_{V,\,\mathrm{tran}})$, vibrations $\left(\mathrm{C}_{V,\,\mathrm{vib}}\right)$, rotational $\left(\mathrm{C}_{V,rot}\right)$ and electronic part $\left(\mathrm{C}_{V,\,\mathrm{elec}}\right)$, and a k_B (in eV) term is added to get C_p value as follows:

$$C_p = k_B + C_{V,\,\mathrm{tran}} + C_{V,vib} + C_{V,rot} + C_{V,elec}$$

For 3-D gas, the translational heat capacity can be calculated as:

$$C_{V,\mathrm{tran}} = \frac{3}{3} k_B$$

Rotational heat capacity can be shown to be:

$$C_{V,\,\mathrm{rot}} = \begin{cases} 0, & \text{Monoatomic species} \\ k_B, & \text{Linear Molecule} \\ 3/2 k_B & \text{Nonlinear Molecule} \end{cases}$$

The integral form of vibrational heat capacity can be shown as:

$$\int_0^T C_{V,\mathrm{vib}} \mathrm{d}T = \sum_i^{\mathrm{vibDOF}} \frac{\epsilon_i}{e^{\epsilon_i / k_{\mathrm{B}} T} - 1}$$

In the case of an ideal gas, we can assume the electronic contribution to the heat capacity as zero since the separation between the lowest excited state and the ground state is much higher than k_B T

The entropy terms for an ideal gas as a function of T and P can be expressed as a sum of of translational ($\mathrm{S}_{\mathrm{trans}}$), rotational ($\mathrm{S}_{\mathrm{rot}}$), electronic ($\mathrm{S}_{\mathrm{elec}}$) and vibrational (S_{vib}) contributions with a pressure correction as:

$$\begin{aligned} S(T,P) &= S(T,P^\circ) - k_\mathrm{B} \ln \frac{P}{P^\circ} \\ &= S_\mathrm{trans} + S_\mathrm{rot} + S_\mathrm{elec} + S_\mathrm{vib} - k_\mathrm{B} \ln \frac{P}{P^\circ} \end{aligned}$$

$$S_\mathrm{trans} = k_\mathrm{B} \left\{ \ln \left[\left(\frac{2\pi M k_\mathrm{B} T}{h^2} \right)^{3/2} \frac{k_\mathrm{B} T}{P^\circ} \right] + \frac{5}{2} \right\}$$

$$S_\mathrm{rot} = \begin{cases} 0 & \text{, if Monoatomic} \\ k_\mathrm{B} \left[\ln \left(\frac{8\pi^2 I k_\mathrm{B} T}{\sigma h^2} \right) + 1 \right] & \text{, if Linear} \\ k_\mathrm{B} \left\{ \ln \left[\frac{\sqrt{\pi I_\mathrm{A} I_\mathrm{B} I_\mathrm{C}}}{\sigma} \left(\frac{8\pi^2 k_\mathrm{B} T}{h^2} \right)^{3/2} \right] + \frac{3}{2} \right\} & \text{, if Nonlinear} \end{cases}$$

$$S_\mathrm{vib} = k_\mathrm{B} \sum_i^\mathrm{vib} \sum_i^\mathrm{DOF} \left[\frac{\epsilon_i}{k_\mathrm{B} T (e^{\epsilon_i / k_\mathrm{B} T} - 1)} - \ln \left(1 - e^{-\epsilon_i / k_\mathrm{B} T} \right) \right]$$

$$S_\mathrm{elec} = k_\mathrm{B} \ln \left[2 \times (\text{ total spin }) + 1 \right]$$

The above enthalpy and entropy descriptions can be used to find the chemical potential of gas phase molecules:

$$G(T,P) = H(T) - TS(T,P)$$

B.4 Grand Canonical Basin Hopping

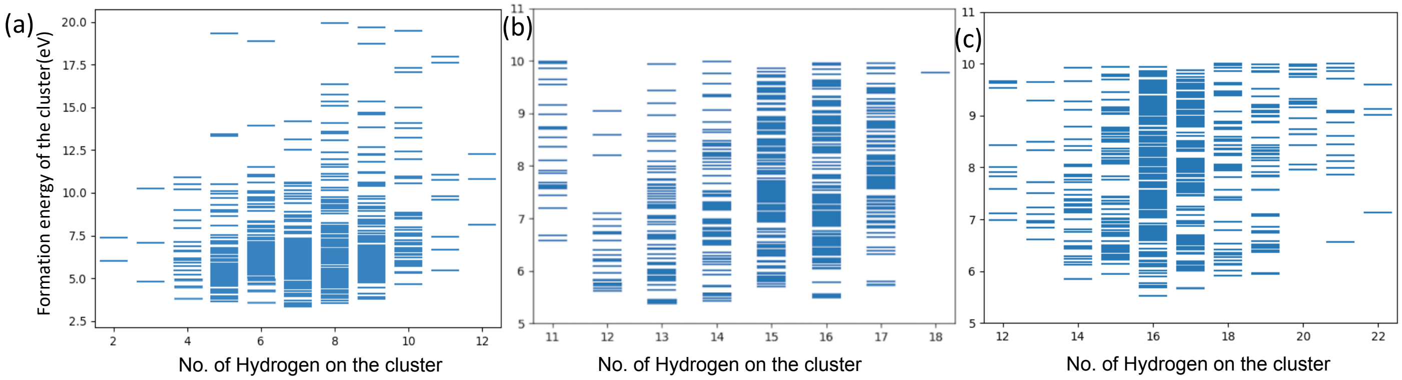

Figure B.1 GCBH results for (a) Pt_4, (b) Pt_7 and (c) Pt_8 with varying H coverage.

Figure B.1 gives all the unique structures found via GCBH calculation on Pt_4Hx, Pt_7Hx and Pt_8Hx structures. The x-axis gives the H-coverage of the different clusters and the y axis gives the Formation energies. Note that these are the direct results of structure exploration from GCBH, the computational parameters used to do the GCBH exploration is much cheaper and coarser compared to the converged computational parameters that we have used to evaluate the final formation energies and structures. After the GCBH exploration with cheaper computational parameters are performed we take the structures in the range of 1.5eV from the global minimum for each cluster size and reoptimize the structures with converged computational parameters to find the final energies.

B.5 HER reaction mechanism on Pt_1H_x/ITO

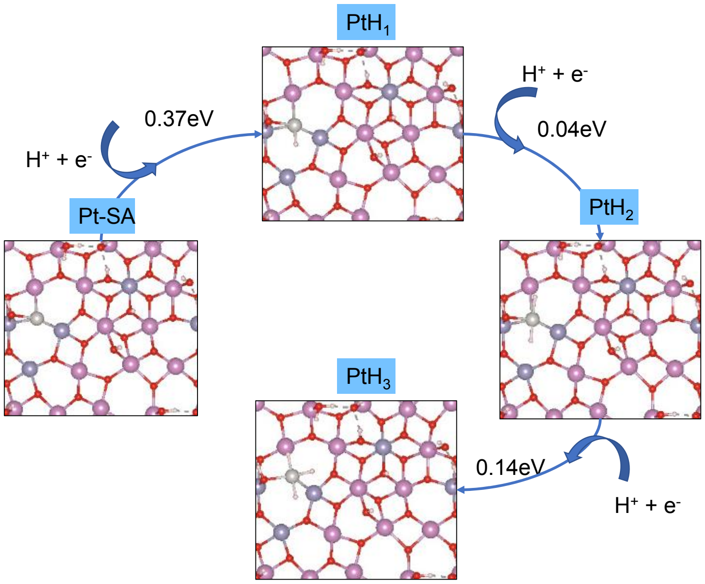

Figure B.2 HER reaction mechanism on Pt_1H_x/ITO

Figure B.2 represents the HER mechanism on Pt_1H_x/ITO. We start with the most stable structure of Pt-SA/ITO which we reported in our previous work[224] and detailed in Chapter 1.

We did not find any nearby metastable structures in the case of Pt-SA which could potentially contribute to the HER current. The first H adsorption step from Pt/ITO to PtH_1/ITO has an over-potential of 0.37eV. Hence, we did not observe any HER currents on the theoretical and experimental voltammograms for the case of Pt_1H_x/ITO in the working potential range.

B.6 HER reaction mechanism on Pt_4H_x/ITO

Figure B.3 shows the potential energy surface of Pt_4H_x/ITO along with the GM and MS structures. The individual currents from the various reaction pathways are shown in (b) and (c). We observe that the most active HER current comes from the Volmer Tafel reaction between 6_1→7→8 H coverage states in the potential range of 0 → -0.05 after which the states 7→8→ 9 H coverage takes over the maximum current.

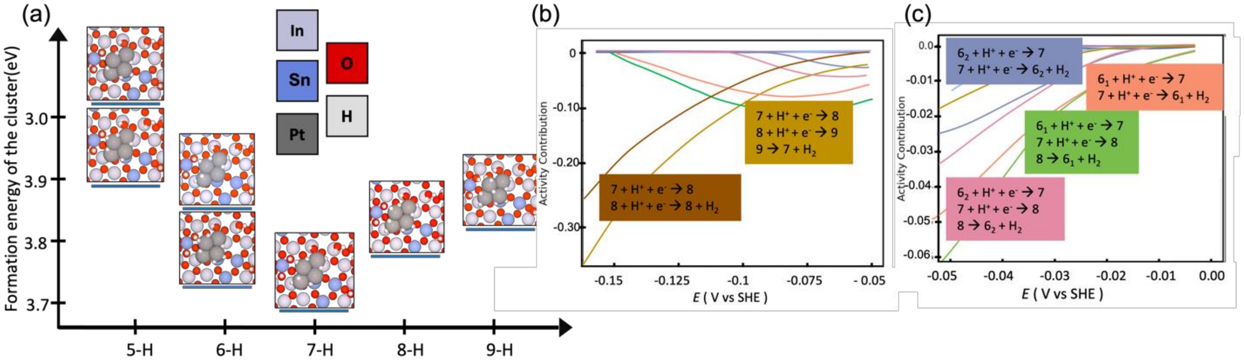

Figure B.3 (a) PES of Pt_4H_x/ITO representing GM and MS structures (b) and (c) represents the theoretical HER current generated by individual reactions.

B.7 HER reaction mechanism on Pt_8H_x/ITO

In the case of Pt_8H_x/ITO, unlike Pt_4H_x/ITO and Pt_7H_x/ITO we have only 1 thermodynamically accessible global minimum for the hydrogen coverages 14,15,16 and 17. The potential energy surface is shown in Figure B.4 (a). The HER currents due to these states are shown in Figure B.4 (b) and (c). We observe that the current is generated almost completely from the Volmer tafel reaction between 15→16→17 states.

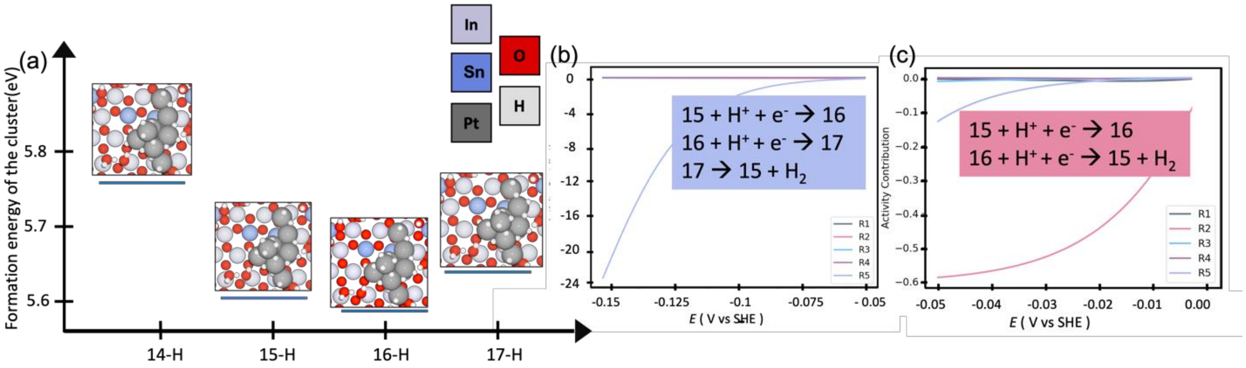

Figure B.4 (a) PES of Pt_8Hx/ITO representing GM and MS structures (b) and (c) represents the theoretical HER current generated by individual reactions.

B.8 Electronic Structure of Pt_8H_{16} projected on the d orbital of Pt.

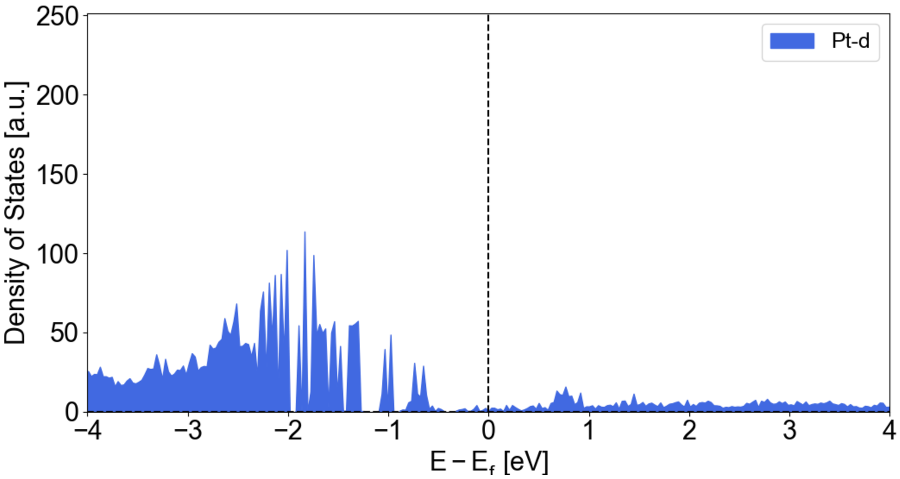

Figure B.5 Density of States projected on the d orbitals of Pt atom for the case of Pt_8H_{16}.

B.9 Theoretical Tafel Slopes:

We have simulated the theoretical tafel slopes from our theoretical CVs at a potential of -0.15V vs SHE for the three different cluster sizes. Please note that the slope numbers here can only be considered qualitatively and not quantitatively. The slopes show that Pt_4 and Pt_7 have similar slopes ~ 240 Arbitrary Units (AU) whereas the slope of Pt_8 is much less at 123.52AU.

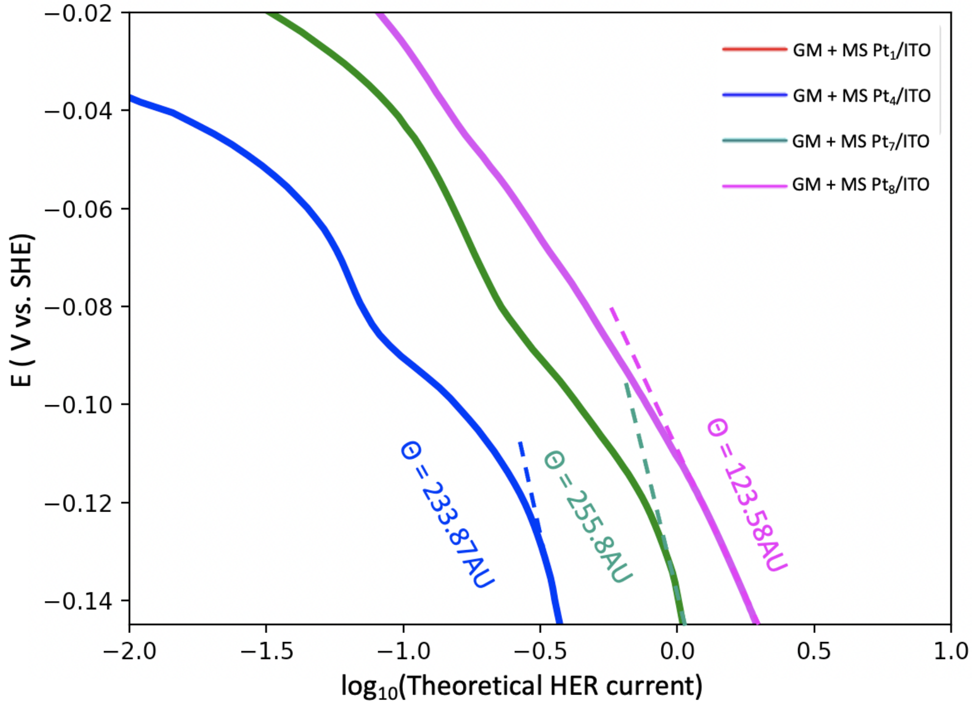

Figure B.6 Theoretical Tafel slopes calculated for Pt_4, Pt_7 and Pt_8. The units on the slopes are Arbitrary units (AU).

B.10 Experimental Setup

All chemicals were commercially available and were used without further purification. 0.1 M $HClO_4$ was prepared from 70% solution (Sigma-Aldrich, 99.999% trace metals basis). Dilute H_2SO_4 was prepared from 95.0–98.0% solution (Sigma-Aldrich, ACS reagent). Concentrate HCl and HNO_3 were purchased from Fisher Chemical (36.5–38.0% HCl, Certified ACS Plus and 68.0–70.0% HNO_3, Certified ACS Plus, respectively). 95% ethanol was obtained from Decon Laboratories. The ITO substrates were 12 mm × 8 mm × 1.1 mm rectangles obtained by dicing ITO-coated glass slides (Sigma-Aldrich, surface resistivity 15–25 Ω square^{-1}). For all purposes, water was 18.2 MΩ cm deionized water obtained from a Barnstead^{TM} MicroPure^{TM} water purification system. Ar and O_2 used for sputtering and annealing were UHP grade gas obtained from Airgas, while standard grade Ar sourced from DJB Gas Services was used for the electrochemical measurements.

All the electrochemical measurements were performed using a bench-top electrochemical measurement system. As depicted in Figure B.7, the system consists of a CHI611E potentiostat (CH Instruments), a cell body machined from polyether ether ketone (PEEK), and an inner glass compartment separated by a fine glass frit housing the counter and reference electrodes. The Pt_n/ITO working electrode is mounted on an X-Y-Z translation stage that allows the electrode to be centered and pressed against a Viton O-ring that seals it to the PEEK cell body, which has a 4 mm diameter opening large enough to ensure that the entire 2 mm cluster spot is in contact with the electrolyte. The electrolyte solution for the working and counter/reference electrode compartments was 0.1 M $HClO_4$. Before each experiment, 10 mL of the electrolyte was sparged with for at least 10 min to remove dissolved O_2. The reference electrode was a leak-free Ag/AgCl electrode purchased from eDAQ (ET072) or Innovative Instruments (LF-2), and the counter electrode was a Pt wire (Alfa Aesar, 0.5 mm in diameter, 99.997% metals basis). The configuration was, thus, a three-compartment cell with working and counter electrode compartments separated by the glass frit, with the reference electrode further isolated by its leakless membrane. This design minimizes contamination of the working electrode by species produced at the counter electrode or diffusing from the reference electrode. Two PEEK needles (Hamilton 8649-01) were used to purge the cell compartments with Ar.

For the small coverage of Pt on the working electrodes, contamination is a serious concern.[165] Glassware was cleaned by rinsing with 18.2 MΩ cm water and 95% ethanol three times each. The cell parts, PEEK needles, and glass frit were sonicated in 18.2 MΩ cm water for 10 min and then in 95% ethanol for 10 min. The reference electrode was stored in 0.05 M H_2SO_4 while not in use, and it was rinsed with 18.2 MΩ cm water prior to use. The counter electrode was dipped for 30 sec in aqua regia (3:1 v/v concentrate HCl and HNO_3), followed by rinsing with 18.2 MΩ cm water.

B.11 Experimental details

Vacuum instrumentation. The home-built ultrahigh vacuum (UHV) end station is a key component in the cluster beam deposition/surface analysis instrument used for this study. The end station is equipped for sample cleaning by sputtering/annealing, gas-surface reactivity studies, ultraviolet and X-ray photoelectron spectroscopy, and low-energy ion scattering experiments. The base pressure in the end station was below 5×10^{-10} mbar for these studies, somewhat elevated compared to our normal UHV conditions because samples were transferred in and out of vacuum. Sub-nano Pt_n^+ cluster ions generated by laser vaporization were guided to a mass-selecting quadruple (QMS), then the mass-selected clusters were passed through a 2-mm diameter deposition mask to deposit on the sample in the UHV end station. More information on this system can be found in previous publications.[165,316–319]

Substrate precleaning. Each ITO substrate was sonicated for 10 min in 18.2 MΩ cm water, followed by 10-min sonication in ethanol (Decon Laboratories, 95%), which we have found to leave undetectably low metal contaminant levels after drying in N_2.

Ar^+ sputtering and annealing. The precleaned ITO substrate was clamped into a substrate holder with a tantalum backing plate held on two tantalum heating wires, with a type C thermocouple spot-welded to the back of the backing plate. The substrate holder was loaded into a small load-lock chamber, pumped down, and transferred into the UHV system, where it was loaded onto a precision X-Y-Z-θ manipulator. The substrate was first sputtered by ~1 μA of 1 keV Ar^+ for 3 min to remove residual adventitious carbon, then to ensure that the ITO surface was fully oxidized, the substrate was annealed at 570 K for 20 min in 1.3×10^{-7} mbar O_2. Von Weber et al.[165] analyzed the ITO surface prepared this way by X-ray photoelectron spectroscopy and confirmed that the In:Sn stoichiometry remained unchanged.

Pt_n^+ cluster deposition. The clean, annealed ITO substrate was positioned ~0.5 mm behind the 2 mm diameter deposition mask, giving a cluster spot with ~0.03 cm^2 area. A fiduciary mark etched on the back side of the substrate was aligned with the mask, so that the spot position could later be aligned with the electrochemical cell. Pt_n^+ clusters were deposited at a kinetic energy of ~1 eV/atom and substrate temperature of 300 K. Deposition at higher energies was found to cause spurious features in cyclic voltammetry, suggesting that the cluster impacts had damaged the electrode. The coverage of the deposited Pt_n clusters was monitored by integrating the neutralization current of the Pt_n^+ clusters landing on the substrate. Unless otherwise noted, each Pt_n/ITO electrode had a single cluster spot containing the selected size Pt_n clusters, with a total of

1.35×10^{12} Pt atoms (0.434 ng), corresponding to a coverage of ~4.50×10^{13} atoms/cm^2, equivalent to ~3% of a close-packed Pt monolayer (0.03 ML). Typical ion currents were several tens of pA, allowing Pt$_n$/ITO electrodes to be prepared with deposition times of 10–20 minutes.

Cyclic voltammetry (CV) and chronoamperometry on the Pt$_n$/ITO working electrodes. After cluster deposition, the Pt$_n$/ITO electrode was first transferred back to the load-lock antechamber, which was then vented with UHP Ar to atmospheric pressure. The electrode was then transferred onto the translation stage and sealed to the electrochemical cell, with the 2 mm cluster spot centered in the 4 mm cell opening. Using a glass syringe (Poulten Graf, with a glass Luer slip tip) and a PEEK needle, the 0.1 M $HClO_4$ electrolyte was injected into the two cell compartments, both of which were bubbled with Ar to purge the electrolyte. The first CV was started after 5 minutes of purging, and Ar continued to flow throughout the measurements. For all the electrodes studied, three different potential windows were examined for CV, and four different potentials were applied to obtain chronoamperometric data. The complete potential wave sequence is depicted in Figure B.8. All the data were recorded at room temperature, which was typically ~21 °C.

B.12 Conversion of recorded potentials to SHE and the accuracy of the potentials

To facilitate comparison with the computational results, the potentials observed vs. Ag/AgCl, denoted E_{obs}, were shifted to reference to the standard hydrogen electrode (SHE). The potential of 0 V vs. normal hydrogen electrode (NHE) is equal to –0.205 V vs. Ag/AgCl (3.5 M KCl) at 25 °C, with a temperature coefficient of 0.73 mV °C^{-1} over the temperature range between 10 and 40 °C.[320] The SHE is 5.7 mV positive of the NHE.[321] These relationships are represented by the equations (1) and (2):

$$E_{\text{NHE}} = E_{\text{obs}} + 0.205\ \text{V} - 0.00073\ \text{V/°C} \cdot (T - 25\text{°C}) \qquad (1)$$

$$E_{SHE} = E_{NHE} + 0.0057 \text{ V} \tag{2}$$

where E_{NHE} and E_{SHE} are the potentials vs. NHE and SHE, respectively. T is the temperature of the electrolyte in °C. Hence, the following equation (3) gives the relationship between E_{SHE} and E_{obs} at the room temperature $T = 21$ °C.

$$E_{\mathrm{SHE}} = E_{\mathrm{obs}} + 0.214 \text{ V} \tag{3}$$

Since the HER onset is quite sharp, it is particularly important to ensure that the potential scale is accurate and stable when data obtained on different days are compared. To this end, after each experiment, additional CVs were taken using a polycrystalline Pt working electrode, and the hydrogen underpotential deposition (H_{upd}) peaks were compared and used to apply small (≤ 10 mV) day-to-day potential corrections. We, thus, estimate that the relative uncertainties for comparing potentials in different CVs are on the order of ± 5 mV.

B.13 Considerations on experimental conditions in the electrochemical measurements

In the bench-top measurements, the Pt_n/ITO electrodes were briefly exposed to air during transfer from the load-lock to the bench-top cell. O_2 dissociatively adsorbs on small Pt clusters,[7] but the resulting O/Pt should be reduced as the electrochemical potential is scanned into the potential range of interest for HER. In addition, we have shown that O_2 is reduced via the ORR at potentials well above the onset of HER or H_{upd},[317,319] thus neither O_2 or O_{ads} should be present in these experiments after the initial scan to reducing potentials. Further evidence suggesting that ORR is not significant in these experiments is discussed below. We also note that, as demonstrated by scanning transmission electron microscopy (S/TEM),[165,322] sub-nano Pt_n clusters appear to be stable with respect to diffusion and sintering on both carbon and oxide surfaces (ultra-thin carbon and alumina grids), even after air exposure and under the influence of the focused electron beam.

B.14 Analysis of experimental currents

The Pt_n/ITO samples have a precisely determined amount of Pt present (0.434 ng), however, the wetted area on the electrodes is not as well defined. The clusters are deposited in a ~2 mm diameter stop, but the Pt coverage in that spot is only ~3% of that in a close-packed Pt surface. Furthermore, the wetted area of ITO is defined by a 4 mm diameter o-ring that seals the electrode to the cell, and that area could vary slightly from day to day due to differences in how the o-ring is pressed to the electrode surface. Therefore, the currents from the CVs and chronoamperometry measurements are simply reported as absolute currents. Because the amount of Pt present on each of the Pt_n/ITO samples is identical, the relative activities of the samples are directly proportional to the relative currents.

After subtraction of the capacitive background currents from the ITO support, the remaining currents originate from under potential deposition or HER at the Pt clusters, and to allow these currents to be compared to currents reported for other types of electrodes, they are reported as mass activities, i.e., the raw currents normalized to the 0.434 ng mass of Pt present, reported as A/mg_{Pt}.

For the Pt_{poly} electrode used to provide CVs for comparison to the Pt_n/ITO data, the electrochemically active surface area (ECSA) was determined by integrating the current associated with underpotential deposition of hydrogen (H_{upd}), assuming that the charge density for Pt_{poly} should be 210 μC cm^{-2}, corresponding to a monolayer of hydrogen electrochemically adsorbed on a polycrystalline Pt surface, i.e., 1:1 H:Pt ratio.[323] This ECSA was then used to calculate the mass of the exposed top surface layer of the Pt_{poly} electrode, which was then used to calculate a "top layer mass activity" for Pt_{poly} (A/mg_{Pt}), as discussed in the manuscript.

B.15 Coverage and potential windows

All the Pt_n/ITO working electrodes used in the main text were prepared by depositing 0.03 ML of Pt. In our previous work,[165]we studied Pt_n/ITO electrodes at 0.1 ML coverage, and while these exhibited larger HER currents, there was evidence in the case of Pt_1/ITO, that there was significant agglomeration/cluster formation on the electrodes. We therefore adopted 0.03 ML equivalent coverage for all experiments, and as shown by the absence of HER signal for Pt_1/ITO, and the strong HER signals observed for even small clusters, agglomeration and clustering for 0.03 ML is negligible. The fact that the ITO supports are rough on the nanometer (and probably the atomic) scale,[165] presumably reduced the tendency toward sintering. The only experiments done at higher coverages were some UPD experiments described in the Supporting Information, done at 0.1 ML coverage for comparison.

The potential windows scanned were typically between –0.196 and 0.514 V vs. SHE so that they fully covered the potential range for HER and H_{upd}, which were the main reactions of interest. Sweeping to more positive potentials can generate O_2 and/or peroxide species in the electrolyte,[319] which could result in interference with the HER/H_{upd} observations from oxygen or peroxide reduction. We also avoided scanning to more negative (reductive) potentials to avoid degradation of the ITO electrode substrate, as has been demonstrated previously.[324]

B.16 Subtraction of background current for Pt_n/ITO

The electrochemical currents measured in the experiments are the sums of Faradaic and non-Faradaic (capacitive) contributions, the latter mostly from the ITO electrode support. A set of experiments measured the capacitive current using a blank ITO working electrode, prepared using the same protocol as the Pt*n*/ITO electrodes, but with no Pt deposited. Because the voltametric response slightly varies depending on the upper/lower potential limits, blank ITO voltammograms were measured for each of the potential windows used in the Pt*n*/ITO HER measurements.

In principle, the capacitive currents measured for blank ITO should be scaled to account for the fact that on the 0.03 ML Pt*n*/ITO electrodes, there is slightly less empty ITO area than on the cluster-free ITO blank electrodes. Note, however, that the wetted ITO area is ~4 times greater than the 2 mm cluster spot, and that the Pt coverage within the spot is only ~3 % of that for close-packed Pt, i.e., the correction to the background currents would be less than 1 %, and that is within the uncertainty in the wetted area due to possible differences in how the o-ring sealing the working electrode is seated. Thus, we have simply subtracted the raw current measured for Pt-free ITO from the currents for the Pt*n*/ITO samples, and the validity of this assumption is supported by the fact that when subtraction is done this way, there is no significant residual current for the Pt*n*/ITO in the 0.4 to 0.5 V vs. SHE potential range, where no reactions occur on the clusters.

Table B.1 Complete data on the UPD integration for the Pt*n*/ITO (*n* = 1, 4, 7, 8) CVs

Catalyst	H_{upd} charge / μC	# of electrons / 10^{12}	# of H_{upd} per Pt atom*
0.03 ML Pt_1/ITO	0.051	0.31	0.23 ± 0.09
0.03 ML Pt_4/ITO	0.32	2.0	1.5 ± 0.6
0.03 ML Pt_7/ITO	0.63	3.9	2.9 ± 1.4
0.03 ML Pt_8/ITO	0.48	3.0	2.2 ± 0.8

*The number of electrons divided by the number of Pt atoms (1.35×10^{12} for all the catalysts). Errors represent the standard deviations of repeated measurements.

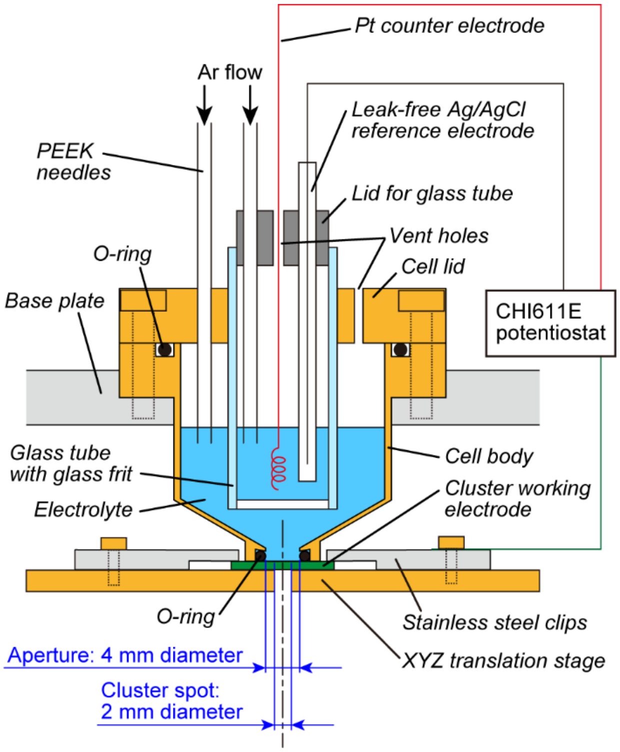

Figure B.7 Schematic view of the bench-top electrochemical measurement system.

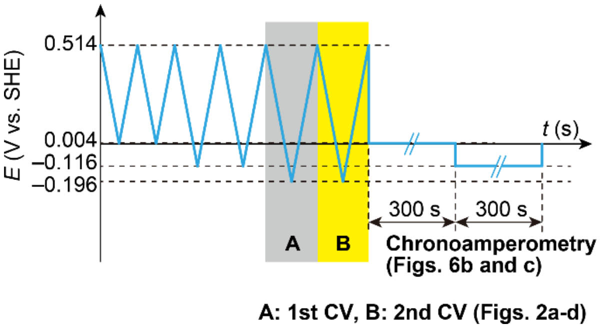

Figure B.8 Potential wave sequence applied in the electrochemical experiments. Three different potential windows were examined by CV, with the potential cycled twice for each potential window to ensure that the electrochemical measurements were performed in steady state conditions. The chronoamperometric measurements were carried out immediately after the CVs with no pause.

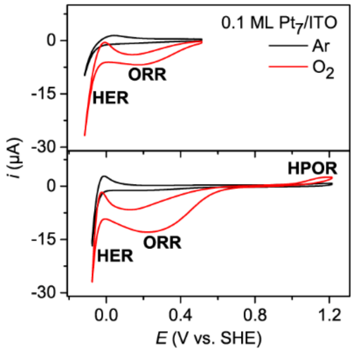

Figure B.9 CVs of 0.1 ML Pt_7/ITO at 0.1 V s^{-1} in 0.1 M $HClO_4$ sparged with Ar and O_2, obtained in narrow and wide potential windows. Signals for the ORR and hydrogen peroxide oxidation reaction (HPOR) are observed in the presence of O_2, as previously reported for Pt_n/ITO in *in situ* electrochemical experiments.[2] For the Ar-sparged experiments, no ORR or HPOR signals were detected. Note also that the onset and peak of the ORR is at potentials well above the potential range where H_{UPD} is observed (see main paper), thus if O_2 were present in those experiment, that signal would easily be distinguishable from H_{upd}.

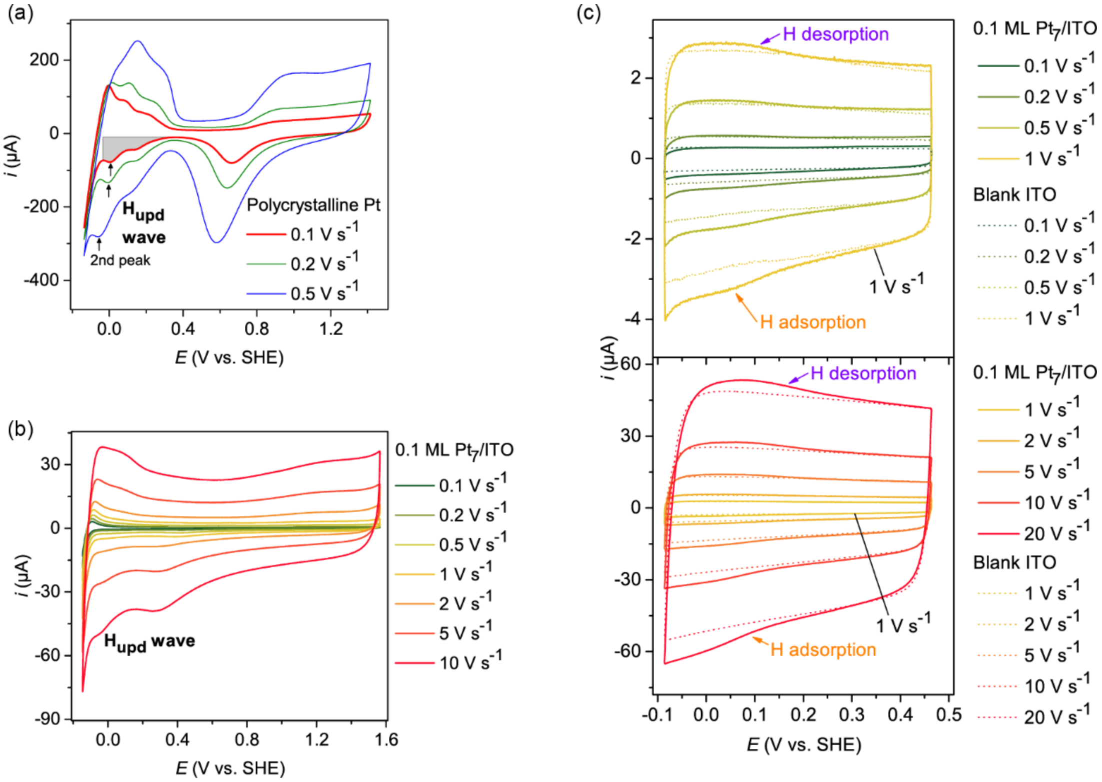

Figure B.10 Scan rate dependence of currents. (a) CVs of a polycrystalline Pt working electrode in 0.1 M $HClO_4$ at scan rates between 0.1 and 0.5 V s^{-1}. For the 0.1 V s^{-1} CV, the gray area represents the H$_{upd}$ integration. The H$_{upd}$ peaks with arrows and labels "2nd peak" were used to look into the current response to the scan rate that was plotted in Figure B.11a. The calculated H$_{upd}$ charges were plotted against the scan rate in Figure B.11b. (b) CVs of 0.1 ML Pt$_7$/ITO in Ar-saturated 0.1 M $HClO_4$ at various scan rates. At higher scan rates, the H$_{upd}$ region started to exhibit wave-like structure, and the H desorption peaks on the positive sweep became were more evident. Note that the ORR contribution to the H$_{upd}$ structures cannot completely be ruled out in this wide potential window, because the potential range extended to the onset of the oxygen evolution reaction. (c) CVs of 0.1 ML Pt$_7$/ITO in Ar-saturated 0.1 M $HClO_4$ at various scan rates over a narrow potential range. The scan rate-dependent CVs of blank ITO are plotted with dotted lines. The background-subtracted data were used to estimate the peak currents and total charges plotted in Figure B.10a and B.10b, respectively. Note that the ORR contribution to the H adsorption currents should be negligible because the potential was not high enough to generate O_2. Note also that if ORR were significant, then that signal would peak in the potential range around 0.2-0.3 V (Figure B.9 top).

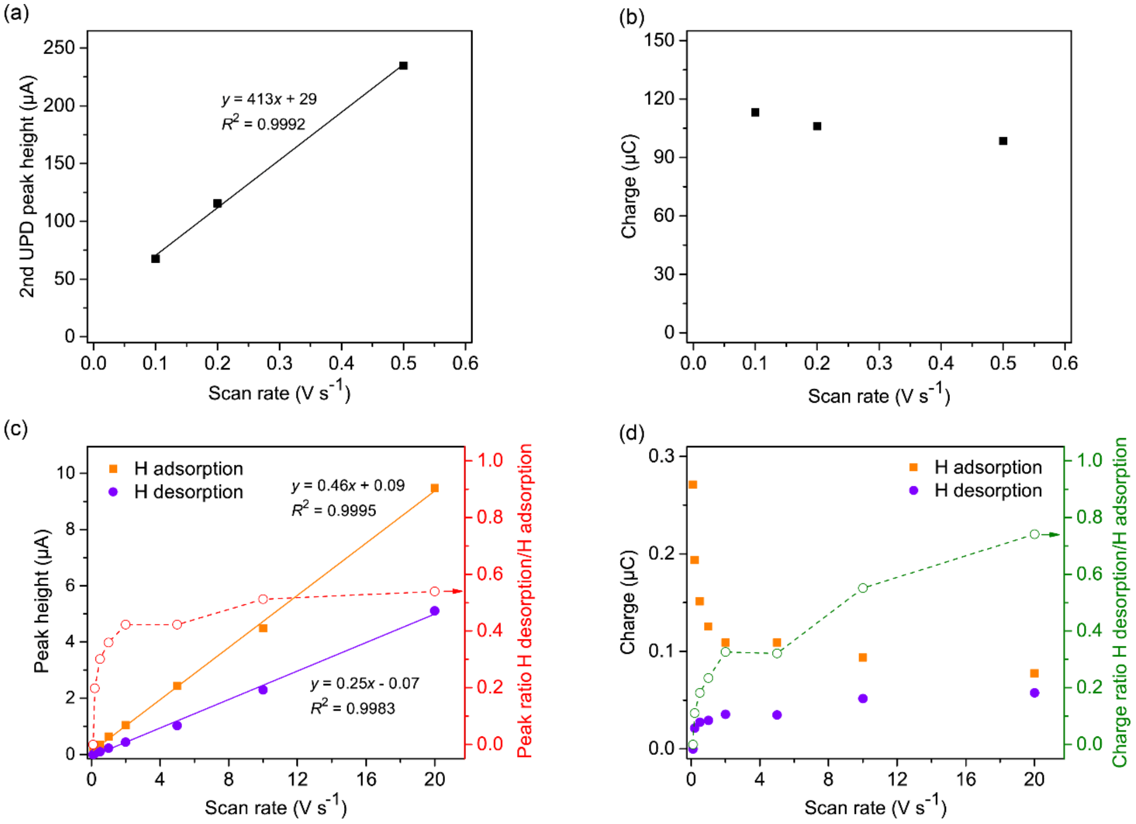

Figure B.11 (a) H_{upd} current (peak tops indicated with arrows in Figure B.10a) and (b) charge responses to the scan rate for polycrystalline Pt. The linear response of the H_{upd} current to the scan rate, as well as the H_{upd} charge independent of the scan rate, shows a H_{upd} nature that the electrochemistry in the H_{upd} region involves an electrode-adsorbed species, which is proton in this case. (c) Peak heights of the H adsorption and desorption currents as a function of the scan rate, extracted from data in Figure B.10c. Least squares regression lines are also drawn. The ratios of the H adsorption and desorption currents are indicated with open circles. (d) Total charges involved in the H adsorption and desorption as a function of the scan rate derived from data in Figure 10.4c. The ratios of the H adsorption and desorption charges are indicated with open circles.

Appendix C Supplementary Information for Chapter 4

C.1 Calculating the $\Delta G^{(U)}$ for each elementary step of OER:

From the reference hydrogen electrode, the energy of the H+ and e$^-$ pairs at 0V vs SHE were considered as the energy of 1/2 H_2. In the framework of the SC approach (discussed in detail in the next section), the energies of each intermediate is determined at a specific potential. The free energies of elementary steps were calculated by the following equations

$$\Delta G_1^{(U)} = G_{*OH}(U) - G_*(U) - E_{H_2O} + \frac{1}{2}E_{H_2} - T\Delta S - eU_{SHE}$$

$$\Delta G_2^{(U)} = G_{*_O}(U) - G_{*_{OH}}(U) + \frac{1}{2}E_{H_2} - T\Delta S - eU_{SHE}$$

$$\Delta G_3^{(U)} = G_{*OOH}(U) - G_{*O}(U) - E_{H_2O} + \frac{1}{2}E_{H_2} - T\Delta S - eU_{SHE}$$

$$\Delta G_4^{(U)} = G_*(U) - G_{*_{OOH}}(U) + \left(2E_{H_2O} - \frac{3}{2}E_{H_2}\right) + 4.92 - T\Delta S - eU_{SHE}$$

Here, the entropy contributions ($T\Delta S$) from the molecules in the gas phase are considered for calculating the free energies.

C.2 Surface Charging (SC) method:

Under the CHE approach, the electrochemical potential is assumed to affect only the chemical potential of the exchanged electrons. Thus, electronic energy is independent with respect to the potential and is taken from neutral systems. However, the free energies for the sites and the intermediates in the "neutral" situation are not the same as the U = 0.0 V situation. To evaluate the potential dependent free energy $PtO_xOH_y(U)$ of each (x,y) in the potential range of 0 – 1.5V vs SHE we have used the surface charging (SC) approach. The SC model considered here is based on the linearized Poisson-Boltzmann (PB) equations and incorporates a few major approximations[178,235,325–331]:

1. Constant surface charge density: The method assumes that the surface charge density is constant, which won't be valid when we have huge charge transfers in the stern layer.

2. Electrolyte concentration: The method assumes that the electrolyte concentration is constant.
3. Linearization of Poisson-Boltzmann equation: The model assumes that the Poisson-Boltzmann equation can be linearized. This approximation can be particularly limiting for systems where the surface potential is high.
4. Constant dielectric constant: The model assumes that the dielectric constant of the solvent is constant, while it could vary with time and space.

C.3 Oxygen Evolution Reaction on Pt-SA on the defected site

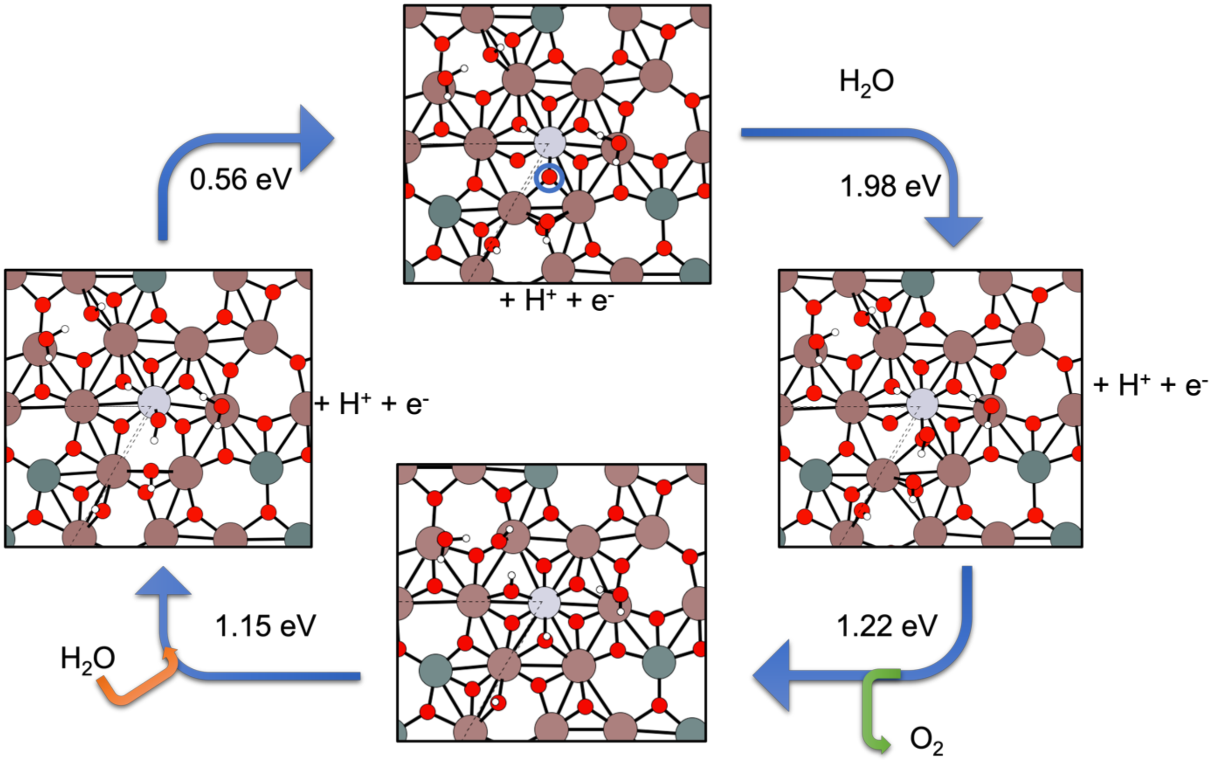

Figure C.1 Oxygen evolution reaction mechanims on Pt-SA replace one of the In atoms.

From our calculations in the Chapter 2, we found that the Pt-SA occupying the defect site is also a possibility at O2 chemical potential higher than -1.5 eV. Hence, we also considered a viable reaction pathway for OER on the Pt-SA/Defected-ITO. We found that the reaction overpotential is very high at 0.75 eV.

C.4 List of other reaction mechanisms with higher overpotential

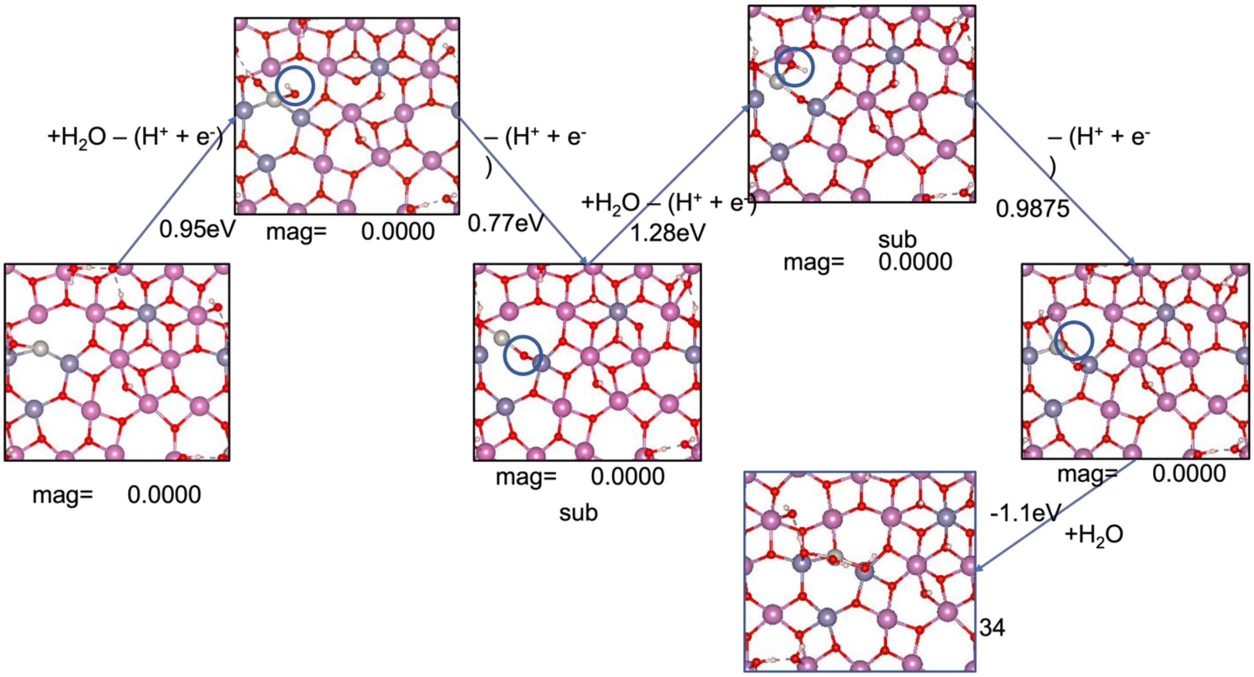

Figure C.2 Reaction Mechanism I for OER starting from Pt-SA/ITO

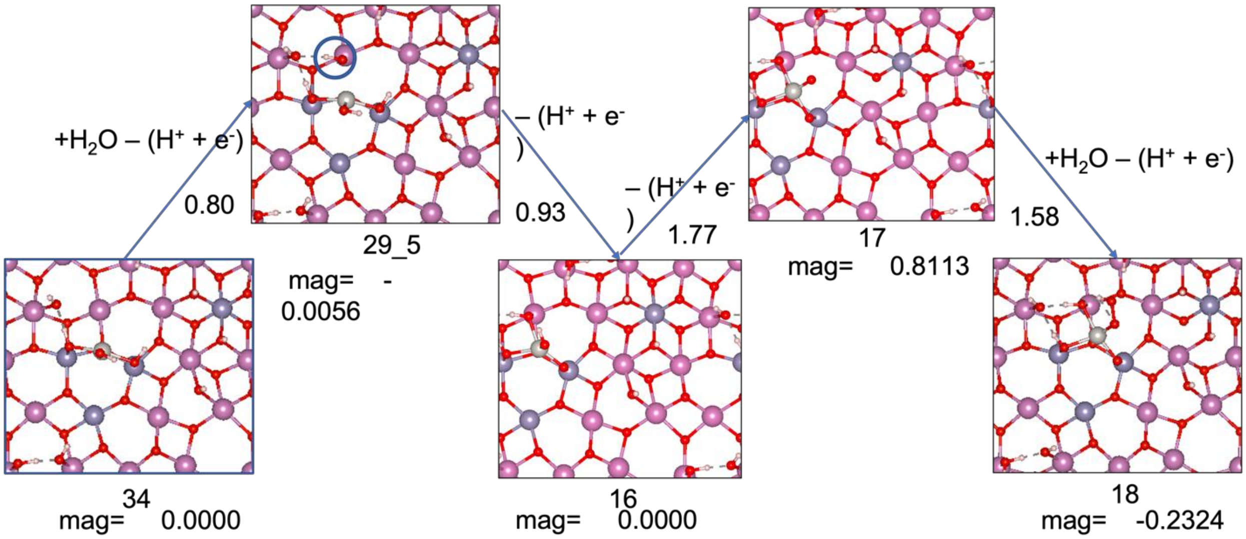

Figure C.3 Reaction Mechanism II for OER starting from Pt-SA/ITO

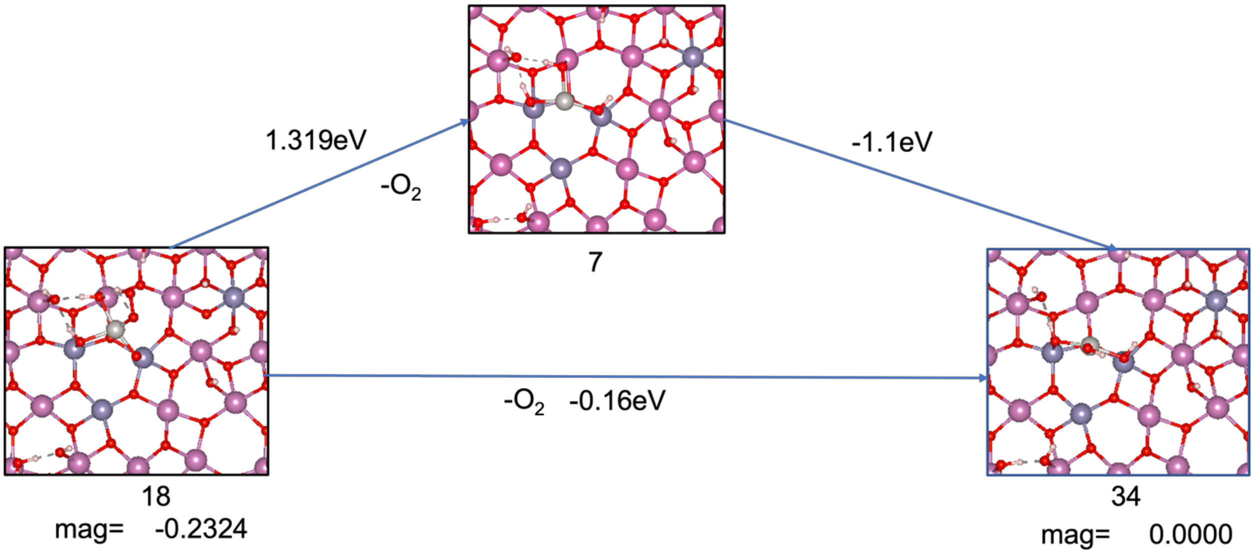

Figure C.4 Reaction Mechanism II for OER starting from Pt-SA/ITO

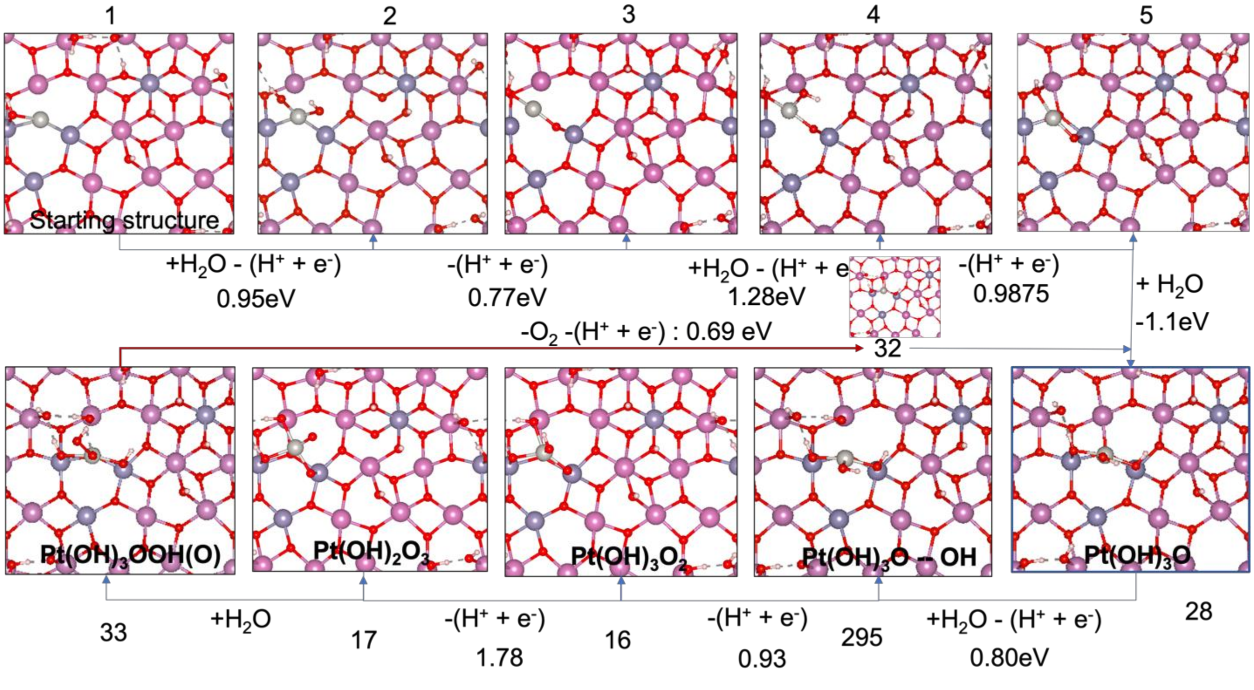

Figure C.5 Reaction Mechanism IV for OER starting from Pt-SA/ITO

Appendix D Supplementary Information for Chapter 5

D.1 Experimental Methods

Electrocatalyst materials and preparation.

Sodium acetate (NaOAc, anhydrous, ≥99%), Cobalt(II) chloride (CoCl2, anhydrous, >98%) and manganese(II) chloride (MnCl2, tetrahydrate, 97%) were purchased from Sigma-Aldrich. Nickel(II) acetate (NiOAc, tetrahydrate, 98%), iron(II) chloride (FeCl2, tetrahydrate, 99%), and copper(II) acetate (Cu(CH3COO)2, anhydrous, 99%) were purchased from Fisher Scientific. Millipore deionized water (18.2 MΩ cm) was used to prepare all of the electrodeposition baths. The concentrations of precursors used in electrodepositions of the different catalysts and specific pH are compiled in Table D.1. Sodium acetate (0.1 M NaOAc) was used in all of the electrodeposition baths as supporting electrolyte. The pH of the baths was adjusted using either 0.1 M acetic acid solution or 0.1 M sodium hydroxide solution. All of the electrodeposition experiments were carried out under atmospheric conditions unless mentioned otherwise.

Table D.1 Concentrations and pH of precursors in the electrodeposition baths

Catalyst	$CoCl_2$	NiOAc	$MnCl_2$	$FeCl_2$	$Cu(CH_3COO)_2$	pH
TiO_x (Substrate)	--	--	--	--	--	--
CoO_x	16 mM	--	--	--	--	5.5-6
NiO_x	--	16 mM	--	--	--	7.5-8
MnO_x	--	--	16 mM	--	--	5.5-6
FeO_x	--	--	--	16mM	--	7.0-7.5
CuO_x	--	--	--	--	16 mM	5.5-6

Catalyst electrodeposition. An Autolab PGSTAT302N potentiostat/galvanostat was used for electrodeposition of the different transition metal oxides in a three-electrode setup with a titanium cylinder substrate (active geometric area = 3 cm^2) as the working electrode, a graphite foil as the counter electrode, and an Ag/AgCl as the reference electrode. Prior to use, the surface of the titanium cylinder electrode was polished using an alumina slurry suspension of 0.05 μm grain size on a microcloth polishing pad (Buehler), rinsed thoroughly with Millipore deionized water (18.2 MΩ cm), and sonicated in deionized water for 10-15 minutes. Prior to electrodeposition, the titanium cylinder electrode was immersed in 2.5 M hydrochloric acid for 60 minutes to remove surface oxides. The titanium cylinders were then rinsed in deionized water and dried under Ar flow. In the electrodeposition process, all the applied potentials were measured against the Ag/AgCl reference electrode. Except for copper, electrodeposition of all the other catalysts was performed by 5 or 100 cycles of consecutive linear sweep voltammetry (LSV) within a specific potential window from 0.8 to 1.1 V vs Ag/AgCl at a scan rate of 10 mV s^{-1}. The deposition of most metal oxides was done using oxidative potentials ($M^{2+}(aq) \rightarrow MOOH(s) + e^- + 3H^+$) where the transition metal deposits on the surface of the electrode directly as an (oxy)hydroxide. As the oxidative electrodeposition proceeds, the oxygen evolution rate increases lowering the local pH and leading to the dissolution of the electrodeposited film. To suppress catalyst dissolution, the most positive potential during the LSV deposition was decreased by 50 mV after the 40th and 70th LSV. Copper, on the other hand was deposited under constant applied potential (−0.18 V vs Ag/AgCl) for 5 min via reductive deposition of the catalyst ($2Cu^{2+} + 2e^- + H_2O \rightarrow Cu_2O + 2H^+$).

Electrochemical rotation cell setup for methane partial oxidation experiments. A gas-tight rotating cylinder electrode (RCE) cell recently reported by us [260,332] was used for all the methane partial oxidation studies in this work. In the RCE cell, a follower magnet inside the cap traces a driver magnet outside the cell via magnetic coupling that allows for the rigorous control of the mass transport in the cell (Figure D.1). The cell's cap carries the electrical connections and is designed to reduce the headspace above the electrolyte in the working electrode compartment. The cap for the working electrode compartment has three threaded ports to accommodate leak-free gas fittings (Swagelok). One of these ports is connected to a glass frit for the feeding of the CH_4 into the working electrode compartment, bringing in the gas feed and bubbling it directly into the electrolyte ensuring a high surface area for contact between the gas and the electrolyte and the consequent saturation of the liquid with dissolved methane. A second port serves as the gas outlet which transfers gaseous products out to the gas chromatogram (GC) connected to the RCE cell for the detection and quantification of gaseous products. The last threaded port is used to draw out liquid aliquots for further quantification of liquid products via nuclear magnetic resonance (NMR). This port is also used to measure the electrolyte temperature at intervals during an experiment. In all experiments involving methane partial oxidation, methane is also bubbled in the counter electrode compartment. This is to keep similar gas environments in both cell compartments thus suppressing dissolved gas crossover. Hex screws that go through the entire lower compartments and nuts are used to compress and seal the cell. A cooling block with a heat-exchange area of 16 cm^2 is positioned below the bottom of the RCE working electrode chamber for temperature control. Liquid products accumulate in the cell over time and thus aliquots are drawn out at intervals of 20 minutes for analysis using a 500 MHz NMR.

Electrochemical measurements. Prior to setting up of the cell, transition metal (oxy)hydroxides were freshly electrodeposited on a titanium cylinder electrode and rinsed thoroughly with deionized water. A three-electrode gas-tight rotation cell setup was used in all electrocatalytic measurements with the cylinder as the working electrode, a 5.8 cm^2 platinum foil (Pt, 0.1 mm thick, 99.99% metal basis, Alfa Aesar) as the counter electrode, a Ag/AgCl/1 M electrode (CH Instruments, Inc.) as the reference electrode, and a solution of 0.1 M potassium carbonate at a pH of 11.68-11.72 (K_2CO_3, Sigma Aldrich, 99.995% trace metals basis) as the electrolyte. After assembling the cell, the circulating bath was used to control and equilibrate the electrolyte temperature inside the working electrode compartment. Before electrochemical measurements, high purity argon gas (Ar, Airgas 99.999%) as the inert gas or methane gas (CH_4, Airgas 99.999%) as the reactant was flowed at a rate of 20 sccm for 30 Minutes in both the working and counter electrode compartments to prepare the gas saturated environments for electrochemical testing. These gas flow rates were maintained throughout the entirety of the electrochemical measurements. In control experiments used to understand the role of carbonate ions, instead of a 0.1 M potassium carbonate solution, a 0.1 M KClO4 (≥99.99% trace metal basis, Sigma-Aldrich) electrolyte adjusted to a pH of 11.8 was used.

In the electrochemical measurements, the uncompensated resistance was determined from the system response at the high frequency (f > 100 kHz) during electrochemical impedance spectroscopy (EIS) measurements. The potential drop across the resistance of the solution from the reference electrode to the cylinder electrode was accordingly corrected. The electrochemical response of the various catalysts was determined by cyclic voltammetry at the scan rate of 10 mV s^{-1}. The long-term electrochemical oxidation of methane was conducted in the RCE cell using chronoamperometry. The overall duration of chronoamperometry was 120 minutes for the electrochemical partial oxidation of methane and multiple gas and liquid samples were taken to quantify products. The specific time of sampling is discussed and shown in the following results and discussion section. Some of the most relevant electrochemical experiments and control experiments were run by duplicate or triplicate to generate statistically significant results. Experiments that were carried only once are shown without standard deviation bars in this manuscript.

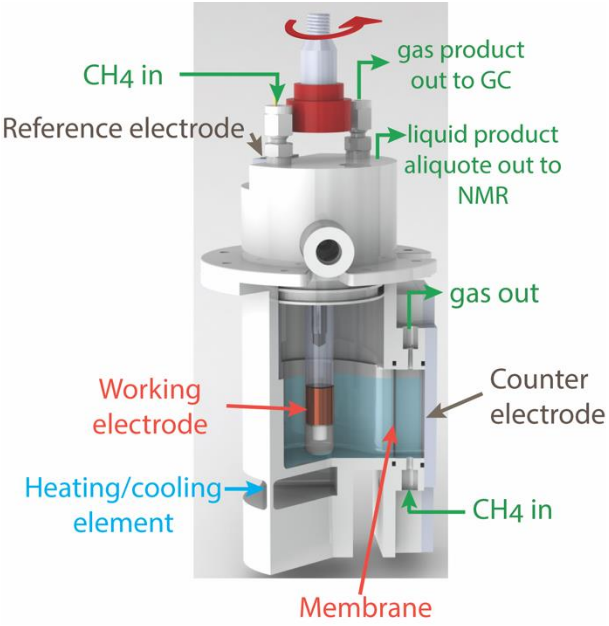

Figure D.1 Schematic of the gas-tight electrochemical cell with a rotating cylinder electrode. Adapted with permission.[27] Copyright 2022 Wiley.

Electrochemical measurements. Prior to setting up of the cell, transition metal (oxy)hydroxides were freshly electrodeposited on a titanium cylinder electrode and rinsed thoroughly with deionized water. A three-electrode gas-tight rotation cell setup was used in all electrocatalytic measurements with the cylinder as the working electrode, a 5.8 cm^2 platinum foil (Pt, 0.1 mm thick, 99.99% metal basis, Alfa Aesar) as the counter electrode, a Ag/AgCl/1 M electrode (CH Instruments, Inc.) as the reference electrode, and a solution of 0.1 M potassium carbonate at a pH of 11.68-11.72 (K_2CO_3, Sigma Aldrich, 99.995% trace metals basis) as the electrolyte. After assembling the cell, the circulating bath was used to control and equilibrate the electrolyte temperature inside the working electrode compartment. Before electrochemical measurements, high purity argon gas (Ar, Airgas 99.999%) as the inert gas or methane gas (CH_4, Airgas 99.999%) as the reactant was flowed at a rate of 20 sccm for 30 Minutes in both the working and counter electrode compartments to prepare the gas saturated environments for electrochemical testing. These gas flow rates were maintained throughout the entirety of the electrochemical measurements. In control experiments used to understand the role of carbonate ions, instead of a 0.1 M potassium carbonate solution, a 0.1 M KClO4 (≥99.99% trace metal basis, Sigma-Aldrich) electrolyte adjusted to a pH of 11.8 was used.

In the electrochemical measurements, the uncompensated resistance was determined from the system response at the high frequency (f > 100 kHz) during electrochemical impedance spectroscopy (EIS) measurements. The potential drop across the resistance of the solution from the reference electrode to the cylinder electrode was accordingly corrected. The electrochemical response of the various catalysts was determined by cyclic voltammetry at the scan rate of 10 mV s^{-1}. The long-term electrochemical oxidation of methane was conducted in the RCE cell using chronoamperometry. The overall duration of chronoamperometry was 120 minutes for the electrochemical partial oxidation of methane and multiple gas and liquid samples were taken to quantify products. The specific time of sampling is discussed and shown in the following results and discussion section. Some of the most relevant electrochemical experiments and control experiments were run by duplicate or triplicate to generate statistically significant results. Experiments that were carried only once are shown without standard deviation bars in this manuscript.

Product detection and quantification. A gas chromatograph (GC) (8610C, SRI Instruments) was used for the detection and quantification of gas products. In methane partial oxidation experiments, the gas environment in the headspace of the cell was allowed to equilibrate and the first injection to the GC was made 20 minutes after the beginning of chronoamperometry measurements. Following injections were made at a 20-minute interval. Each GC run consisted of 14 minutes of running time and 6 minutes of cool-down between samples. Therefore, the gas product was sampled after 20, 40, 60, 80, 100, and 120 minutes after the beginning of the electrolysis, and each injection was used to calculate the Faradaic efficiency towards oxygen and , CO and CO_2 products when generated. The detection limit for the detection of oxygen, CO and CO_2 gases is 250, 1 and 2 μA cm^{-2}, respectively.

Nuclear magnetic resonance spectroscopy (1D ^1H NMR 500 MHz with cryoprobe, Bruker) was used for the detection and quantification of liquid products. During the methane partial oxidation experiments, liquid aliquots were also collected at 20 minutes intervals (at 0, 20, 40, 60, 80, 100, and 120 minutes of electrolysis). Phenol (≥99.5%, Sigma-Aldrich) and dimethyl sulfoxide (DMSO, ≥99.9%, Sigma-Aldrich) were used as the internal standard for the quantification of liquid products. The internal standard was prepared by making a 52.5 mM of phenol and 2.1 mM of DMSO solution in deuterium oxide (D2O, 99.9%, EMD Millipore). Calibration of the NMR signals was done by calculating the ratio of the integration value of the signals for the different protons and the external standards for standard solutions containing known concentrations of each product. To quantify methanol partial oxidation products, all samples were prepared by pipetting 35 μL of the internal standard and 700 μL of the liquid aliquot into a new NMR tube. From the resulting 1D ^1H NMR spectra, the signal areas were normalized by that of DMSO, and the normalized signal areas were compared to the standard curve to calculate concentrations of liquid products during the partial methane oxidation reaction.

D.2 SEM and XPS Characterization of Electrocatalyst Films

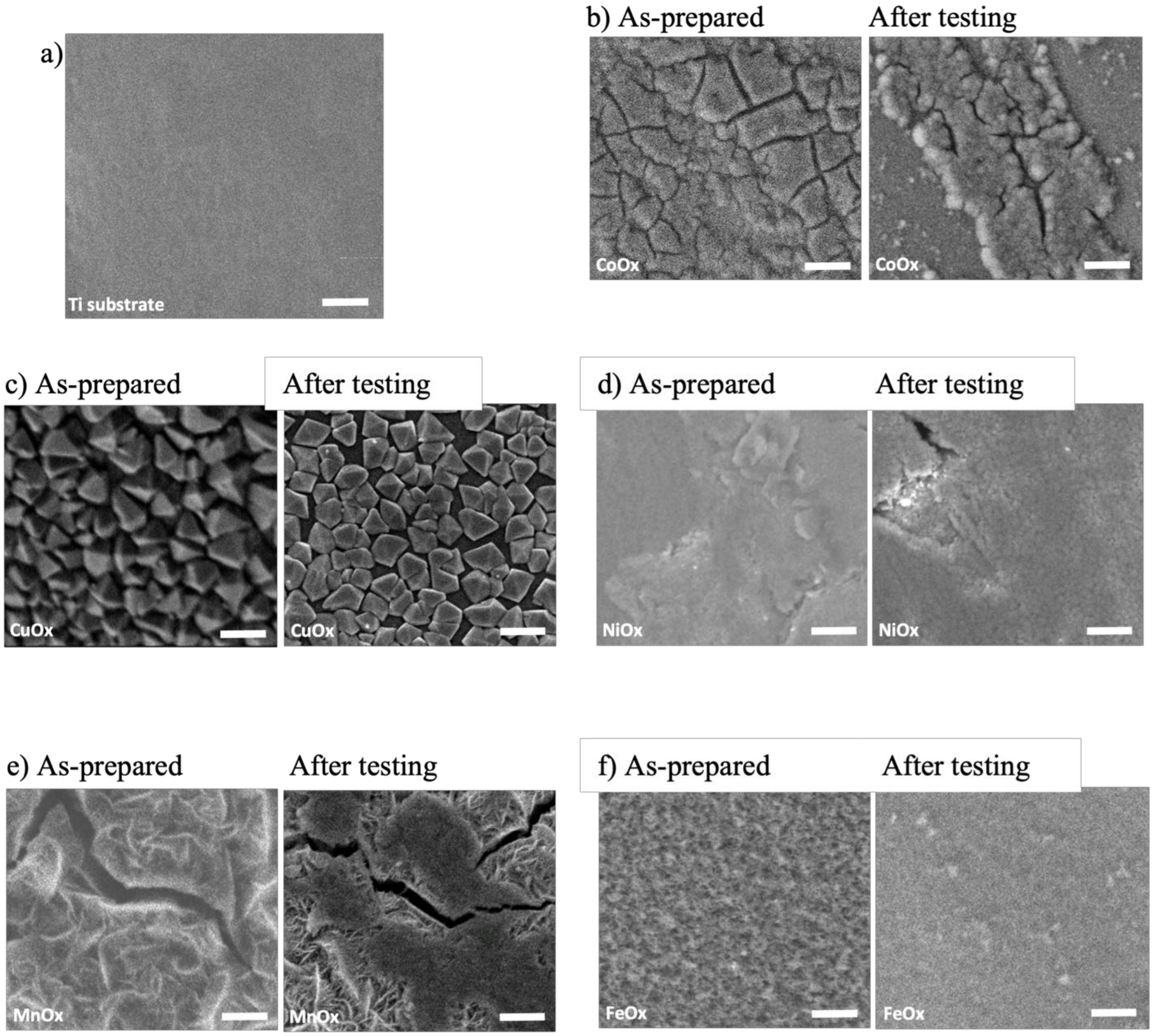

Figure D.2 SEM images of (a) blank titanium, (b) CoO_x, (c) CuO_x, (d) NiO_x, (e) MnO_x, and (f) FeO_x electrodeposited on a titanium cylinder electrode. SEM images are shown for the as-prepared samples and after electrochemical oxidation of methane for 2 hours. The scale bars in all the samples correspond to 1 μm.

Appendix E Supplementary Information for Chapter 6

E.1 Free Energy Surface [Reaction condition: Pressure = 0.013atm, Conversion = 2%, Temperature = 500K, CO_2/H_2 ratio: 1:9]

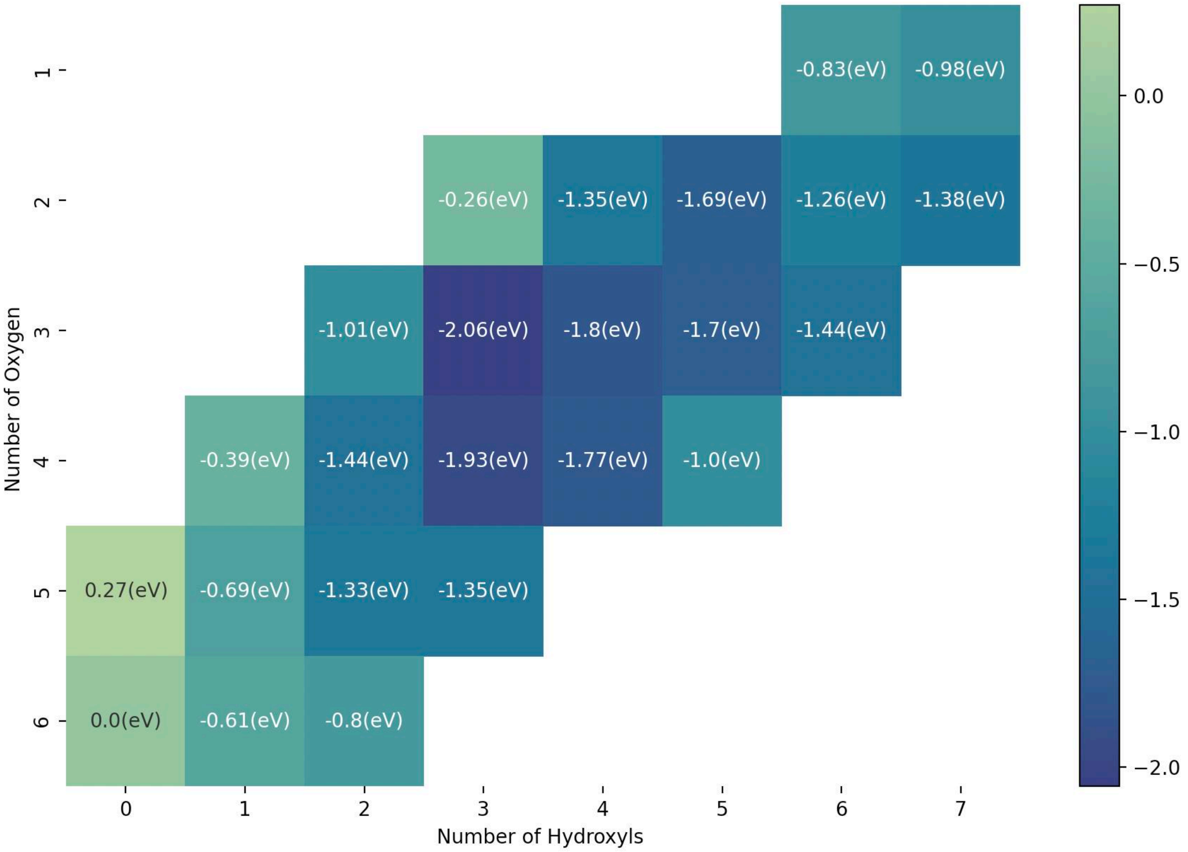

Figure E.1 FES of the structures with no formates in the reaction condition: Pressure = 0.013atm, Conversion = 2%, Temperature = 500K, CO_2/H_2 ratio: 1:9. The x axis represents the number of hydroxyls and the y axis represents the number of Oxygens on the Zr cluster. The color gradient represents the adsorption energy of the ligand wrt the Zr_3O_6/Cu 111 surface. The annotations on figure represents the adsorption energy.

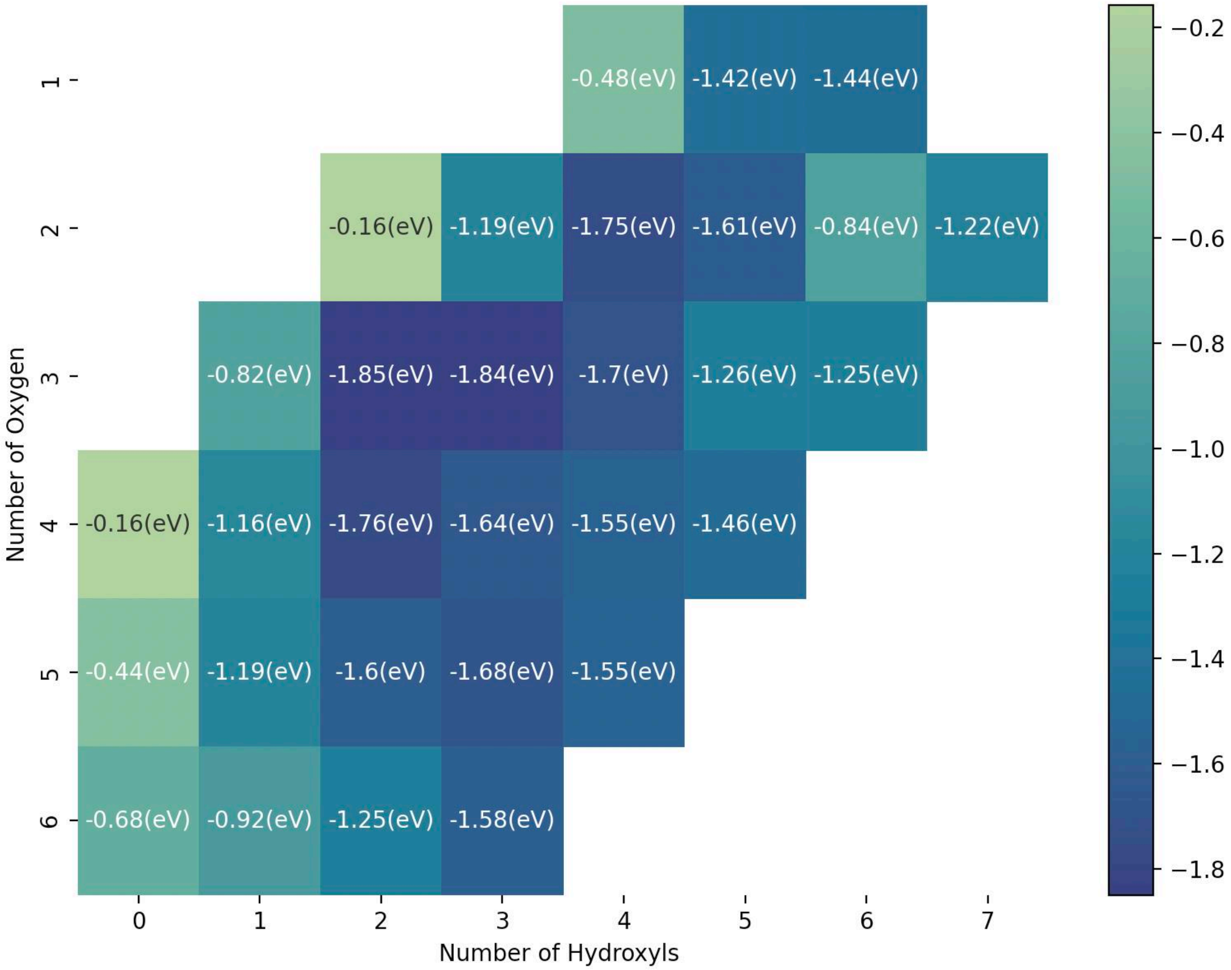

Figure E.2 FES of the structures with 1 formate in the reaction condition: Pressure = 0.013atm, Conversion = 2%, Temperature = 500K, CO_2/H_2 ratio: 1:9. The x axis represents the number of hydroxyls and the y axis represents the number of Oxygens on the Zr cluster. The color gradient represents the adsorption energy of the ligand wrt the Zr_3O_6/Cu 111 surface. The annotations on figure represents the adsorption energy.

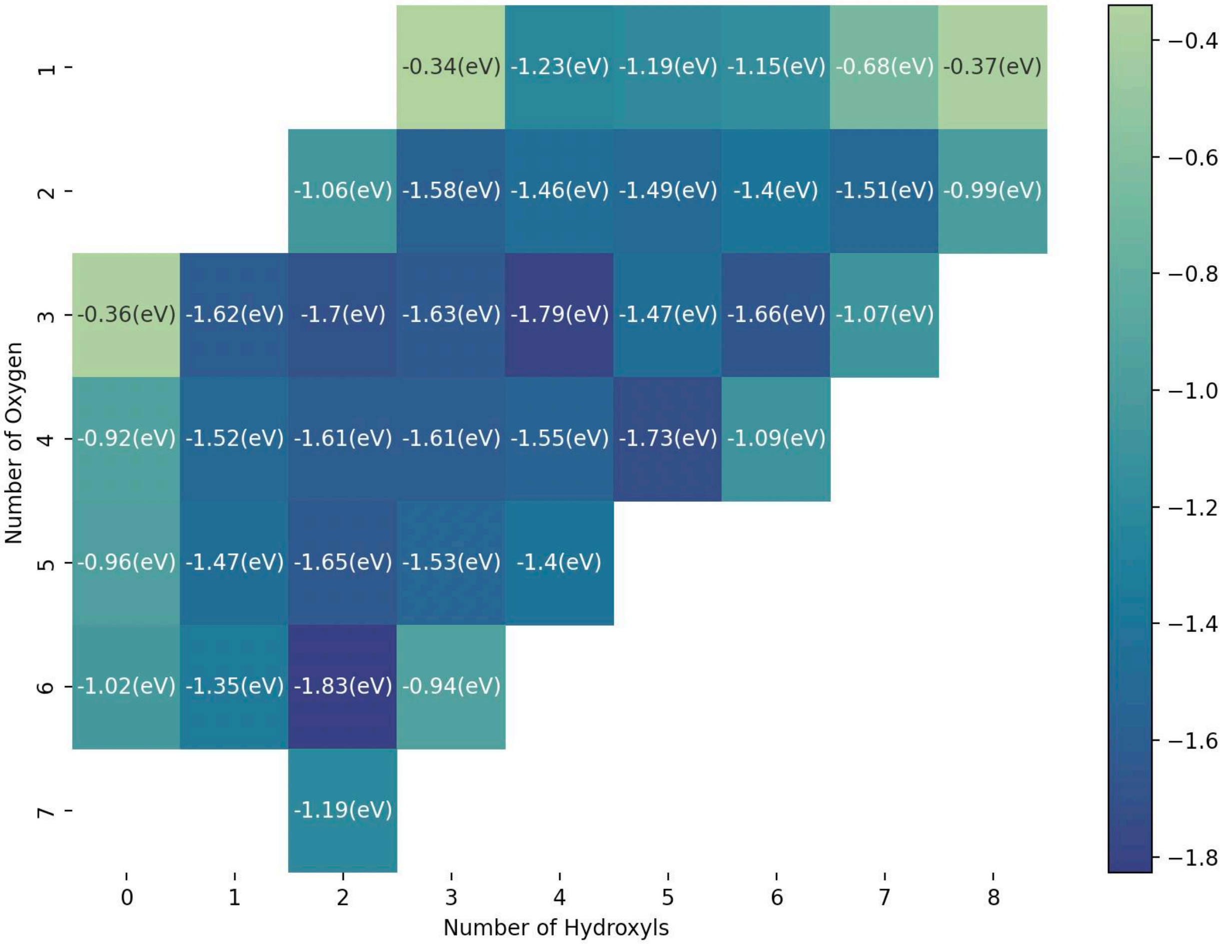

Figure E.3 FES of the structures with 2 formates in the reaction condition: Pressure = 0.013atm, Conversion = 2%, Temperature = 500K, CO_2/H_2 ratio: 1:9. The x axis represents the number of hydroxyls and the y axis represents the number of Oxygens on the Zr cluster. The color gradient represents the adsorption energy of the ligand wrt the Zr_3O_6/Cu 111 surface. The annotations on figure represents the adsorption energy.

E.2 Free Energy Surface [Reaction Condition : Pressure = 4.93 atm, Conversion = 0.8%, CO_2/H_2 ratio = 1:3, and Temperature = 493.15K]

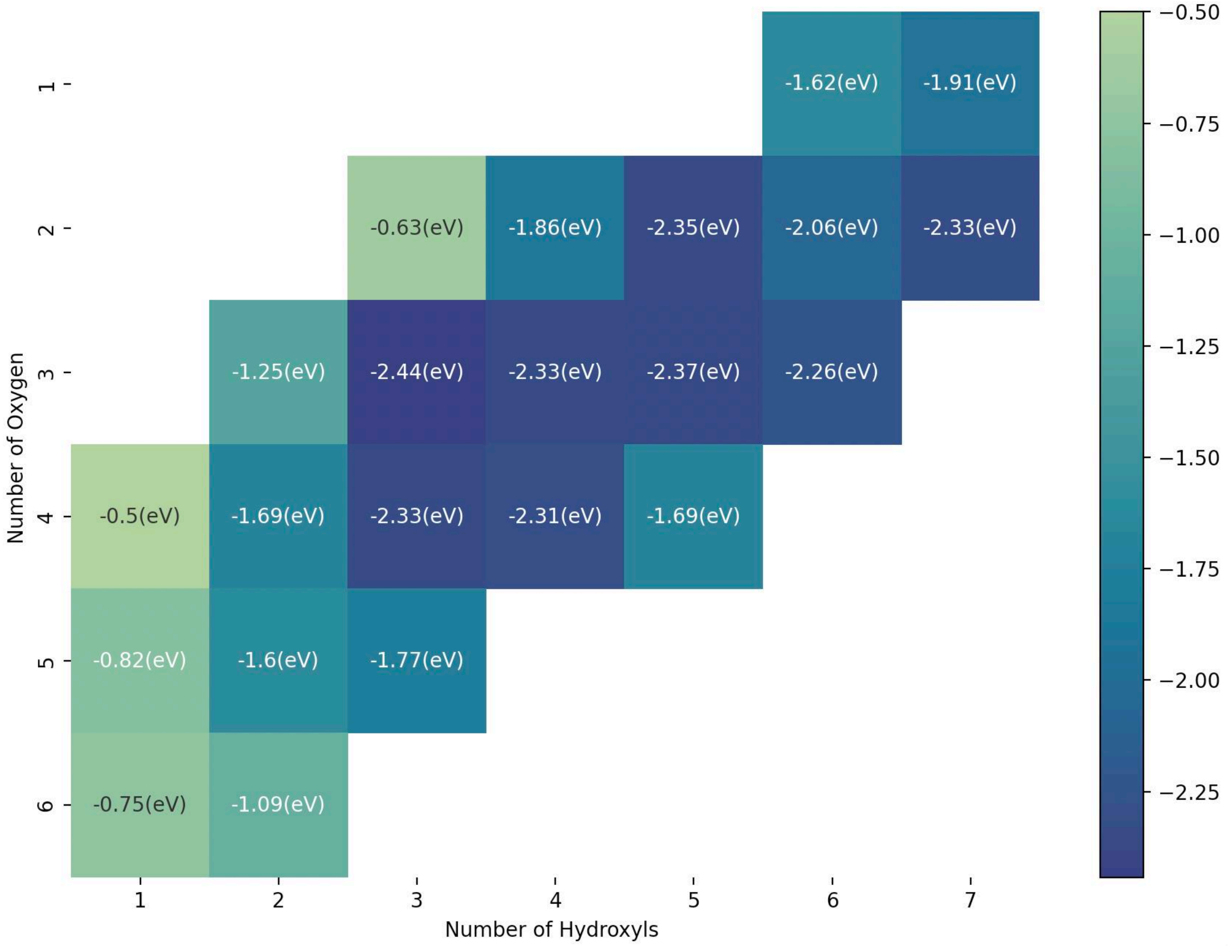

Figure E.4 FES of the structures with no formates in the reaction condition: Pressure = 4.93 atm, Conversion = 0.8%, CO_2/H_2 ratio = 1:3, and Temperature = 493.15K The x axis represents the number of hydroxyls and the y axis represents the number of Oxygens on the Zr cluster. The color gradient represents the adsorption energy of the ligand wrt the Zr_3O_6/Cu 111 surface. The annotations on figure represents the adsorption energy.

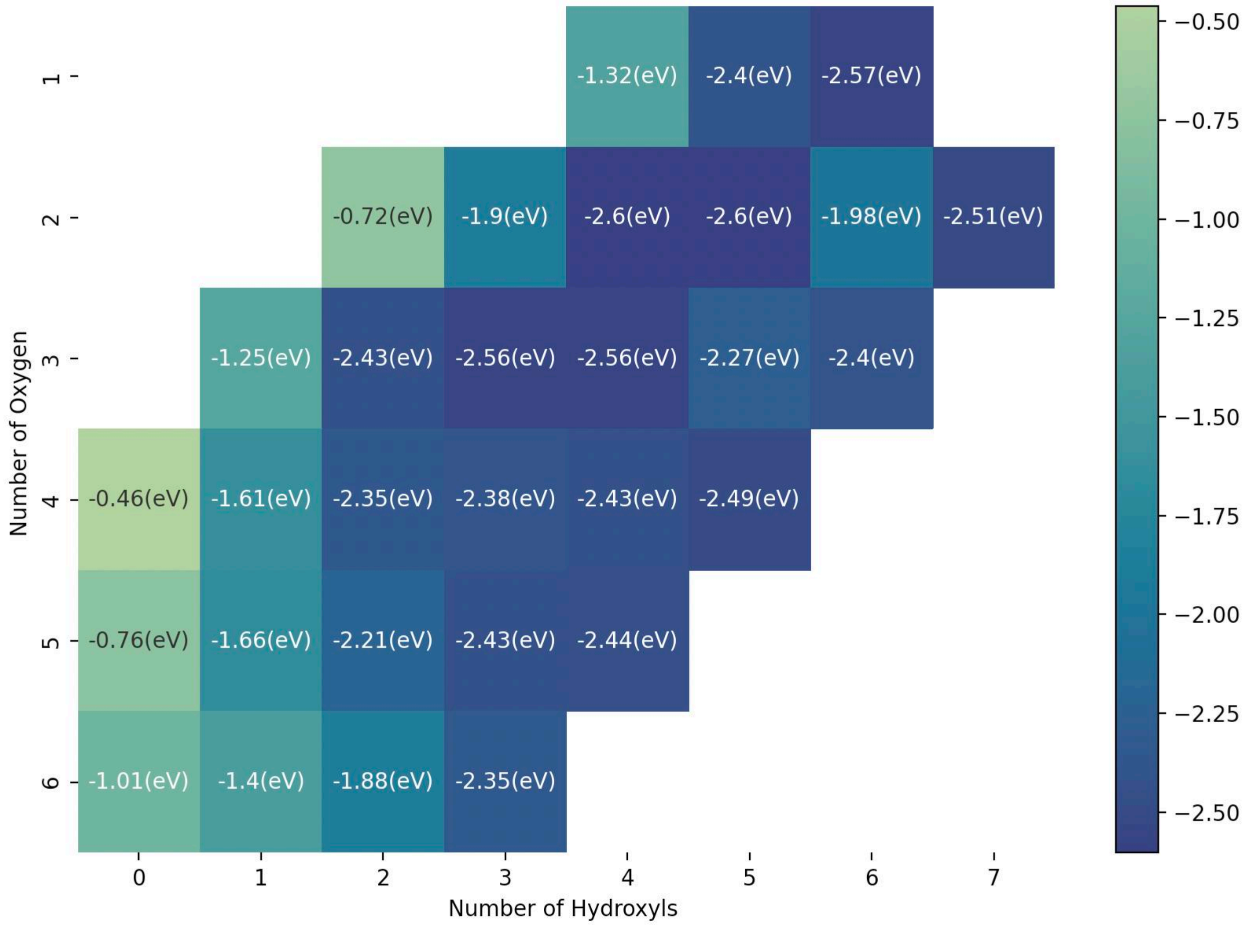

Figure E.5 FES of the structures with 1 formate in the reaction condition: Pressure = 4.93 atm, Conversion = 0.8%, CO_2/H_2 ratio = 1:3, and Temperature = 493.15K. The x axis represents the number of hydroxyls and the y axis represents the number of Oxygens on the Zr cluster. The color gradient represents the adsorption energy of the ligand wrt the Zr_3O_6/Cu 111 surface. The annotations on figure represents the adsorption energy.

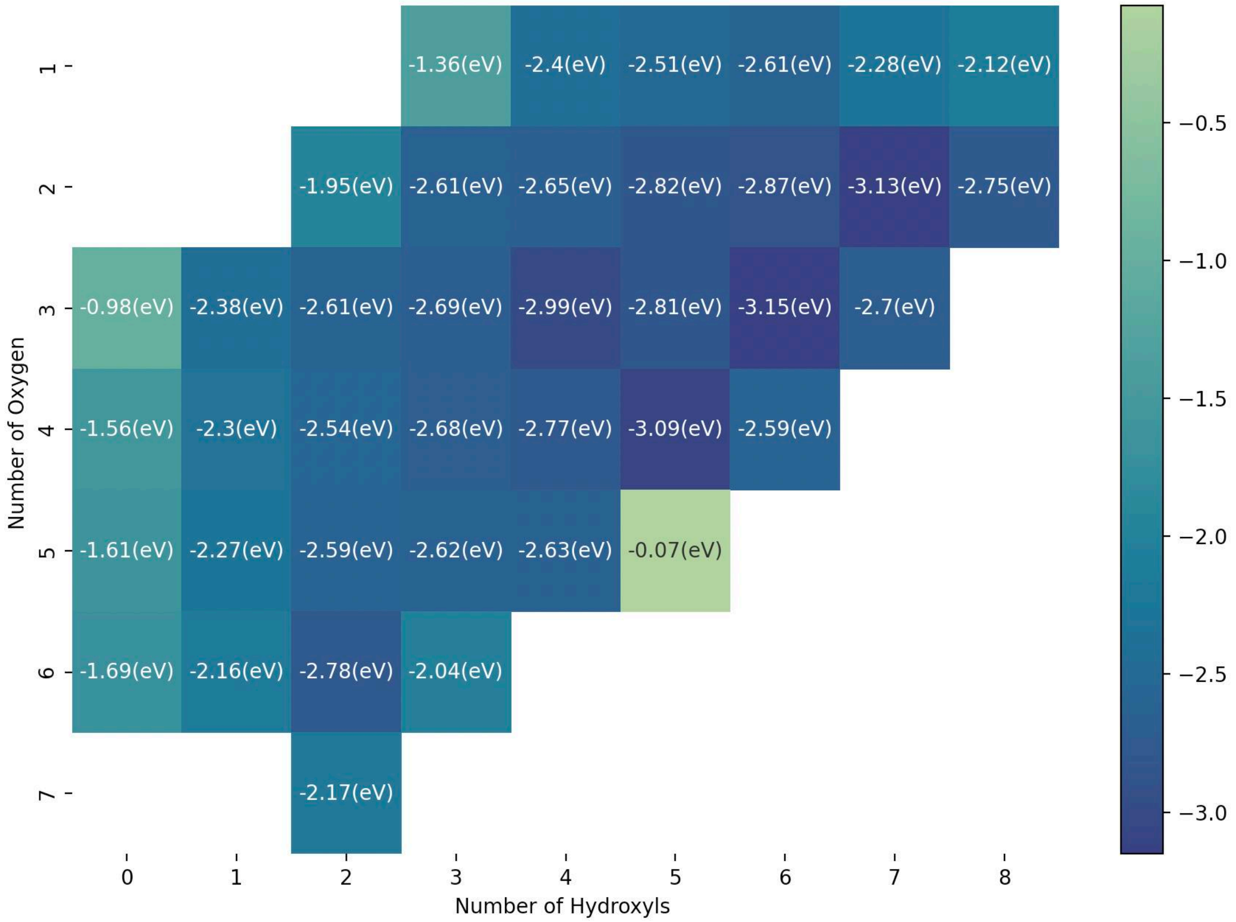

Figure E.6 FES of the structures with 2 formate in the reaction condition: Pressure = 4.93 atm, Conversion = 0.8%, CO_2/H_2 ratio = 1:3, and Temperature = 493.15K. The x axis represents the number of hydroxyls and the y axis represents the number of Oxygens on the Zr cluster. The color gradient represents the adsorption energy of the ligand wrt the Zr_3O_6/Cu 111 surface. The annotations on figure represents the adsorption energy.

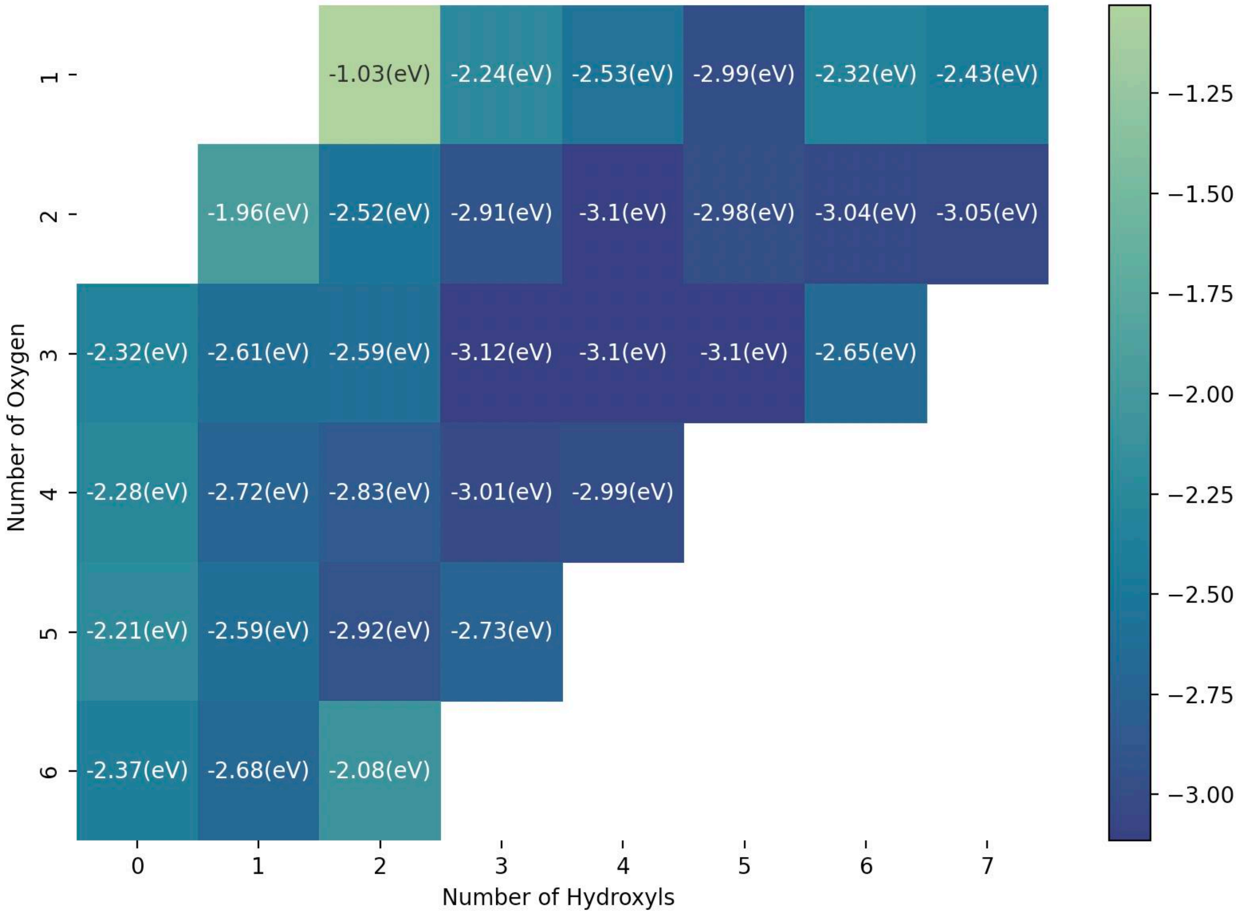

Figure E.7 FES of the structures with 3 formate in the reaction condition: Pressure = 4.93 atm, Conversion = 0.8%, CO_2/H_2 ratio = 1:3, and Temperature = 493.15K. The x axis represents the number of hydroxyls and the y axis represents the number of Oxygens on the Zr cluster. The color gradient represents the adsorption energy of the ligand wrt the Zr_3O_6/Cu 111 surface. The annotations on figure represents the adsorption energy.

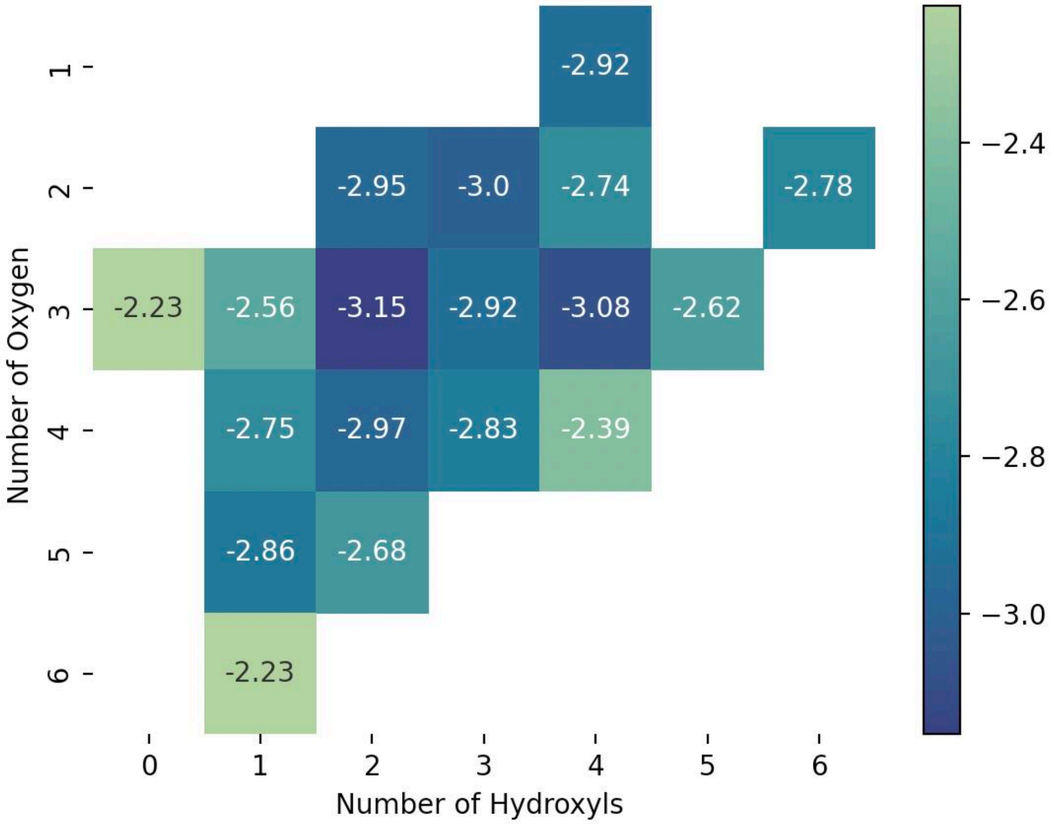

Figure E.8 FES of the structures with 4 formate in the reaction condition: Pressure = 4.93 atm, Conversion = 0.8%, CO_2/H_2 ratio = 1:3, and Temperature = 493.15K. The x axis represents the number of hydroxyls and the y axis represents the number of Oxygens on the Zr cluster. The color gradient represents the adsorption energy of the ligand wrt the Zr_3O_6/Cu 111 surface. The annotations on figure represents the adsorption energy.

Bibliography

(1) ERTL, G. HETEROGENEOUS CATALYSIS: WHERE ARE WE? **2018**, 61–62. https://doi.org/10.1142/9789813237179_0012.

(2) Thomas, J.; Thomas, W. *Principles and Practice of Heterogeneous Catalysis*; 2014.

(3) Bond, G. C. Heterogeneous Catalysis. Oxford University Press,New York, NY January 1, 1987.

(4) Catalysts, J. V.-; 2017, undefined. Heterogeneous Catalysis on Metal Oxides. *mdpi.com* **2017**, *7* (11). https://doi.org/10.3390/catal7110341.

(5) Surface Processes and Composition of Metal Oxide Surfaces. **2005**, 133–154. https://doi.org/10.1201/9781420028126-9.

(6) Chizallet, C.; Costentin, G.; Che, M.; Delbecq, F.; Sautet, P. Revisiting Acido-Basicity of the MgO Surface by Periodic Density Functional Theory Calculations: Role of Surface Topology and Ion Coordination on Water Dissociation. *J Phys Chem B* **2006**, *110* (32), 15878–15886. https://doi.org/10.1021/JP060840L.

(7) Coluccia, S.; Tench, A. J. Spectroscopic Studies of Hydrogen Adsorption on Highly Dispersed Mgo. *Stud Surf Sci Catal* **1981**, *7*, 1154–1169. https://doi.org/10.1016/S0167-2991(08)64722-9.

(8) Yang, X. F.; Wang, A.; Qiao, B.; Li, J.; Liu, J.; Zhang, T. Single-Atom Catalysts: A New Frontier in Heterogeneous Catalysis. *Acc Chem Res* **2013**, *46* (8), 1740–1748. https://doi.org/10.1021/AR300361M/ASSET/IMAGES/LARGE/AR-2012-00361M_0009.JPEG.

(9) Vajda, S.; White, M. G. Catalysis Applications of Size-Selected Cluster Deposition. *ACS Catal* **2015**, *5* (12), 7152–7176. https://doi.org/10.1021/ACSCATAL.5B01816.

(10) Crampton, A. S.; Rötzer, M. D.; Ridge, C. J.; Schweinberger, F. F.; Heiz, U.; Yoon, B.; Landman, U. Structure Sensitivity in the Nonscalable Regime Explored via Catalysed Ethylene Hydrogenation on Supported Platinum Nanoclusters. *Nat Commun* **2016**, *7*. https://doi.org/10.1038/NCOMMS10389.

(11) Heiz, U.; Sanchez, A.; Abbet, S.; Schneider, W. D. Catalytic Oxidation of Carbon Monoxide on Monodispersed Platinum Clusters: Each Atom Counts. *J Am Chem Soc* **1999**, *121* (13), 3214–3217. https://doi.org/10.1021/JA983616L.

(12) Heiz, U.; Bullock, E. L. Fundamental Aspects of Catalysis on Supported Metal Clusters. *J Mater Chem* **2004**, 564–577. https://doi.org/10.1039/B313560H.

(13) Van Hardeveld, R.; Hartog, F. The Statistics of Surface Atoms and Surface Sites on Metal Crystals. *Surf Sci* **1969**, *15* (2), 189–230. https://doi.org/10.1016/0039-6028(69)90148-4.

(14) Lopez, N.; Janssens, T. V. W.; Clausen, B. S.; Xu, Y.; Mavrikakis, M.; Bligaard, T.; Nørskov, J. K. On the Origin of the Catalytic Activity of Gold Nanoparticles for Low-Temperature CO Oxidation. *J Catal* **2004**, *223* (1), 232–235. https://doi.org/10.1016/J.JCAT.2004.01.001.

(15) Sun, G.; Alexandrova, A. N.; Sautet, P. Pt8 Cluster on Alumina under a Pressure of Hydrogen: Support-Dependent Reconstruction from First-Principles Global Optimization. *J Chem Phys* **2019**, *151* (19), 194703. https://doi.org/10.1063/1.5129296.

(16) Kumari, S.; Masubuchi, T.; White, H. S.; Alexandrova, A.; Anderson, S. L.; Sautet, P. Electrocatalytic Hydrogen Evolution at Full Atomic Utilization over ITO-Supported Sub-

Nano-Ptn Clusters: High, Size-Dependent Activity Controlled by Fluxional Pt Hydride Species. *J Am Chem Soc* **2023**. https://doi.org/10.1021/JACS.2C13063.

(17) Sato, K.; Aoki, M.; Ogawa, M.; Hashimoto, T.; Noyori, R.; Rudolph, see J.; Reddy, K. L.; Chiang, J. P.; Sharpless, K. B. Onset of Catalytic Activity of Gold Clusters on Titania with the Appearance of Nonmetallic Properties. *Science (1979)* **1998**, *281* (5383), 1647–1650. https://doi.org/10.1126/SCIENCE.281.5383.1647.

(18) Li, J.; Li, X.; Zhai, H. J.; Wang, L. S. Au20: A Tetrahedral Cluster. *Science (1979)* **2003**, *299* (5608), 864–867. https://doi.org/10.1126/SCIENCE.1079879.

(19) Campbell, C. T. Electronic Perturbations. *Nature Chemistry 2012 4:8* **2012**, *4* (8), 597–598. https://doi.org/10.1038/nchem.1412.

(20) Yoon, B.; Häkkinen, H.; Landman, U.; Wörz, A. S.; Antonietti, J. M.; Abbet, S.; Judai, K.; Heiz, U. Charging Effects on Bonding and Catalyzed Oxidation of CO on Au8 Clusters on MgO. *Science (1979)* **2005**, *307* (5708), 403–407. https://doi.org/10.1126/SCIENCE.1104168.

(21) Call, S. T.; Zubarev, D. Y.; Boldyrev, A. I. Global Minimum Structure Searches via Particle Swarm Optimization. *J Comput Chem* **2007**, *28* (7), 1177–1186. https://doi.org/10.1002/JCC.20621.

(22) Avendaño-Franco, G.; Romero, A. H. Firefly Algorithm for Structural Search. *J Chem Theory Comput* **2016**, *12* (7), 3416–3428. https://doi.org/10.1021/ACS.JCTC.5B01157.

(23) Alexandrova, A. N.; Boldyrev, A. I. Search for the Lin0/+1/-1 (N= 5-7) Lowest-Energy Structures Using the Ab Initio Gradient Embedded Genetic Algorithm (Gega). Elucidation

of the Chemical Bonding in the Lithium Clusters. *J Chem Theory Comput* **2005**, *1* (4), 566–580. https://doi.org/10.1021/CT050093G.

(24) Alexandrova, A. N. H·(H2O)n Clusters: Microsolvation of the Hydrogen Atom via Molecular Ab Initio Gradient Embedded Genetic Algorithm (GEGA). *Journal of Physical Chemistry A* **2010**, *114* (48), 12591–12599. https://doi.org/10.1021/JP1092543.

(25) Kanters, R. P. F.; Donald, K. J. CLUSTER: Searching for Unique Low Energy Minima of Structures Using a Novel Implementation of a Genetic Algorithm. *J Chem Theory Comput* **2014**, *10* (12), 5729–5737. https://doi.org/10.1021/CT500744K.

(26) Davis, J. B. A.; Shayeghi, A.; Horswell, S. L.; Johnston, R. L. The Birmingham Parallel Genetic Algorithm and Its Application to the Direct DFT Global Optimisation of IrN (N = 10-20) Clusters. *Nanoscale* **2015**, *7* (33), 14032–14038. https://doi.org/10.1039/C5NR03774C.

(27) Oganov, A. R. Modern Methods of Crystal Structure Prediction.

(28) Zhai, H. J.; Zhao, Y. F.; Li, W. L.; Chen, Q.; Bai, H.; Hu, H. S.; Piazza, Z. A.; Tian, W. J.; Lu, H. G.; Wu, Y. B.; Mu, Y. W.; Wei, G. F.; Liu, Z. P.; Li, J.; Li, S. D.; Wang, L. S. Observation of an All-Boron Fullerene. *Nat Chem* **2014**, *6* (8), 727–731. https://doi.org/10.1038/NCHEM.1999.

(29) Sun, G.; Sautet, P. Metastable Structures in Cluster Catalysis from First-Principles: Structural Ensemble in Reaction Conditions and Metastability Triggered Reactivity. *J Am Chem Soc* **2018**, *140* (8), 2812–2820. https://doi.org/10.1021/JACS.7B11239/ASSET/IMAGES/JA-2017-11239P_M008.GIF.

(30) Sun, G.; Alexandrova, A. N.; Sautet, P. Structural Rearrangements of Subnanometer Cu Oxide Clusters Govern Catalytic Oxidation. *ACS Catal* **2020**, *10* (9), 5309–5317. https://doi.org/10.1021/ACSCATAL.0C00824/SUPPL_FILE/CS0C00824_SI_002.PDF.

(31) Wang, J.; Ma, L.; Zhao, J.; Jackson, K. A. Structural Growth Behavior and Polarizability of Cdn Te n (N=1-14) Clusters. *Journal of Chemical Physics* **2009**, *130* (21). https://doi.org/10.1063/1.3147519.

(32) Baxter, E. T.; Ha, M. A.; Cass, A. C.; Alexandrova, A. N.; Anderson, S. L. Ethylene Dehydrogenation on Pt4,7,8 Clusters on Al2O3: Strong Cluster Size Dependence Linked to Preferred Catalyst Morphologies. *ACS Catal* **2017**, *7* (5), 3322–3335. https://doi.org/10.1021/ACSCATAL.7B00409/ASSET/IMAGES/CS-2017-00409T_M003.GIF.

(33) Ha, M. A.; Baxter, E. T.; Cass, A. C.; Anderson, S. L.; Alexandrova, A. N. Boron Switch for Selectivity of Catalytic Dehydrogenation on Size-Selected Pt Clusters on Al2O3. *J Am Chem Soc* **2017**, *139* (33), 11568–11575. https://doi.org/10.1021/JACS.7B05894/SUPPL_FILE/JA7B05894_SI_001.PDF.

(34) Crabtree, G. W.; Dresselhaus, M. S.; Buchanan, M. V. The Hydrogen Economy. *Phys Today* **2004**, *57* (12), 39–44. https://doi.org/10.1063/1.1878333.

(35) Yu, K. M. K.; Tong, W.; West, A.; Cheung, K.; Li, T.; Smith, G.; Guo, Y.; Tsang, S. C. E. Non-Syngas Direct Steam Reforming of Methanol to Hydrogen and Carbon Dioxide at Low Temperature. *Nature Communications 2012 3:1* **2012**, *3* (1), 1–7. https://doi.org/10.1038/ncomms2242.

(36) Subbaraman, R.; Tripkovic, D.; Chang, K. C.; Strmcnik, D.; Paulikas, A. P.; Hirunsit, P.; Chan, M.; Greeley, J.; Stamenkovic, V.; Markovic, N. M. Trends in Activity for the Water Electrolyser Reactions on 3d M(Ni,Co,Fe,Mn) Hydr(Oxy)Oxide Catalysts. *Nature Materials 2012 11:6* **2012**, *11* (6), 550–557. https://doi.org/10.1038/nmat3313.

(37) Subbaraman, R.; Tripkovic, D.; Strmcnik, D.; Chang, K. C.; Uchimura, M.; Paulikas, A. P.; Stamenkovic, V.; Markovic, N. M. Enhancing Hydrogen Evolution Activity in Water Splitting by Tailoring Li+-Ni(OH)2-Pt Interfaces. *Science (1979)* **2011**, *334* (6060), 1256–1260. https://doi.org/10.1126/SCIENCE.1211934/SUPPL_FILE/SUBBARAMAN.SOM.PDF.

(38) Yin, H.; Zhao, S.; Zhao, K.; Muqsit, A.; Tang, H.; Chang, L.; Zhao, H.; Gao, Y.; Tang, Z. Ultrathin Platinum Nanowires Grown on Single-Layered Nickel Hydroxide with High Hydrogen Evolution Activity. *Nature Communications 2015 6:1* **2015**, *6* (1), 1–8. https://doi.org/10.1038/ncomms7430.

(39) García-Mota, M.; Vojvodic, A.; Metiu, H.; Man, I. C.; Su, H. Y.; Rossmeisl, J.; Nørskov, J. K. Tailoring the Activity for Oxygen Evolution Electrocatalysis on Rutile TiO2(110) by Transition-Metal Substitution. *ChemCatChem* **2011**, *3* (10). https://doi.org/10.1002/cctc.201100160.

(40) Zhao, Y.; Yang, K. R.; Wang, Z.; Yan, X.; Cao, S.; Ye, Y.; Dong, Q.; Zhang, X.; Thorne, J. E.; Jin, L.; Materna, K. L.; Trimpalis, A.; Bai, H.; Fakra, S. C.; Zhong, X.; Wang, P.; Pan, X.; Guo, J.; Flytzani-Stephanopoulos, M.; Brudvig, G. W.; Batista, V. S.; Wang, D. Stable Iridium Dinuclear Heterogeneous Catalysts Supported on Metal-Oxide Substrate for Solar Water Oxidation. *Proc Natl Acad Sci U S A* **2018**, *115* (12). https://doi.org/10.1073/pnas.1722137115.

(41) Zhao, Y.; Yan, X.; Yang, K. R.; Cao, S.; Dong, Q.; Thorne, J. E.; Materna, K. L.; Zhu, S.; Pan, X.; Flytzani-Stephanopoulos, M.; Brudvig, G. W.; Batista, V. S.; Wang, D. End-On Bound Iridium Dinuclear Heterogeneous Catalysts on WO3 for Solar Water Oxidation. *ACS Cent Sci* **2018**, *4* (9). https://doi.org/10.1021/acscentsci.8b00335.

(42) Zhu, C.; Shi, Q.; Feng, S.; Du, D.; Lin, Y. Single-Atom Catalysts for Electrochemical Water Splitting. *ACS Energy Lett* **2018**, *3* (7), 1713–1721. https://doi.org/10.1021/ACSENERGYLETT.8B00640.

(43) Fei, H.; Dong, J.; Feng, Y.; Allen, C. S.; Wan, C.; Volosskiy, B.; Li, M.; Zhao, Z.; Wang, Y.; Sun, H.; An, P.; Chen, W.; Guo, Z.; Lee, C.; Chen, D.; Shakir, I.; Liu, M.; Hu, T.; Li, Y.; Kirkland, A. I.; Duan, X.; Huang, Y. General Synthesis and Definitive Structural Identification of MN4C4 Single-Atom Catalysts with Tunable Electrocatalytic Activities. *Nat Catal* **2018**, *1* (1). https://doi.org/10.1038/s41929-017-0008-y.

(44) Cao, L.; Luo, Q.; Chen, J.; Wang, L.; Lin, Y.; Wang, H.; Liu, X.; Shen, X.; Zhang, W.; Liu, W.; Qi, Z.; Jiang, Z.; Yang, J.; Yao, T. Dynamic Oxygen Adsorption on Single-Atomic Ruthenium Catalyst with High Performance for Acidic Oxygen Evolution Reaction. *Nat Commun* **2019**, *10* (1). https://doi.org/10.1038/s41467-019-12886-z.

(45) Ganguli, S.; Das, S.; Kumari, S.; Inta, H. R.; Tiwari, A. K.; Mahalingam, V. Effect of Intrinsic Properties of Anions on the Electrocatalytic Activity of NiCo2O4 and NiCo2OxS4- x Grown by Chemical Bath Deposition. *ACS Omega* **2018**, *3* (8), 9066–9074. https://doi.org/10.1021/ACSOMEGA.8B00952/ASSET/IMAGES/LARGE/AO-2018-00952Q_0002.JPEG.

(46) Lebedev, D.; Ezhov, R.; Heras-Domingo, J.; Comas-Vives, A.; Kaeffer, N.; Willinger, M.; Solans-Monfort, X.; Huang, X.; Pushkar, Y.; Copéret, C. Atomically Dispersed Iridium on Indium Tin Oxide Efficiently Catalyzes Water Oxidation. *ACS Cent Sci* **2020**, *6* (7), 1189–1198. https://doi.org/10.1021/ACSCENTSCI.0C00604/SUPPL_FILE/OC0C00604_LIVESLIDES.MP4.

(47) Shi, Q.; Zhu, C.; Du, D.; Lin, Y. Robust Noble Metal-Based Electrocatalysts for Oxygen Evolution Reaction. *Chem Soc Rev* **2019**, *48* (12), 3181–3192. https://doi.org/10.1039/C8CS00671G.

(48) Lee, Y.; Suntivich, J.; May, K. J.; Perry, E. E.; Shao-Horn, Y. Synthesis and Activities of Rutile IrO2 and RuO2 Nanoparticles for Oxygen Evolution in Acid and Alkaline Solutions. *J Phys Chem Lett* **2012**, *3* (3), 399–404. https://doi.org/10.1021/JZ2016507.

(49) McCrory, C. C. L.; Jung, S.; Peters, J. C.; Jaramillo, T. F. Benchmarking Heterogeneous Electrocatalysts for the Oxygen Evolution Reaction. *J Am Chem Soc* **2013**, *135* (45), 16977–16987. https://doi.org/10.1021/JA407115P/SUPPL_FILE/JA407115P_SI_001.PDF.

(50) Montoya, J. H.; Seitz, L. C.; Chakthranont, P.; Vojvodic, A.; Jaramillo, T. F.; Nørskov, J. K. Materials for Solar Fuels and Chemicals. *Nature Materials 2017 16:1* **2016**, *16* (1), 70–81. https://doi.org/10.1038/nmat4778.

(51) Wei, C.; Rao, R. R.; Peng, J.; Huang, B.; Stephens, I. E. L.; Risch, M.; Xu, Z. J.; Shao-Horn, Y. Recommended Practices and Benchmark Activity for Hydrogen and Oxygen Electrocatalysis in Water Splitting and Fuel Cells. *Adv Mater* **2019**, *31* (31). https://doi.org/10.1002/ADMA.201806296.

(52) Suen, N. T.; Hung, S. F.; Quan, Q.; Zhang, N.; Xu, Y. J.; Chen, H. M. Electrocatalysis for the Oxygen Evolution Reaction: Recent Development and Future Perspectives. *Chem Soc Rev* **2017**, *46* (2), 337–365. https://doi.org/10.1039/C6CS00328A.

(53) Hunter, B. M.; Gray, H. B.; Müller, A. M. Earth-Abundant Heterogeneous Water Oxidation Catalysts. *Chem Rev* **2016**, *116* (22), 14120–14136. https://doi.org/10.1021/ACS.CHEMREV.6B00398.

(54) Han, L.; Dong, S.; Wang, E. Transition-Metal (Co, Ni, and Fe)-Based Electrocatalysts for the Water Oxidation Reaction. *Adv Mater* **2016**, *28* (42), 9266–9291. https://doi.org/10.1002/ADMA.201602270.

(55) Wang, H.; Lee, H. W.; Deng, Y.; Lu, Z.; Hsu, P. C.; Liu, Y.; Lin, D.; Cui, Y. Bifunctional Non-Noble Metal Oxide Nanoparticle Electrocatalysts through Lithium-Induced Conversion for Overall Water Splitting. *Nature Communications 2015 6:1* **2015**, *6* (1), 1–8. https://doi.org/10.1038/ncomms8261.

(56) Xia, B. Y.; Yan, Y.; Li, N.; Wu, H. Bin; Lou, X. W. D.; Wang, X. A Metal-Organic Framework-Derived Bifunctional Oxygen Electrocatalyst. *NatEn* **2016**, *1* (1), 15006. https://doi.org/10.1038/NENERGY.2015.6.

(57) Han, L.; Yu, X. Y.; Lou, X. W. (David). Formation of Prussian-Blue-Analog Nanocages via a Direct Etching Method and Their Conversion into Ni-Co-Mixed Oxide for Enhanced Oxygen Evolution. *Adv Mater* **2016**, *28* (23), 4601–4605. https://doi.org/10.1002/ADMA.201506315.

(58) Bao, J.; Zhang, X.; Fan, B.; Zhang, J.; Zhou, M.; Yang, W.; Hu, X.; Wang, H.; Pan, B.; Xie, Y. Ultrathin Spinel-Structured Nanosheets Rich in Oxygen Deficiencies for Enhanced

Electrocatalytic Water Oxidation. *Angew Chem Int Ed Engl* **2015**, *54* (25), 7399–7404. https://doi.org/10.1002/ANIE.201502226.

(59) Gao, X.; Zhang, H.; Li, Q.; Yu, X.; Hong, Z.; Zhang, X.; Liang, C.; Lin, Z. Hierarchical NiCo2 O4 Hollow Microcuboids as Bifunctional Electrocatalysts for Overall Water-Splitting. *Angew Chem Int Ed Engl* **2016**, *55* (21), 6290–6294. https://doi.org/10.1002/ANIE.201600525.

(60) Yu, L.; Yang, J. F.; Guan, B. Y.; Lu, Y.; Lou, X. W. D. Hierarchical Hollow Nanoprisms Based on Ultrathin Ni-Fe Layered Double Hydroxide Nanosheets with Enhanced Electrocatalytic Activity towards Oxygen Evolution. *Angew Chem Int Ed Engl* **2018**, *57* (1), 172–176. https://doi.org/10.1002/ANIE.201710877.

(61) Wu, T.; Sun, S.; Song, J.; Xi, S.; Du, Y.; Chen, B.; Sasangka, W. A.; Liao, H.; Gan, C. L.; Scherer, G. G.; Zeng, L.; Wang, H.; Li, H.; Grimaud, A.; Xu, Z. J. Iron-Facilitated Dynamic Active-Site Generation on Spinel CoAl2O4 with Self-Termination of Surface Reconstruction for Water Oxidation. *Nature Catalysis 2019 2:9* **2019**, *2* (9), 763–772. https://doi.org/10.1038/s41929-019-0325-4.

(62) Chen, Y.; Li, H.; Wang, J.; Du, Y.; Xi, S.; Sun, Y.; Sherburne, M.; Ager, J. W.; Fisher, A. C.; Xu, Z. J. Exceptionally Active Iridium Evolved from a Pseudo-Cubic Perovskite for Oxygen Evolution in Acid. *Nature Communications 2019 10:1* **2019**, *10* (1), 1–10. https://doi.org/10.1038/s41467-019-08532-3.

(63) Tung, C. W.; Hsu, Y. Y.; Shen, Y. P.; Zheng, Y.; Chan, T. S.; Sheu, H. S.; Cheng, Y. C.; Chen, H. M. Reversible Adapting Layer Produces Robust Single-Crystal Electrocatalyst for Oxygen Evolution. *Nat Commun* **2015**, *6*. https://doi.org/10.1038/NCOMMS9106.

(64) Xu, X.; Song, F.; Hu, X. A Nickel Iron Diselenide-Derived Efficient Oxygen-Evolution Catalyst. *Nature Communications 2016 7:1* **2016**, *7* (1), 1–7. https://doi.org/10.1038/ncomms12324.

(65) *Energy Outlook | Energy economics | Home*. https://www.bp.com/en/global/corporate/energy-economics/energy-outlook.html (accessed 2023-05-23).

(66) *Mission Possible: Reaching Net-Zero Carbon Emissions - ETC*. https://www.energy-transitions.org/publications/mission-possible/ (accessed 2023-05-16).

(67) Jang, J.; Shen, K.; Morales-Guio, C. G. Electrochemical Direct Partial Oxidation of Methane to Methanol. *Joule* **2019**, *3*, 2589.

(68) Renewable Energy Agency, I.; Methanol Institute, the. INNOVATION OUTLOOK RENEWABLE METHANOL in Partnership With. **2021**.

(69) Graciani, J.; Mudiyanselage, K.; Xu, F.; Baber, A. E.; Evans, J.; Senanayake, S. D.; Stacchiola, D. J.; Liu, P.; Hrbek, J.; Fernández Sanz, J.; Rodriguez, J. A. Catalysis. Highly Active Copper-Ceria and Copper-Ceria-Titania Catalysts for Methanol Synthesis from CO_2. *Science* **2014**, *345* (6196), 546–550. https://doi.org/10.1126/SCIENCE.1253057.

(70) Centi, G.; Quadrelli, E. A.; Perathoner, S. Catalysis for CO2 Conversion: A Key Technology for Rapid Introduction of Renewable Energy in the Value Chain of Chemical Industries. *Energy Environ Sci* **2013**, *6* (6), 1711–1731. https://doi.org/10.1039/C3EE00056G.

(71) Dorner, R. W.; Hardy, D. R.; Williams, F. W.; Willauer, H. D. Heterogeneous Catalytic CO 2 Conversion to Value-Added Hydrocarbons. *Energy Environ Sci* **2010**, *3* (7), 884–890. https://doi.org/10.1039/C001514H.

(72) Inui, T.; Takeguchi, T. Effective Conversion of Carbon Dioxide and Hydrogen to Hydrocarbons. *Catal Today* **1991**, *10* (1), 95–106. https://doi.org/10.1016/0920-5861(91)80077-M.

(73) Kondratenko, E. V.; Mul, G.; Baltrusaitis, J.; Larrazábal, G. O.; Pérez-Ramírez, J. Status and Perspectives of CO2 Conversion into Fuels and Chemicals by Catalytic, Photocatalytic and Electrocatalytic Processes. *Energy Environ Sci* **2013**, *6* (11), 3112–3135. https://doi.org/10.1039/C3EE41272E.

(74) Behrens, M.; Studt, F.; Kasatkin, I.; Kühl, S.; Hävecker, M.; Abild-Pedersen, F.; Zander, S.; Girgsdies, F.; Kurr, P.; Kniep, B. L.; Tovar, M.; Fischer, R. W.; Nørskov, J. K.; Schlögl, R. The Active Site of Methanol Synthesis over Cu/ZnO/Al2O3 Industrial Catalysts. *Science* **2012**, *336* (6083), 893–897. https://doi.org/10.1126/SCIENCE.1219831.

(75) Nie, X.; Esopi, M. R.; Janik, M. J.; Asthagiri, A. Selectivity of CO2 Reduction on Copper Electrodes: The Role of the Kinetics of Elementary Steps. *Angewandte Chemie - International Edition* **2013**, *52* (9), 2459–2462. https://doi.org/10.1002/ANIE.201208320.

(76) Yang, H.; Xu, Z.; Fan, M.; Gupta, R.; Slimane, R. B.; Bland, A. E.; Wright, I. Progress in Carbon Dioxide Separation and Capture: A Review. *Journal of Environmental Sciences* **2008**, *20* (1), 14–27. https://doi.org/10.1016/S1001-0742(08)60002-9.

(77) Aresta, M.; Dibenedetto, A.; Angelini, A. Catalysis for the Valorization of Exhaust Carbon: From CO2 to Chemicals, Materials, and Fuels. Technological Use of CO2. *Chem Rev* **2014**, *114* (3), 1709–1742. https://doi.org/10.1021/CR4002758.

(78) Studt, F.; Sharafutdinov, I.; Abild-Pedersen, F.; Elkjær, C. F.; Hummelshøj, J. S.; Dahl, S.; Chorkendorff, I.; Nørskov, J. K. Discovery of a Ni-Ga Catalyst for Carbon Dioxide

Reduction to Methanol. *Nat Chem* **2014**, *6* (4), 320–324. https://doi.org/10.1038/NCHEM.1873.

(79) Porosoff, M. D.; Yan, B.; Chen, J. G. Catalytic Reduction of CO2 by H2 for Synthesis of CO, Methanol and Hydrocarbons: Challenges and Opportunities. *Energy Environ Sci* **2016**, *9* (1), 62–73. https://doi.org/10.1039/C5EE02657A.

(80) Morales-Guio, C.; Shen, K.; Yu-Chao, H.; Jang, J. Electrochemical Oxidation of Methane to Methanol on Electrodeposited Transition Metal Oxides. **2022**. https://doi.org/10.29363/NANOGE.NFM.2022.212.

(81) Liu, L.; Corma, A. Metal Catalysts for Heterogeneous Catalysis: From Single Atoms to Nanoclusters and Nanoparticles. *Chemical Reviews*. 2018. https://doi.org/10.1021/acs.chemrev.7b00776.

(82) Boudart, M. Turnover Rates in Heterogeneous Catalysis. *Chem Rev* **1995**. https://doi.org/10.1021/cr00035a009.

(83) Schlögl, R. Heterogeneous Catalysis. *Angewandte Chemie - International Edition*. 2015. https://doi.org/10.1002/anie.201410738.

(84) Munnik, P.; De Jongh, P. E.; De Jong, K. P. Recent Developments in the Synthesis of Supported Catalysts. *Chemical Reviews*. 2015. https://doi.org/10.1021/cr500486u.

(85) Meunier, F. C. Bridging the Gap between Surface Science and Industrial Catalysis. *ACS Nano* **2008**, *2* (12), 2441–2444. https://doi.org/10.1021/nn800787e.

(86) Haruta, M. Size- and Support-Dependency in the Catalysis of Gold. *Catal Today* **1997**, *36* (1), 153–166. https://doi.org/10.1016/S0920-5861(96)00208-8.

(87) Freund, H. J. Clusters and Islands on Oxides: From Catalysis via Electronics and Magnetism to Optics. *Surf Sci* **2002**, *500* (1–3), 271–299. https://doi.org/10.1016/S0039-6028(01)01543-6.

(88) Bansmann, J.; Baker, S. H.; Binns, C.; Blackman, J. A.; Bucher, J. P.; Dorantes-Dávila, J.; Dupuis, V.; Favre, L.; Kechrakos, D.; Kleibert, A.; Meiwes-Broer, K. H.; Pastor, G. M.; Perez, A.; Toulemonde, O.; Trohidou, K. N.; Tuaillon, J.; Xie, Y. Magnetic and Structural Properties of Isolated and Assembled Clusters. *Surface Science Reports*. Elsevier B.V. 2005, pp 189–275. https://doi.org/10.1016/j.surfrep.2004.10.001.

(89) Somorjai, G. A.; Frei, H.; Park, J. Y. Advancing the Frontiers in Nanocatalysis, Biointerfaces, and Renewable Energy Conversion by Innovations of Surface Techniques. *Journal of the American Chemical Society*. 2009, pp 16589–16605. https://doi.org/10.1021/ja9061954.

(90) Wang, A.; Li, J.; Zhang, T. Heterogeneous Single-Atom Catalysis. *Nature Reviews Chemistry*. 2018. https://doi.org/10.1038/s41570-018-0010-1.

(91) Tang, Y.; Asokan, C.; Xu, M.; Graham, G. W.; Pan, X.; Christopher, P.; Li, J.; Sautet, P. Rh Single Atoms on TiO2 Dynamically Respond to Reaction Conditions by Adapting Their Site. *Nat Commun* **2019**. https://doi.org/10.1038/s41467-019-12461-6.

(92) Liu, Q.; Zhang, Z. Platinum Single-Atom Catalysts: A Comparative Review towards Effective Characterization. *Catal Sci Technol* **2019**. https://doi.org/10.1039/c9cy01028a.

(93) Zhai, Y.; Pierre, D.; Si, R.; Deng, W.; Ferrin, P.; Nilekar, A. U.; Peng, G.; Herron, J. A.; Bell, D. C.; Saltsburg, H.; Mavrikakis, M.; Flytzani-Stephanopoulos, M. Alkali-Stabilized Pt-OHx

Species Catalyze Low-Temperature Water-Gas Shift Reactions. *Science (1979)* **2010**. https://doi.org/10.1126/science.1192449.

(94) Jung, N.; Chung, D. Y.; Ryu, J.; Yoo, S. J.; Sung, Y. E. Pt-Based Nanoarchitecture and Catalyst Design for Fuel Cell Applications. *Nano Today*. 2014. https://doi.org/10.1016/j.nantod.2014.06.006.

(95) Lin, J.; Wang, X.; Zhang, T. Recent Progress in CO Oxidation over Pt-Group-Metal Catalysts at Low Temperatures. *Cuihua Xuebao/Chinese Journal of Catalysis*. 2016. https://doi.org/10.1016/S1872-2067(16)62513-5.

(96) Lykhach, Y.; Bruix, A.; Fabris, S.; Potin, V.; Matolínová, I.; Matolín, V.; Libuda, J.; Neyman, K. M. Oxide-Based Nanomaterials for Fuel Cell Catalysis: The Interplay between Supported Single Pt Atoms and Particles. *Catalysis Science and Technology*. Royal Society of Chemistry October 2, 2017, pp 4315–4345. https://doi.org/10.1039/c7cy00710h.

(97) Ding, K.; Gulec, A.; Johnson, A. M.; Schweitzer, N. M.; Stucky, G. D.; Marks, L. D.; Stair, P. C. Identification of Active Sites in CO Oxidation and Water-Gas Shift over Supported Pt Catalysts. *Science (1979)* **2015**. https://doi.org/10.1126/science.aac6368.

(98) Bruix, A.; Neyman, K. M. Modeling Ceria-Based Nanomaterials for Catalysis and Related Applications. *Catal Letters* **2016**. https://doi.org/10.1007/s10562-016-1799-1.

(99) Yan, Z.; Xu, Z.; Yu, J.; Jaroniec, M. Highly Active Mesoporous Ferrihydrite Supported Pt Catalyst for Formaldehyde Removal at Room Temperature. *Environ Sci Technol* **2015**. https://doi.org/10.1021/acs.est.5b00532.

(100) Crampton, A. S.; Rötzer, M. D.; Ridge, C. J.; Schweinberger, F. F.; Heiz, U.; Yoon, B.; Landman, U. Structure Sensitivity in the Nonscalable Regime Explored via Catalysed

Ethylene Hydrogenation on Supported Platinum Nanoclusters. *Nat Commun* **2016**. https://doi.org/10.1038/ncomms10389.

(101) Dong, C.; Li, Y.; Cheng, D.; Zhang, M.; Liu, J.; Wang, Y. G.; Xiao, D.; Ma, D. Supported Metal Clusters: Fabrication and Application in Heterogeneous Catalysis. *ACS Catal* **2020**. https://doi.org/10.1021/acscatal.0c02818.

(102) Vajda, S.; Pellin, M. J.; Greeley, J. P.; Marshall, C. L.; Curtiss, L. A.; Ballentine, G. A.; Elam, J. W.; Catillon-Mucherie, S.; Redfern, P. C.; Mehmood, F.; Zapol, P. Subnanometre Platinum Clusters as Highly Active and Selective Catalysts for the Oxidative Dehydrogenation of Propane. *Nat Mater* **2009**. https://doi.org/10.1038/nmat2384.

(103) Sanchez, S. I.; Menard, L. D.; Bram, A.; Kang, J. H.; Small, M. W.; Nuzzo, R. G.; Frenkel, A. I. The Emergence of Nonbulk Properties in Supported Metal Clusters: Negative Thermal Expansion and Atomic Disorder in Pt Nanoclusters Supported on γ-Al 2O 3. *J Am Chem Soc* **2009**. https://doi.org/10.1021/ja809182v.

(104) Qiao, B.; Liang, J. X.; Wang, A.; Xu, C. Q.; Li, J.; Zhang, T.; Liu, J. J. Ultrastable Single-Atom Gold Catalysts with Strong Covalent Metal-Support Interaction (CMSI). *Nano Res* **2015**, *8* (9), 2913–2924. https://doi.org/10.1007/s12274-015-0796-9.

(105) Zhang, J.; Wu, X.; Cheong, W. C.; Chen, W.; Lin, R.; Li, J.; Zheng, L.; Yan, W.; Gu, L.; Chen, C.; Peng, Q.; Wang, D.; Li, Y. Cation Vacancy Stabilization of Single-Atomic-Site Pt 1 /Ni(OH) x Catalyst for Diboration of Alkynes and Alkenes. *Nat Commun* **2018**, *9* (1), 1–8. https://doi.org/10.1038/s41467-018-03380-z.

(106) Wan, J.; Chen, W.; Jia, C.; Zheng, L.; Dong, J.; Zheng, X.; Wang, Y.; Yan, W.; Chen, C.; Peng, Q.; Wang, D.; Li, Y. Defect Effects on TiO $_2$ Nanosheets: Stabilizing Single Atomic Site Au

and Promoting Catalytic Properties. *Advanced Materials* **2018**, *30* (11), 1705369. https://doi.org/10.1002/adma.201705369.

(107) Mager-Maury, C.; Bonnard, G.; Chizallet, C.; Sautet, P.; Raybaud, P. H2-Induced Reconstruction of Supported Pt Clusters: Metal–Support Interaction versus Surface Hydride. *Wiley Online Library* **2011**, *3* (1), 200–207. https://doi.org/10.1002/cctc.201000324.

(108) Tang, Y.; Asokan, C.; Xu, M.; Graham, G. W.; Pan, X.; Christopher, P.; Li, J.; Sautet, P. Rh Single Atoms on TiO2 Dynamically Respond to Reaction Conditions by Adapting Their Site. *Nat Commun* **2019**, *10* (1). https://doi.org/10.1038/s41467-019-12461-6.

(109) Lang, R.; Xi, W.; Liu, J. C.; Cui, Y. T.; Li, T.; Lee, A. F.; Chen, F.; Chen, Y.; Li, L.; Li, L.; Lin, J.; Miao, S.; Liu, X.; Wang, A. Q.; Wang, X.; Luo, J.; Qiao, B.; Li, J.; Zhang, T. Non Defect-Stabilized Thermally Stable Single-Atom Catalyst. *Nat Commun* **2019**, *10* (1), 1–10. https://doi.org/10.1038/s41467-018-08136-3.

(110) Hu, C. H.; Chizallet, C.; Mager-Maury, C.; Corral-Valero, M.; Sautet, P.; Toulhoat, H.; Raybaud, P. Modulation of Catalyst Particle Structure upon Support Hydroxylation: Ab Initio Insights into Pd13 and Pt13/γ-Al 2O3. *J Catal* **2010**, *274* (1), 99–110. https://doi.org/10.1016/j.jcat.2010.06.009.

(111) Valero, M. C.; Raybaud, P.; Sautet, P. Influence of the Hydroxylation of γ-Al2O3 Surfaces on the Stability and Diffusion of Single Pd Atoms: A DFT Study. *Journal of Physical Chemistry B* **2006**, *110* (4), 1759–1767. https://doi.org/10.1021/jp0554240.

(112) Lee, J.; Jang, E. J.; Kwak, J. H. Effect of Number and Properties of Specific Sites on Alumina Surfaces for Pt-Al2O3 Catalysts. *Appl Catal A Gen* **2019**, *569*, 8–19. https://doi.org/10.1016/j.apcata.2018.10.004.

(113) Chambers, S. A.; Droubay, T.; Jennison, D. R.; Mattsson, T. R. Laminar Growth of Ultrathin Metal Films on Metal Oxides: Co on Hydroxylated α-Al2O3(0001). *Science (1979)* **2002**, *297* (5582), 827–831. https://doi.org/10.1126/science.1073404.

(114) Addou, R.; Senftle, T. P.; O'Connor, N.; Janik, M. J.; Van Duin, A. C. T.; Batzill, M. Influence of Hydroxyls on Pd Atom Mobility and Clustering on Rutile TiO2(011)-2 × 1. *ACS Nano* **2014**, *8* (6), 6321–6333. https://doi.org/10.1021/nn501817w.

(115) Kwon, Y.; Kim, T. Y.; Kwon, G.; Yi, J.; Lee, H. Selective Activation of Methane on Single-Atom Catalyst of Rhodium Dispersed on Zirconia for Direct Conversion. *J Am Chem Soc* **2017**, *139* (48), 17694–17699. https://doi.org/10.1021/jacs.7b11010.

(116) Thang, H. V.; Pacchioni, G. On the Real Nature of Rh Single-Atom Catalysts Dispersed on the ZrO $_2$ Surface. *ChemCatChem* **2020**, *12* (9), 2595–2604. https://doi.org/10.1002/cctc.201901878.

(117) Thang, H. V.; Tosoni, S.; Fang, L.; Bruijnincx, P.; Pacchioni, G. Nature of Sintering-Resistant, Single-Atom Ru Species Dispersed on Zirconia-Based Catalysts: A DFT and FTIR Study of CO Adsorption. *ChemCatChem* **2018**, *10* (12), 2634–2645. https://doi.org/10.1002/cctc.201800246.

(118) Thang, H. V.; Pacchioni, G.; DeRita, L.; Christopher, P. Nature of Stable Single Atom Pt Catalysts Dispersed on Anatase TiO2. *J Catal* **2018**, *367*, 104–114. https://doi.org/10.1016/j.jcat.2018.08.025.

(119) Ye, X.; Yang, C.; Pan, X.; Ma, J.; Zhang, Y.; Ren, Y.; Liu, X.; Li, L.; Huang, Y. Highly Selective Hydrogenation of CO2to Ethanol via Designed Bifunctional Ir1-In2O3Single-Atom Catalyst. *J Am Chem Soc* **2020**, *142* (45), 19001–19005. https://doi.org/10.1021/jacs.0c08607.

(120) Fujimori, Y.; Kaden, W. E.; Brown, M. A.; Roldan Cuenya, B.; Sterrer, M.; Freund, H. J. Hydrogen Evolution from Metal-Surface Hydroxyl Interaction. *Journal of Physical Chemistry C* **2014**, *118* (31), 17717–17723. https://doi.org/10.1021/jp504655e.

(121) Parkinson, G. S.; Novotny, Z.; Argentero, G.; Schmid, M.; Pavelec, J.; Kosak, R.; Blaha, P.; Diebold, U. Carbon Monoxide-Induced Adatom Sintering in a Pd-Fe3 O 4 Model Catalyst. *Nat Mater* **2013**, *12* (8), 724–728. https://doi.org/10.1038/nmat3667.

(122) Eranna, G.; Joshi, B. C.; Runthala, D. P.; Gupta, R. P. Oxide Materials for Development of Integrated Gas Sensors - A Comprehensive Review. *Critical Reviews in Solid State and Materials Sciences* **2004**, *29* (3–4), 111–188. https://doi.org/10.1080/10408430490888977.

(123) Ye, J.; Liu, C.; Mei, D.; Ge, Q. Active Oxygen Vacancy Site for Methanol Synthesis from CO2 Hydrogenation on In2O3(110): A DFT Study. *ACS Catal* **2013**, *3* (6), 1296–1306. https://doi.org/10.1021/cs400132a.

(124) Ye, J.; Liu, C.; Ge, Q. DFT Study of CO 2 Adsorption and Hydrogenation on the in 2O 3 Surface. *Journal of Physical Chemistry C* **2012**, *116* (14), 7817–7825. https://doi.org/10.1021/jp3004773.

(125) *H. L. Hartnagel, A. L. Dawar, A. K. Jain, and C.... - Google Scholar*. https://scholar.google.com/scholar?hl=en&q=H.+L.+Hartnagel%2C+A.+L.+Dawar%2C+A.+

K.+Jain%2C+and+C.+Jagadish%2C+Semiconducting+Transparent+Thin+Films+%28Institute+of+Physics%2C+Bristol%2C+1995%29. (accessed 2021-03-28).

(126) Von Weber, A.; Anderson, S. L. Electrocatalysis by Mass-Selected Ptn Clusters. *Acc Chem Res* **2016**, *49* (11), 2632–2639. https://doi.org/10.1021/acs.accounts.6b00387.

(127) Von Weber, A.; Baxter, E. T.; White, H. S.; Anderson, S. L. Cluster Size Controls Branching between Water and Hydrogen Peroxide Production in Electrochemical Oxygen Reduction at Ptn/ITO. *Journal of Physical Chemistry C* **2015**, *119* (20), 11160–11170. https://doi.org/10.1021/jp5119234.

(128) Von Weber, A.; Baxter, E. T.; Proch, S.; Kane, M. D.; Rosenfelder, M.; White, H. S.; Anderson, S. L. Size-Dependent Electronic Structure Controls Activity for Ethanol Electro-Oxidation at Pt n /Indium Tin Oxide (n = 1 to 14). *Physical Chemistry Chemical Physics* **2015**, *17* (27), 17601–17610. https://doi.org/10.1039/C5CP01824B.

(129) Kresse, G.; Furthmüller, J. Software VASP, Vienna. *Phys Rev B* **1996**.

(130) Kresse, G. Ab Initio Molecular Dynamics for Liquid Metals. *J Non Cryst Solids* **1995**. https://doi.org/10.1016/0022-3093(95)00355-X.

(131) Blöchl, P. E. Projector Augmented-Wave Method. *Phys Rev B* **1994**. https://doi.org/10.1103/PhysRevB.50.17953.

(132) Perdew, J. P.; Burke, K.; Ernzerhof, M. Generalized Gradient Approximation Made Simple. *Phys Rev Lett* **1996**. https://doi.org/10.1103/PhysRevLett.77.3865.

(133) Marezio, M. Refinement of the Crystal Structure of In 2 O 3 at Two Wavelengths . *Acta Crystallogr* **1966**. https://doi.org/10.1107/s0365110x66001749.

(134) Monkhorst, H. J.; Pack, J. D. Special Points for Brillouin-Zone Integrations. *Phys Rev B* **1976**, *13* (12), 5188–5192. https://doi.org/10.1103/PhysRevB.13.5188.

(135) Wales, D. J.; Doye, J. P. K. Global Optimization by Basin-Hopping and the Lowest Energy Structures of Lennard-Jones Clusters Containing up to 110 Atoms. *Journal of Physical Chemistry A* **1997**. https://doi.org/10.1021/jp970984n.

(136) Mizuhashi, M. Electrical Properties of Vacuum-Deposited Indium Oxide and Indium Tin Oxide Films. *Thin Solid Films* **1980**, *70* (1), 91–100. https://doi.org/10.1016/0040-6090(80)90415-0.

(137) Morales, E. H.; He, Y.; Vinnichenko, M.; Delley, B.; Diebold, U. Surface Structure of Sn-Doped In2O3 (111) Thin Films by STM. *New J Phys* **2008**, *10* (11pp), 125030. https://doi.org/10.1088/1367-2630/10/12/125030.

(138) Silber, D.; Kowalski, P. M.; Traeger, F.; Buchholz, M.; Bebensee, F.; Meyer, B.; Wöll, C. Adsorbate-Induced Lifting of Substrate Relaxation Is a General Mechanism Governing Titania Surface Chemistry. *Nat Commun* **2016**. https://doi.org/10.1038/ncomms12888.

(139) Wagner, M.; Lackner, P.; Seiler, S.; Brunsch, A.; Bliem, R.; Gerhold, S.; Wang, Z.; Osiecki, J.; Schulte, K.; Boatner, L. A.; Schmid, M.; Meyer, B.; Diebold, U. Resolving the Structure of a Well-Ordered Hydroxyl Overlayer on In2O3(111): Nanomanipulation and Theory. *ACS Nano* **2017**. https://doi.org/10.1021/acsnano.7b06387.

(140) Bauer, T.; Schmaltz, T.; Lenz, T.; Halik, M.; Meyer, B.; Clark, T. Phosphonate- and Carboxylate-Based Self-Assembled Monolayers for Organic Devices: A Theoretical Study of Surface Binding on Aluminum Oxide with Experimental Support. *ACS Appl Mater Interfaces* **2013**. https://doi.org/10.1021/am4008374.

(141) Matthey, D.; Wang, J. G.; Wendt, S.; Matthiesen, J.; Schaub, R.; Lægsgaard, E.; Hammer, B.; Besenbacher, F. Enhanced Bonding of Gold Nanoparticles on Oxidized TiO2(110). *Science (1979)* **2007**, *315* (5819), 1692–1696. https://doi.org/10.1126/science.1135752.

(142) Chen, Z.; Duan, X.; Wei, W.; Wang, S.; Ni, B. J. Iridium-Based Nanomaterials for Electrochemical Water Splitting. *Nano Energy* **2020**, *78*, 105270. https://doi.org/10.1016/J.NANOEN.2020.105270.

(143) Zhang, Z.; Zandkarimi, B.; Munarriz, J.; Dickerson, C. E.; Alexandrova, A. N. Fluxionality of Subnano Clusters Reshapes the Activity Volcano of Electrocatalysis. *ChemCatChem* **2022**, *14* (15), e202200345. https://doi.org/10.1002/CCTC.202200345.

(144) Kumari, S.; Sautet, P. Highly Dispersed Pt Atoms and Clusters on Hydroxylated Indium Tin Oxide: A View from First-Principles Calculations. *J Mater Chem A Mater* **2021**, *9* (28), 15724–15733. https://doi.org/10.1039/D1TA03177E.

(145) Munarriz, J.; Zhang, Z.; Sautet, P.; Alexandrova, A. N. Graphite-Supported Pt n Cluster Electrocatalysts: Major Change of Active Sites as a Function of the Applied Potential . *ACS Catal* **2022**, 14517–14526. https://doi.org/10.1021/ACSCATAL.2C04643/ASSET/IMAGES/LARGE/CS2C04643_0004.JPEG.

(146) Hartl, K.; Nesselberger, M.; Mayrhofer, K. J. J.; Kunz, S.; Schweinberger, F. F.; Kwon, G.; Hanzlik, M.; Heiz, U.; Arenz, M. Electrochemically Induced Nanocluster Migration. *Electrochim Acta* **2010**, *56* (2), 810–816. https://doi.org/10.1016/J.ELECTACTA.2010.10.005.

(147) Zhang, Z.; Zandkarimi, B.; Alexandrova, A. N. Ensembles of Metastable States Govern Heterogeneous Catalysis on Dynamic Interfaces. *Acc Chem Res* **2020**, *53* (2), 447–458. https://doi.org/10.1021/ACS.ACCOUNTS.9B00531/ASSET/IMAGES/MEDIUM/AR9B00531_0007.GIF.

(148) Baxter, E. T.; Ha, M. A.; Cass, A. C.; Alexandrova, A. N.; Anderson, S. L. Ethylene Dehydrogenation on Pt4,7,8 Clusters on Al2O3: Strong Cluster Size Dependence Linked to Preferred Catalyst Morphologies. *ACS Catal* **2017**, *7* (5), 3322–3335. https://doi.org/10.1021/ACSCATAL.7B00409/ASSET/IMAGES/CS-2017-00409T_M003.GIF.

(149) Gorey, T. J.; Zandkarimi, B.; Li, G.; Baxter, E. T.; Alexandrova, A. N.; Anderson, S. L. Coking-Resistant Sub-Nano Dehydrogenation Catalysts: PtnSnx/SiO2 (n = 4, 7). *ACS Catal* **2020**, *10* (8), 4543–4558. https://doi.org/10.1021/ACSCATAL.0C00668/SUPPL_FILE/CS0C00668_SI_002.XLSX.

(150) Ha, M. A.; Baxter, E. T.; Cass, A. C.; Anderson, S. L.; Alexandrova, A. N. Boron Switch for Selectivity of Catalytic Dehydrogenation on Size-Selected Pt Clusters on Al2O3. *J Am Chem Soc* **2017**, *139* (33), 11568–11575. https://doi.org/10.1021/JACS.7B05894/ASSET/IMAGES/LARGE/JA-2017-05894H_0004.JPEG.

(151) Ghosh, P.; Farnesi Camellone, M.; Fabris, S. Fluxionality of Au Clusters at Ceria Surfaces during CO Oxidation: Relationships among Reactivity, Size, Cohesion, and Surface Defects from DFT Simulations. *Journal of Physical Chemistry Letters* **2013**, *4* (14), 2256–2263. https://doi.org/10.1021/JZ4009079/SUPPL_FILE/JZ4009079_SI_001.PDF.

(152) Nørskov, J. K.; Bligaard, T.; Logadottir, A.; Kitchin, J. R.; Chen, J. G.; Pandelov, S.; Stimming, U. Trends in the Exchange Current for Hydrogen Evolution. *J Electrochem Soc* **2005**, *152* (2), J23–J26. https://doi.org/10.1149/1.1856988.

(153) Okamoto, Y. Comparison of Hydrogen Atom Adsorption on Pt Clusters with That on Pt Surfaces: A Study from Density-Functional Calculations. *Chem Phys Lett* **2006**, *429* (1–3), 209–213. https://doi.org/10.1016/J.CPLETT.2006.08.013.

(154) Zhou, C.; Wu, J.; Nie, A.; Forrey, R. C.; Tachibana, A.; Cheng, H. On the Sequential Hydrogen Dissociative Chemisorption on Small Platinum Clusters: A Density Functional Theory Study. *Journal of Physical Chemistry C* **2007**, *111* (34), 12773–12778. https://doi.org/10.1021/JP073597E/ASSET/IMAGES/LARGE/JP073597EF00007.JPEG.

(155) Sihag, A.; Xie, Z. L.; Thang, H. V.; Kuo, C. L.; Tseng, F. G.; Dyer, M. S.; Chen, H. Y. T. DFT Insights into Comparative Hydrogen Adsorption and Hydrogen Spillover Mechanisms of Pt4/Graphene and Pt4/Anatase (101) Surfaces. *Journal of Physical Chemistry C* **2019**, *123* (42), 25618–25627. https://doi.org/10.1021/ACS.JPCC.9B04419/ASSET/IMAGES/LARGE/JP9B04419_0009.JPEG.

(156) Jones, J.; Xiong, H.; DeLaRiva, A. T.; Peterson, E. J.; Pham, H.; Challa, S. R.; Qi, G.; Oh, S.; Wiebenga, M. H.; Hernández, X. I. P.; Wang, Y.; Datye, A. K. Thermally Stable Single-Atom Platinum-on-Ceria Catalysts via Atom Trapping. *Science (1979)* **2016**, *353* (6295), 150–154. https://doi.org/10.1126/SCIENCE.AAF8800/SUPPL_FILE/JONES.SM.PDF.

(157) Yang, X.-F.; Wang, A.; Qiao, B.; Li, J.; Liu, J.; Zhang, T. Single-Atom Catalysts: A New Frontier in Heterogeneous Catalysis. *Acc. Chem. Res.* **2013**, *46* (8), 1740–1748. https://doi.org/10.1021/ar300361m.

(158) Cheng, N.; Stambula, S.; Wang, D.; Banis, M. N.; Liu, J.; Riese, A.; Xiao, B.; Li, R.; Sham, T.-K.; Liu, L.-M.; Botton, G. A.; Sun, X. Platinum Single-Atom and Cluster Catalysis of the Hydrogen Evolution Reaction. *Nat. Commun.* **2016**, *7*, 13638. https://doi.org/10.1038/ncomms13638.

(159) Park, J.; Lee, S.; Kim, H.-E.; Cho, A.; Kim, S.; Ye, Y.; Han, J. W.; Lee, H.; Jang, J. H.; Lee, J. Investigation of the Support Effect in Atomically Dispersed Pt on WO3-X for Utilization of Pt in the Hydrogen Evolution Reaction. *Angew. Chem. Int. Ed Engl.* **2019**, *58* (45), 16038–16042. https://doi.org/10.1002/anie.201908122.

(160) Halder, A.; Curtiss, L. A.; Fortunelli, A.; Vajda, S. Perspective: Size Selected Clusters for Catalysis and Electrochemistry. *J Chem Phys* **2018**, *148* (11), 110901. https://doi.org/10.1063/1.5020301.

(161) Kwon, G.; Ferguson, G. A.; Heard, C. J.; Tyo, E. C.; Yin, C.; Debartolo, J.; Seifert, S.; Winans, R. E.; Kropf, A. J.; Greeley, J.; Johnston, R. L.; Curtiss, L. A.; Pellin, M. J.; Vajda, S. Size-Dependent Subnanometer Pd Cluster (Pd4, Pd6, and Pd17) Water Oxidation Electrocatalysis. *ACS Nano* **2013**, *7* (7), 5808–5817. https://doi.org/10.1021/NN400772S/SUPPL_FILE/NN400772S_SI_001.PDF.

(162) Lu, J.; Cheng, L.; Lau, K. C.; Tyo, E.; Luo, X.; Wen, J.; Miller, D.; Assary, R. S.; Wang, H. H.; Redfern, P.; Wu, H.; Park, J. B.; Sun, Y. K.; Vajda, S.; Amine, K.; Curtiss, L. A. Effect of the Size-Selective Silver Clusters on Lithium Peroxide Morphology in Lithium–Oxygen

Batteries. *Nature Communications 2014 5:1* **2014**, *5* (1), 1–8. https://doi.org/10.1038/ncomms5895.

(163) Kunz, S.; Hartl, K.; Nesselberger, M.; Schweinberger, F. F.; Kwon, G.; Hanzlik, M.; Mayrhofer, K. J. J.; Heiz, U.; Arenz, M. Size-Selected Clusters as Heterogeneous Model Catalysts under Applied Reaction Conditions. *Physical Chemistry Chemical Physics* **2010**, *12* (35), 10288–10291. https://doi.org/10.1039/C0CP00288G.

(164) Nesselberger, M.; Roefzaad, M.; Fayçal Hamou, R.; Ulrich Biedermann, P.; Schweinberger, F. F.; Kunz, S.; Schloegl, K.; Wiberg, G. K. H.; Ashton, S.; Heiz, U.; Mayrhofer, K. J. J.; Arenz, M. The Effect of Particle Proximity on the Oxygen Reduction Rate of Size-Selected Platinum Clusters. *Nature Materials 2013 12:10* **2013**, *12* (10), 919–924. https://doi.org/10.1038/nmat3712.

(165) Von Weber, A.; Baxter, E. T.; Proch, S.; Kane, M. D.; Rosenfelder, M.; White, H. S.; Anderson, S. L. Size-Dependent Electronic Structure Controls Activity for Ethanol Electro-Oxidation at Ptn/Indium Tin Oxide (n = 1 to 14). *Phys. Chem. Chem. Phys.* **2015**, *17* (27), 17601–17610. https://doi.org/10.1039/c5cp01824b.

(166) Jones, J.; Xiong, H.; DeLaRiva, A. T.; Peterson, E. J.; Pham, H.; Challa, S. R.; Qi, G.; Oh, S.; Wiebenga, M. H.; Hernández, X. I. P.; Wang, Y.; Datye, A. K. Thermally Stable Single-Atom Platinum-on-Ceria Catalysts via Atom Trapping. *Science (1979)* **2016**. https://doi.org/10.1126/science.aaf8800.

(167) Deng, J.; Li, H.; Xiao, J.; Tu, Y.; Deng, D.; Yang, H.; Tian, H.; Li, J.; Ren, P.; Bao, X. Triggering the Electrocatalytic Hydrogen Evolution Activity of the Inert Two-Dimensional MoS 2

Surface via Single-Atom Metal Doping. *Energy Environ Sci* **2015**, *8* (5), 1594–1601. https://doi.org/10.1039/C5EE00751H.

(168) Qiao, B.; Wang, A.; Yang, X.; Allard, L. F.; Jiang, Z.; Cui, Y.; Liu, J.; Li, J.; Zhang, T. Single-Atom Catalysis of CO Oxidation Using Pt1/FeOx. *Nature Chemistry 2011 3:8* **2011**, *3* (8), 634–641. https://doi.org/10.1038/nchem.1095.

(169) Kresse, G.; Furthmüller, J. Efficient Iterative Schemes for Ab Initio Total-Energy Calculations Using a Plane-Wave Basis Set. *Phys Rev B Condens Matter Mater Phys* **1996**, *54* (16), 11169–11186. https://doi.org/10.1103/PhysRevB.54.11169.

(170) Kresse, G. Ab Initio Molecular Dynamics for Liquid Metals. *J Non Cryst Solids* **1995**, *192–193*, 222–229. https://doi.org/10.1016/0022-3093(95)00355-X.

(171) Blöchl, P. E. Projector Augmented-Wave Method. *Phys Rev B* **1994**, *50* (24), 17953–17979. https://doi.org/10.1103/PhysRevB.50.17953.

(172) Perdew, J. P.; Burke, K.; Ernzerhof, M. Generalized Gradient Approximation Made Simple. *Phys Rev Lett* **1996**, *77* (18), 3865–3868. https://doi.org/10.1103/PhysRevLett.77.3865.

(173) Mathew, K.; Sundararaman, R.; Letchworth-Weaver, K.; Arias, T. A.; Hennig, R. G. Implicit Solvation Model for Density-Functional Study of Nanocrystal Surfaces and Reaction Pathways. *Journal of Chemical Physics* **2014**, *140* (8), 0–8. https://doi.org/10.1063/1.4865107.

(174) *henniggroup/VASPsol: Solvation model for the plane wave DFT code VASP http://vaspsol.mse.ufl.edu/*. https://github.com/henniggroup/VASPsol (accessed 2022-10-10).

(175) Mathew, K.; Kolluru, V. S. C.; Mula, S.; Steinmann, S. N.; Hennig, R. G. Implicit Self-Consistent Electrolyte Model in Plane-Wave Density-Functional Theory. *J Chem Phys* **2019**, *151* (23), 234101. https://doi.org/10.1063/1.5132354.

(176) Mathew, K.; Sundararaman, R.; Letchworth-Weaver, K.; Arias, T. A.; Hennig, R. G. Implicit Solvation Model for Density-Functional Study of Nanocrystal Surfaces and Reaction Pathways. *J Chem Phys* **2014**, *140* (8), 084106. https://doi.org/10.1063/1.4865107.

(177) Taylor, C. D.; Wasileski, S. A.; Filhol, J. S.; Neurock, M. First Principles Reaction Modeling of the Electrochemical Interface: Consideration and Calculation of a Tunable Surface Potential from Atomic and Electronic Structure. *Phys Rev B Condens Matter Mater Phys* **2006**, *73* (16), 165402. https://doi.org/10.1103/PHYSREVB.73.165402/FIGURES/9/MEDIUM.

(178) Steinmann, S. N.; Sautet, P. Assessing a First-Principles Model of an Electrochemical Interface by Comparison with Experiment. *Journal of Physical Chemistry C* **2016**, *120* (10). https://doi.org/10.1021/acs.jpcc.6b01938.

(179) Goodpaster, J. D.; Bell, A. T.; Head-Gordon, M. Identification of Possible Pathways for C-C Bond Formation during Electrochemical Reduction of CO2: New Theoretical Insights from an Improved Electrochemical Model. *Journal of Physical Chemistry Letters* **2016**, *7* (8). https://doi.org/10.1021/acs.jpclett.6b00358.

(180) Xiao, H.; Cheng, T.; Goddard, W. A.; Sundararaman, R. Mechanistic Explanation of the PH Dependence and Onset Potentials for Hydrocarbon Products from Electrochemical Reduction of CO on Cu (111). *J Am Chem Soc* **2016**, *138* (2). https://doi.org/10.1021/jacs.5b11390.

(181) Schwarz, K.; Xu, B.; Yan, Y.; Sundararaman, R. Partial Oxidation of Step-Bound Water Leads to Anomalous PH Effects on Metal Electrode Step-Edges. *Physical Chemistry Chemical Physics* **2016**, *18* (24). https://doi.org/10.1039/c6cp01652a.

(182) Schwarz, K. A.; Sundararaman, R.; Moffat, T. P.; Allison, T. C. Formic Acid Oxidation on Platinum: A Simple Mechanistic Study. *Physical Chemistry Chemical Physics* **2015**, *17* (32). https://doi.org/10.1039/c5cp03045e.

(183) Sweany, R. L.; Church, S. P.; Grevels, F.-W.; Hermann, H.; Schafiner, K. J.; Kubas, G. J.; Ryan, R. R.; Swanson, B. I.; Vergamini, P. J.; Wasser-Man, H.; Morris, R.; Jolly, P. W.; Wilke, G. Chemistry of Platinum Hydrides: A Platinum(II) Cis-Dihydride or a Platinum(O) N2-Dihydrogen Complex? *J Am Chem Soc* **1986**, *108* (13), 3829–3830. https://doi.org/10.1021/JA00273A047.

(184) Zhang, X.; Liu, G.; Ganteför, G.; Bowen, K. H.; Alexandrova, A. N. PtZnH5-, A σ-Aromatic Cluster. *Journal of Physical Chemistry Letters* **2014**, *5* (9), 1596–1601. https://doi.org/10.1021/JZ500322N/SUPPL_FILE/JZ500322N_SI_001.PDF.

(185) Scheler, T.; Degtyareva, O.; Marqués, M.; Guillaume, C. L.; Proctor, J. E.; Evans, S.; Gregoryanz, E. Synthesis and Properties of Platinum Hydride. *Phys Rev B Condens Matter Mater Phys* **2011**, *83* (21), 214106. https://doi.org/10.1103/PHYSREVB.83.214106/FIGURES/3/MEDIUM.

(186) Itoi, H.; Nishihara, H.; Kogure, T.; Kyotani, T. Three-Dimensionally Arrayed and Mutually Connected 1.2-Nm Nanopores for High-Performance Electric Double Layer Capacitor. *J Am Chem Soc* **2011**, *133* (5), 1165–1167. https://doi.org/10.1021/JA108315P/SUPPL_FILE/JA108315P_SI_001.PDF.

(187) Zhang, Z.; Cui, Z. H.; Jimenez-Izal, E.; Sautet, P.; Alexandrova, A. N. Hydrogen Evolution on Restructured B-Rich WB: Metastable Surface States and Isolated Active Sites. *ACS Catal* **2020**, *10* (23), 13867–13877. https://doi.org/10.1021/acscatal.0c03410.

(188) Shinagawa, T.; Garcia-Esparza, A. T.; Takanabe, K. Insight on Tafel Slopes from a Microkinetic Analysis of Aqueous Electrocatalysis for Energy Conversion. *Sci Rep* **2015**, *5* (1), 13801. https://doi.org/10.1038/srep13801.

(189) Yang, R. T.; Wang, Y. Catalyzed Hydrogen Spillover for Hydrogen Storage. *J. Am. Chem. Soc.* **2009**, *131* (12), 4224–4226. https://doi.org/10.1021/ja808864r.

(190) Wei, Z.-W.; Wang, H.-J.; Zhang, C.; Xu, K.; Lu, X.-L.; Lu, T.-B. Reversed Charge Transfer and Enhanced Hydrogen Spillover in Platinum Nanoclusters Anchored on Titanium Oxide with Rich Oxygen Vacancies Boost Hydrogen Evolution Reaction. *Angew. Chem. Int. Ed Engl.* **2021**, *60* (30), 16622–16627. https://doi.org/10.1002/anie.202104856.

(191) Dai, J.; Zhu, Y.; Chen, Y.; Wen, X.; Long, M.; Wu, X.; Hu, Z.; Guan, D.; Wang, X.; Zhou, C.; Lin, Q.; Sun, Y.; Weng, S.-C.; Wang, H.; Zhou, W.; Shao, Z. Hydrogen Spillover in Complex Oxide Multifunctional Sites Improves Acidic Hydrogen Evolution Electrocatalysis. *Nat. Commun.* **2022**, *13* (1), 1189. https://doi.org/10.1038/s41467-022-28843-2.

(192) Bonanni, S.; Aït-Mansour, K.; Harbich, W.; Brune, H. Effect of the TiO 2 Reduction State on the Catalytic CO Oxidation on Deposited Size-Selected Pt Clusters. *J Am Chem Soc* **2012**, *134* (7), 3445–3450. https://doi.org/10.1021/JA2098854/SUPPL_FILE/JA2098854_SI_001.PDF.

(193) Fabbri, E.; Habereder, A.; Waltar, K.; Kötz, R.; Schmidt, T. J. Developments and Perspectives of Oxide-Based Catalysts for the Oxygen Evolution Reaction. *Catal. Sci. Technol.* **2014**, *4* (11), 3800–3821. https://doi.org/10.1039/c4cy00669k.

(194) Zhang, X.; Bieberle-Hütter, A. Modeling and Simulations in Photoelectrochemical Water Oxidation: From Single Level to Multiscale Modeling. *ChemSusChem* **2016**, *9* (11), 1223–1242. https://doi.org/10.1002/cssc.201600214.

(195) Nørskov, J. K.; Rossmeisl, J.; Logadottir, A.; Lindqvist, L.; Kitchin, J. R.; Bligaard, T.; Jónsson, H. Origin of the Overpotential for Oxygen Reduction at a Fuel-Cell Cathode. *J. Phys. Chem. B* **2004**, *108* (46), 17886–17892. https://doi.org/10.1021/jp047349j.

(196) Rossmeisl, J.; Qu, Z. W.; Zhu, H.; Kroes, G. J.; Nørskov, J. K. Electrolysis of Water on Oxide Surfaces. *J. Electroanal. Chem.* **2007**, *607* (1–2), 83–89. https://doi.org/10.1016/j.jelechem.2006.11.008.

(197) Qiao, B.; Wang, A.; Yang, X.; Allard, L. F.; Jiang, Z.; Cui, Y.; Liu, J.; Li, J.; Zhang, T. Single-Atom Catalysis of CO Oxidation Using Pt1/FeOx. *Nat Chem* **2011**, *3* (8). https://doi.org/10.1038/nchem.1095.

(198) Peterson, E. J.; DeLaRiva, A. T.; Lin, S.; Johnson, R. S.; Guo, H.; Miller, J. T.; Kwak, J. H.; Peden, C. H. F.; Kiefer, B.; Allard, L. F.; Ribeiro, F. H.; Datye, A. K. Low-Temperature Carbon Monoxide Oxidation Catalysed by Regenerable Atomically Dispersed Palladium on Alumina. *Nat Commun* **2014**, *5*. https://doi.org/10.1038/ncomms5885.

(199) DeRita, L.; Resasco, J.; Dai, S.; Boubnov, A.; Thang, H. V.; Hoffman, A. S.; Ro, I.; Graham, G. W.; Bare, S. R.; Pacchioni, G.; Pan, X.; Christopher, P. Structural Evolution of Atomically

Dispersed Pt Catalysts Dictates Reactivity. *Nat Mater* **2019**, *18* (7). https://doi.org/10.1038/s41563-019-0349-9.

(200) Yoo, M.; Yu, Y. S.; Ha, H.; Lee, S.; Choi, J. S.; Oh, S.; Kang, E.; Choi, H.; An, H.; Lee, K. S.; Park, J. Y.; Celestre, R.; Marcus, M. A.; Nowrouzi, K.; Taube, D.; Shapiro, D. A.; Jung, W. C.; Kim, C.; Kim, H. Y. A Tailored Oxide Interface Creates Dense Pt Single-Atom Catalysts with High Catalytic Activity. *Energy Environ Sci* **2020**, *13* (4). https://doi.org/10.1039/c9ee03492g.

(201) Yan, H.; Lin, Y.; Wu, H.; Zhang, W.; Sun, Z.; Cheng, H.; Liu, W.; Wang, C.; Li, J.; Huang, X.; Yao, T.; Yang, J.; Wei, S.; Lu, J. Bottom-up Precise Synthesis of Stable Platinum Dimers on Graphene. *Nat Commun* **2017**, *8* (1). https://doi.org/10.1038/S41467-017-01259-Z.

(202) Li, J.; Guan, Q.; Wu, H.; Liu, W.; Lin, Y.; Sun, Z.; Ye, X.; Zheng, X.; Pan, H.; Zhu, J.; Chen, S.; Zhang, W.; Wei, S.; Lu, J. Highly Active and Stable Metal Single-Atom Catalysts Achieved by Strong Electronic Metal-Support Interactions. *J Am Chem Soc* **2019**, *141* (37), 14515–14519. https://doi.org/10.1021/JACS.9B06482/SUPPL_FILE/JA9B06482_SI_001.PDF.

(203) Cheng, N.; Stambula, S.; Wang, D.; Banis, M. N.; Liu, J.; Riese, A.; Xiao, B.; Li, R.; Sham, T. K.; Liu, L. M.; Botton, G. A.; Sun, X. Platinum Single-Atom and Cluster Catalysis of the Hydrogen Evolution Reaction. *Nature Communications 2016 7:1* **2016**, *7* (1), 1–9. https://doi.org/10.1038/ncomms13638.

(204) Chen, Y.; Ji, S.; Chen, C.; Peng, Q.; Wang, D.; Li, Y. Single-Atom Catalysts: Synthetic Strategies and Electrochemical Applications. *Joule* **2018**, *2* (7), 1242–1264. https://doi.org/10.1016/j.joule.2018.06.019.

(205) Shang, R.; Steinmann, S. N.; Xu, B. Q.; Sautet, P. Mononuclear Fe in N-Doped Carbon: Computational Elucidation of Active Sites for Electrochemical Oxygen Reduction and Oxygen Evolution Reactions. *Catal Sci Technol* **2020**, *10* (4), 1006–1014. https://doi.org/10.1039/C9CY01935A.

(206) Kumari, S.; Masubuchi, T.; White, H. S.; Alexandrova, A.; Anderson, S. L.; Sautet, P. Electrocatalytic Hydrogen Evolution at Full Atomic Utilization over ITO-Supported Sub-Nano Ptn Clusters: High, Size-Dependent Activity Controlled by Fluxional Pt Hydride Species. **2022**. https://doi.org/10.26434/CHEMRXIV-2022-5870P.

(207) Lee, B. H.; Park, S.; Kim, M.; Sinha, A. K.; Lee, S. C.; Jung, E.; Chang, W. J.; Lee, K. S.; Kim, J. H.; Cho, S. P.; Kim, H.; Nam, K. T.; Hyeon, T. Reversible and Cooperative Photoactivation of Single-Atom Cu/TiO2 Photocatalysts. *Nat Mater* **2019**, *18* (6). https://doi.org/10.1038/s41563-019-0344-1.

(208) Daelman, N.; Capdevila-Cortada, M.; López, N. Dynamic Charge and Oxidation State of Pt/CeO2 Single-Atom Catalysts. *Nat Mater* **2019**, *18* (11). https://doi.org/10.1038/s41563-019-0444-y.

(209) Liu, P.; Zhao, Y.; Qin, R.; Mo, S.; Chen, G.; Gu, L.; Chevrier, D. M.; Zhang, P.; Guo, Q.; Zang, D.; Wu, B.; Fu, G.; Zheng, N. Catalysis: Photochemical Route for Synthesizing Atomically Dispersed Palladium Catalysts. *Science (1979)* **2016**, *352* (6287). https://doi.org/10.1126/science.aaf5251.

(210) Gu, J.; Hsu, C. S.; Bai, L.; Chen, H. M.; Hu, X. Atomically Dispersed Fe3+ Sites Catalyze Efficient CO2 Electroreduction to CO. *Science (1979)* **2019**, *364* (6445), 1091–1094. https://doi.org/10.1126/SCIENCE.AAW7515/SUPPL_FILE/AAW7515-GU-SM.PDF.

(211) Xiao, M.; Zhu, J.; Li, G.; Li, N.; Li, S.; Cano, Z. P.; Ma, L.; Cui, P.; Xu, P.; Jiang, G.; Jin, H.; Wang, S.; Wu, T.; Lu, J.; Yu, A.; Su, D.; Chen, Z. A Single-Atom Iridium Heterogeneous Catalyst in Oxygen Reduction Reaction. *Angewandte Chemie - International Edition*. 2019. https://doi.org/10.1002/anie.201905241.

(212) Yang, X. F.; Wang, A.; Qiao, B.; Li, J.; Liu, J.; Zhang, T. Single-Atom Catalysts: A New Frontier in Heterogeneous Catalysis. *Acc Chem Res* **2013**, *46* (8), 1740–1748. https://doi.org/10.1021/AR300361M/ASSET/IMAGES/MEDIUM/AR-2012-00361M_0001.GIF.

(213) Zhang, B.; Sun, G.; Ding, S.; Asakura, H.; Zhang, J.; Sautet, P.; Yan, N. Atomically Dispersed Pt $_1$ –Polyoxometalate Catalysts: How Does Metal–Support Interaction Affect Stability and Hydrogenation Activity? *J Am Chem Soc* **2019**, jacs.9b00486. https://doi.org/10.1021/jacs.9b00486.

(214) Zhang, L.; Doyle-Davis, K.; Sun, X. Pt-Based Electrocatalysts with High Atom Utilization Efficiency: From Nanostructures to Single Atoms. *Energy Environ Sci* **2019**, *12* (2), 492–517. https://doi.org/10.1039/C8EE02939C.

(215) Babic, U.; Suermann, M.; Büchi, F. N.; Gubler, L.; Schmidt, T. J. Critical Review—Identifying Critical Gaps for Polymer Electrolyte Water Electrolysis Development. *J Electrochem Soc* **2017**, *164* (4). https://doi.org/10.1149/2.1441704jes.

(216) Suen, N. T.; Hung, S. F.; Quan, Q.; Zhang, N.; Xu, Y. J.; Chen, H. M. Electrocatalysis for the Oxygen Evolution Reaction: Recent Development and Future Perspectives. *Chemical Society Reviews*. 2017. https://doi.org/10.1039/c6cs00328a.

(217) Curutchet, A.; Colinet, P.; Michel, C.; Steinmann, S. N.; Le Bahers, T. Two-Sites Are Better than One: Revisiting the OER Mechanism on CoOOH by DFT with Electrode Polarization. *Physical Chemistry Chemical Physics* **2020**, *22* (13), 7031–7038. https://doi.org/10.1039/D0CP00281J.

(218) Nurlaela, E.; Wang, H.; Shinagawa, T.; Flanagan, S.; Ould-Chikh, S.; Qureshi, M.; Mics, Z.; Sautet, P.; Le Bahers, T.; Cánovas, E.; Bonn, M.; Takanabe, K. Enhanced Kinetics of Hole Transfer and Electrocatalysis during Photocatalytic Oxygen Evolution by Cocatalyst Tuning. *ACS Catal* **2016**, *6* (7), 4117–4126. https://doi.org/10.1021/ACSCATAL.6B00508.

(219) Hosseini Benhangi, P.; Gyenge, E.; Alfantazi, A.; Liang, Q.; Brocks, G.; Bieberle-Hütter, A. Oxygen Evolution Reaction (OER) Mechanism under Alkaline and Acidic Conditions. *Journal of Physics: Energy* **2021**, *3* (2), 026001. https://doi.org/10.1088/2515-7655/ABDC85.

(220) Ye, J.; Liu, C.; Ge, Q. DFT Study of CO 2 Adsorption and Hydrogenation on the in 2O 3 Surface. *Journal of Physical Chemistry C* **2012**, *116* (14), 7817–7825. https://doi.org/10.1021/JP3004773/ASSET/IMAGES/MEDIUM/JP-2012-004773_0010.GIF.

(221) Hartnagel, H.; A. L. Dawar; C. Jagadish; A. K. Jain. *Semiconducting Transparent Thin Films*; CRC Press, 1995.

(222) Von Weber, A.; Baxter, E. T.; White, H. S.; Anderson, S. L. Cluster Size Controls Branching between Water and Hydrogen Peroxide Production in Electrochemical Oxygen Reduction at Ptn/ITO. *Journal of Physical Chemistry C* **2015**. https://doi.org/10.1021/jp5119234.

(223) Geiger, S.; Kasian, O.; Mingers, A. M.; Mayrhofer, K. J. J.; Cherevko, S. Stability Limits of Tin-Based Electrocatalyst Supports. *Scientific Reports 2017 7:1* **2017**, *7* (1), 1–7. https://doi.org/10.1038/s41598-017-04079-9.

(224) Kumari, S.; Sautet, P. Highly Dispersed Pt Atoms and Clusters on Hydroxylated Indium Tin Oxide: A View from First-Principles Calculations. *J Mater Chem A Mater* **2021**, *9* (28), 15724–15733. https://doi.org/10.1039/d1ta03177e.

(225) Dou, J.; Sun, Z.; Opalade, A. A.; Wang, N.; Fu, W.; Tao, F. Operando Chemistry of Catalyst Surfaces during Catalysis. *Chem Soc Rev* **2017**, *46* (7), 2001–2027. https://doi.org/10.1039/C6CS00931J.

(226) Friebel, D.; Miller, D. J.; O'Grady, C. P.; Anniyev, T.; Bargar, J.; Bergmann, U.; Ogasawara, H.; Wikfeldt, K. T.; Pettersson, L. G. M.; Nilsson, A. In Situ X-Ray Probing Reveals Fingerprints of Surface Platinum Oxide. *Physical Chemistry Chemical Physics* **2010**, *13* (1), 262–266. https://doi.org/10.1039/C0CP01434F.

(227) Banis, M. N.; Yadegari, H.; Sun, Q.; Regier, T.; Boyko, T.; Zhou, J.; Yiu, Y. M.; Li, R.; Hu, Y.; Sham, T. K.; Sun, X. Revealing the Charge/Discharge Mechanism of Na–O2 Cells by in Situ Soft X-Ray Absorption Spectroscopy. *Energy Environ Sci* **2018**, *11* (8), 2073–2077. https://doi.org/10.1039/C8EE00721G.

(228) Zhang, J.; Zhao, Y.; Guo, X.; Chen, C.; Dong, C. L.; Liu, R. S.; Han, C. P.; Li, Y.; Gogotsi, Y.; Wang, G. Single Platinum Atoms Immobilized on an MXene as an Efficient Catalyst for the Hydrogen Evolution Reaction. *Nature Catalysis 2018 1:12* **2018**, *1* (12), 985–992. https://doi.org/10.1038/s41929-018-0195-1.

(229) Lu, Y.; Wang, J.; Yu, L.; Kovarik, L.; Zhang, X.; Hoffman, A. S.; Gallo, A.; Bare, S. R.; Sokaras, D.; Kroll, T.; Dagle, V.; Xin, H.; Karim, A. M. Identification of the Active Complex for CO Oxidation over Single-Atom Ir-on-MgAl2O4 Catalysts. *Nature Catalysis 2018 2:2* **2018**, *2* (2), 149–156. https://doi.org/10.1038/s41929-018-0192-4.

(230) Dessal, C.; Len, T.; Morfin, F.; Rousset, J. L.; Aouine, M.; Afanasiev, P.; Piccolo, L. Dynamics of Single Pt Atoms on Alumina during CO Oxidation Monitored by Operando X-Ray and Infrared Spectroscopies. *ACS Catal* **2019**, *9* (6), 5752–5759. https://doi.org/10.1021/ACSCATAL.9B00903/SUPPL_FILE/CS9B00903_SI_001.PDF.

(231) Li, J.; Banis, M. N.; Ren, Z.; Adair, K. R.; Doyle-Davis, K.; Meira, D. M.; Finfrock, Y. Z.; Zhang, L.; Kong, F.; Sham, T. K.; Li, R.; Luo, J.; Sun, X. Unveiling the Nature of Pt Single-Atom Catalyst during Electrocatalytic Hydrogen Evolution and Oxygen Reduction Reactions. *Small* **2021**, *17* (11), 2007245. https://doi.org/10.1002/SMLL.202007245.

(232) Cao, L.; Liu, W.; Luo, Q.; Yin, R.; Wang, B.; Weissenrieder, J.; Soldemo, M.; Yan, H.; Lin, Y.; Sun, Z.; Ma, C.; Zhang, W.; Chen, S.; Wang, H.; Guan, Q.; Yao, T.; Wei, S.; Yang, J.; Lu, J. Atomically Dispersed Iron Hydroxide Anchored on Pt for Preferential Oxidation of CO in H2. *Nature 2019 565:7741* **2019**, *565* (7741), 631–635. https://doi.org/10.1038/s41586-018-0869-5.

(233) Cao, L.; Luo, Q.; Liu, W.; Lin, Y.; Liu, X.; Cao, Y.; Zhang, W.; Wu, Y.; Yang, J.; Yao, T.; Wei, S. Identification of Single-Atom Active Sites in Carbon-Based Cobalt Catalysts during Electrocatalytic Hydrogen Evolution. *Nature Catalysis 2018 2:2* **2018**, *2* (2), 134–141. https://doi.org/10.1038/s41929-018-0203-5.

(234) Munnik, P.; De Jongh, P. E.; De Jong, K. P. Recent Developments in the Synthesis of Supported Catalysts. *Chemical Reviews*. American Chemical Society July 22, 2015, pp 6687–6718. https://doi.org/10.1021/cr500486u.

(235) Peterson, A. A.; Abild-Pedersen, F.; Studt, F.; Rossmeisl, J.; Nørskov, J. K. How Copper Catalyzes the Electroreduction of Carbon Dioxide into Hydrocarbon Fuels. *Energy Environ Sci* **2010**, *3* (9), 1311–1315. https://doi.org/10.1039/C0EE00071J.

(236) *Global Gas Flaring Reduction Partnership (GGFR) Homepage*. https://www.worldbank.org/en/programs/gasflaringreduction (accessed 2023-05-16).

(237) *World Energy Outlook 2020 – Analysis - IEA*. https://www.iea.org/reports/world-energy-outlook-2020 (accessed 2023-05-16).

(238) Renewable Energy Agency, I.; Methanol Institute, the. INNOVATION OUTLOOK RENEWABLE METHANOL in Partnership With. **2021**.

(239) Soucie, H.; Elam, M.; Mustain, W. E. Practical Assessment for At-Scale Electrochemical Conversion of Methane to Methanol. *ACS Energy Lett.* **2023**, *8*, 1218.

(240) Yuan, S.; Li, Y. D.; Peng, J. Y.; Questell-Santiago, Y. M.; Akkiraju, K.; Giordano, L.; Zheng, D. J.; Bagi, S.; Roman-Leshkov, Y.; Shao-Horn, Y. Conversion of Methane into Liquid Fuels-Bridging Thermal Catalysis with Electrocatalysis. *Adv. Energy Mater.* **2020**, *10*, 2002154.

(241) Mostaghimi, A. H. B.; Al-Attas, T. A.; Kibria, M. G.; Siahrostami, S. A Review on Electrocatalytic Oxidation of Methane to Oxygenates. *J. Mater. Chem. A* **2020**, *8*, 15575.

(242) Sher Shah, M. S. A.; Oh, C.; Park, H.; Hwang, Y.; Ma, M.; Park, J. Catalytic Oxidation of Methane to Oxygenated Products: Recent Advancements and Prospects for

Electrocatalytic and Photocatalytic Conversion at Low Temperatures. *Adv. Sci.* **2020**, *7*, 2001946.

(243) Deng, J.; Lin, S.; Fuller, J.; Iñiguez, J.; Xiang, D.; Yang, D.; Chan, G.; Chen, H.; Alexandrova, A.; Liu, C. Ambient Methane Functionalization Initiated by Electrochemical Oxidation of a Vanadium (V)-Oxo Dimer. *Nat. Commun.* **2020**, *11*, 3686.

(244) Kim, R. S.; Surendranath, Y. Electrochemical Reoxidation Enables Continuous Methane-to-Methanol Catalysis with Aqueous Pt Salts. *ACS Cent. Sci.* **2019**, *5*, 1179.

(245) Foster, N. R. Direct Catalytic Oxidation of Methane to Methanol - a Review. *Appl. Catal.* **1985**, *19*, 1.

(246) Sushkevich, V. L.; Palagin, D.; Ranocchiari, M.; van Bokhoven, J. A. Selective Anaerobic Oxidation of Methane Enables Direct Synthesis of Methanol. *Science (1979)* **2017**, *356*, 523.

(247) Gunsalus, N. J.; Koppaka, A.; Park, S. H.; Bischof, S. M.; Hashiguchi, B. G.; Periana, R. A. Homogeneous Functionalization of Methane. *Chem. Rev.* **2017**, *117*, 8521.

(248) Ravi, M.; Ranocchiari, M.; van Bokhoven, J. A. The Direct Catalytic Oxidation of Methane to Methanol-A Critical Assessment. *Angew. Chem., Int. Ed.* **2017**, *56*, 16464.

(249) Mahyuddin, M. H.; Shiota, Y.; Yoshizawa, K. Methane Selective Oxidation to Methanol by Metal-Exchanged Zeolites: A Review of Active Sites and Their Reactivity. *Catal. Sci. Technol.* **2019**, *9*, 1744.

(250) Andrikopoulos, P. C.; Michel, C.; Chouzier, S.; Sautet, P. In Silico Screening of Iron-Oxo Catalysts for CH Bond Cleavage. *ACS Catal.* **2015**, *5*, 2490.

(251) Ensing, B.; Buda, F.; Gribnau, M.; Baerends, E. Methane-to-Methanol Oxidation by the Hydrated Iron(IV) Oxo Species in Aqueous Solution: A Combined DFT and Car-Parrinello Molecular Dynamics Study. *J. Am. Chem. Soc.* **2004**, *126*, 4355.

(252) Szécsényi, Á.; Li, G.; Gascon, J.; Pidko, E. Mechanistic Complexity of Methane Oxidation with H2O2 by Single-Site Fe/ZSM-5 Catalyst. *ACS Catal.* **2018**, *8*, 7961.

(253) Sirajuddin, S.; Rosenzweig, A. C. Enzymatic Oxidation of Methane. *Biochemistry* **2015**, *54*, 2283.

(254) Lee, S. J.; McCormick, M.; Lippard, S.; Cho, U. Control of Substrate Access to the Active Site in Methane Monooxygenase. *Nature* **2013**, *494*, 380.

(255) Omasta, T. J.; Rigdon, W. A.; Lewis, C. A.; Stanis, R. J.; Liu, R.; Fan, C. Q.; Mustain, W. E. Two Pathways for Near Room Temperature Electrochemical Conversion of Methane to Methanol. *ECS Trans* **2015**, *66* (8), 129–136. https://doi.org/10.1149/06608.0129ECST.

(256) Spinner, N.; Mustain, W. Influence of Non-Conducting Zirconia on the Electrochemical Performance of Nickel Oxide in Alkaline Media at Room Temperature. *J. Electrochem. Soc.* **2012**, *159*, E187.

(257) Spinner, N.; Mustain, W. Electrochemical Methane Activation and Conversion to Oxygenates at Room Temperature. *J. Electrochem. Soc.* **2013**, *160*, F1275.

(258) Ma, M.; Jin, B. J.; Li, P.; Jung, M. S.; Kim, J. Il; Cho, Y.; Kim, S.; Moon, J. H.; Park, J. H. Ultrahigh Electrocatalytic Conversion of Methane at Room Temperature. *Advanced Science* **2017**, *4* (12). https://doi.org/10.1002/ADVS.201700379.

(259) Oh, C.; Kim, J.; Hwang, Y. J.; Ma, M.; Park, J. H. Electrocatalytic Methane Oxidation on Co3O4- Incorporated ZrO2 Nanotube Powder. *Appl. Catal., B* **2021**, *283*, 119653.

(260) Jang, J.; Rüscher, M.; Winzely, M.; Morales-Guio, C. G. Gastight Rotating Cylinder Electrode: Toward Decoupling Mass Transport and Intrinsic Kinetics in Electrocatalysis. *AIChE J.* **2022**, *68*, e17605.

(261) Song, Y. F.; Zhao, Y. H.; Nan, G. Z.; Chen, W.; Guo, Z. K.; Li, S. G.; Tang, Z. Y.; Wei, W.; Sun, Y. H. Electrocatalytic Oxidation of Methane to Ethanol via NiO/Ni Interface. *Appl. Catal., B* **2020**, *270*, 118888.

(262) Guo, Z.; Chen, W.; Song, Y.; Dong, X.; Li, G.; Wei, W.; Sun, Y. Efficient Methane Electrocatalytic Conversion over a Ni-Based Hollow Fiber Electrode. *Chin. J. Catal.* **2020**, *41*, 1067.

(263) Li, J. L.; Yao, L. B.; Wu, D. Z.; King, J.; Chuang, S. S. C.; Liu, B.; Peng, Z. M. Electrocatalytic Methane Oxidation to Ethanol on Iron-Nickel Hydroxide Nanosheets. *Appl. Catal., B* **2022**, *316*, 121657.

(264) Prajapati, A.; Collins, B. A.; Goodpaster, J. D.; Singh, M. R. Fundamental Insight into Electrochemical Oxidation of Methane towards Methanol on Transition Metal Oxides. *Proc. Natl. Acad. Sci.* **2021**, *118*, e2023233118.

(265) Prajapati, A.; Sartape, R.; Kani, N.; Gauthier, J.; Singh, M. Chloride-Promoted High-Rate Ambient Electrooxidation of Methane to Methanol on Patterned Cu-Ti Bimetallic Oxides. *ACS Catal.* **2022**, *12*, 14321.

(266) Boyd, M. J.; Latimer, A.; Dickens, C.; Nielander, A.; Hahn, C.; Norskov, J.; Higgins, D.; Jaramillo, T. Electro-Oxidation of Methane on Platinum under Ambient Conditions. *ACS Catal.* **2019**, *9*, 7578.

(267) García-Mota, M.; Bajdich, M.; Viswanathan, V.; Vojvodic, A.; Bell, A.; Norskov, J. Importance of Correlation in Determining Electrocatalytic Oxygen Evolution Activity on Cobalt Oxides. *J. Phys. Chem. C* **2012**, *116*, 21077.

(268) Bajdich, M.; Garcia-Mota, M.; Vojvodic, A.; Norskov, J.; Bell, A. Theoretical Investigation of the Activity of Cobalt Oxides for the Electrochemical Oxidation of Water. *J. Am. Chem. Soc.* **2013**, *135*, 13521.

(269) Nurlaela, E.; Shinagawa, T.; Qureshi, M.; Dhawale, D. S.; Takanabe, K. Temperature Dependence of Electrocatalytic and Photocatalytic Oxygen Evolution Reaction Rates Using NiFe Oxide. *ACS Catal* **2016**, *6* (3), 1713–1722. https://doi.org/10.1021/ACSCATAL.5B02804/ASSET/IMAGES/CS-2015-02804P_M011.GIF.

(270) Chivot, J.; Mendoza, L.; Mansour, C.; Pauporte, T.; Cassir, M. New Insight in the Behaviour of Co-H2O System at 25-150 OC, Based on Revised Pourbaix Diagrams. *Corros. Sci.* **2008**, *50*, 62.

(271) Dudarev, S. L.; Botton, G.; Savrasov, S.; Humphreys, C.; Sutton, A. Electron-Energy-Loss Spectra and the Structural Stability of Nickel Oxide: An LSDA+U Study. *Phys. Rev. B* **1998**, *57*, 1505.

(272) Morales-Guio, C. G.; Mayer, M.; Yella, A.; Tilley, S.; Gratzel, M.; Hu, X. An Optically Transparent Iron Nickel Oxide Catalyst for Solar Water Splitting. *J. Am. Chem. Soc.* **2015**, *137*, 9927.

(273) Kanan, M. W.; Surendranath, Y.; Nocera, D. Cobalt-Phosphate Oxygen-Evolving Compound. *Chem. Soc. Rev.* **2009**, *38*, 109.

(274) Stevens, M. B.; Enman, L.; Korkus, E.; Zaffran, J.; Trang, C.; Asbury, J.; Kast, M.; Toroker, M.; Boettcher, S. Ternary Ni-Co-Fe Oxyhydroxide Oxygen Evolution Catalysts: Intrinsic Activity Trends, Electrical Conductivity, and Electronic Band Structure. *Nano Res.* **2019**, *12*, 2288.

(275) Morales-Guio, C. G.; Liardet, L.; Hu, X. Oxidatively Electrodeposited Thin-Film Transition Metal (Oxy)Hydroxides as Oxygen Evolution Catalysts. *J. Am. Chem. Soc.* **2016**, *138*, 8946.

(276) Gerken, J. B.; McAlpin, J.; Chen, J.; Rigsby, M.; Casey, W.; Britt, R.; Stahl, S. Electrochemical Water Oxidation with Cobalt-Based Electrocatalysts from PH 0-14: The Thermodynamic Basis for Catalyst Structure, Stability, and Activity. *J. Am. Chem. Soc.* **2011**, *133*, 14431.

(277) Gannouni, A.; Delbecq, F.; Zina, M.; Sautet, P. Oxidation of Methane to Methanol over Single Site Palladium Oxide Species on Silica: A Mechanistic View from DFT. *J. Phys. Chem. A* **2017**, *121*, 5500.

(278) Göltl, F.; Michel, C.; Andrikopoulos, P.; Love, A.; Hafner, J.; Hermans, I.; Sautet, P. Computationally Exploring Confinement Effects in the Methane-to-Methanol Conversion over Iron-Oxo Centers in Zeolites. *ACS Catal.* **2016**, *6*, 8404.

(279) Wang, Y.; Kattel, S.; Gao, W.; Li, K.; Liu, P.; Chen, J. G.; Wang, H. Exploring the Ternary Interactions in Cu–ZnO–ZrO 2 Catalysts for Efficient CO 2 Hydrogenation to Methanol. *Nat Commun* **2019**, *10* (1). https://doi.org/10.1038/S41467-019-09072-6.

(280) Rungtaweevoranit, B.; Baek, J.; Araujo, J. R.; Archanjo, B. S.; Choi, K. M.; Yaghi, O. M.; Somorjai, G. A. Copper Nanocrystals Encapsulated in Zr-Based Metal-Organic Frameworks for Highly Selective CO2 Hydrogenation to Methanol. *Nano Lett* **2016**, *16*

(12), 7645–7649. https://doi.org/10.1021/ACS.NANOLETT.6B03637/ASSET/IMAGES/LARGE/NL-2016-03637E_0004.JPEG.

(281) Studt, F.; Behrens, M.; Kunkes, E. L.; Thomas, N.; Zander, S.; Tarasov, A.; Schumann, J.; Frei, E.; Varley, J. B.; Abild-Pedersen, F.; Nørskov, J. K.; Schlögl, R. The Mechanism of CO and CO2 Hydrogenation to Methanol over Cu-Based Catalysts. *ChemCatChem* **2015**, *7* (7), 1105–1111. https://doi.org/10.1002/CCTC.201500123.

(282) Waugh, K. C. Methanol Synthesis. *Catal Today* **1992**, *15* (1), 51–75. https://doi.org/10.1016/0920-5861(92)80122-4.

(283) Liu, X. M.; Lu, G. Q.; Yan, Z. F.; Beltramini, J. Recent Advances in Catalysts for Methanol Synthesis via Hydrogenation of CO and CO2. *Ind Eng Chem Res* **2003**, *42* (25), 6518–6530. https://doi.org/10.1021/IE020979S/ASSET/IMAGES/MEDIUM/IE020979SE00022.GIF.

(284) Yang, Y.; Evans, J.; Rodriguez, J. A.; White, M. G.; Liu, P. Fundamental Studies of Methanol Synthesis from CO2 Hydrogenation on Cu(111), Cu Clusters, and Cu/ZnO(000). *Physical Chemistry Chemical Physics* **2010**, *12* (33), 9909–9917. https://doi.org/10.1039/C001484B.

(285) Yang, Y.; White, M. G.; Liu, P. Theoretical Study of Methanol Synthesis from CO 2 Hydrogenation on Metal-Doped Cu(111) Surfaces. *Journal of Physical Chemistry C* **2012**, *116* (1), 248–256. https://doi.org/10.1021/JP208448C/ASSET/IMAGES/LARGE/JP-2011-08448C_0004.JPEG.

(286) Rui, N.; Shi, R.; Gutiérrez, R. A.; Rosales, R.; Kang, J.; Mahapatra, M.; Ramírez, P. J.; Senanayake, S. D.; Rodriguez, J. A. CO2 Hydrogenation on ZrO2/Cu(111) Surfaces:

Production of Methane and Methanol. *Ind Eng Chem Res* **2021**. https://doi.org/10.1021/ACS.IECR.1C03229.

(287) Tada, S.; Kayamori, S.; Honma, T.; Kamei, H.; Nariyuki, A.; Kon, K.; Toyao, T.; Shimizu, K. I.; Satokawa, S. Design of Interfacial Sites between Cu and Amorphous ZrO2 Dedicated to CO2-to-Methanol Hydrogenation. *ACS Catal* **2018**, *8* (9), 7809–7819. https://doi.org/10.1021/ACSCATAL.8B01396.

(288) Witoon, T.; Chalorngtham, J.; Dumrongbunditkul, P.; Chareonpanich, M.; Limtrakul, J. CO2 Hydrogenation to Methanol over Cu/ZrO2 Catalysts: Effects of Zirconia Phases. *Chemical Engineering Journal* **2016**, *293*, 327–336. https://doi.org/10.1016/J.CEJ.2016.02.069.

(289) Witoon, T.; Chalorngtham, J.; Dumrongbunditkul, P.; Chareonpanich, M.; Limtrakul, J. CO2 Hydrogenation to Methanol over Cu/ZrO2 Catalysts: Effects of Zirconia Phases. *Chem. Eng. J.* **2016**, *293*, 327–336. https://doi.org/10.1016/j.cej.2016.02.069.

(290) Reichenbach, T.; Mondal, K.; Jäger, M.; Vent-Schmidt, T.; Himmel, D.; Dybbert, V.; Bruix, A.; Krossing, I.; Walter, M.; Moseler, M. Ab Initio Study of CO2 Hydrogenation Mechanisms on Inverse ZnO/Cu Catalysts. *J Catal* **2018**, *360*, 168–174. https://doi.org/10.1016/J.JCAT.2018.01.035.

(291) Wu, C.; Lin, L.; Liu, J.; Zhang, J.; Zhang, F.; Zhou, T.; Rui, N.; Yao, S.; Deng, Y.; Yang, F.; Xu, W.; Luo, J.; Zhao, Y.; Yan, B.; Wen, X. D.; Rodriguez, J. A.; Ma, D. Inverse ZrO2/Cu as a Highly Efficient Methanol Synthesis Catalyst from CO2 Hydrogenation. *Nat Commun* **2020**, *11* (1). https://doi.org/10.1038/S41467-020-19634-8.

(292) Hong, Q. J.; Liu, Z. P. Mechanism of CO2 Hydrogenation over Cu/ZrO2($\bar{2}12$) Interface from First-Principles Kinetics Monte Carlo Simulations. *Surf Sci* **2010**, *604* (21–22), 1869–1876. https://doi.org/10.1016/J.SUSC.2010.07.018.

(293) Zhuang, H. D.; Bai, S. F.; Liu, X. M.; Yan, Z. F. Structure and Performance of Cu/ZrO2 Catalyst For the Synthesis of Methanol from CO2 Hydrogenation. *Journal of Fuel Chemistry and Technology* **2010**, *38* (4), 462–467. https://doi.org/10.1016/S1872-5813(10)60041-2.

(294) Zhao, H.; Yu, R.; Ma, S.; Xu, K.; Chen, Y.; Jiang, K.; Fang, Y.; Zhu, C.; Liu, X.; Tang, Y.; Wu, L.; Wu, Y.; Jiang, Q.; He, P.; Liu, Z.; Tan, L. The Role of Cu1–O3 Species in Single-Atom Cu/ZrO2 Catalyst for CO2 Hydrogenation. *Nature Catalysis 2022 5:9* **2022**, *5* (9), 818–831. https://doi.org/10.1038/s41929-022-00840-0.

(295) Wang, Y.; Kattel, S.; Gao, W.; Li, K.; Liu, P.; Chen, J. G.; Wang, H. Exploring the Ternary Interactions in Cu-ZnO-ZrO2 Catalysts for Efficient CO2 Hydrogenation to Methanol. *Nat. Commun.* **2019**, *10* (1). https://doi.org/10.1038/s41467-019-09072-6.

(296) Wang, J.; Li, G.; Li, Z.; Tang, C.; Feng, Z.; An, H.; Liu, H.; Liu, T.; Li, C. A Highly Selective and Stable ZnO-ZrO2 Solid Solution Catalyst for CO2 Hydrogenation to Methanol. *Sci. Adv.* **2017**, *3* (10), e1701290. https://doi.org/10.1126/sciadv.1701290.

(297) Guo, X.; Mao, D.; Lu, G.; Wang, S.; Wu, G. Glycine-Nitrate Combustion Synthesis of CuO-ZnO-ZrO2 Catalysts for Methanol Synthesis from CO2 Hydrogenation. *J Catal* **2010**, *271* (2), 178–185. https://doi.org/10.1016/J.JCAT.2010.01.009.

(298) Samson, K.; Sliwa, M.; Socha, R. P.; Góra-Marek, K.; Mucha, D.; Rutkowska-Zbik, D.; Paul, J. F.; Ruggiero-Mikoajczyk, M.; Grabowski, R.; Soczyński, J. Influence of ZrO2 Structure

and Copper Electronic State on Activity of Cu/ZrO2 Catalysts in Methanol Synthesis from CO2. *ACS Catal* **2014**, *4* (10), 3730–3741. https://doi.org/10.1021/CS500979C/SUPPL_FILE/CS500979C_SI_002.PDF.

(299) Kattel, S.; Yan, B.; Yang, Y.; Chen, J. G.; Liu, P. Optimizing Binding Energies of Key Intermediates for CO2 Hydrogenation to Methanol over Oxide-Supported Copper. *J Am Chem Soc* **2016**, *138* (38), 12440–12450. https://doi.org/10.1021/JACS.6B05791.

(300) Li, K.; Chen, J. G. CO2 Hydrogenation to Methanol over ZrO2-Containing Catalysts: Insights into ZrO2 Induced Synergy. *ACS Catal* **2019**, *9* (9), 7840–7861. https://doi.org/10.1021/ACSCATAL.9B01943.

(301) Larmier, K.; Liao, W. C.; Tada, S.; Lam, E.; Verel, R.; Bansode, A.; Urakawa, A.; Comas-Vives, A.; Copéret, C. CO2-to-Methanol Hydrogenation on Zirconia-Supported Copper Nanoparticles: Reaction Intermediates and the Role of the Metal–Support Interface. *Angewandte Chemie International Edition* **2017**, *56* (9), 2318–2323. https://doi.org/10.1002/ANIE.201610166.

(302) Ma, Y.; Wang, J.; Goodman, K. R.; Head, A. R.; Tong, X.; Stacchiola, D. J.; White, M. G. Reactivity of a Zirconia−Copper Inverse Catalyst for CO 2 Hydrogenation. *J. Phys. Chem. C* **2020**, *124*. https://doi.org/10.1021/acs.jpcc.0c06624.

(303) Munarriz, J.; Zhang, Z.; Sautet, P.; Alexandrova, A. N. Graphite-Supported PtnCluster Electrocatalysts: Major Change of Active Sites as a Function of the Applied Potential. *ACS Catal* **2022**, *12* (23), 14517–14526. https://doi.org/10.1021/ACSCATAL.2C04643/ASSET/IMAGES/LARGE/CS2C04643_0004.JPEG.

(304) Zhang, Z.; Masubuchi, T.; Sautet, P.; Anderson, S. L.; Alexandrova, A. N.; Zhang, Z.; Sautet, P.; Alexandrova, A. N.; Masubuchi, T.; Anderson, S. L. Hydrogen Evolution on FTO-Supported Ptn Clusters: Ensemble of Hydride States Governs the Size Dependent Reactivity. **2022**. https://doi.org/10.26434/CHEMRXIV-2022-SSH9N.

(305) Kumari, S.; Sautet, P. Elucidation of the Active Site for the Oxygen Evolution Reaction on a Single Pt Atom Supported on Indium Tin Oxide. *Journal of Physical Chemistry Letters* **2023**, 2635–2643. https://doi.org/10.1021/ACS.JPCLETT.3C00160.

(306) Liu, L.; Su, X.; Zhang, H.; Gao, N.; Xue, F.; Ma, Y.; Jiang, Z.; Fang, T. Zirconia-Modified Copper Catalyst for CO2 Conversion to Methanol from DFT Study. *Appl Surf Sci* **2020**, *528*, 146900. https://doi.org/10.1016/J.APSUSC.2020.146900.

(307) Tang, X.; Zhang, H.; Sun, C.; Qiao, X.; Ju, D. Adsorption Mechanisms over ZrO2-Modified Cu(1 1 1) Surface for X (CH3OH, H2O and CO): A DFT+U Study. *Surf Sci* **2022**, *716*, 121976. https://doi.org/10.1016/J.SUSC.2021.121976.

(308) Ha, M. A.; Dadras, J.; Alexandrova, A. Rutile-Deposited Pt-Pd Clusters: A Hypothesis Regarding the Stability at 50/50 Ratio. *ACS Catal* **2014**, *4* (10), 3570–3580. https://doi.org/10.1021/CS5011426.

(309) Meng, G.; Arkus, N.; Brenner, M. P.; Manoharan, V. N. The Free-Energy Landscape of Clusters of Attractive Hard Spheres. *Science (1979)* **2010**, *327* (5965), 560–563. https://doi.org/10.1126/SCIENCE.1181263/SUPPL_FILE/MENG.SOM.PDF.

(310) Campbell, C. T.; Ernst, K.-H. Forward and Reverse Water—Gas Shift Reactions on Model Copper Catalysts. **1992**, 130–142. https://doi.org/10.1021/BK-1992-0482.CH008.

(311) Klier, K. Methanol Synthesis. *Advances in Catalysis* **1982**, *31* (C), 243–313. https://doi.org/10.1016/S0360-0564(08)60455-1.

(312) Chinchen, G. C.; Denny, P. J.; Parker, D. G.; Spencer, M. S.; Whan, D. A. Mechanism of Methanol Synthesis from CO2/CO/H2 Mixtures over Copper/Zinc Oxide/Alumina Catalysts: Use Of14C-Labelled Reactants. *Appl Catal* **1987**, *30* (2), 333–338. https://doi.org/10.1016/S0166-9834(00)84123-8.

(313) Saito, M.; Fujitani, T.; Takeuchi, M.; Watanabe, T. Development of Copper/Zinc Oxide-Based Multicomponent Catalysts for Methanol Synthesis from Carbon Dioxide and Hydrogen. *Appl Catal A Gen* **1996**, *138* (2), 311–318. https://doi.org/10.1016/0926-860X(95)00305-3.

(314) Toyir, J.; De la Piscina, P. R.; Fierro, J. L. G.; Homs, N. Catalytic Performance for CO2 Conversion to Methanol of Gallium-Promoted Copper-Based Catalysts: Influence of Metallic Precursors. *Appl Catal B* **2001**, *34* (4), 255–266. https://doi.org/10.1016/S0926-3373(01)00203-X.

(315) Zhang, Z.; Cui, Z. H.; Jimenez-Izal, E.; Sautet, P.; Alexandrova, A. N. Hydrogen Evolution on Restructured B-Rich WB: Metastable Surface States and Isolated Active Sites. *ACS Catal* **2020**, *10* (23), 13867–13877. https://doi.org/10.1021/ACSCATAL.0C03410/SUPPL_FILE/CS0C03410_SI_001.PDF.

(316) Boyd, K. J.; Łapicki, A.; Aizawa, M.; Anderson, S. L. A Phase-Space-Compressing, Mass-Selecting Beamline for Hyperthermal, Focused Ion Beam Deposition. *Rev. Sci. Instrum.* **1998**, *69* (12), 4106–4115. https://doi.org/10.1063/1.1149242.

(317) Proch, S.; Wirth, M.; White, H. S.; Anderson, S. L. Strong Effects of Cluster Size and Air Exposure on Oxygen Reduction and Carbon Oxidation Electrocatalysis by Size-Selected Ptn (n ≤ 11) on Glassy Carbon Electrodes. *J. Am. Chem. Soc.* **2013**, *135* (8), 3073–3086. https://doi.org/10.1021/ja309868z.

(318) von Weber, A.; Anderson, S. L. Electrocatalysis by Mass-Selected Pt $_n$ Clusters. *Acc Chem Res* **2016**, *49* (11), 2632–2639. https://doi.org/10.1021/acs.accounts.6b00387.

(319) Von Weber, A.; Baxter, E. T.; White, H. S.; Anderson, S. L. Cluster Size Controls Branching between Water and Hydrogen Peroxide Production in Electrochemical Oxygen Reduction at Ptn/ITO. *J. Phys. Chem. C* **2015**, *119* (20), 11160–11170. https://doi.org/10.1021/jp5119234.

(320) Sawyer, D. T.; Sobkowiak, A.; Roberts, J. L. *Electrochemistry for Chemists, 2nd Edition*; Wiley & Sons: New York, 1995.

(321) Ramette, R. W. Outmoded Terminology: The Normal Hydrogen Electrode. *J. Chem. Educ.* **1987**, *64* (10), 885. https://doi.org/10.1021/ed064p885.

(322) Li, G.; Poths, P.; Masubuchi, T.; Morgan, H. W. T.; Alexandrova, A. N.; Anderson, S. L. Got Coke? Self-Limiting Poisoning Makes an Ultra Stable and Selective Sub-Nano Cluster Catalyst. **2022**. https://doi.org/10.26434/CHEMRXIV-2022-L10K7.

(323) Conway, B. E.; Tilak, B. v. Interfacial Processes Involving Electrocatalytic Evolution and Oxidation of H2, and the Role of Chemisorbed H. *Electrochim. Acta* **2002**, *47* (22), 3571–3594. https://doi.org/10.1016/S0013-4686(02)00329-8.

(324) Geiger, S.; Kasian, O.; Mingers, A. M.; Mayrhofer, K. J. J.; Cherevko, S. Stability Limits of Tin-Based Electrocatalyst Supports. *Sci. Rep.* **2017**, *7* (1), 4595. https://doi.org/10.1038/s41598-017-04079-9.

(325) Steinmann, S. N.; Sautet, P.; Michel, C. Solvation Free Energies for Periodic Surfaces: Comparison of Implicit and Explicit Solvation Models. *Physical Chemistry Chemical Physics* **2016**, *18* (46). https://doi.org/10.1039/c6cp04094b.

(326) Sundararaman, R.; Schwarz, K. Evaluating Continuum Solvation Models for the Electrode-Electrolyte Interface: Challenges and Strategies for Improvement. *Journal of Chemical Physics* **2017**, *146* (8). https://doi.org/10.1063/1.4976971.

(327) Ringe, S.; Hörmann, N. G.; Oberhofer, H.; Reuter, K. Implicit Solvation Methods for Catalysis at Electrified Interfaces. *Chemical Reviews*. 2022. https://doi.org/10.1021/acs.chemrev.1c00675.

(328) Lespes, N.; Filhol, J. S. Using Implicit Solvent in Ab Initio Electrochemical Modeling: Investigating Li+/Li Electrochemistry at a Li/Solvent Interface. *J Chem Theory Comput* **2015**, *11* (7). https://doi.org/10.1021/acs.jctc.5b00170.

(329) Skyner, R. E.; McDonagh, J. L.; Groom, C. R.; Van Mourik, T.; Mitchell, J. B. O. A Review of Methods for the Calculation of Solution Free Energies and the Modelling of Systems in Solution. *Physical Chemistry Chemical Physics*. 2015. https://doi.org/10.1039/c5cp00288e.

(330) Hagopian, A.; Falcone, A.; Ben Yahia, M.; Filhol, J. S. Ab Initio Modelling of Interfacial Electrochemical Properties: Beyond Implicit Solvation Limitations. *Journal of Physics Condensed Matter* **2021**, *33* (30). https://doi.org/10.1088/1361-648X/ac0207.

(331) Cheng, D.; Zhao, Z. J.; Zhang, G.; Yang, P.; Li, L.; Gao, H.; Liu, S.; Chang, X.; Chen, S.; Wang, T.; Ozin, G. A.; Liu, Z.; Gong, J. The Nature of Active Sites for Carbon Dioxide Electroreduction over Oxide-Derived Copper Catalysts. *Nature Communications 2021 12:1* **2021**, *12* (1), 1–8. https://doi.org/10.1038/s41467-020-20615-0.

(332) Richard, D.; Tom, M.; Jang, J.; Yun, S. G.; Christofides, P. D.; Morales-Guio, C. G. Quantifying Transport and Electrocatalytic Reaction Processes in a Gastight Rotating Cylinder Electrode Reactor via Integration of Computational Fluid Dynamics Modeling and Experiments. *Electrochim. Acta* **2023**, *440*, 141698.